# Imaging of HIV-1 Spread from T cells and Macrophages to Astrocytes

Thesis submitted for the degree of
Doctor of Philosophy
Michaelmas 2014

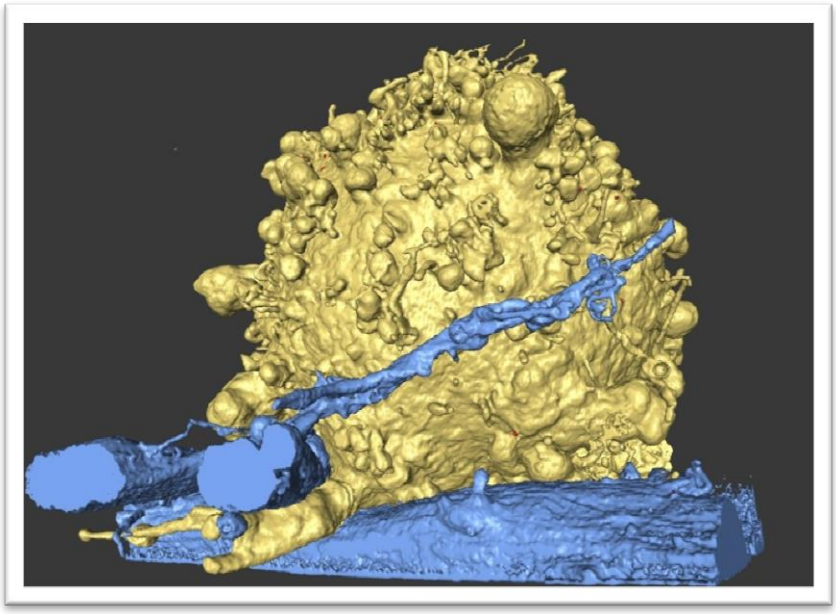


## Thao Phuong Do

Sir William Dunn School of Pathology
Green Templeton College
University of Oxford, United Kingdom

Laboratory of Cell Biology
National Cancer Institute
National Institutes of Health, United States

# Contents

# Abstract


**Imaging of HIV-1 Spread from T cells and Macrophages to Astrocytes**

Written by Thao Do, Green Templeton College, Submitted for the degree of Doctor of Philosophy at University of Oxford, Michaelmas Term 2014

CD4+ T cells and macrophages are the principal targets of HIV-1. They can be productively infected with the virus and transfer virions to contacting bystander cells. It has been suggested that soon after initial infection, free virions and virus-bearing or infected T cells and macrophages can enter the brain, triggering a cascade of inflammatory signals and recruitment of other immune cells. Chronic inflammation and increased viral antigens in the brain lead to HIV-1 associated neuropathy.

Once free virions or infected cells enter the central nervous system, the first type of brain cells that they are likely to encounter are astrocytes, which extend endfeet around the blood vessels. These cells have been observed to contain virions and viral products, but their permissivity to productive infection has not been clearly demonstrated. By contrast, productive infection of resident microglia and perivascular macrophages is well established.

Here, I investigate the permissivity of astrocytes to HIV-1 infection and found no evidence of infection by the free route. However, I found that astrocytes intimately contact HIV-1 infected macrophages and CD4+ T cells and, in some cases, extend filopodial membrane toward the infected cell. In astrocyte-T cell contact sites, termed synapses, virions appear to move along the astrocytic filopodia from the T cell to the astrocyte. In this case, the target cell mediated viral transfer across the intercellular gap.

HIV-1-infected macrophages released virus that associated with astrocytes, remaining either on the surface of the astrocytes or within intracellular compartments. HIV-1 bound to astrocytes could be transmitted efficiently to permissive cells *in trans*. However, astrocyte-associated virus was sensitive to inhibitors including proteases and neutralizing antibodies, suggesting a surface-accessible compartment. This work provides insight into mechanisms of HIV-1 spread in the brain from infected CD4+ T cells and macrophages to astrocytes and their potential as virus reservoirs.

I also optimized high resolution, correlative focused ion beam scanning electron microscopy technology to answer fundamental biological questions. I demonstrate the application of the technology to study skeletal muscle cell differentiation mechanisms. I combine the power of genetic mapping with structural analysis to qualitatively and quantitatively describe cellular states and functions. Using semi-automatic image processing analysis, I was able to compute high volumes of data and generate statistics that relate quantitative measurements of cellular structures to functions. The toolset developed here will be instrumental in studying cells and tissues in both research and clinical applications.

## Acknowledgement

I thank Dr. Sriram Subramaniam and Professor Quentin Sattentau for guiding me through my Ph.D experience. They have challenged and motivated me to become a better research scientist and I am very privileged to have them as my advisors. I appreciate the opportunity to work in their laboratories and access a diverse range of expertise and resources.

I am thankful to have worked with amazing colleagues in both the Subramaniam and Sattentau laboratories. From the US side, I would like to especially thank Madhvi Venkatesh, Jason Murray, Dr. Ambika Bumb, Prashant Rao, Dr. Audray Harris, Dan Shi, Lisa Hartnell, Dr. Lesley Earl, Dr. Tommie White, Dr. Kedar Narayan, Dr. Gavin Murphy, Aaron Neal, Casmir Turnquist and Bobby Hollingsworth for teaching me microscopy and cell biology and making science fun! I thank the NIH-OxCam MD-PhD students, especially Andrew Ishizuka, for organizing the Clinical Case Studies. Discussing clinical cases from a doctor's perspective reminds me of why I do biomedical research.

From the UK side, I would like to thank Adjoa Smalls-Mantey, Torben Schiffner, Dr. Rebecca Moore, Dr. Chris Duncan, Dr. Amy Baxter, Dr. Sophie Fleurdepine, Dr. Sally Cowley, Dr. Kenny Moore, Julian Buchrieser, Damien Warner, Cathy Browne, and Professor Sally Cowley for teaching me virology, stem cell culture, and making UK a home-away-from-home for me. I especially thank Richard Stillion for teaching me histology. I also thank my friends Darren Neo, Perry Trafford, Wayne Prescott, and the Ferry Leisure Center badminton club for keeping me active. I thank Keith and Theresa Frayn, Rowan Barnden, and Mark Ovland for bringing me so much joy with their smiles and kindness. They have become my extended family and I really appreciate their support.

I thank the NIH-OxCam administrators, Matt Vogt, Bridget Lampert, and Dr. Michael Lenardo, the LCB/NIH administrator, Consuelo Holguin, the FAES housing managers, Rose McNeely and Carline Coote, and the OSAP housing manager, Adam Brown and Andrew Camden, for supporting my basic needs like providing housing, scheduling travel arrangements, and organizing colloquium events.

I am thankful for my aunts, uncles, cousins, and grandmother for always being proud of me and sharing my accomplishments with everyone. I am thankful for the Miracle family, Charlie, Betty, Aaron, Jack, Sarah, Erik, Isaac, the doggies, Peanut, Petunia, Penelope, Claude, and the guinea pigs, Thor and Hulk, for keeping me entertained.

I am thankful for my parents Bieu Do and Anh Dao Nguyen and my big brother Thong Do for always being there to celebrate my achievements. My parents were instrumental in making my transitions between my international travels go smoothly. I can always count on them to drive me back and forth from home to the airports, provide yummy food and clothes, and give me lots of love!

I especially thank Michael Miracle for always being there for me throughout the process and keeping me motivated. He is my rock and provides me with housing, food, and all the comforts of home while making the writing process fun!

## Thesis contribution

I especially thank Torben Schiffner for contributing Env images for Figure 1.2 and providing neutralizing antibodies, Dr. Jakub Chojnacki for contributing the STED images for Figure 4.7, 4.8, Dr. Jeffrey Spector for contributing the SIM images for Figure 3.2, Figure 5.3, Dr. Guanhan Li for collaborating with me in the tissue culture steps for Chapter 5, Kunio Nagashima and Errin Johnson for teaching me EM, and Kent McDonald for teaching me HPF-QS.

## Abbreviations

| | |
|---|---|
| 2-ME | 2-Mercaptoethanol |
| 2D or 3D | 2 or 3 dimensional |
| 3TC | lamivudine |
| ABC | abacavir |
| AIDS | acquired immune deficiency syndrome |
| APC | antigen presenting cells |
| APOBEC3G | apolipoprotein B mRNA editing enzyme, catalytic polypeptide-like3G ATV atazanavir |
| AZT | zidovudine |
| BBB | blood brain barrier |
| B.C. | Ben Chen |
| BMVE | brain microvascular endothelial cells |
| bNabs | broadly neutralizing antibodies |
| BSA | bovine serum albumin |
| CA | capsid protein |
| CCD | charged couple device |
| CCL | chemokine (C-C motif) ligand |
| CCR5 | C-C Chemokine Receptor Type 5 |
| CHR | C-terminal heptad repeat |
| CNS | central nervous system |
| CTL | cytotoxic T lymphocyte |
| CXCR4 | C-X-C Chemokine Receptor Type 4 |
| D.p.i | days post infection |
| D4T | stavudine |
| DAPI | 4',6-diamidino-2-phenylindole |
| DC | dendritic cells |
| DIC | differential interference contrast |
| DMEM | Dulbecco's Modified Eagle Medium |
| DMSO | dimethyl sulfoxide |
| DRV | darunavir |
| EB | embryonic bodies |
| EDTA | Ethylenediaminetetraacetic acid |
| EFV | efavirenz |
| ELISA | enzyme-linked immunosorbent assay |
| ENF | enfuvirtide |
| ER | endoplasmic reticulum |
| ESCRT | endosomal sorting complexes required for transport |
| ETR | etravirine |
| FBS | fetal bovine serum |
| FDC | follicular dendritic cells |

| | |
|---|---|
| FIB-SEM | focused ion beam scanning electron microscopy |
| F-RLU | Firefly relative luminescent unit |
| FTC | emtricitabine |
| GalCer | galactosylceramide |
| GALT | gut associated lymphoid tissue |
| GFAP | glial fibrillary acidic protein |
| GFP | green fluorescence protein |
| H&E | hematoxylin and eosin stain |
| HAART | highly active antiretroviral therapy |
| HAD | HIV-1 associated dementia |
| HFA | human fetal astrocytes |
| HIV | human immunodeficiency virus |
| HMDS | hexamethyldisiloxane |
| HRP | horseradish peroxidase |
| ICAM | intercellular adhesion molecule |
| IFN | interferon |
| IL | interleukin |
| IMC | infectious molecular clones |
| IN | integrase |
| iPS-MDM | induced pluripotent stem cell monocyte derived macrophages |
| IS | immunological synapse |
| LFA | lymphocyte function-associated antigen |
| LPS | lipopolysaccharide |
| LTR | long terminal repeats |
| LucR | Renilla luciferase |
| MA | matrix protein |
| MCP | monocyte chemotactic protein |
| MCSF | macrophage colony-stimulating factor |
| MDM | monocyte derived macrophage |
| MEF | mouse embryonic fibroblasts |
| MG | malignant glioma |
| MHC | major histocompatibility complex |
| MMP | matrix metallopeptidases |
| MPER | membrane proximal external region |
| MRF | myogenic regulatory factors |
| mRNA | messenger RNA |
| Nabs | neutralizing antibodies |
| NC | nucleocapsid protein |
| Nef | negative regulatory factor |
| NFAT | nuclear factor of activated T cells |
| NF-kB | nuclear factor kappa-light-chain-enhancer of activated B cells |
| NHR | N-terminal heptad repeat |
| NIH | National Institutes of Health, USA |
| NK | natural killer cells |
| NKT | natural killer T cells |
| NMR | nuclear magnetic resonance |
| NNRTIs | non-nucleoside reverse transcriptase inhibitors |
| NPC | nuclear pore complex |
| NRTIs | nucleoside/nucleotide reverse transcriptase inhibitors |
| NVP | nevirapine |
| P/S | penicillin/streptomycin |
| P.B. | Phillipe Benaroch |

| | |
|---|---|
| PBMC | peripheral blood mononuclear cells |
| Pbs | primer binding site |
| PBS | Phosphate Buffered Saline |
| PCR | polymerase chain reactions |
| PHA | Phytohaemagglutinin |
| PIC | pre-integration complex |
| PLT | peripheral lymphoid tissues |
| PPT | polypurine tract |
| PR | protease |
| P-TEFb | positive transcription elongation factor b |
| HPF-QS | quick substitution-high pressure freezing |
| RAL | raltegravir |
| RANTES | regulated on activation, normal T cell expressed and secreted |
| Rev | regulator of virion |
| RLU | relative luminescent unit |
| RNA | ribonucleic acid |
| ROI | regions of interest |
| RPMI | Roswell Park Memorial Institute |
| R-RLU | Renilla relative luminescent unit |
| RT | reverse transcriptase |
| rt | room temperature |
| RTC | reverse transcription complex |
| SAMHD1 | deoxynucleoside triphosphate triphosphohydrolase |
| SBF-SEM | serial block face scanning electron microscopy |
| SCB | Sodium Cacodylate Buffer |
| SD | standard deviation |
| SIM | structure illumination microscopy |
| SIV | simian immunodeficiency virus |
| SQV | saquinavir |
| SRL | ScienCell Research Laboratories |
| STED | stimulated emission depletion microscopy |
| SU | surface protein |
| TAR | trans-activating response element |
| Tat | trans-activator of transcription |
| TBS | Tris-buffered saline |
| TEM | transmission electron microscopy |
| TM | transmembrane protein |
| TNF | tumor necrosis factor |
| tRNA | transfer RNA |
| VCC | virus containing compartment |
| vDNA | viral DNA |
| Vif | viral infectivity factor |
| Vpr, Vpu, Vpx | viral protein r, viral protein u, viral protein x |
| vRNA | viral RNA |
| VS | virological synapse |

# 1 Introduction

## 1.1 Origins and discovery

More than 34 million people worldwide are infected with HIV and more than 30 million have died from HIV-related causes (1). HIV is a lentivirus in the *Retroviridae* family that causes acquired immunodeficiency syndrome (AIDS). There are two types of HIV: HIV-1 and HIV-2. HIV originated in chimpanzees (HIV-1) and sooty mangabeys (HIV-2) that were infected with simian immunodeficiency virus (SIV). Humans who hunted or sold bushmeat often acquired SIV (2). Through serial passages of SIV between humans, possibly by cross-contaminated vaccine and drug injections in Africa between 1950-1970, SIV mutated into HIV (3).

HIV-1 has increased virulence (4) and a higher rate of transmission (5, 6) than HIV-2. Thus, HIV-1 is spread globally, especially in developing countries, and accounts for most of the total HIV infection while HIV-2 is mainly confined in West Africa (7, 8). This thesis focuses on HIV-1. HIV-1 can be transmitted from human to human through contaminated blood (blood transfusions, needle stick injury, intravenous drug sharing) and fluid transfer from mother to baby (breastfeeding, pregnancy), but the dominant mode of spread is between sexual partners (75-85% of HIV infection worldwide) (9).

The earliest case of HIV-1 infection was dated to 1959 (10) but it was not until June 1981 when the first documented cases were reported. Healthy gay men in New York and California were hospitalized after contracting *Pneumocystis carinii* pneumonia and a rare skin cancer called Kaposi's sarcoma (11). Baffled by the new disease, doctors could only provide palliative care to patients, who often died within months of diagnosis (12). In 1983, Luc

Montagnier's team in France (13) and Robert Gallo's group in the United States (14) made a breakthrough when they finally linked HIV-1 to AIDS.

## 1.2 Structure of the HIV-1 virus

HIV-1 virions are spherical with an average diameter of ~145 nm with cone-shaped cores (15) (Figure 1.1). The viral particle is bound by a lipid membrane, inside of which is the p17 matrix protein (MA). The viral envelope is decorated with gp120 surface glycoprotein and gp41 transmembrane glycoprotein; together, these envelope (Env) glycoprotein trimers form the characteristic spikes that allow the virus to bind to the cellular receptors. The Env trimers are masked by complex carbohydrate glycans to evade immune recognition (Figure 1.2). Gp120 has five relatively conserved regions (C1-C5) and five variable regions (V1-V5) organized into inner and outer domains connected by 4-stranded anti-parallel β sheet, called the bridging sheet (16).

HIV-1 particles also contain viral enzymes (reverse transcriptase (RT), integrase (IN), and protease (PR)), viral accessory proteins (viral protein u (Vpu), viral infectivity factor (Vif), viral protein r (Vpr), p6, negative regulatory factor (Nef)), and viral regulatory proteins (regulator of virion (Rev) and trans-activator of transcription (Tat)).

Within the spherical shell, p24 capsid protein (CA) makes up the conical core with a length of ~100-120 nm and a diameter of ~50-60 nm (15, 17) that harbors the genomic viral ribonucleic acid (vRNA) coated with p7 nucleocapsid protein (NC) and associated with RT, IN, MA, and Vpr. These products are encoded in nine different HIV genes: gag (MA, CA, NC, p6), pol (PR, RT, IN), env (SU, TM), tat, rev, nef, vpr, vif, vpu (Figure 1.3 A) on two identical positive single stranded RNA (ssRNA).

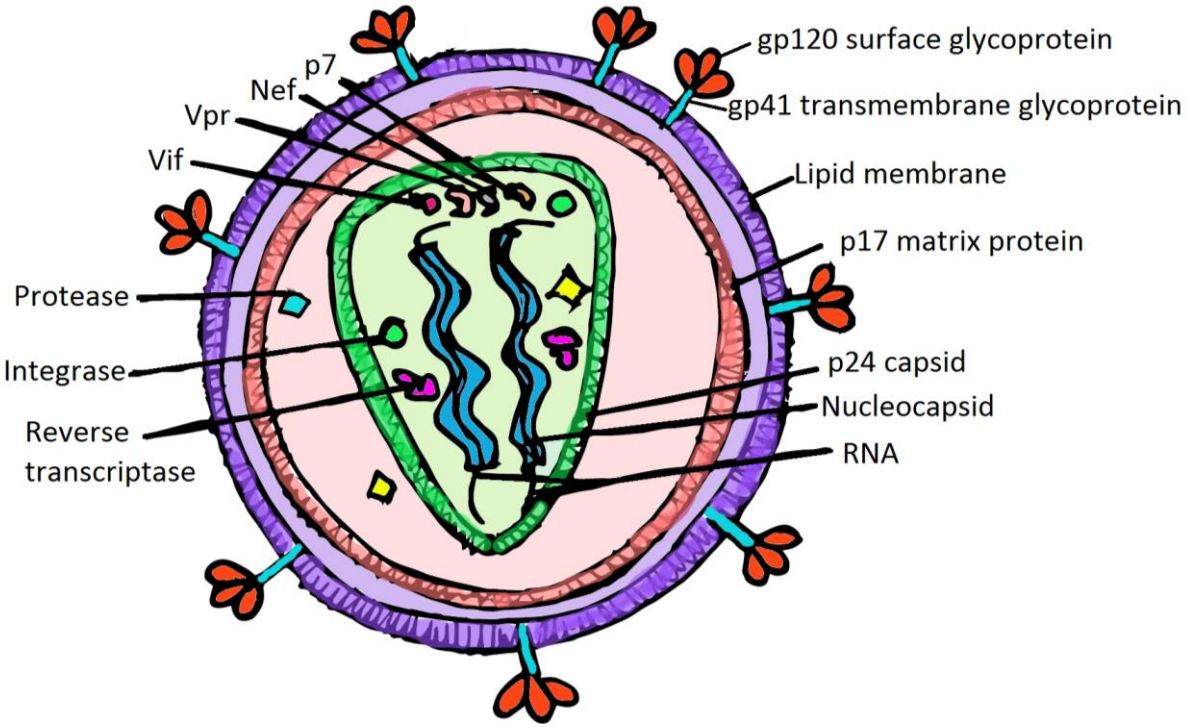


**Figure 1.1** Structure of HIV-1 virus shows two copies of RNA and viral proteins inside a conical p24 capsid contained within p17 matrix protein and lipid membrane. The envelope contains trimeric gp120 and gp41 glycoproteins.

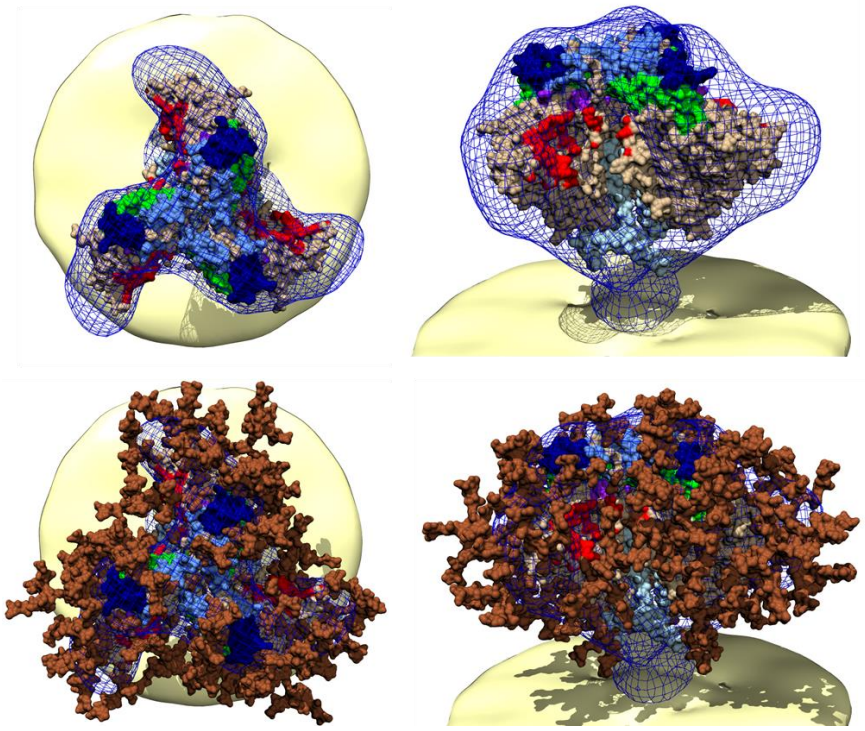

**Figure 1.2** Model of gp120/gp41 on HIV-1 envelope from cryo-transmission electron microscopy (cryo-TEM) created by Torben Schiffner. Top: glycans are removed. Bottom: glycans are present. Left: top view. Right: side view. Viral envelope (yellow), sub-volume averaging of electron tomography of Env (mesh), gp120 (tan), gp41 (sky), CD4 binding site (red), V1/V2 loops (navy), V3 (green), co-receptor binding site (purple), N-linked glycans (brown).

## 1.3 HIV-1 replication cycle

A summary of the HIV-1 replication process is reviewed in (18–21) (Figure 1.3 B). HIV-1 subverts many host cell mechanisms to replicate.

### 1.3.1 Viral entry: Env cluster

To establish infection, Env spikes form a tight cluster at the contact zone, creating an “entry claw” to facilitate entry (22). The efficiency of HIV-1 entry is directly correlated with its ability to form an Env cluster (23), possibly because the low number (~8-10) of Env trimers available on the envelope require a concerted localised action (24). Env clustering is induced by the maturation process through the interactions between Gag and Env proteins prior to CD4 engagement. When immature virion buds from a cell membrane, Env trimers incorporate into the virion in a randomly dispersed distribution through the interactions of gp41 C-terminal tail and the Gag polyprotein (Figure 1.3 C) (25–27). At this stage, Env lateral movement is limited by the rigid immature hexameric Gag lattice. When the virion matures, PR cleaves the Gag polyprotein, separating the MA and CA and allowing Env trimers to mobilize to a single focal point and engage with the CD4 receptor on the target cells (23).

### 1.3.2 Viral attachment: cellular receptors

In most cases, HIV-1 gp120 attaches to the cellular surface receptor CD4 (28, 29) and subsequently to a chemokine co-receptor, either C-X-C Chemokine Receptor Type 4 (CXCR4) (30) or C-C Chemokine Receptor Type 5 (CCR5) (31, 32), on the host cell membrane. The binding of gp120 to CD4 is often weak because of the low number of CD4 receptors on most HIV-1 permissive cells and the limited accessibility to the sterically-restricted CD4-binding site on the Env trimer (33). Other molecules have been reported to stabilize and enhance viral attachment (reviewed in (33)), such as heparin sulphate

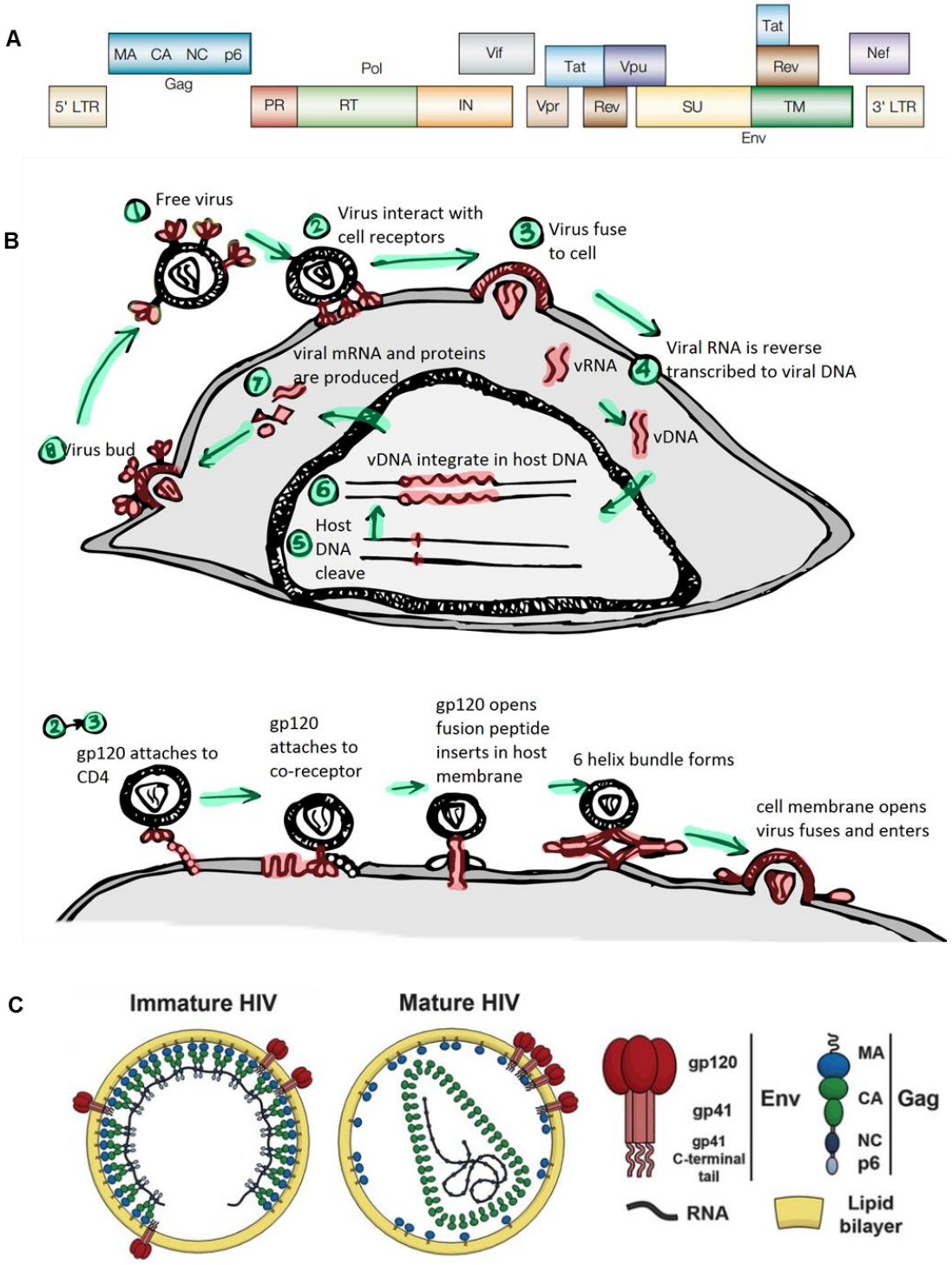


**Figure 1.3** HIV-1 genome contains nine different HIV genes: gag (MA, CA, NC, p6), pol (PR, RT, IN), env (SU, TM), tat, rev, nef, vpr, vif, vpu. Figure from (508) (A). Replication cycle of HIV-1: virus engages with cellular receptors and fuses with the cell membrane, allowing the viral RNA to enter. The viral RNA is reverse transcribed into viral DNA, which integrate into the host genome. Through normal cellular processes, mRNA and proteins are produced. Viral components are packaged at the cell membrane and new virions bud, taking some of the cell membrane. Maturation of the HIV-1 virion induces the cleavage of Gag polyproteins, separating the matrix and capsid proteins, and triggers Env clustering. (C). Figure from (23).

proteoglycans (34, 35), lymphocyte function-associated antigen 1 (LFA-1) (36, 37) and other integrins (37–39), intercellular adhesion molecules 1-3 (ICAM-1, ICAM-2, ICAM-3) (36, 37, 40), galactosylceramide (GalCer) (41), and C-type lectins (33, 42) including mannose receptors (43–45) and dendritic cell-specific intercellular adhesion molecule-3-Grabbing Non-integrin (DC-SIGN) (42, 46, 47).

### 1.3.3 Viral tropism

Viral tropism can be classified by co-receptor usage and replication capacity in specific cell types. Viruses are identified by co-receptor mediated entry such as CXCR4 (CXCR4-tropic, X4), CCR5 (CCR5-tropic, R5), and both (R5X4). CD4+ T cells and macrophages are the main target cells for HIV-1 *in vivo* (48); thus, virus isolates are also categorized as macrophage (M-tropic), T cell (T-tropic), or dual (D-tropic) (49). Transmitted or founder viruses found immediately after HIV-1 enter a new host use CCR5 almost without exception (50, 51) to target macrophages and dendritic cells (DC) in the mucosa and gut associated lymphoid tissue (GALT) in sexual transmission (52). These R5 viruses inefficiently infect cells initially but evolve to have increased positive charge (53) or switch to CXCR4 (2-63% isolates) over time in 50% of infected individuals (54, 55). These later X4 variants can have reduced abilities to infect cells using R5-mediated entry, suggesting that the switch might be linked to the declining infectious capability of R5 isolates in an adapting immune system (55). Co-receptor switching is associated with faster disease progression toward AIDS and decreasing CD4 count (56–58).

Initially, viruses that target macrophages were generally classified as R5, and those that target T cells were classified as X4, however, it is now recognized that macrophages and T cells can be infected by X4, R5, or R5X4

viruses. The classification of viral tropism has changed over time as new evidence shows that although co-receptor usage is related to target cell tropism, they are distinct from each other (59). For example, both macrophages and lymphocytes express CCR5 and CXCR4 at varying levels, but R5X4 strains mainly use CXCR4 to enter T lymphocytes even though T lymphocytes are permissive to CCR5-mediated entry by R5 strains. In contrast, R5X4 strains use both CCR5 and CXCR4 to enter macrophages (59, 60). Although macrophages are primarily infected by R5 viruses, resulting in varying (up to 1000 fold) replication capacities, many R5 viruses cannot infect macrophages (61) and some X4 viruses can infect sub-populations of macrophages (49, 62). This evidence suggests that viral tropism is driven, at least in part, by the target cell.

#### *1.3.3.1 CD4+ T cells*

T cells are classified as CD4+ T helper cells, CD8+ cytotoxic T cells, regulatory T cells, and natural killer T cells (NKT). CD4+ T helper cells are the main HIV-1 targets. Naïve T cells (not yet exposed to antigens) express CXCR4 but not CCR5 and so are targeted by X4-tropic but not R5 viruses while activated memory T cells (antigen experienced) are targeted primarily by R5-tropic viruses (63). Virus entry in CD4+ T cells can result in productive infection in activated T cells or latent infection in resting T cells. Latent infection in resting T cells is restricted by deoxynucleoside triphosphate triphosphohydrolase (SAMHD1). SAMHD1 is abundantly expressed in resting T cells but can be degraded by viral proteins in some HIV-1 strains, leading to viral entry and integration but not necessarily viral production or T cell activation (64, 65).

#### *1.3.3.2 Macrophages*

Macrophages are professional antigen presenting cells (APC) that are derived and replenished by circulating monocytes originating from the bone

marrow (66). They are present in all tissues and modulate homeostasis by engulfing cellular debris and foreign antigens in a process termed phagocytosis (67). Macrophages also regulate inflammatory responses by producing cytokines and chemokines that recruit leukocytes to tissues and trigger or suppress cellular activation *in situ* (68). Macrophages are highly diverse and plastic: they can polarize toward a pro-inflammatory M1 state (classically activated) to promote host cell defense against insults or an anti-inflammatory M2 state (alternatively activated) to support tissue remodelling (69). Compared to T cells, macrophages express low levels of CD4 (70) and activation of T cells can down-regulate CD4 expression in macrophages (71).

Tissue-specific heterogeneity can influence HIV-1 permissivity in macrophages. For example, productive infection occurs in vaginal macrophages but not in intestinal macrophages (72). The non-permissiveness of intestinal macrophages is probably due to down regulation of CD4 and CCR5 expression and nuclear factor kappa-light-chain enhancer of activated B cells (NF-κb) activation (73). In immune tissues in late disease stages, HIV-1 strains are predominantly non-M-tropic with high positive charge on the gp120 V3 loop, whereas in brain tissue and cerebrospinal fluid, HIV-1 strains are predominantly M-tropic with lower gp120 charge (53, 74). M-tropic variants mainly target perivascular macrophages and resident microglia in the brain (74). Brain macrophages express CCR5 but very low levels of CD4; this limitation is overcome by changes in gp120 that enhance the ability of M-tropic isolates to interact with CD4 and CCR5 (75–77). Thus, in the brain, M-tropic viruses have evolved to infect cells with low levels of CD4 (78).

#### *1.3.3.3 HIV-1 receptor negative cells*

Many cells do not express HIV-1 receptors (CD4, CXCR4, CCR5) at detectable levels but may associate with HIV-1 virions. For example, CD4- astrocytes, neurons, brain microvascular endothelial cells (BMVE), epithelial cells, lymphocytes, thymocytes and cardiomyocytes have all been reported to contain HIV-1 *in vivo* (79). In the brain, astrocytes, oligodendrocytes, neurons, and BMVE do not have CD4 receptors and therefore are unlikely to become productively infected (80). HIV-1 bound to CD4- cells, such as fibroblastoid cells and astrocytes, can transfer HIV-1 to T cells, leading to productive infection (81, 82). CD4- cells, including epithelial, endothelial, and astrocytes, can receive HIV-1 virions by cell-cell contact with macrophages (83). Previous studies proposed that infected cells prime contacting CD4- or co-receptor- cells, such as astrocytes, in a cooperative *trans*-receptor mechanism that allows the target cell to acquire the HIV-1 receptors and become susceptible to infection (79, 84).

### 1.3.4 HIV-1 transmission mechanisms

HIV-1 transmission occurs through the transfer of free virus or, more efficiently, through the transfer of cell-associated virus from one cell to another, termed “cell-cell transfer” in sexual transmission (85, 86). HIV-1 transfer can occur by three main mechanisms: 1) direct free virus infection, 2) *trans*-infection from virus-bearing cells (e.g. DC –T cell) or 3) direct infection from infected cells (e.g. T cell-T cell, macrophage-T cell) (87).

#### *1.3.4.1 Free virus infection*

Free virus infection can occur at the surface plasma membrane (88). At the early stage of infection, Langerhans cells (89) and DCs at the mucosa surfaces in the vagina, ectocervix, and male foreskin can become infected with free virus mediated by the CCR5 co-receptor (90). Immature DCs use DC-SIGN

and HIV-1 entry receptors to facilitate infection and *de novo* viral production; these newly synthesized particles are transferred to T cells and contribute to long-term HIV-1 transmission (91, 92).

#### *1.3.4.2 Trans-infection: Immunological synapse*

DCs participate in viral transmission using the *in trans* mechanism via the immunological synapse (IS) (93). The IS is defined as an intercellular junction where immunological events occur, such as receptor engagement and cytokine secretion between T cells and APC (87, 94). At the IS, many types of non-HIV-1-specific interaction can occur that promote viral transfer. In DC-T cell IS, cell surface C-type lectins, such as DC-SIGN, bind to HIV-1 mannose glycan on Env and mediate viral adsorption at the mucosa (42). DCs internalize HIV-1 inside intracellular compartments and migrate to the lymph nodes. Upon contact with CD4+ T cells, virions are relocated from the DC compartments to the IS, resulting in CD4+ T cell infection *in trans* without the DCs becoming infected (Figure 1. B).

#### *1.3.4.3 Direct infection: Virological synapse*

Virions can also be transferred from an infected cell to a target cell across a virological synapse (VS). A VS is similar to, but distinct from, an IS and defined as a cytoskeleton-dependent, stable adhesive junction formed between two contacting but non-fused cells, where viral material can be directly transferred from the effector cell to the target cell by the cellular machinery (87, 95). In T cell-T cell VS, the binding of an HIV-1 infected T cell to a CD4+ target T cell results in rapid actin-dependent polarized accumulation of Env and Gag in capped, lipid raft assembly domains on the effector cell and CD4, CXCR4, talin, LFA-1 on the target cell (36, 95, 96). ICAM-1 on the effector cell engages with LFA-1 on the target cell to stabilize the transient cellular contacts (36, 94). The

microtubule organizing center (MTOC) in the infected T cell reorients toward the target T cell to support direct virion transfer by the cell secretory pathway (97) (Figure 1. A, D). The VS structure can contain interdigitated membrane sheet and/or filopodial protrusions from both host and target cells (98), such as in DC-T cell IS (99, 100) or T cells VS (101, 102) that facilitate viral transfer. The actin and tubulin cytoskeletons play an active role in the accumulation of HIV-1 viral products at the VS (103). Macrophages that phagocytose HIV-1 infected and dead/dying CD4+ T cells can become productively infected with various HIV-1 clones, including transmitted/founder isolates that inefficiently replicate in macrophages through free virus entry (unpublished results: Baxter *et al.*).

#### *1.3.4.4 Virus containing compartments*

In a mechanism similar in features to both the DC-T cell IS and T cell-T cell VS, macrophages can transfer virions to T cells across a VCC-dependent VS (104). In macrophages, virions can bud inside surface-connected virus containing compartments (VCC) via an actin-dependent mechanism (105–109). The complex tubular VCC are distinct from late endosomes and multi-vesicular bodies and have near-neutral pH (reviewed in (110)). Virions that bud inside the intracellular VCC can resurface to the cell membrane and cross the VS, stabilized by ICAM-1/LFA-1 interactions, to a target cell. This transmission mechanism results in highly efficient T cell productive infection (Figure 1. C) (108). Virions hidden inside VCC are protected from immune recognition and antibody neutralization, thus macrophage VCC can serve as viral reservoirs for long term infection.

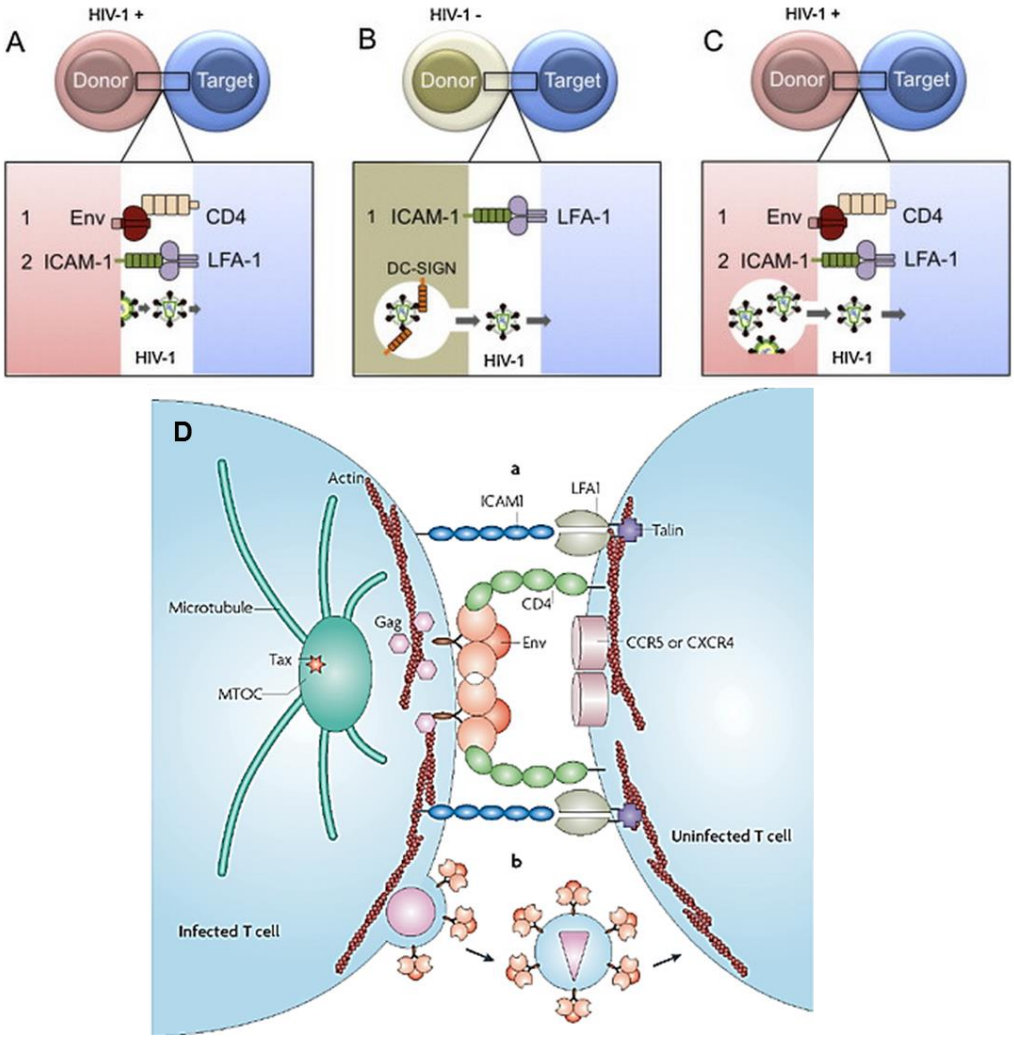


**Figure 1.4** T cell VS is stabilized by interactions between ICAM-1 and LFA-1 (A). Mature virions are captured by DC-SIGN inside surface-connecting compartments and are transferred across IS from DC to target cell (B). Virions bud inside macrophage VCC and cross the VS to the target cell (C). Figures from (48).VS between HIV-1 infected T cells shows LFA-1/-ICAM-1 binding, actin and MTOC polarization (E). Figure from (94).

### 1.3.5 Viral fusion: Env conformation changes

Binding of gp120 to CD4 and a co-receptor induces a cascade of conformational changes in the Env trimer. First, gp120 changes from a closed to open conformation (111, 112). The V1/V2 loops at the apex at the center of the Env trimer (112), which support co-receptor binding and shield conserved elements of gp120 from neutralizing antibodies by modulating length and carbohydrate density at N-linked glycosylation sites, rearrange to the outer regions (113). V3 loops originally located on the outside edge of the apex of the

gp120 are now exposed and reposition to the center of the trimer (112). The V3 loop and the bridging sheet mini-domain mediate the selection and binding of a co-receptor, which unlock the potential energy for gp41 mediated fusion (113–116).

In the Env open conformation, the previously hidden gp41 becomes exposed. Gp41 forms a “bridge” between virus and target cell by extending the carboxy-C-terminal heptad repeat (CHR) and amino-N-terminal heptad repeat (NHR) and inserting the fusion peptide into the host cell in the pre-hairpin intermediate state. In a “spring-loaded mechanism,” the trimeric helices CHR and NHR fold at a hinge region and align anti-parallel to each other to form six-helix bundles, which pull the two membranes together in the fusogenic state.

Finally, the viral and host membranes fuse together, creating fusion pore that allows the viral core to enter the cell cytoplasm. Fusion can occur at the cell plasma membrane (21) or inside macropinocytic vacuoles (117) and endosomal vesicles (118) (48, 88). One model suggests that in acutely infected T cells, immature virions can temporarily accumulate inside endosomal compartments. Over the next several hours, the virions mature by proteolytic cleavage of Gag polyproteins inside target cell endosomes (Figure 1.3C). Once maturation completes, the gp120/gp41 glycoproteins accumulate on the viral envelope and the virions fuse with the endosomal membrane (119). In contrast, in established chronic infection, mature virions can immediately fuse with the cell plasma membrane (120) (reviewed in (48)).

### 1.3.6 Viral reverse transcription: viral RNA to DNA

Inside the cytosol, the viral core CA protein disassociates in a process named viral uncoating (17, 121, 122). There are several hypotheses about when and where uncoating occurs: at the plasma membrane where uncoating

initiates the formation of the  reverse transcription complex (RTC), gradually during transport toward the nucleus, or at the nuclear pore induced by a DNA flap after completion of reverse transcription (17). Reverse transcription begins after the formation of a mature RTC, which contains vRNA, primer transfer tRNA $^{Lys3}$ annealed to vRNA, NC, RT, MA, Vpr, and IN (17, 121, 123). Reverse transcription follows these steps (Figure 1.5) (124):

A. tRNA hybridizes to the primer binding site (pbs) at the 5' end of the vRNA
B. (-) strand strong stop ssDNA is synthesized from the 3' to 5' direction and the complementary ssRNA is degraded by the RNase,
C. RT "jumps" to the 3' ssRNA end and completes the (-) strand synthesis
D. vRNA is degraded except for the polypurine tract (PPT)
E. 1$^{st}$ (+) strand strong stop ssDNA is synthesized from the PPT
F. 1$^{st}$ and 2$^{nd}$ DNA strands hybridize at the primer binding site and form a temporary circular complex
G. RT completes both strands to form a linear double stranded DNA (dsRNA) with a overlapping (+) strand DNA flap and long terminal repeats (LTR)

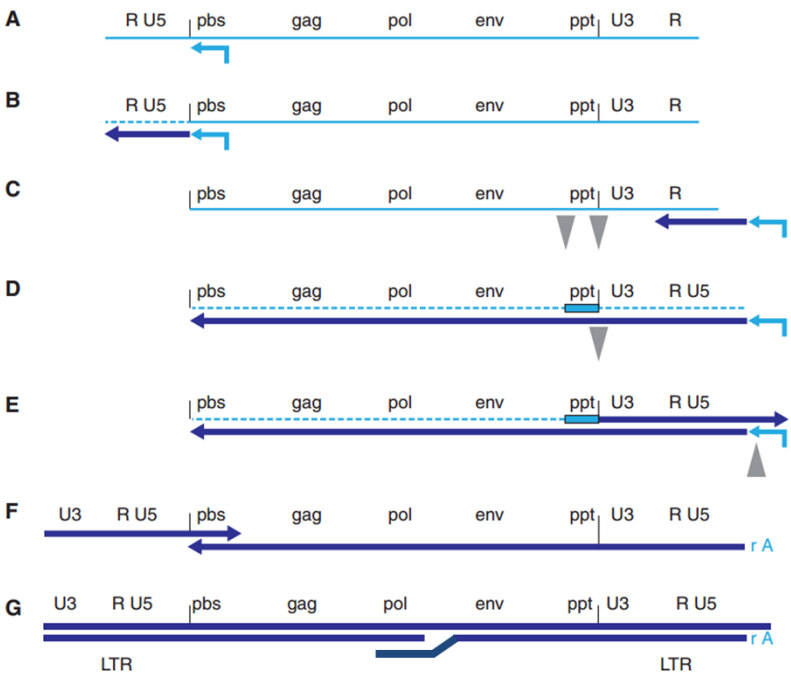


**Figure 1.5** HIV-1 reverse transcriptions from vRNA to vDNA. Figure from (124).

### 1.3.7 Viral integration: proviral DNA

After reverse transcription, the RTC is now integration competent, termed the pre-integration complex (PIC), and enters the nucleus (17, 121, 122). There are many hypotheses on how active nuclear import occurs: cellular machinery mediates entry through the nuclear pore complex (NPC), Vpr induces reversible breaks in nuclear membrane and guides the PIC into the nucleus, MA, IN, and Vpr are karyophilic (attracted to the nucleus) agents that localize PIC at the nucleus, and/or the viral DNA (vDNA) flap facilitates nuclear entry (17, 121, 125). After nuclear import, unintegrated viral DNA can exist in a linear form and integrate into the host genome or remain un-integrated in various circular forms in the nucleus (126, 127). Integration occurs when IN joins vDNA (Figure 1.3B) into the host genome following these steps (Figure 1.6) (128):

A. vDNA localizes to the target cell DNA,
B. two nucleotides are removed from each 3' ends of vDNA
C. 3' ends of vDNA covalently bind to 5' end of target DNA
D. two unpaired nucleotides at the 5' end of vDNA are removed, single strand gaps on the target DNA are completed
E. the 5' ends of vDNA and target DNA are ligated, vDNA is now proviral DNA

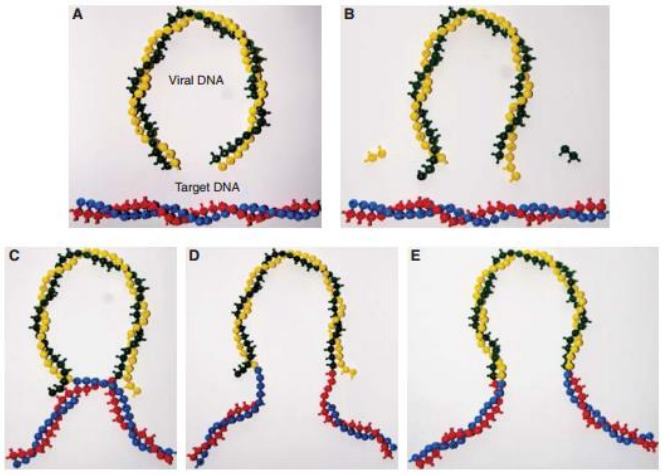


**Figure 1.6** HIV-1 vDNA integration into host genome. Figure from (128).

### 1.3.8 Viral transcription and translation: mRNA and proteins

Viral transcription occurs when the host cell RNA polymerase II transcribes the genome containing proviral DNA; thus, viral production or latency is influenced by target cell transcriptional activity. Viral transcription begins with the HIV-1 promoter at the LTR (129), which contains a unique 3' end (U3), a repeat (R), and a unique 5' end (U5) under the control of NF-κB (130) and nuclear factor of activated T cells (NFAT) (131). The efficiency of transcription depends on the viral protein Tat, which stimulates and enhances transcriptional elongation by binding to the trans-activating response element (TAR) on the LTR (131–134). Tat protein increases the efficiency of transcription by amplifying the stochastic viral gene expression in a positive feedback loop, which can act as a molecular switch that determines productive or latent infection (133, 134). The Tat-transactivation process is dependent on the cell positive transcription elongation factor b (P-TEFb), which is a cyclin-dependent kinase that controls RNA polymerase II (18, 135, 136).

Transcription of the cell DNA strand by the RNA polymerase produces genomic vRNA and messenger RNA (mRNA) that undergo complex splicing to produce un-spliced or incompletely spliced gag, pol, env, vpu, vif, vpr mRNAs, and completely spliced tat, rev, and nef mRNAs. Because un-spliced and incompletely spliced transcripts are typically degraded, HIV-1 uses Rev protein, which interacts with the Rev-responsive element on the RNA to facilitate the transport of RNA out of the nucleus. Tat, Rev, and Nef move to the cytoplasm by an endogenous cellular pathway independent of Rev protein (137). Outside of the nucleus, Gag and Gag-Pro-Pol are translated at the cytosolic polysomes, which are clusters of ribosomes not bound to endoplasmic reticulum (ER). Because gag and pol genes overlap, HIV-1 uses programmed frame shifting to

change reading frame during translation (137, 138). The gag gene is translated into polyproteins that are later cleaved by PR during virion maturation. Env, Vpu and other proteins are translated at the ribosomes on rough ER. Env undergoes glycosylation and oligomerization in the rough ER and is transported to the Golgi, where Env is further processed into gp120 and gp41.

### 1.3.9 Viral assembly: budding and maturation

The Gag protein drives the assembly (packaging of viral products necessary for subsequent infection) and viral release at the plasma membrane. Newly synthesized Gag proteins move to the plasma membrane using cellular trafficking machinery, such as motor protein kinesin KIF4 (139), and assemble together to form a multimeric, membrane associated immature lattice. The gp120/gp41 complex moves to the plasma membrane through the cell secretory pathway (97). At the plasma membrane, most Env proteins are endocytosed and degraded within endosomes that mature into lysosomes, but some are recycled to the plasma membrane through recycling endosomes (140). These Env molecules are incorporated into virions possibly through passive, direct regulated, or indirect regulated mechanism through Gag-Env interactions (Section 1.3.1) (reviewed in (140)).

The remaining viral proteins also traffic to the site and are packaged into immature virions that bud out of the cell membrane, taking some of the cell lipid bilayer with them. Budding and release of immature virions is mediated by the cell endosomal sorting complexes required for transport (ESCRT) machinery (141). Viral release is inhibited in human cells by tetherin proteins expressed constitutively or induced by interferon IFN-α, which retain fully formed virions on the cell membrane. Vpu protein antagonizes this antiviral activity, allowing HIV-1 release (142). Finally, the PR cleaves the Gag polyprotein, inducing

rearrangements of molecules and resulting in Env clustering and formation of the conical core by CA proteins (23) (Figure 1.3 C). After cleavage, the particles mature into their final infectious forms. In myeloid-lineage immune cells, such as macrophages and DC, HIV-1 is assembled and stored in intracellular compartments that are frequently connected to the cell surface membrane via narrow conduits (105–109). These virions are protected from the hostile intra- and extra-cellular milieu inside viral reservoirs and can later be transferred to other permissive cells (110).

### 1.3.10 Viral consequences: cell death

The viral replication cycle often kills the host cell. Cells can be killed directly by the viral replication cycle that interferes with the cellular machinery and budding virions that rupture the cellular membrane (143). Other cytopathic effects have been observed in T cells including syncytium formation that leads to giant multinucleated cells and balloon degeneration that induces the cells to swell up past the cell membrane volume limit and consequently lyse (144). CD4+ T cells can be depleted by abortive infection, which occurs when the viral reverse transcription or integration steps trigger pro-apoptotic events (145). Viral proteins can activate cellular death pathways such as autophagy (146) or programmed caspase-3-mediated apoptosis and caspase-1-mediated pyroptosis (147–149) that trigger cellular suicide. Cells decorated with viral proteins, including uninfected bystander cells, can be targeted and killed by cytotoxic T cells, natural killer (NK), and NKT cells through direct or antibody-dependent cellular cytotoxicity mechanism (150).

## 1.4 HIV-1 pathogenesis

### 1.4.1 Innate immune response and inflammation

HIV-1 transmission occurs primarily through sexual intercourse and, in some cases, contaminated needle sharing, blood transfusion, and mother-to-child vertical transmission. In sexual transmission, virions in semen or vaginal secretions breach the epithelial cell layer in the genitals through skin lesions or transcytosis of infected cells (151, 152). Male circumcision removes the foreskin, reduces the epithelial cell surface area and HIV-1-susceptible cells, changes microflora and tissue structure of the penis, and provides a protective advantage against HIV-1 transmission (153).

After HIV-1 enters the body, Langerhans cells (non-migratory DC) and DC near the lamina propia of mucosal tissues quickly become infected through direct infection or adsorb on the surface by C-type lectins and other attachment molecules. The immune system produces acute-phase cytokines and chemokines triggered by early pro-inflammatory cytokines (tumor necrosis factor TNFα, interleukin IL-1β, IL-12 (154)). Type-1 IFN (IFN-1) has been found to decrease viral effects and slow disease progression in SIV infected rhesus macaques but continued IFN-1 expression in chronic infection results in desensitization and decreased antiviral gene expression (155). During the first 5-10 days after transmission when HIV-1 is not detectable in the plasma, termed the “eclipse phase” (156, 157), the virus could potentially be eliminated. However, once the viruses disseminate and establishes latent reservoirs, then it is almost impossible to eradicate the virus completely (158).

Langerhans cells and DCs are proposed to take up virus after transmission across the sexual mucosa and migrate to the draining lymph nodes (159, 160) (Figure 1.7). HIV-1 infection reaches the lamina propia of

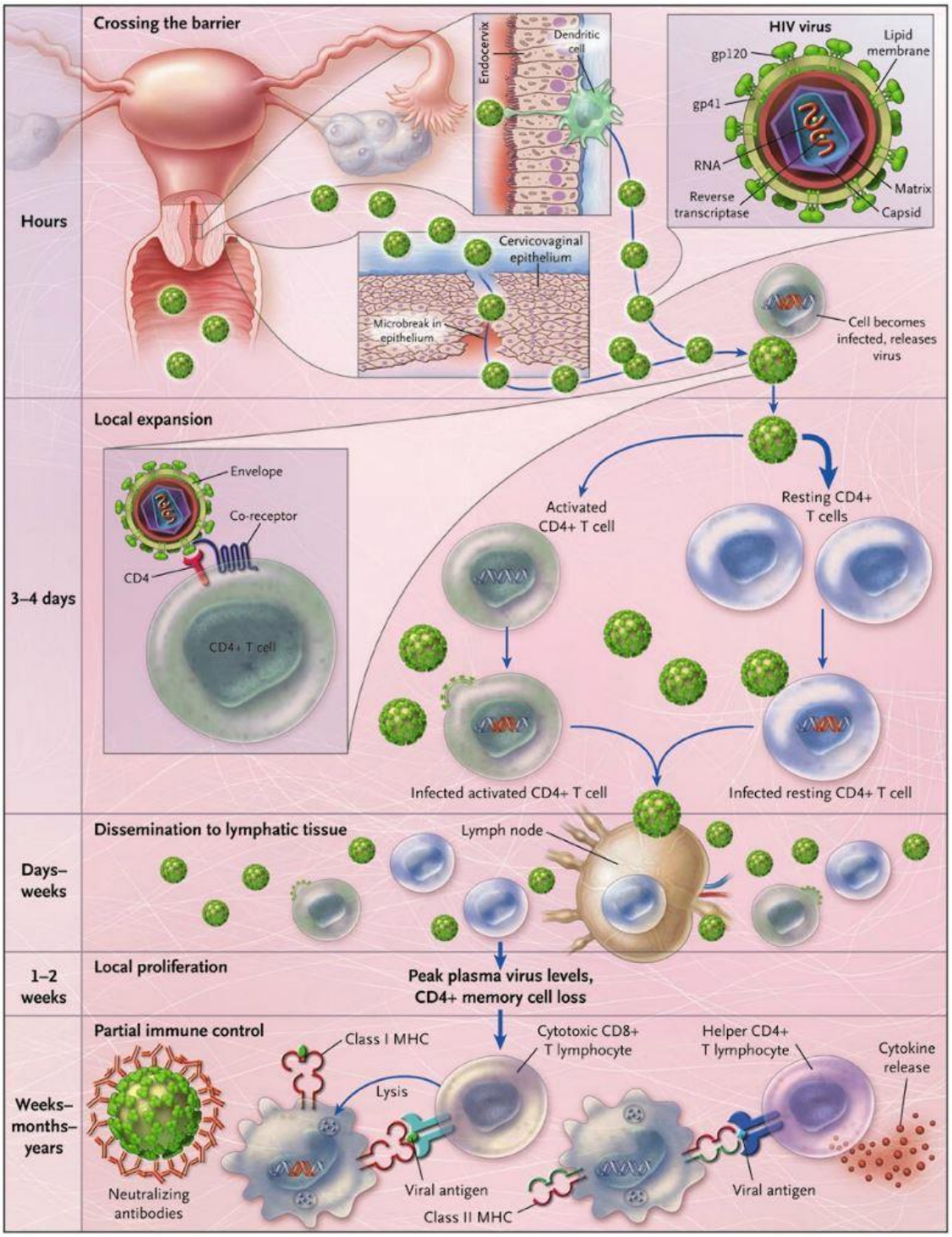


**Figure 1.7** Summary of early events in vaginal transmission of HIV-1 based on studies of SIV in nonhuman primates. Figure from (175).

GALT tissues and peripheral lymphoid tissues (PLT) within a few weeks. T cells home to secondary lymphoid tissues where they encounter virus-bearing DCs that may propagate the infection. HIV-1 infected immature DCs are induced by viral infection and exposure to cytokines in the extracellular milieu to differentiate into mature DCs. As APCs, mature DCs present HIV-1 antigens to

T cells in the lymphoid tissues (Figure 1.7) (161–164). Through direct or *trans*-infection, DCs transfer viral particles to T cells leading to productive infection. During DC migration and settlement in lymphoid tissues, HIV-1 is protected from degradation by residing inside the DC intracellular compartments.

CD4+ T cells travel through the follicular DC (FDC) network during their migration through the lymphatic system. Infected T cells can spread virions to FDCs, which take up infectious virus and infect T cells *in trans*. Throughout HIV-1 disease progression, active HIV-1 infection largely surrounds FDCs suggesting that these sites are major HIV-1 reservoirs (161–166). FDCs inside germinal centers endocytose virions inside endosomal compartments through receptor-dependent mechanism and trap the virions inside interdendritic spaces; these virions may later escape into the cell cytoplasm (164). FDCs secrete signals that increase HIV-1 infection and replication in T cells and macrophages (162, 167). In this way, FDCs mask HIV-1 in hidden reservoirs and play a major role in facilitating infection of CD4+ T cells. Because these environments are rich with activated CD4+ T cells and pro-inflammatory cytokines, the virus proliferate quickly in GALT and PLT (42, 168). Virus reservoirs in FDCs and virus replication in GALT leads to long term persistence of HIV-1 despite antiretroviral therapy (154, 169, 170).

Early after infection, HIV-1 cross the blood brain barrier (BBB) and enter the brain through transcytosis of virions across endothelial cells, virus-bearing monocytes or infected T cells and macrophages, or physical BBB breach (80, 171). Virions also enter the brain much later in infection when the immune system has weakened (172). HIV-1 in the brain hides in long-lived resident macrophages, microglia, and astrocytes and evolves separately from isolates in peripheral tissues (173). Although viruses are highly compartmentalized in brain

and peripheral tissues, the meningeal tissues, which envelope the central nervous system (CNS) and separate the brain from peripheral tissues, harbor HIV-1 isolates identified in both tissues. This evidence suggests that HIV-1 can migrate out of the brain across the meninges into peripheral tissues. Because the brain is an immune privileged area that can protect HIV-1 from immune system responses and antiretroviral therapy, the brain can become a major long term reservoir (174).

Viremia level peaks within 3-6 weeks after exposure. Activated CD4+ T cells become infected with HIV-1 and disseminate the virus throughout the organism via the lymphatic system within days to weeks post infection (175) (**Error! Reference source not found.**). Resting CD4+ T cells can become atently infected with HIV-1 and serve as cellular reservoirs. In particular, central and transitional memory CD4+ T cells are major cellular reservoirs driven by cellular survival and antigen-mediated proliferation (176–178). DC and CD4+ T cell counts significantly decrease during this acute infection stage (179). CD4+ macrophages may attempt to trap and eliminate HIV virions and infected cells, but in the process become infected and generate productive reservoirs that protect virions from the hostile extracellular milieu (110, 180). CD34+ multipotent hematopoietic progenitor cells can become latently infected with HIV-1, contributing to stable viral reservoirs (181). Differentiation of CD34+ progenitor cells can lead to activation of viral production and proliferation of infected cells. Viral production induces NK cells to become activated, expand, and attack HIV-1 infected cells (156, 182, 183).

### 1.4.2 Adaptive immune response and evasion

A few weeks later, the adaptive immune system enters the fight to control viral replication. CD8+ cytotoxic T cells and NKT cells expand and attack HIV-1

infected cells through cytolysis of infected cells and production of antiviral cytokines and chemokines (156). CD8+ T cell expansion generally peaks 1-2 weeks after viremia level peaks; this event results in reduced viremia (184–186). Up to this point, the initial transmitted-founder virus sequence (51) has been relatively homogenous but the viral genome begins to evolve dramatically after the peak of the CD8+ T cell response as an immune evasion strategy (187, 188). Studies reported that mutations could be detected within 10 days (156). After two months, the transmitted-founder virus genome can mutate at 2-5 locations and by 12-20 months, the virus can mutate at 17-34 locations (188). Mutations can continue to occur at a rate of 2% per year (187). In many cases, mutations could cause co-receptor switching from CCR5 to CXCR4 mediated by variations in the V3 loop (52, 58). Escape mutations can be selected by CD8+ T cells, neutralizing antibodies (Nabs), or NK responses and trigger changes in viral proteins in different epitopes to evade immune recognition (156). In this way, immune responses that target specific HIV-1 isolates quickly become obsolete with the emergence of new escape mutants.

CD4+ T cells expand to support the adaptive immune response but become preferential targets of the virus. CD4+ T cells rapidly decline in numbers due to the cytopathic effects associated with infection, lysis by CD8+ T cell, NKT cells, and NK, and activation-induced cell death (189). The decline of CD4+ and CD8+ T cells due to pyroptosis (147) and apoptosis correlates with immune activation and disease progression (190–192). CD4+ T cell death results in secretion of inflammatory cytokines and release of cytoplasmic content into the extracellular milieu (193). In the SIV infected macaque model, 30-60% of memory CD4+ T cells are infected by the peak of infection and most are killed within 4 days (194).

In the seroconversion phase, 3-4 weeks after initial infection, B cells mature into plasma cells and produce antibodies specific to all viral proteins, although the only antibodies with antiviral functions are against Env. Affinity maturation of Env-specific antibodies may result in Nab production, which can inhibit HIV-1 infection in a strain-specific manner, and in rare cases broadly neutralizing antibody (bNabs) production, which can neutralize multiple strains of HIV-1 by both cell free (195) and cell-cell transmission (196) routes. For example, the VCR01/VCR02 bNabs neutralize ~90% of HIV-1 isolates (197) and 10E8 bNab neutralizes ~98% of tested viruses (198). The timetable for detection of antibody production is summarized in (Figure 1.8) (156).

| Antibody specificity | Time of onset after transmission (days) |
|---|---|
| gp41 | 23 |
| gp120 | 38 |
| Non-neutralizing to CD4-binding site, MPER, CD4-inducible epitope | 40-70 |
| Autologous neutralizing antibodies | Earliest ~84 |
| Broadly neutralizing antibodies to CD4-binding site, carbohydrate, MPER | Not usually made, ~30 months after transmission in chronic infection |

**Figure 1.8** Timetable of antibody responses detected in acute HIV-1 infection. Figure from (156).

Many B cells, especially those in HIV-1 rich environments such as Peyer's patches, lymph node follicles and germinal centers, are quickly killed early during the course of infection (156, 199). In SIV infected macaques, activated memory B cells are rapidly depleted by the programmed death 1 pathway within 2 weeks of exposure (200) . This early loss of B cells may contribute to the delay in producing HIV-1 specific antibodies (200). Eventually CD4+ T cells level decrease dangerously low and the immune system becomes weakened enough that the viremia level peaks again. At this stage, opportunistic infections and HIV-1 related cancers can attack the host and eventually kill the HIV-1 infected individual.

### 1.4.3 Clinical progression of HIV-1 disease

Untreated HIV-1 infection generally occurs in three phases: primary acute infection, chronic clinical latency, and AIDS (Figure 1.9). During primary infection, the majority (70-80%) of HIV-1 infected patients experience a surge of viremia and as a result of this massive viral replication the CD4+ T cell counts fall rapidly (201, 202). Patients can experience varying severity of mononucleosis-like or influenza-like symptoms, termed acute retroviral syndrome. Over time, the immune system and other factors reduce the level of virus by a factor of 10-100 on average (175) to a stable viral set point, and CD4+ T cell counts increase slightly but generally do not return to pre-infection levels (500-1600 cells/ $mm^3$ (203, 204)). Patients experience no or mild symptoms in the clinical latency stage (202, 205) but CD4 levels continue to progressively decrease; this stage can last for many years.

The vast majority of untreated HIV-1 infected patients eventually progress to the final stage of HIV-1 infection, AIDS, which is defined by low (<200 cells/$mm^3$ of blood (203, 204)) CD4+ cell count or the occurrence of opportunistic diseases and HIV-1 related cancers (202–204, 206). The viremia levels increase rapidly. Without treatments, AIDS patients typically live for 3 years and those with opportunistic infections survive for 1 year (204). For this reason, patients are advised to begin HIV-1 treatment before CD4 counts fall below 350 cells/$mm^3$ to delay the onset of AIDS (203). A rare number of HIV-1 infected individuals can control HIV-1 infection without treatment, known as “elite controllers or “long term non-progressors (156, 207, 208).” These patients often have low viral load and intact lymph nodes and immune system.

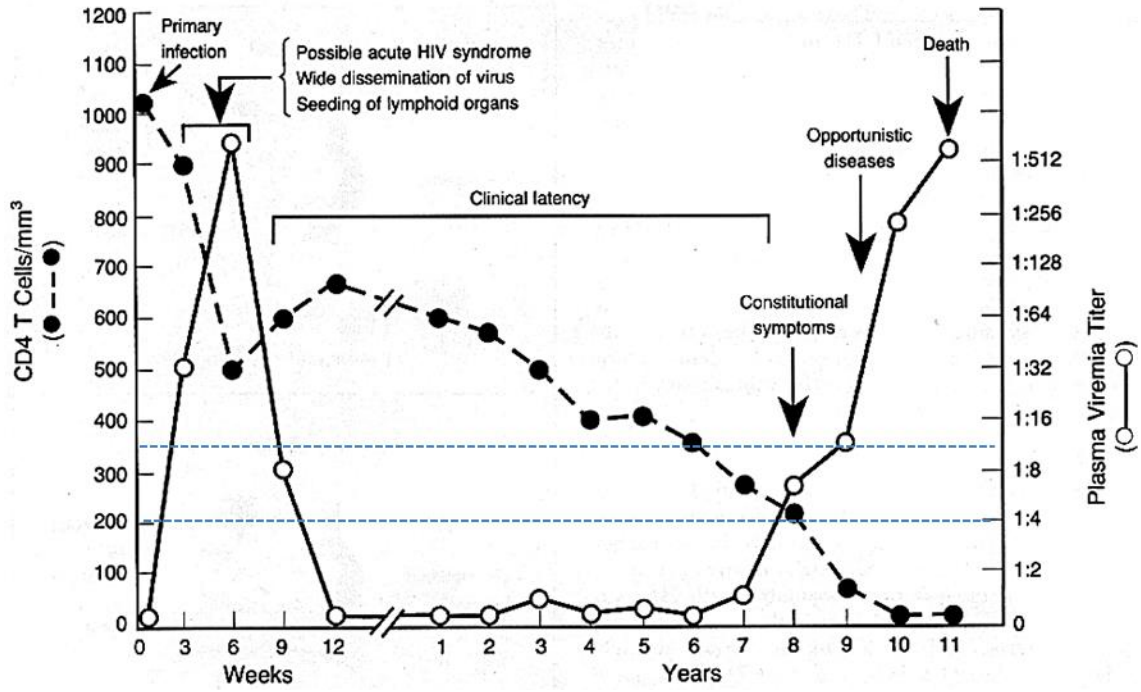


**Figure 1.9** Graph of the clinical progression of HIV over time shows changes in CD4+ T cells count and levels of viremia during primary infection, clinical latency, and AIDS. Figure adapted from (206) and www.niaid.nih.gov.

## 1.5 Antiretroviral drugs

Since 1983, many drugs have been developed to combat HIV-1 infection and if given early in the course of disease progression, these drugs can significantly prolong the lives of HIV infected patients. Several drugs are given to HIV-1 infected patient to suppress HIV-1 replication, maintain the immune system, and delay the onset of AIDS; this is known as highly active antiretroviral therapy (HAART). The drugs are typically given in combination to counteract the HIV-1 dynamic mutations that can result in drug-resistant variants after only two weeks (209). The drugs target four steps in the HIV-1 replication cycle: entry, reverse transcription, integration, and protease activity (Figure 1.3 B). Entry or fusion inhibitors include maraviroc, which binds to the CCR5 co-receptor (210), and enfuvirtide (ENF) which interacts with gp41 to prevent viral attachment and fusion into the host cell (211). Nucleoside/nucleotide reverse transcriptase inhibitors (NRTIs), such as emtricitabine (FTC), lamivudine (3TC), zidovudine

(AZT), stavudine (d4T), abacavir (ABC), and tenofovir (TDF) act as chain terminators by preventing additional nucleotides to be added to the DNA strain during the conversion of RNA to DNA (212). Non-nucleoside reverse transcriptase inhibitors (NNRTIs), such as etravirine (ETR), nevirapine (NVP) and efavirenz (EFV), bind to the RT enzyme's allosteric "pocket" site to cause a conformational change in the enzyme and interfere with its function (213, 214). Integrase inhibitors, such as raltegravir (RAL) (215), inhibit the integration of viral DNA into host cell DNA by interfering with the IN enzyme. Protease inhibitors, such as saquinavir (SQV), darunavir (DRV) (216) and atazanavir (ATV), prevent the PR enzyme from cleaving the polyproteins and block the maturation of budding virions (217).

## 1.6 Vaccine

Currently, there are many challenges to the development of a prophylactic HIV-1 vaccine (218, 219). The main challenge lies in the extensive variability in HIV-1 sequences caused by the error-prone RT enzyme and the ability of the virus to evade recognition by the cell immune system (220). Vaccine approaches introduce immunogens, which are antigens designed to stimulate cell-mediated immune responses (e.g. cytotoxic T lymphocytes (CTL)) (221) and production of Nabs (222)), to naïve macaques (the most used animal model) or human vaccinees. In the few clinical efficacy trials that have been undertaken, vaccines have been given to individuals at high-risk of infection. Immunogens that have been tested include live attenuated viruses, whole inactivated viruses, proteins, live vectors expressing HIV-1 genes, and plasmid DNA (156, 218, 219, 222). Major clinical trials include the AIDSVAX vaccine, which introduced gp120 proteins to induce antibody production (223) and the STEP vaccine, which introduced recombinant replication-deficient adenovirus

expressing HIV-1 Gag, Pol, and Nef to induce CD8+ CTL response (224, 225). All previous HIV-1 vaccine trials have experienced no success with the exception of the Phase III RV144 Trial in Thailand published in 2009, which showed 31% efficacy in preventing HIV-1 infection (222, 226–229). This trial combined two approaches to boost the immune system: a canary pox viral vector expressing gp120 and Gag, followed by the AIDSVAX gp120 vaccine.

Approximately 20% of HIV-1 patients generate bNabs that can neutralize multiple strains of HIV-1 (195, 196, 230). Most bNabs can be categorized based on the conserved epitopes on the Env spike that they recognize, such as the CD4-binding site, V1/V2 glycopeptide epitopes, glycan V3 epitope, and the membrane proximal external region (MPER) (reviewed in (195)) (Figure 1.10). Production of bNabs that target the evolutionary conserved epitopes of HIV-1 proteins (231) can overcome the diversity of HIV-1.

However, HIV-1 uses many strategies to evade Nabs (reviewed in (232). Env is covered with carbohydrates, which mask most conserved regions of the spike and sterically impede antibody access to the CD4 binding site on gp120 (Figure 1.2). This shield may contribute to the low efficacy of Env-based HIV-1 vaccines (233, 234). The variable loops on gp120 are highly flexible, glycosylated, and able to elongate and shorten, thereby effectively shielding conserved epitopes on Env spike (113). HIV-1 also changes the conformation of receptor binding sites upon antibody recognition, enabling HIV-1 to bind to receptors and simultaneously evade neutralization using “conformational masking” (235). The spatial arrangement and low density of Env spikes on HIV-1 can limit the avidity of antibody binding (232). Steric constraints restrict antibody access to narrow pockets of conserved co-receptor binding sites on gp120 (236). HIV-1 uses cell-cell transmission to transfer virions across

interdigitated or tightly apposed synaptic structures; these structures can become steric barriers that prevent Nabs from accessing the occluded cell-cell junction (48, 237). The effectiveness of Nabs can also be limited by kinetic and timing constraints (48). For example, Nabs may access newly formed VS but not previously formed VS. Monoclonal antibodies targeted against CD4-binding site are potent against free transmission but lose potency during cell-cell transfer (237), and mAbs to the MPER lose potency against HIV-1 spreading directly from macrophages to T cells (238). The time between viral budding and CD4 attachment is short, which restricts efficient coverage of CD4-binding sites by Nabs. The kinetic rates of antibodies binding can also contribute to neutralization activity (239).

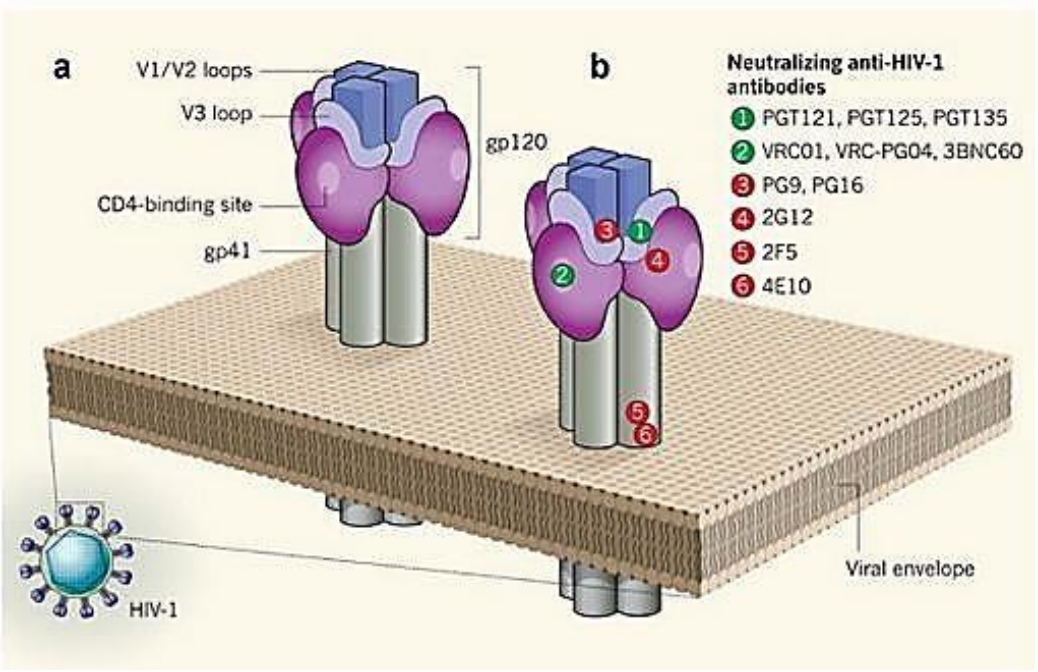


**Figure 1.10** BNabs (listed) can bind to the conserved epitopes on the Env spike that recognize the CD4-binding site, V1/V2 glycopeptide epitopes, glycan V3 epitope, and the MPER. Figure from (511).

## 1.7 HIV infection in the brain

HIV-1 infection can result in HIV-1-associated neurological complications in 40% and HIV-associated dementia (HAD) in 20-30% of HIV-1 infected patients (80, 240–242), leading to impaired cognitive and motor functions (243).

HIV-1 crosses the selectively permeable blood brain barrier (BBB) into the brain early after peripheral infection, summarized in Figure 1.11.

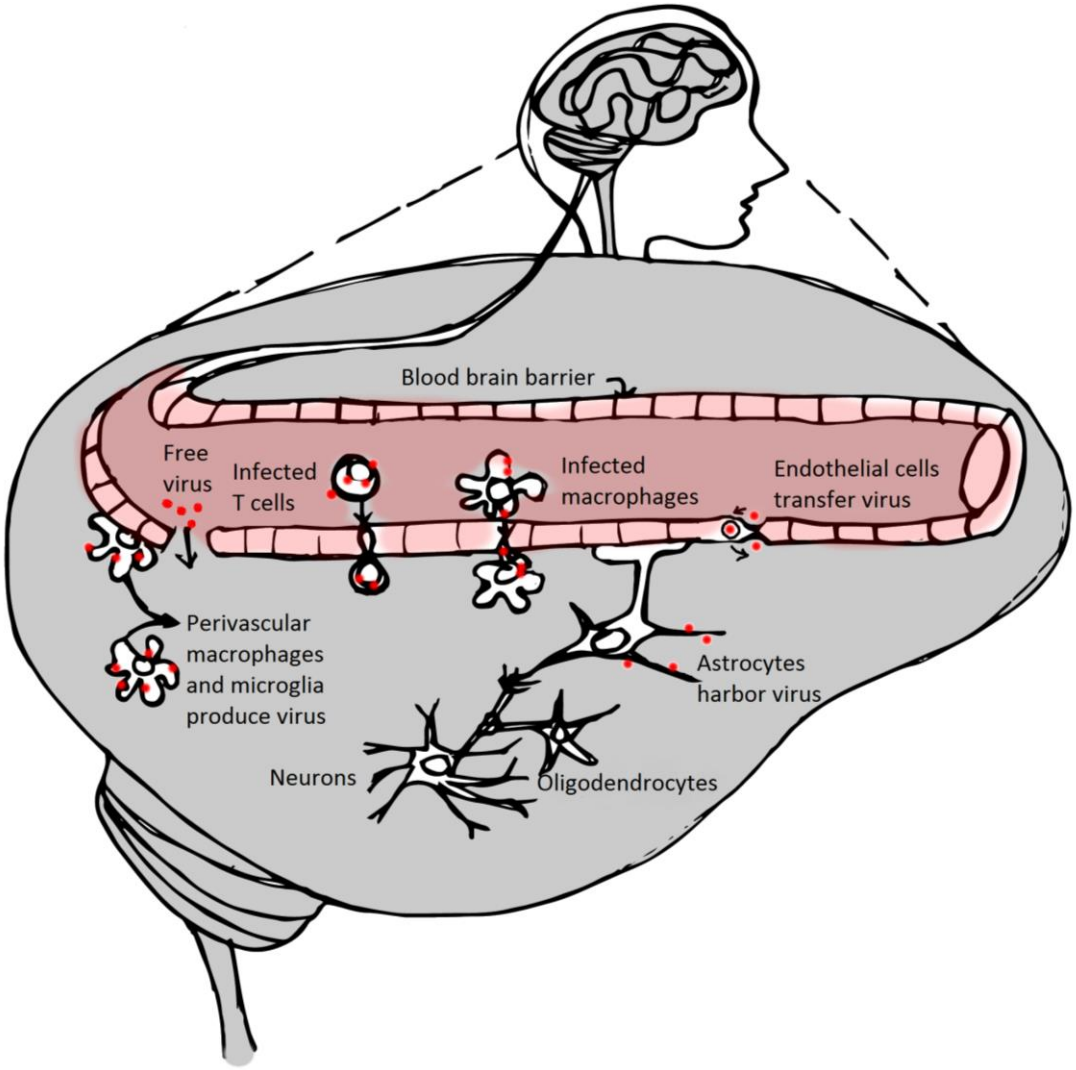


**Figure 1.11** Virus can cross the blood brain barrier and enter the brain (gray) as free virus through brain lesions or as passengers on infected or virus-bearing T cells and macrophages traveling along blood vessels (pink) or as packages that are transcytosed by endothelial cells. Inside the brain parenchyma, perivascular macrophages and microglia become productively infected and replicate virions while astrocytes take up virus.

In the CNS, there are five main types of brain cell: astrocytes, oligodendrocytes, neurons, perivascular microglia, and macrophages. Perivascular macrophages and microglia are most commonly infected by HIV-1 (80, 244–252). Although both macrophages and microglia share similar morphology and phagocytic function, they have different origins. Microglia are derived from mesodermal erythromyeloid progenitors (253) and migrate from

the yolk sac to the neuroepithelium during embryonic and fetal development (254, 255). Microglia function autonomously and self-renew locally. In contrast, perivascular macrophages are derived from hematopoietic stem cells located in the bone marrow. Macrophages are replenished frequently by circulating monocytes in the blood stream, which enable HIV-1 entry (80). The presence of HIV-1 in the brain can trigger inflammatory responses and induce the production of chemo-attractant proteins that recruit virus-bearing monocytes or infected T cells and macrophages to the injury site, which can increase the viral load in the CNS (256–258). In contrast to macrophages and microglia, astrocytes, oligodendrocytes, and neurons do not appear to be productively infected with HIV-1, in keeping with their lack of viral receptors (see section on tropism), and yet virions have been detected in astrocytes, suggesting that astrocytes may harbor virus as cellular reservoirs (80, 259).

### 1.7.1 Astrocytes

Astrocytes make up most of the brain mass (40-60%) and provide structural support in the CNS by existing as a network of  cells (260–262). Astrocytes enable intercellular communication, synaptic transmission, neurovascular coupling, deliver nutrients, and guide neuronal growth and differentiation (263, 264). Their intricate processes contact thousands of synapses while their endfeet contact capillaries and arterioles (263). Astrocytic endfeet structures form *glia limitans* around the BBB, which modulate passage of materials to maintain homeostasis in the brain. Astrocytes become activated in a process known as reactive astrogliosis in response to CNS injuries, such as stroke, trauma, tumor growth, or neurodegenerative diseases. When activated, astrocytes express glial fibrillary acidic protein (GFAP), undergo hypertrophy,

proliferate, and migrate toward the site of injury to form glial scars to wall-off lesions but also physically prevent neuronal reconnections (265–268).

### 1.7.2 Evidence of HIV-1 in astrocytes *in vivo*

Electron microscopy images of post-mortem brain sections from AIDS patients with HIV-associated encephalopathy revealed virions inside the astrocytes (269). Integrated HIV-1 proviral DNA, viral RNA, mRNA (nef, gag, pol, env, tat, and rev) and viral proteins (Rev, Nef) have been detected in astrocytes from post-mortem human brain and spinal cord tissues of HIV-1 infected patients. Astrocytes were identified and isolated using immunohistochemistry, immunocytochemistry, laser capture micro-dissection and viral products were analyzed by polymerase chain reaction (PCR), triple-nested Alu-PCR, *in situ* hybridization DNA PCR, *in situ* hybridization RT PCR, (246, 248, 270–277). These studies are summarized in (243, 259). Cumulative data showed that astrocytes primarily express early viral markers, such as viral DNA and nef mRNA, and occasionally late markers, such as gag and env mRNA. In contrast, macrophages and microglia expressed viral components in all stages of the HIV-1 replication cycle, suggesting that microglia/macrophages are the predominant targets for viral production (Figure 1.12) (259).

| Temporal marker | Viral component | n* | Microglia/ macrophage (%) | Astrocytes (%) |
|---|---|---|---|---|
| Late | Gag | 60 | 48 | 10 |
| | Env | 213/121† | 33 | 0 |
| Early + late | HIV-RNA | 41 | 56 | 22 |
| Early | Nef | 20 | 10 | 41 |
| | DNA | 47 | 85 | 83 |

*n, number of cases examined; †213 cases: microglia/macrophages, 121 cases: astrocytes.

**Figure 1.12** Frequency of viral components detected in microglia/macrophage and astrocytes in the brain tissues of HIV-1 infected patients. Figure from (259).

About 2.6% of astrocytes and 7.5% of microglia/macrophages in infected brain tissue contain HIV-1 products (246, 277). However, the number of astrocytes (40-60% brain mass) is approximately 2-3 times that of microglia/macrophages (12-20% brain mass) (260–262), thus, the total number of HIV-1+ astrocytes may be equivalent to, or more than, that of microglia/macrophages. In fact, the number of HIV-1+ astrocytes may be under-represented because GFAP, which is only expressed in activated astrocytes, was used as an astrocyte-specific cell marker. Therefore, astrocytes positive for HIV-1 but negative for GFAP may have been missed (259). Interestingly, it has been noted that HIV-1 infected astrocytes are commonly found near perivascular mononuclear cells in the brain (275), which suggests that viral transfer might occur between the two cells.

### 1.7.3 Evidence of HIV-1 in astrocytes *in vitro*

*In vitro*, astrocytes have been exposed to M-tropic viruses, such as SF128A, SF162, JR-FL, and Ada-M, and to a lesser extent T-tropic viruses, particularly SF2, NL4-3, SG3.1, JR-CSF, and IIIB (259, 278, 279). The presence of HIV-1 in astrocytes *in vitro* has been detected primarily using astrocyte tumor-derived cell lines, including TH4-7-5 (280), U373 malignant glioma (MG) (281–283), U87 (29, 83, 284, 285), 489 MG (283), 138 MG (283, 286), U138 (29), U343 (287), U251 (287), H4 (288), SH-EP (289), SF609 (287), SF611 (287), SF612 (287), primary human fetal astrocytes (HFA) (287), or human embryo brain cells (290). In these studies, astrocytes were exposed to purified HIV-1, supernatant from HIV-1 infected peripheral blood mononuclear cells (PBMC) (287), HIV-1 infected PBMC (283), T cells (278, 288), or macrophages (83). Detection of viral presence was performed using TEM, immunofluorescence against p15 and p24 antigens, anti-HIV antiserum,

immunocytochemistry, flow cytometry, Northern blot, *in situ* hybridization, chloramphenicol acetyltransferase assay, immunoperoxidase staining, immunoblot analysis, proviral DNA and RT activity by PCR, and p24 and nef ELISA (279–281, 283, 284, 286, 291). Astrocytes exposed to virus produced a low-level and transient viral release detected by persistent expressions of vif, tat, rev, and nef gene activity, low levels of p24, and HIV-1 structural proteins expressions on 1-5% of cells (259, 282, 283). There were no cytopathic effects observed in astrocytes even after months of exposure although the growth rate decreased slightly (278, 283, 291). Astrocytes exposed to HIV-1 did not form multinucleated giant cells as seen in macrophages and T cells (292–296).

Astrocytes exposed to HIV-1 were co-cultured with uninfected PBMC (283, 287), lymphocyte and monocyte cell lines, such as C8166 (29, 280, 297), SUP-T1 (282), U937 (283). Detection of viral antigens was performed by proviral DNA and RT activity PCR, p24 levels ELISA, immunofluorescence, and syncytia formation. T lymphocytes, monocytes, and PBMC co-cultured with HIV-1-exposed astrocytes expressed viral products, suggesting that viral transfer occurred (29, 282, 283, 286, 287). In some cases, the presence of virus was not detected in astrocytes but recovered only in co-cultured target cells (29).

HIV-1 entry into astrocytes appeared to be CD4-independent because astrocytes intrinsically express undetectable levels of CD4 and the major HIV-1 co-receptors, CXCR4 and CCR5 (83, 284, 285, 287, 288, 298–302). Blocking CD4 did not prevent HIV-1 entry into astrocytes (284, 298, 299, 303). Many reports suggest that HIV-1 entry into astrocytes occurs through an alternative pathway mediated by the mannose receptor (284), an unknown 65 kDA cell surface molecule which is neither CD4 or galactocerebroside (304), CD81-coated vesicles (305), co-receptor CC chemokine receptor D6 (306), CCR5 and

DC-SIGN (307), or an unspecified endocytic pathway (304, 307, 308). Because of limited viral activity, antigen presence, and virion production from astrocytes, HIV-1 activity in astrocytes is termed “restricted” or “latent.” Studies in which the viral genome has been transfected into astrocytes or pseudo-typed envelope virus have been added to astrocytes (309, 310) to overcome the entry block resulted in productive infection. Some reports suggest that viral production can be restricted at multiple stages of the HIV-1 replication: viral entry, reverse transcription, HIV-1 RNA transport from nucleus to cytoplasm, translation of RNA, and virion maturation (311).

### 1.7.4 Restricted HIV-1 expression in transfected astrocytes

To evaluate the effects of HIV-1 in astrocytes, HFA and astrocytoma-derived cell lines have been transfected with HIV-1 infectious molecular clones (IMC) (279, 291, 296). In transfected astrocytes, HIV-1 antigens and RNA were detected by immunofluorescence, *in situ* hybridization, and p24 ELISA. HIV-1-transfected astrocytes showed no cytopathic effects, such as lysis or syncytial fusion, but showed some morphological changes, including swelling and detachment (291). In one study (296) the p24 antigen levels produced by transfected astrocytes were monitored over a month. P24 levels increased rapidly, peaked within the first 2-3 days and progressively decreased, resulting in latent infection when neither viral antigens nor virions could be reliably detected after 1 week. However, the infection could be reactivated with the introduction of pro-inflammatory cytokines TNF-α or IL-1β, or by co-culture with CD4+ T cells either by direct contact or across a Transwell membrane (296, 312). Reactivated astrocytes produced p24 antigens at a lower level than the initial post-transfection level and eventually the production progressively decreased back to the level of latent infection.

In summary, HIV-1 infection after transfection of human astrocytes with an infectious viral clone has been described in three stages (Figure 1.13). 1. The initial stage resulted in rapid pro-viral production and progressively decreased to a latent infection. 2. The addition of cytokines and CD4+ lymphocytes can reactivate viral production. 3. The new viral production again progressively decreased back to the latent infection. Thus, transfected astrocytes serve as a persistent reservoir of HIV-1 *in vitro*, but this is obviously not a reflection of events taking place *in vivo*.

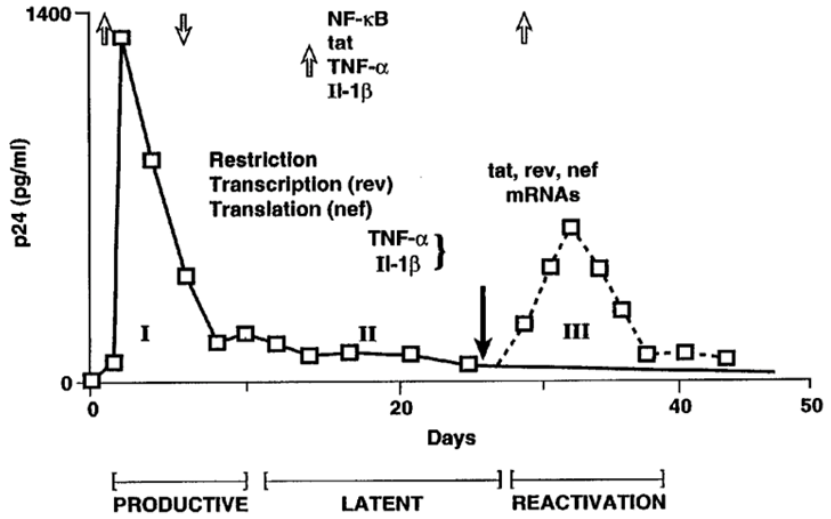


**Figure 1.13** HFA was transfected with pNL4.3 DNA. HIV-1 p24 was measured by ELISA for 7 weeks post-infection. Open arrows indicate DNA binding activity of NF-κB and the closed arrow indicates the introduction of cytokines TNF-α and IL-1β. Figure from (312).

### 1.7.5 Effects of HIV-1 presence on astrocytes

HIV-1 bearing astrocytes disrupt the structural integrity of the BBB by inducing apoptosis of the endothelial cells that line the BBB and by changing the morphology of the endfeet (303), which increases permeability allowing pathogens normally excluded from the brain parenchyma to enter the CNS. HIV-1 containing astrocytes transfer toxic signals, amplified by gap junctions, to uninfected astrocytes, causing apoptosis of surrounding healthy cells, while

remaining resistant to apoptosis themselves (313). In this way, astrocytes can propagate damage throughout the CNS.

HIV-1 proteins can trigger astrocytes to produce neurotoxic chemicals directly or indirectly via interactions with HIV-1-infected lymphocytes and monocytes. The addition of M-tropic HIV-1 JRFL or T-tropic HIV-1 IIIB induced astrocytes and microglia to increase the expression level of inflammatory cytokines IL-1 and TNF-α (314). Inflammatory cytokines, such as IL-1β and IFN-γ, viral proteins including gp120, Tat, and gp41, can induce astrocytes to generate nitric oxide (315–317). Nitric oxide is the primary inducer of neuronal damage (240) and can trigger astrocytes to express GFAP, which is expressed during astrogliosis (317). Neuronal death and astrogliosis are the hallmarks of HIV-1 neuropathology (316).

Activation of astrocytes or exposure to cytokines, including TNF-α and IL-1β, induces astrocytes to up-regulate CXCR4 expression, which might, in principle, enhance entry of CD4-independent strains of X4 HIV-1 (300, 318). Cytokines, such as TNF-α, IL-1β, and IFN-γ, were shown to induce astrocytes to generate monocyte and lymphocyte chemotactic proteins including IL-8 (neutrophil), chemokine (C-C motif) ligand /monocyte chemotactic protein (CCL2/MCP-1) and CCL5/regulated on activation normal T cell expressed and secreted (CCL5/RANTES), which recruit additional leukocytes into the brain (257, 319), resulting in enhanced inflammation and viral load. Similarly, astrocytes exposed to HIV-1-infected T cells secrete TNFα, IL-1α, IL-6, and matrix metallopeptidases MMP-3 (activates MMP-9) and MMP-9 (assists IL-8 mobilization of leukocytes) (320). Astrocytes exposed to HIV-1-infected macrophages with elevated virus-induced TNF-α produce CCL2/MCP-1 (318,

319). The presence of TNFα, IL-1β, and CD4+ lymphocytes can cause reactivation of HIV-1 production in transfected astrocytes (312).

Taken together, the indirect and direct effects of HIV-1 and viral products disrupt astrocytic functions by inducing astrocytes to up-regulate chemotactic cytokines, induce apoptosis of neighbouring astrocytes, and disrupt BBB functions. These activities facilitate the entry of pathogens and virus-bearing leukocytes into the brain parenchyma. Astrocytes also produce inflammatory cytokines and neurotoxins that perpetuate prolonged inflammation and cellular activation in the brain. These factors contribute to neuronal death and lead to HIV-1 pathogenesis in the brain. Because astrocytes are the most abundant cells in the brain, efforts to inhibit HIV-1 effects on astrocytes may help to minimize the pathological sequelae associated with HIV-1 infection, including dementia and cognitive disturbances.

## 1.8 Evidence for and against astrocyte infection

Although there is evidence in the literature that supports the idea that HIV-1 can be found in astrocytes, some reports question whether astrocytes can be infected with HIV-1 (321). Astrocytes may take up cell free viral particles from the extracellular milieu or HIV-1 infected macrophages and T cells, but cell-cell transfer is likely to be a more efficient mechanism because large numbers of virions can be targeted to the contact junction. The ability of astrocytes to take up viruses, transfer virions to another cell, activate inflammatory responses, and recruit immune cells to the site of insult may play a central role in HIV-1 associated neuropathology.

Astrocytes have been reported to have phagocytosis capabilities similar to microglia and macrophages (322, 323). Astrocytes express receptors involved in phagocytic pathways including pattern recognition receptors, such

as Toll-like receptors, scavenger receptors, mannose receptors and components involved in the complement pathway (e.g. opsonin receptors) (reviewed in (324)). Receptor activation in astrocytes can trigger phagocytosis and production of regulatory cytokines that amplify or repress the immune system. Astrocytes have been observed to actively collect and engulf whole apoptotic or dead cells without adverse effects, and are thought to do so to protect neighboring neurons. Engulfed materials are stored rather than degraded through lysosomal pathways (325), suggesting that virions and virus-associated cell debris might be archived for future release. Astrocytes also have a constitutive endocytotic pathway that can internalize extracellular molecules, provide stable, long term viral reservoirs (284, 326) and protect virions from the immune system and entry inhibitors (88).

Astrocytes can take up viruses using non-specific mechanisms by simply trapping virions on their extensive and intricate “bush-like” processes. Astrocytes are highly susceptible to viral exposure because they modulate the permeability of blood vessels, a site where incoming virions and infected cells cross the BBB to enter the brain parenchyma. Astrocytes are also motile and undergo rapid proliferation and hypertrophy, especially in response to neuropathology. In the journey to the site of insult, astrocytes can quickly become exposed to virions and virus-containing cells. These infectious products may be trapped in the astrocytic network of processes and be transferred to bystander cells.

Taken together, these findings may explain how early stage viral mRNA, viral DNA, and viral proteins can be detected in astrocytes despite the fact that astrocytes contain undetectable levels of viral entry receptors. Additionally, astrocytes show few cytotoxic effects associated with HIV-1 exposure and have

no or low viral productivity. The high viremia levels that decrease rapidly over time in HIV-1- astrocyte cultures might be attributed to lingering virions adsorbed on the cell surface that degrade over time. Astrocytes exposed to HIV-1 may transfer virions to lymphocytes or monocytes in a similar *trans*-infection mechanism as shown in DC to T cell without becoming infected themselves. In this way, naïve leukocytes that have been co-cultured with HIV-1 exposed astrocytes can become infected themselves.

## 1.9 Hypothesis

I hypothesized, based on all the evidence presented above, that astrocytes do not actually become infected with HIV-1 but simply take up virions and/or infected cell debris and therefore appear to be infected. The virus remain outside of the cell instead of inside the cell as whole virus or viral components (Figure 1.14). I propose that astrocytes bearing virions or virus-containing debris can transfer infectious viral particles to another HIV-1 permissible target cell leading to productive infection.

This hypothesis raises many questions about HIV-1 permissivity in astrocytes. Do astrocytes become infected with HIV-1? Or do astrocytes simply take up viruses and virus-bearing cellular debris? If yes, where do the viruses go after they are taken up by astrocytes; in intracellular vesicles or surface-connected compartments or surface-bound? Can HIV-1 infected macrophages and T cells transfer virions to astrocytes? If so, what is the structure of the VS? Do astrocytes transfer virions or virus-bearing debris to neighboring cells? To answer these fundamental questions, I apply biological and virological techniques in combination with advanced microscopy strategies.

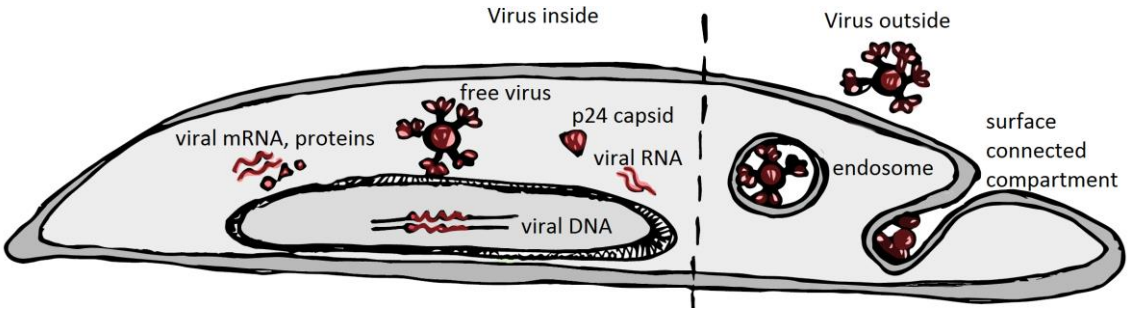


**Figure 1.14** Virus can exist inside the cell as whole virus or viral components (capsid, vRNA, vDNA, viral mRNA and proteins) or outside the cell in endosome, surface connected compartment or surface-bound.

## 1.10 Microscopy

Powerful imaging instruments are currently available and they provide a glimpse into the structures, organization, and functions of biological systems. Microscopes were developed to visualize small objects that are invisible to the naked eye. Each type of microscope is limited by the resolution, which is defined as the shortest distance between two points that can be distinguished as separate entities. The resolution is inversely proportional to the wavelength of light observed, thus, shorter wavelength results in higher resolution images. Combining multiple types of microscopy enables visualization of small features in exquisite detail and their relationships to other features in the larger context of whole organisms. The scale of biological specimens are summarized in (Figure 1.15).

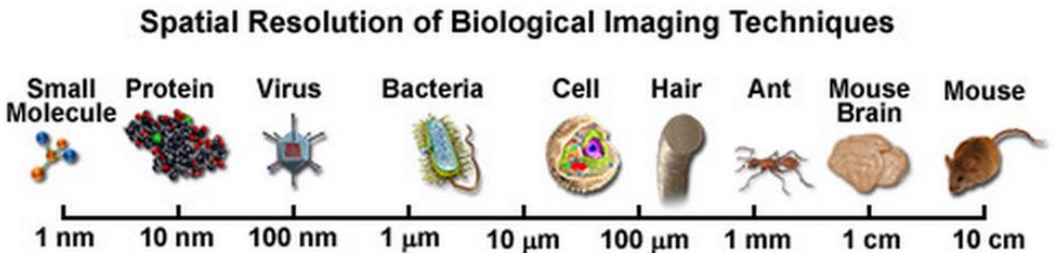


**Figure 1.15** The scale of biological specimens. Figure from www.zeiss.com.

### 1.10.1 Optical microscopy

The first type of microscope was optical microscope developed in the 1500's, which uses light to view objects through magnifying lenses. The invention of fluorescence probes enabled organic or inorganic substances to be tagged and imaged through optical microscopes. This technique is named fluorescence microscopy and is now commonly used in biology to identify the proteins of interest. Main types of optical microscopy include widefield microscopy and confocal microscopy, which can achieve resolutions of ~230 nm and ~180 nm, respectively. The resolution is limited by the diffraction of light, which has a wavelength of ~400-700 nm (327, 328). Super-resolution microscopy overcomes this limit by changing the excitation light temporally or spatially. For example, structured illumination microscopy (SIM) uses superimposed striped illumination patterns to create moiré fringes that results increased resolution by a factor of 2 to ~100 nm (Figure 1.16) (328–330). Stimulated emission depletion (STED) microscopy uses a donut-shaped depletion laser beam to inhibit the peripheral fluorescence in the outer regions of the point-spread function, allowing only the fluorescence signal in the centre to be recorded. This technique increases the resolution by a factor of 8-9 to ~20-50 nm (23, 331–335). Optical microscopy enables live cell imaging, which captures the kinetic and temporal patterns of biological activities. Currently the best live cell imaging system is the fluorescence confocal microscope because of its wide availability, ease of use, and short imaging time, which lowers the possibility of introducing photo-toxicity. Efforts are being made to optimize super-resolution microscopy for this application as well.

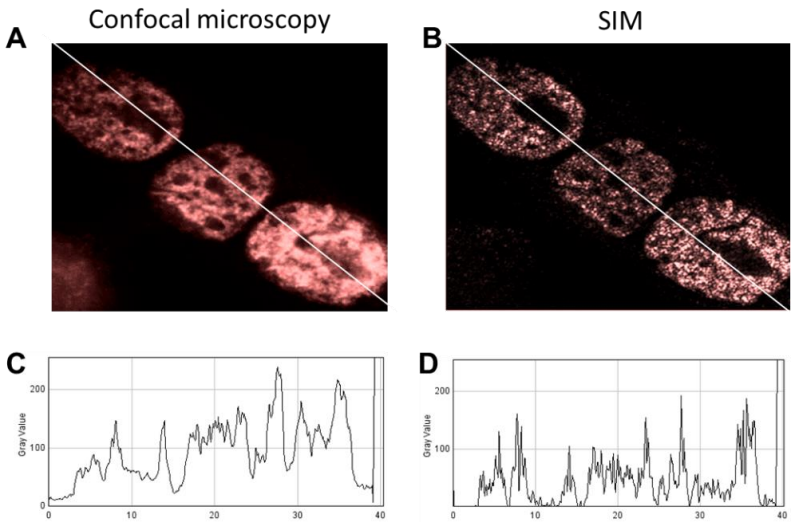


**Figure 1.16** Image of C2C12 muscle cell nuclei stained by anti-Myogenin antibody taken by confocal microscopy (A) and super resolution SIM (B). Line plot profile histograms of the fluorescence signals captured in the two images show SIM (D) provides more details than confocal microscopy (C).

### 1.10.2 Electron microscopy

In the 1900s, electron microscopy was developed to visualize even smaller features. This type of microscope takes advantage of the shorter wavelength of electrons compared to visible light to increase the imaging resolution. Scanning electron microscope (SEM) uses an electron beam to raster across the surface of a specimen coated with metals and relays an image of the sample topography as visualized in three dimensions (3D). The resolution of SEM is ~1 nm (336–338). Alternatively, TEM transmits a beam of electrons through an ultra-thin <200 nm specimen (stained with metals, embedded in polymer resin, and ultra-microtomed (~100-150 nm slices)) or cryopreserved in thin amorphous ice films. The interactions of the electrons with the molecules on the specimen are recorded using a charge-coupled device (CCD) camera. TEM can produce images at a resolution of ~0.1 nm (339, 340). 3D TEM images, or tomograms, can be produced by tilting the samples and image the sample. The tilt series tomogram is computationally reconstructed to model a

3D structure. To achieve even higher resolution, X-ray crystallography is available and can reveal molecular structures at Ångstrom resolution (341).

### 1.10.3 Focused ion beam scanning electron microscopy

In this thesis, I mainly focus on cell and virus interactions, which requires the visualization of small features (viruses, organelles) in the larger context (whole cells, tissues). A new technology has been developed that addresses this need by combining the power of optical microscopy with electron microscopy, named correlative focused ion beam scanning electron microscopy (FIB-SEM). With this system, the observer can visualize whole cells and quickly identify features of interest by immunocytochemistry and fluorescence microscopy, and then visualize the ultrastructure and subcellular structures with high resolution 3D FIB-SEM (Figure 1.17).

There are many ways to visualize cellular structures in 3D electron microscopy. In serial section TEM (342, 343), the sample is stained with heavy metals, dehydrated, embedded in plastic resin, and ultra-microtomed in ~100-150 nm sections. The sections are collected in a sequential order, imaged in TEM, and reconstructed into 3D structures. This technique requires skill and patience to preserve the nanometer-thin plastic sections, relocate the regions of interest, and align the images to produce an uninterrupted structure. Sections could be damaged or lost in the process, resulting in gaps in the final structure. Another technique is serial block face SEM (SBF-SEM), which physically sections the sample using a diamond knife placed inside the vacuum chamber and then image the sample with the SEM (344, 345). Although this technique is much easier than serial section TEM, the resolution in the z-direction is limited to the thickness of the slices ~50-70 nm (345). For my projects, I used FIB-SEM to abrade a resin layer of ~10-45 nm (z resolution) from the sample block face

with a FIB and then record the backscattered electrons using SEM at 1.5 kV to create an image of the sample block face at ~3-15 nm pixel sizes (x-y resolution).

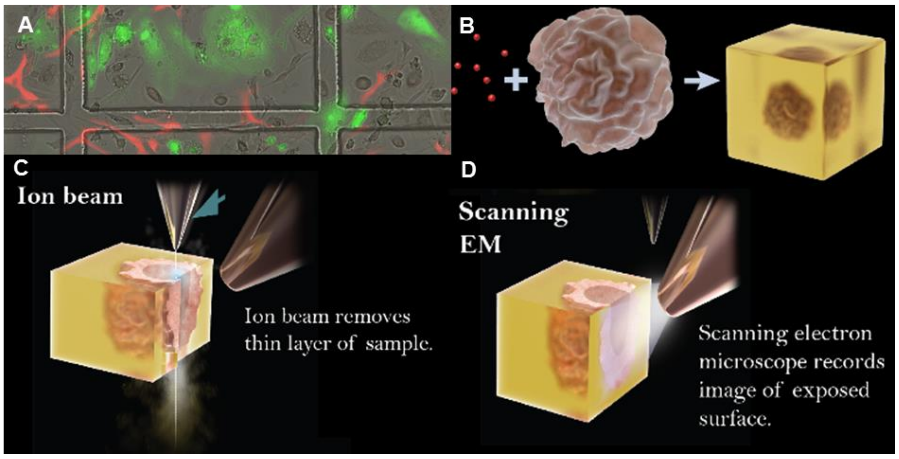


**Figure 1.17** Correlative FIB-SEM steps: features of interest are labelled and identified using alpha-numeric gridded coverslips (A), samples are fixed, dehydrated, stained, and embedded in polymer resin (B), plastic resin is thinly abraded by FIB (C), and the block face is imaged using SEM (D). Panels (B-D) are from (512).

To take a correlative FIB-SEM image, first, the regions of interest (ROI) are located using SEM based on the alphanumeric grid or surface topography of the sample. The plastic blocks are aligned at a 54º angle so that the sample surface is perpendicular to the ion beam and at an angle to the electron beam (Figure 1.18 A). Working with FIBICS, the Subramaniam lab has developed a technique to simultaneously image sub-volumes at high resolution and large fields of view at low resolution (346). This keyframe imaging technique enables ROI imaging in minute detail while also placing the structure in the context of the whole cells or tissues.

To accomplish this, the alignment of the image must be near-perfect. First, a thin 1 µm layer of carbon is deposited on top of the ROI, then a low dose 70 pA ion beam is used to score a pattern, and finally, this pattern is protected with a thin 0.5 µm layer of platinum (Figure 1.18 B). Alternating carbon and platinum deposition enhances pattern contrast for image alignment and protect

the sample surface. A large trapezoidal trench is created in front of the ROI by rastering FIB side to side, starting from the outer region advancing toward the ROI at progressively lower dose (27 nA, 13 nA, 3 nA, 700 pA, 300 pA) (Figure 1.18**Error! Reference source not found.** C). The block face is polished with 00 pA ion beam revealing the cross section of the sample, which is imaged by the SEM. Contrast is visualized by the varying levels of electron densities in cellular features with the optimum-stained lipids typically appearing as most electron dense features. The sub-volume and large ROIs are selected for SEM imaging and can be changed during the imaging process (Figure 1.18 D).

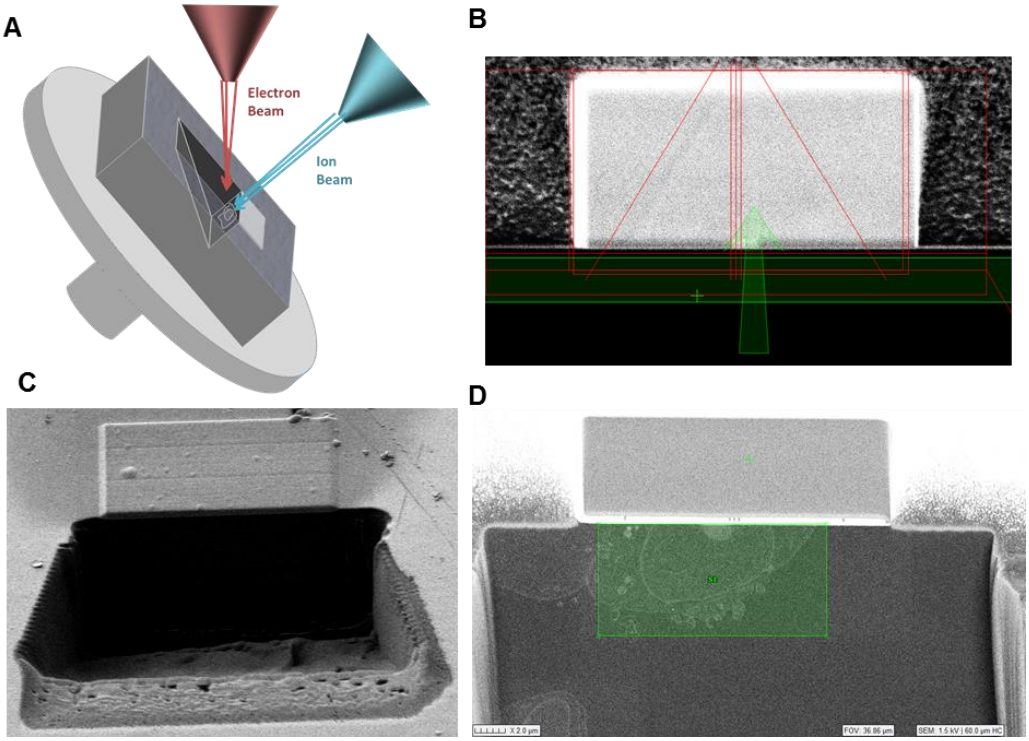


**Figure 1.18** Correlative FIB-SEM steps: sample is aligned with electron and ion beams (A), a pattern is etched on the surface and the sample surface is covered with a platinum and carbon layer to create a high contrast pattern and protect the sample surface (B), a trench is created in front of the features of the interest (C), and ROIs are imaged using electron beam (D).

Imaging a cell with a diameter of 10 µm and a thickness of 3-5 µm can take 3-7 days to complete from sample preparation to imaging. Although this process is destructive, the final product is a 3D reconstructed volume of an ROI in high resolution and a 3D visualization of the surrounding regions in low

resolution. This powerful technique provides temporal, spatial, and compositional information about cells and tissues. With further development, this emerging technology can be operated faster at low cost and increased throughput, making it a powerful tool for biological research.

## 1.11 Aims of thesis

In this thesis, my principal aim was to analyze the interactions taking place between HIV-1-infected immune cells and astrocytes, with relevance to HIV-1-induced neuropathy.

To gain experience in the techniques I would require for this, I first carried out an analysis of muscle cell morphogenesis using novel correlative light and electron microscopy techniques (chapter 3). This allowed me to master cell culture and imaging techniques in a simple system that did not require exposure to infectious virus or virus-infected cells. Once I had achieved this, I subsequently applied these and other virological techniques to the analysis of HIV-1-infected macrophage interactions with astrocytes (chapter 4) and HIV-1 infected T cell interactions with astrocytes (chapter 5).

**Chapter 3. Image cellular differentiation mechanism of skeletal muscle cell using correlative FIB-SEM**

**Aim 3.1.** Characterize the genetic and morphological phenotypes of skeletal muscle cells by immunofluorescence using super-resolution microscopy

**Aim 3.2.** Compare FIB-SEM preparation techniques and optimize them for correlative fluorescence and electron microscopy imaging

**Aim 3.3.** Image the ultrastructure and sub-cellular features of myoblast and myotube muscle cells by correlative FIB-SEM

**Aim 3.4.** Develop semi-automatic image processing techniques and quantitative metrics to describe qualitative characteristics of cellular structures

**Chapter 4. Characterize HIV-1 transfer from macrophages to astrocytes**

**Aim 4.1.** Determine whether astrocytes can become infected with HIV-1

**Aim 4.2.** Determine where HIV-1 goes after the virus becomes associated with astrocytes: surface bound or intracellular compartment?

**Aim 4.3.** Determine whether astrocytes can transfer virions to another cell

**Aim 4.4.** Determine whether macrophages can transfer virions to astrocytes

**Chapter 5. Characterize HIV-1 transfer from T cells to astrocytes**

**Aim 5.1.** Determine whether T cells can transfer virions to astrocytes

**Aim 5.2.** Analyze the effects of HIV-1 on astrocyte activation

**Aim 5.3.** Characterize the VS structure between T cells and astrocytes

# 2 Materials and Methods

## 2.1 Primary cell culture

### 2.1.1 Primary human fetal astrocytes

Human fetal astrocytes (HFA) were isolated from second trimester fetal cerebral cortex, purchased from ScienCell Research Laboratories (SRL) (Catalogue #1800), and cultured with no chemical or genetic modifications. HFA were highly proliferative with high purity (>95% according to SRL) based on GFAP expression. The growth rate and GFAP expression decreased gradually in later passages. HFA were plated at 500,000 cells per T75 flask, which took 10 days to reach 90% confluence, or 1,000,000 cells per T75 flask, which took 5 days to reach 90% confluence. HFA were cultured in Astrocyte Media from SRL (Catalogue #1801) which included basal media using modified MCDB 131, 1% astrocyte growth supplement with optimized concentrations of insulin, transferrin, FGF, IGF-1, hydrocortisone and progesterone to support proliferation, 1% penicillin/streptomycin (P/S), and 2% fetal bovine serum (FBS) (Figure 2.1 A-B).

Alternatively, HFA were cultured from human fetal brain tissue at 98-day gestation in accordance with the National Institutes of Health (NIH) guidelines (102, 278). The fetal brain tissue was carefully cleaned and re-suspended in Dulbecco's Modified Eagle Medium (DMEM) (Life Technologies), 10% FBS (Mediatech, Inc.) and 1% P/S (Life Technologies), incubated at 37ºC with 5% $CO_2$ for 2 weeks without disturbance and then passaged once or twice a week. Isolation and culture of HFA by this method was done by our collaborator Dr. Guanhan Li from the NIH. Cells were incubated at 37°C in 5% $CO_2$.

### 2.1.2 Primary peripheral blood mononuclear cells

Primary human PBMC were isolated as described in (238) from human leukocyte cones obtained from the National Blood Service at the John Radcliffe Hospital, Oxford, UK. The cone exterior was sterilized with 70% Ethanol. The blood was ejected from the cone using an empty syringe filled with air then with 10 mL Phosphate Buffered Saline (PBS). PBMC were isolated by Ficoll density-gradient centrifugation. Using a sterile pipette 20-25 mL Ficoll Histopague (Sigma) was added at the bottom of a 50 mL conical tube and 20-25 mL blood was slowly layered on top of the Ficoll layer to preserve the smooth interface. The conical tube was centrifuged at 400 g for 30 minutes at ~20-22ºC room temperature (rt) with no acceleration or deceleration. The result was a red erythrocytes layer at the bottom, followed by a thick transparent Ficoll layer, a thin white PBMC layer, and a thick yellow plasma layer on top. The PBMC were carefully transferred to a new 50 mL conical tube and washed with PBS by centrifugation at 250 g for 10 minutes with normal acceleration. PBMC were cryopreserved or used fresh for experimentation.

### 2.1.3 Primary human monocyte-derived macrophages

Human primary monocyte-derived macrophages (MDM) were isolated from PBMC by using a Human Monocyte Isolation Kit II (Miltenyl Biotec) or EasySep Human Monocyte Enrichment Kit without CD16 Depletion (Stem Cell Technologies) following the manufacturer's instructions (108, 238). Briefly, non-CD14+ cells were labelled with a cocktail of antibody-magnetic beads and placed in a magnet that captured labelled unwanted cells in a small column or tube. Unlabelled CD14+ cells were collected. Monocytes were matured in macrophage differentiation medium consisting of Roswell Park Memorial Institute (RPMI) 1640 (Sigma) supplemented with 10% FBS, 1% P/S, 1%

Glutamax (GIBCO), and 100 ng/mL macrophage colony-stimulating factor (MCSF) (GIBCO) (347), which yielded both round, pancake-like and elongated monocyte-derived macrophages (MDM), typical of M1 and M2 MDM, respectively (348) (Figure 2.1 C). MDM had 92-95% CD14 purity, a monocyte/macrophage marker, as measured by flow cytometry with few contaminating leukocytes. I chose this method over an alternative method, which uses Xvivo 10 media (Lonza) with 1% heat inactivated filtered human serum (104, 238) because Xvivo media yielded mostly round MDM and less adherent cells compared to RPMI/MSCF media (Figure 2.1 D). MDM were matured for 5-7 days (104). Media were replaced every 7 days.

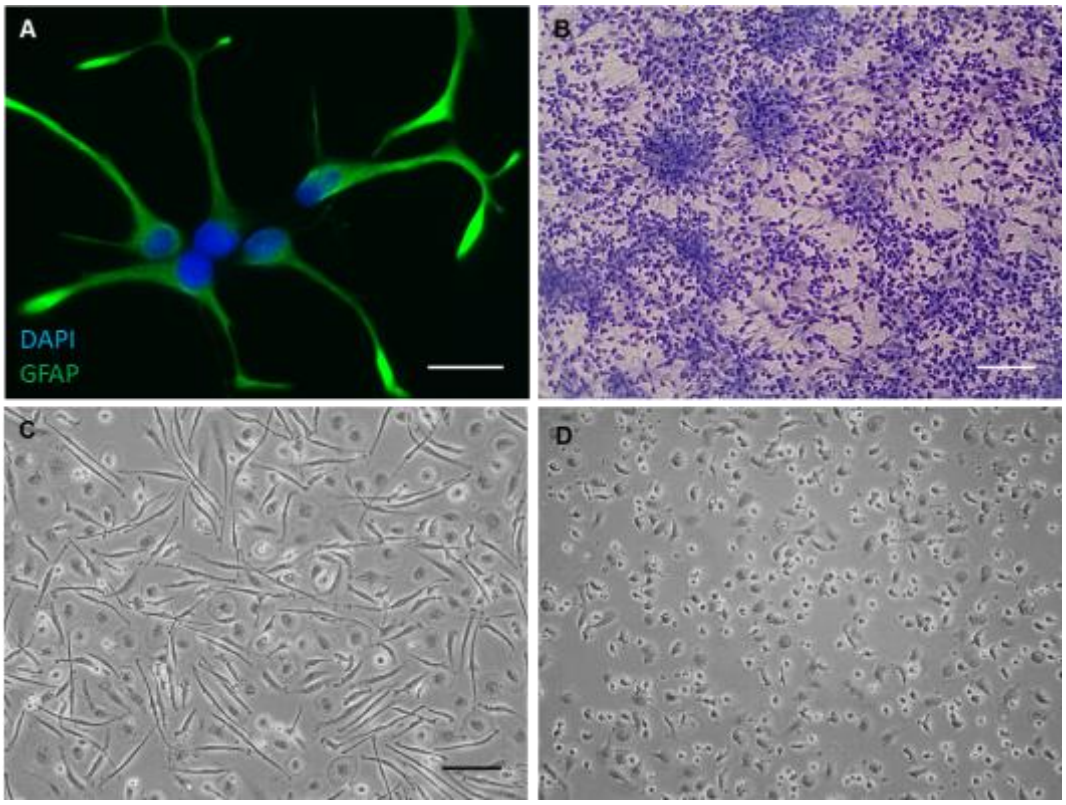


**Figure 2.1** HFA and MDM observed by light microscopy. HFA were stained with DNA marker, 4', 6-diamidino-2-phenylindole (DAPI) and GFAP (A). Scale bar: 50 µm. Confluent culture of HFA stained with haematoxylin and eosin stain (B). Scale bar: 200 µm. MDM matured with RPMI 1640, 10% FBS, 1% P/S, 1% Glutamax, and 100 ng/mL MCSF (C) and with Xvivo 10 media with 1% human serum for 7 days (D). Scale bar: 100 µm.

### 2.1.4 Primary human T cells

Non-adherent PBMC were cultured in RPMI 1640 supplemented with 10% FBS and 1% P/S and activated with 1 µg/mL Phytohaemagglutinin (PHA) (Sigma) and IL-2 (10 IU/mL CFAR, NIBSC) for 3 days. Human primary T cells were isolated using the Human CD4+ T cell Isolation Kit (Miltenyl Biotec) or EasySep Human CD4+ T cell Isolation Kit (Stem Cell Technologies) (104, 108). Briefly, non-CD4+ cells were labelled with a cocktail of antibody-tagged magnetic beads and placed in a magnet that captured labelled unwanted cells in a small column or tube. Unlabelled CD4+ cells were collected. T cells were used immediately after the isolation step.

## 2.2 Stem cell culture

### 2.2.1 Induced pluripotent stem cell monocyte-derived macrophage

Human induced pluripotent stem cell monocyte-derived macrophage (iPS-MDM) were cultured as described in (347). In summary, iPS cells derived from a human donor's fibroblasts were cultured on top of a substrate made of mouse embryonic fibroblasts (MEF) (Figure 2.2 A). After a few days, the iPS cells formed large clusters (Figure 2.2 B) that can be sectioned and passaged on a low-adherence culture dish. These clusters formed tight embryonic bodies (EB) (Figure 2.2 C). The EBs were transferred back to an adherent culture dish with monocyte media, which induced the EBs to turn into factories that produced monocytes (Figure 2.2 D). These monocytes were matured into large and elongated MDM.

First, a 6-well tissue culture dish was coated with 0.1% gelatin for 30 minutes to help MEF cells adhere then washed with PBS. Mitomycin C-inactivated MEF were plated on the gelatin coated surface at 300,000 cells per well in 2 mL Advanced DMEM with 10% PBS, 1% P/S, 1% Glutamax and 0.1%

2-Mercaptoethanol (2-ME) (GIBCO) and cultured overnight. Next day, the culture medium was replaced with iPS medium consisting of knock-out DMEM (Invitrogen), 10% knock-out-Serum Replacement (Invitrogen), 2 mM Glutamax-I (Gibco), 100 U/mL penicillin (Invitrogen), 100 µg/mL streptomycin (Invitrogen), 1% non-essential amino acids (Invitrogen), 0.055 mM β-mercaptoethanol (R&D), 10 ng/mL bFGF (R&D), 5 µg/mL heparin (Sigma) and 0.5% Albumin (Sigma) supplemented with 1 mM Rock inhibitor (Y27632; Calbiochem) for 1 hour. Rock inhibitor was only used in the initial seeding stage to help iPS adhere after they had been detached and passaged using TrypLE Express (Life Technologies).

iPS cells, isolated from an anonymized human donor's skin biopsy, named NHDF-1, in the James William Stem Cell lab were plated at 300,000 cells per well. The medium was changed daily by removing 50% and adding fresh iPS medium without Rock inhibitor. After 6 days, a syringe needle was used to scratch 100 square grids in the wells and a large cell scraper was used to detach the MEF and iPS cells from the well. This detachment technique lifted the cells in small tight clusters, which encouraged formation of EBs.

The cluster of iPS cells was seeded into a well of a 6-well Ultra-Low Attachment Surface Plate (Costar) to form EBs and fed with iPS medium every other day. After 4 days of culture, the EBs were placed in a 15 mL conical tube until all the cells had settled at the bottom of the tube. The supernatant was removed and the pellet was re-suspended in 3-4 mL of monocyte factory medium consisting of Xvivo 15 (Lonza), 1% Glutamax, 0.1% 2-ME, 100 ng/mL MCSF, 0.05% IL-3 (GIBCO), and 1% P/S and re-plated in a 6 well tissue culture dish with about 15-20 EBs per well. The cells were 50% fed every 5-7 days. After 4-6 weeks, the factories started to produce monocytes, which were 97.7%

CD14+ by flow cytometry (Figure 2.2 E-F). Monocytes were harvested by

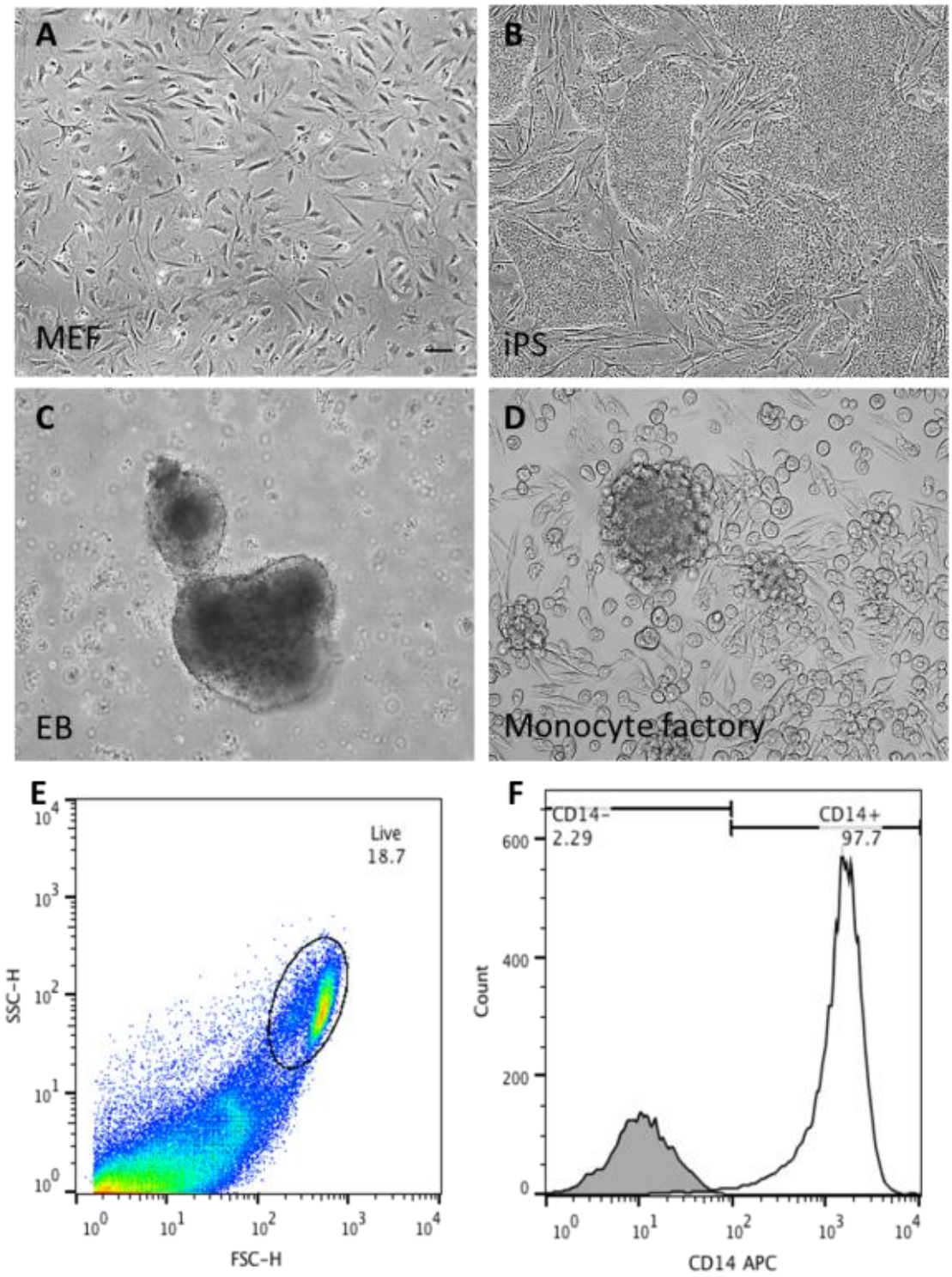


**Figure 2.2** Stem cell culture of Human iPS cells into MDM. Light microscopy images of MEF (A), iPS cells cultured on MEF substrate (B), dark EBs formed from iPS cells cluster (C), and monocyte factory (center) producing MDM (elongated cells) (D). Panels A-D scale bars: 50 µm. Flow cytometry shows live cell gating (E) and CD14 gating (F); iPS-MDM are 97.7% CD14+.

removing 2 mL of media, gently adding back the media on top of the cell layer drop by drop, and finally removing 2 mL of media without any EB contaminants.

The monocytes were matured in RPMI 1640 media supplemented with 10% FBS, 1% P/S, 1% Glutamax, and 100 ng/mL MCSF for 5-7 days. Cells were incubated at 37°C in 5% $CO_2$.

## 2.3 Cell line culture

### 2.3.1 C2C12 skeletal muscle cells

C2C12 mouse skeletal muscle cells (349) isolated from mouse tissue were obtained from the Vittorio Sartorelli laboratory (350) at NIH. They were cultured in complete DMEM growth medium containing 10% FBS and 1% P/S. Cells were grown to 70% confluence and then seeded into different flasks at 30-40% confluence. To differentiate, cells were grown to 90% confluence. The growth medium was replaced with a differentiation medium containing 2% horse serum, 1% Insulin-Transferrin-Selenium 100x, and 1% P/S in DMEM. Medium was exchanged every 3 days. Cells were incubated at 37°C in 5% $CO_2$.

### 2.3.2 TZM-bl

TZM-bl is an indicator cell line, previously designated as JC.53 (clone 13), derived from Hela cells (NIH AIDS Reagent Program) (351, 352). Hela is an immortal human epithelial cell line derived from cervical cancer cells of a patient named Henrietta Lacks in 1951. This cell line proliferates rapidly and is frequently used in research. TZM-bl stably expresses endogenous CXCR4 and transgenic human CD4 and CCR5 and is highly infectible with diverse strains of HIV-1 and HIV-2. These cells also contain integrated transgenic copies of luciferase and ß-galactosidase genes controlled by the HIV-1 promoter. Infection with HIV-1 induces the cells to express luciferase, which can be detected by Bright-Glo Luciferase System (Promega) substrate (353). The cells were cultured in complete DMEM containing 10% FBS, 1% P/S. The cell

population doubled every day, and the culture was split at 70-80% confluence. Cells were incubated at 37°C in 5% $CO_2$.

### 2.3.3 293T

293T is a variant of the human embryonic kidney cells (HEK) cell line that stably expresses the Simian Vacuolating Virus (SV40) Large T-antigen, which is an oncogene that perturbs tumor suppressor proteins including retinoblastoma (pRB) and p53 (354, 355). The cell population doubles every day. These cells can be easily transfected with different plasmids to produce infectious virus or single cycle pseudoviruses (356–358). They were grown in complete DMEM containing 10% FBS and 1% P/S. The culture was split at 70-80% confluence. Cells were incubated at 37°C in 5% $CO_2$.

### 2.3.4 Jurkat-Tat-CCR5 cell line

Jurkat-Tat-CCR5 (ARP094, National Institute for Biological Standards and Controls Centre for AIDS Reagents) is a human T cell line that has endogenous CXCR4 and CD4 expression, and is stably transfected with human CCR5. This cell line is susceptible to infection by CCR5, CXCR4, and CCR5-CXCR4 dependent HIV-1 isolates (120). Jurkat-Tat-CCR5 was cultured in RPMI supplemented with 10% FBS, 1% P/S and 1 mg/mL of G418 (GIBCO) in a flask until ready for infection. G418 was the selectable marker antibiotic used to maintain the level of CCR5 expression. During infection, cells were cultured in medium without G418. Cells were were incubated at 37°C in 5% $CO_2$ and were split 1:10 every 2-3 days.

## 2.4 General cell culture techniques

### 2.4.1 Detach adherent cells

To lift mature MDM from the tissue culture surface, the growth medium was removed, the culture surface was washed with PBS once, and the cells were incubated for 30-60 minutes in 12 mM Lidocaine 5 mM Ethylenediaminetetra-acetic acid (EDTA) at 4°C. After incubation, most cells typically rounded up, and gentle pipetting easily lifted the cells off. Highly adherent MDM sometimes required further scraping but this was avoided as it often resulted in lower viability.

To lift all other adherent cells, the growth medium was removed and set aside for the neutralization step. The culture was washed with PBS once, incubated for 5 minutes in 0.25% Trypsin-EDTA (Life Technologies) at 37°C, and the old growth medium containing serum was used to neutralize Trypsin. The cells were counted, centrifuged, and re-plated with fresh medium or cryopreserved.

### 2.4.2 Cryopreserve cells

Cells were counted and centrifuged at 1500-1700 rpm for 5 minutes. The pellet was re-suspended in 4°C cell freezing solution containing 500 µL growth media and 500 µL of 80% FBS and 20% dimethyl sulfoxide (DMSO) or 1 mL of 90% FBS and 10% DMSO, and immediately added to a cryovial. The cryovial was placed in a Nalgene Mr. Frosty freezing container or Cool Cell freezing container and immediately placed in -80°C freezer overnight. The next day, the cells were transferred to liquid nitrogen dewar for long term storage.

### 2.4.3 Thaw cells

Cryovials were rapidly thawed by gentle agitation in a water bath for 30 seconds. At this point, the cells were still in a semi-frozen state. PBS at rt was added and pipetted up and down repeatedly until the cells were completely thawed. The cells were re-suspended in 9 mL of PBS for every 1 mL of cell solution thawed, centrifuged at 1500-1700 rpm for 5 minutes to remove residual DMSO and counted. At this point, the cells were ready for seeding. This method yielded 80-90% viability by the Trypan blue exclusion counting method. With fragile cells, such as HFA during initial seeding, cryovials were thawed in the water bath and the cells were diluted at a 1:10 ratio of cells to fresh media and immediately seeded to the culture dish. The next day, the growth medium was exchanged with fresh growth medium to remove residual DMSO. This alternative method avoided the centrifugation step, which sometimes damaged the fragile cells.

## 2.5 Virus preparation

### 2.5.1 HIV-1 Infectious molecular clones

HIV-1 viruses were made by transforming competent E.coli bacteria with replication-competent viral plasmid and transfecting 293T cells. After 2 days, transfected 293T cells produced viruses into the supernatant, which was harvested and cryopreserved for experiments. The following table lists the infectious molecular clones (IMC) used for my experiments.

| Name of HIV-1 plasmid | Tropism | Source |
|---|---|---|
| JRFL | R5 | Center for AIDS Research National Institute for Biological Standards and Control |
| Bal | R5 | Center for AIDS Research National Institute for Biological Standards and Control |
| NL4.3-RFP(mCherry).T2A.CH077.ecto | R5 | John Kappes, University of Alabama at Birmingham |
| 2263 pNLENGi-Bal-GFP.ecto | R5 | John Kappes, University of Alabama |
| NL4.3-eGFP | X4 | Barbara Mueller, University of Heidelberg, Germany |
| NL4.3-HIV-Gag-iGFP-JRFL | R5 | Francois-Xavier Gobert, Philippe Benaroch, Institut Curie |
| NL4.3-HIV-Gag-iGFP-JRFL | R5 | Dr. Benjamin Chen, NIH AIDS Reagent Program |
| 2613 NL4.3-LucRenilla-T2A-Bal.ecto | R5 | Christina Ochsenbauer, University of Alabama at Birmingham |
| 2921 NL4.3-LucRenilla-T2A-YU2.ecto | R5 | Christina Ochsenbauer, University of Alabama at Birmingham |
| 2492 NL4.3-LucRenilla-T2A.ecto | X4 | Christina Ochsenbauer, University of Alabama at Birmingham |

### 2.5.2 Transforming bacteria

One shot Stbl3 chemically competent E.coli cells (Life Technologies) were transformed with HIV-1 plasmid following the manufacturer's instructions. Cells were frozen at -80°C and thawed slowly on wet ice. About 1-2 µL of soluble Ampicillin-resistant viral plasmid was added to competent bacteria and swirled gently. If the plasmid was not dissolved in aqueous solution but stored in dried droplets on small pieces of Whatman filter paper, then the filter paper was soaked in 100 µL of Tris-EDTA (TE) buffer Sigma and 10 µL of solution was added to the competent bacteria. The bacteria were incubated in wet ice for 30 minutes to allow the plasmid to attach to the bacteria. Bacteria were incubated in 42ºC water bath for 45 seconds and placed back into wet ice for 2 minutes to

induce the heat shock effect. The rapid change in the temperature induced the bacteria to take up the plasmids.

The bacteria were propagated in 500 µL Luria Broth (LB) at 37ºC with shaking at 250 rpm for 1 hour. About 300 µL of bacteria and plasmid were added to a 10 cm agar plate containing 100 µg/mL Ampicillin and spread thinly using a bacterial spreader. The plates were placed in 37ºC incubator upside down overnight. Because the agar plates contained Ampicillin, only bacteria that have taken up the Ampicillin-resistant viral plasmid propagated in this culture and formed colonies overnight.

The next day a single bacterial colony was selected by dragging a 200 µL pipette tip across the colony and placing the pipette tip in a small tube with 2 mL of LB broth containing 100 µg/mL Ampicillin and incubated in 37ºC with shaking at 180 rpm for 6 hours. The bacteria were expanded in a T-175 flask with 150 mL of LB broth containing 100 µg/mL Ampicillin overnight in a 37ºC incubator with shaking at 180 rpm. The next day the bacteria were lysed using GenElute HP Plasmid Maxiprep Kit (Sigma) according to manufacturer's instructions, which typically yielded 1-3 mL of plasmid in Elution solution. Viral plasmid was quantified by placing 2 µL of plasmid on a NanoDrop 2000 UV-Vis Spectrophotometer (Thermo Scientific), calibrated with 2 µL of Elution solution from the Maxiprep kit as the base level. The machine measured the quantity of nucleic acid in µg/mL. The viral plasmid was stored in 1 mL Eppendorf tubes at -20°C.

### 2.5.3 Transfecting 293T cells

293T cells were transfected with viral plasmid complexed with a cationic gene delivery compound, known as Polyethylenimine (PEI) (359). PEI complex is a simple, inexpensive, and effective method to deliver plasmid DNA into cells.

293T cells were plated overnight at $4x10^6$ cells per 10 cm petri dish in 5 mL of complete DMEM consisting of DMEM supplemented with 10% FBS and 1% P/S. The next day, 2.5 mL of complete DMEM containing 100 µL of 10 µM PEI was added drop by drop in 2.5 mL of complete DMEM containing 20 µg viral plasmid in a 50 mL tube on a vortex mixer to create a constant vortex. The DNA-PEI mixture was incubated at rt for 20 minutes to allow the plasmid-PEI complex to form. 293T medium was replaced with 5 mL of PEI-plasmid and incubated at 37°C for 4 hours. Next, fresh complete DMEM was exchanged and cells were cultured for an additional 48 hours.

### 2.5.4 Harvesting virus

Supernatant from 293T cells was collected and filtered through a 0.45 µm syringe filter. One volume of Lenti-X Concentrator (Clontech) was added to 3 volumes of virus supernatant and incubated in 4ºC for 30 minutes. The solution was centrifuged at 1500 g for 45 minutes at 4ºC. After centrifugation, the supernatant was removed carefully. The pellet was re-suspended in complete RPMI consisting of RPMI supplemented with 10% FBS and 1% P/S at $1/10^{th}$ of original volume of 293T cell supernatant and frozen at -80 ºC in Eppendorf tubes.

## 2.6 Luciferase assay

In summary, the luciferase assay is highly sensitive technique that can be used to quantify transcriptional activity when the luciferase reporter gene is cloned downstream of a suitable promoter. Cells, such as TZM-bl, and some IMC have been engineered to contain a luciferase reporter gene fused to the HIV-1 promoter region. This gene encodes a luciferase enzyme that catalyzes the oxidation of luciferin, which releases excess energy by emitting light. The fluorescence signal is proportional to the steady state mRNA level; thus, the cell

transcriptional activity can be measured by the released light (360). In this assay system, cells are lysed with a detergent-based buffer and rapid temperature changes (22°C to -80°C to 22°C). The cell lysate containing the luciferase enzyme is mixed with a luciferin substrate, which induces fluorescence signal that can be measured by a luminometer. Data are expressed in relative luminescent units (RLU).

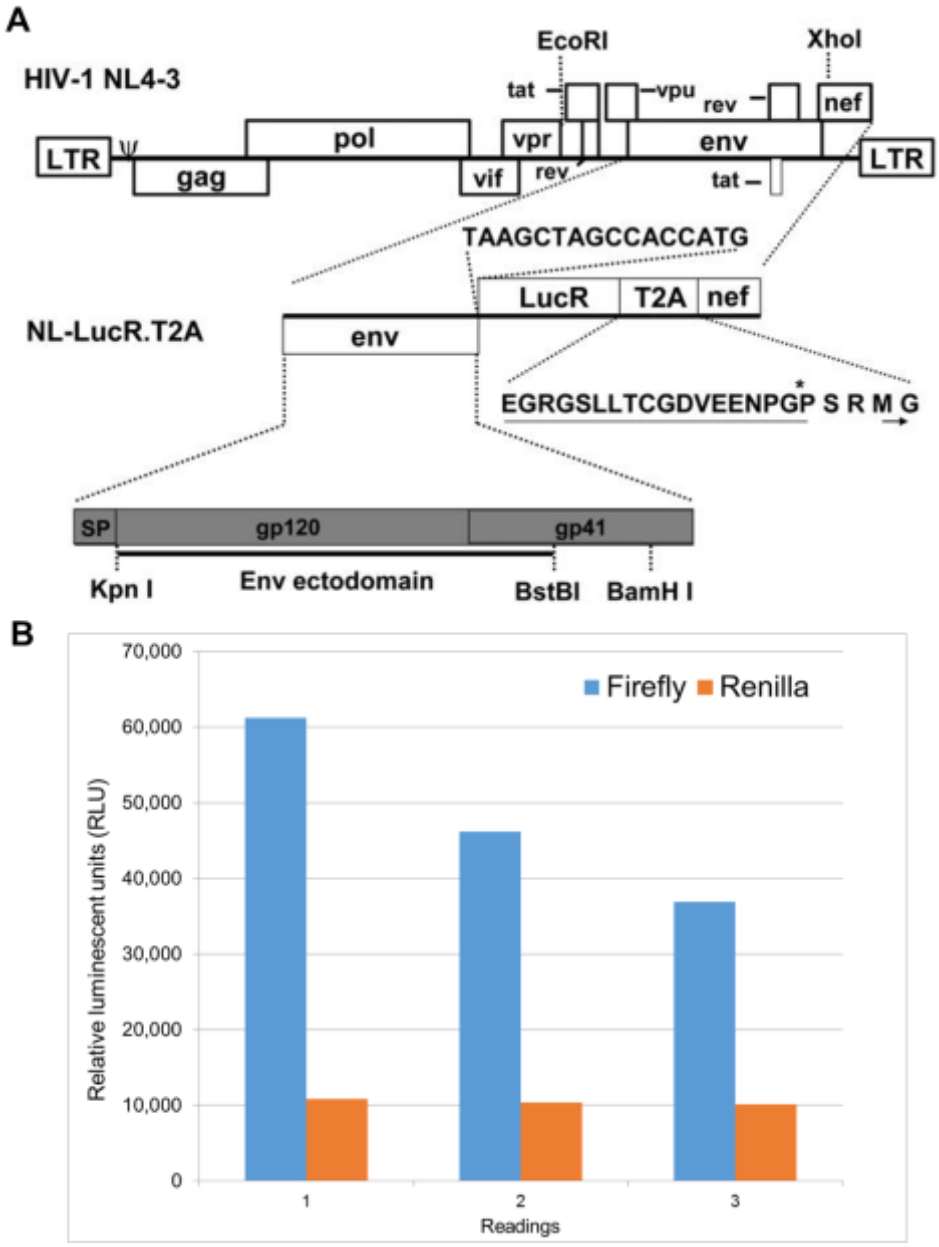


**Figure 2.3.** Schematic representation of the LucR gene inserted into the NL4.3 viral backbone of LucR HIV-1 viruses, reproduced from (362). Comparison of RLU values produced by Firefly versus Renilla luciferase systems using Bal-LucR infected TZM-bl taken at 3 consecutive time points. Graph shows the average values of triplicate samples.

### 2.6.1 TZM-bl titration infectivity assay

Viral titres were analyzed by TZM-bl infectivity assay (353, 361). TZM-bl were plated in triplicates of 12 wells in a 96 well flat bottom plate at 10,000 cells in 100 µL complete DMEM media per well. Virus was added to the first well at 1:4-1:10 dilution and serially diluted at 1 to 3 by taking 50 µL of media from one well and adding it to the next well, skipping the last control wells for background readings. Cells were incubated for 24 hours. The medium was removed from all wells and replaced with 100 µL of reporter lysis buffer (Promega). The cell solution was incubated at rt for a few minutes and then froze at -80ºC overnight. Next day, lysed cells were thawed at rt in the dark and 50 µL of lysate was added to 50 µL Bright-Glo Firefly Luciferase Substrate (Promega) in a white 96 well flat bottom luminescence plate (Corning). After 2 minutes, the plate was analysed using a M5 SpectraMax plate reader (Molecular Devices) on Luminescent setting with 1000 milliseconds integration to obtain Firefly RLU (F-RLU). The background values were multiplied by 2 to determine the cut off values. Raw values that were above the cuff off values were counted and input into a $TCID_{50}$ v5.0 software (NIH), which calculates the infectious units.

### 2.6.2 Cell free virus luciferase infectivity assay

A cell free virus luciferase infectivity assay was performed using replication competent viruses with the Renilla Luciferase (LucR) gene inserted into HIV-1 proviral backbone, pNL4-3 DNA, after Env and fused with Nef via the T2A peptide sequence (Figure 2.3 A). These reporter viruses contain various HIV-1 Envs and stably express LucR over multiple replications (362). For my experiments, I used 2613 NL4.3-LucRenilla-T2A-Bal.ecto (Bal-LucR), 2921 NL4.3-LucRenilla-T2A-YU2.ecto (YU2-LucR) and 2492 NL4.3-LucRenilla-T2A.ecto (NL4.3-LucR).

HFA and TZM-bl were plated at 2,500 cells per well in a 96 flat bottom well plate and allowed to adhere to the culture plates overnight. Cells were infected with Bal-LucR, YU2-LucR, and NL4.3-LucR reporter viruses at various multiplicities of infection (MOI) from $10^{-3}$ to $10^{1}$ (108, 238) overnight in a 37°C incubator and the virions were removed by PBS washes. At 2, 4, 7, 9, 11 days post infection (d.p.i.), the culture medium was removed and 50 µL of Glo-Lysis buffer (Promega) was added. The plate was left at rt for a few minutes and then frozen at -80ºC overnight. Lysed cells were thawed at rt in the dark. 50 µL of lysate was mixed with 50 µL Renilla Luciferase Substrate (Promega) in a white luminescence plate. After 2 minutes, the plate was analysed using a M5 SpectraMax plate reader on Luminescent setting with 1000 milliseconds integration to obtain Renilla RLU (R-RLU).

### 2.6.3 Cell-cell luciferase virus transfer assay

100,000 monocytes per well were plated in a 96 flat bottom well plate and allowed to mature for 5-7 days. When MDM had matured, 2,500 HFA were plated overnight and both cells were infected with Bal-LucR, YU2-LucR, and NL4.3-LucR viruses at MOI from $10^{-3}$ to $10^{0}$ (108, 238). Next day, cells were washed with PBS and 10,000 TZM-bl or 50,000 activated CD4+ T cells per well were added. Cells were plated at different seeding densities and time points to account for the various cellular growth rates and cell body sizes.

At days 2, 4, 7, 9, 11 d.p.i., the co-cultures containing TZM-bl were washed with PBS and analysed for luminescent signal using Bright-Glo Luciferase Firefly Substrate as described in 2.6.1. Only TZM-bl express luminescent signal in response to Luciferase Firefly Substrate, therefore, it was not necessary to separate the cells in this co-culture system. Alternatively, the non-adherent T cells were gently transferred to a replicate 96 well plate (>94-

99% CD4+ purity by flow cytometry) and analyzed for luminescent signal using Renilla Luciferase Substrate as described in 2.6.2.

Of note, although both Firefly and Renilla luciferase systems provide information about HIV-1 promoter activity through light emission, there are some small differences. When I compared the F-RLU and R-RLU values taken from triplicate samples of TZM-bl infected with Bal-LucR after 3 consecutive readings, I noticed that F-RLU values were higher and decreased more rapidly than R-RLU values (Figure 2.3 B). I concluded that for purposes of comparisons, it was important to compare RLU values within the same experiment. When comparing different experiments, it was important to remember that F-RLU yields an intrinsically higher signal than R-RLU; thus, higher F-RLU compared to lower R-RLU does not necessarily equate to higher HIV-1 promoter activity.

### 2.6.4 HIV-1 neutralization/trans-infection luciferase assay

MDM from 2 donors and HFA were infected with Bal-LucR, YU2-LucR, and NL4.3-LucR viruses at MOIs from $10^{-3}$ to $10^{0}$ (108, 238) overnight. Next day, cells were washed and incubated with 0.25% Trypsin for 5 minutes (363, 364), or 10 µg/mL bNabs (10E8, PGT121, VRC01) (353, 362, 365) (a gracious gift from Torben Schiffner) for 1 hour at 37ºC, or 200 µg/mL Pronase (47, 363, 364, 366) for 30 minutes at 4ºC. Cells were washed and 10,000 TZM-bl were added on days 2, 4, 7, 9, 11 d.p.i. and co-cultured for 3 days, then F-RLU was measured.

### 2.6.5 HIV-1 inhibition luciferase assay

HFA were incubated with 10 µM PRO 2000 (Endo Pharmaceuticals) (367, 368) or 10 mM Mannan (Sigma) (369–372) or 10 µg/mL anti-ICAM-1 antibody LB-2 IgG2b (BD Biosciences) (238) or 5 mM EDTA (371, 373)(Sigma)

or 5 μM jasplakinolide (Sigma) (96, 103, 238) or 10 U/mL heparinase cocktail (I and III) (Sigma) (35, 374–376) at 37ºC or 200 μg/mL pronase (Sigma) (47, 363, 364, 366) at 4ºC for 90 minutes or 0.25% trypsin (363, 364) at 37ºC for 5 minutes. Next, HFA were incubated with Bal-LucR, YU2-LucR, and NL4.3-LucR viruses at MOI from $10^{-3}$ to $10^{0}$ (108, 238) for 4-6 hours. Cells were washed and TZM-bl was added. Three days after co-culture F-RLU was measured.

### 2.6.6 Statistics

In all experiments, samples were performed in triplicate in 2-4 independent experiments. The average background values were subtracted from raw values to produce adjusted values. Replicate adjusted values for each sample were averaged. Mann-Whitney unpaired non-parametric *t*-test was used to compare control and test samples; $*p<0.1$. Luciferase data were analysed using Prism (GraphPad) software and graphed with mean and standard deviations (SD).

## 2.7 P24 Enzyme-linked immunosorbent assay

In summary, p24 HIV-1 antigen enzymbe-linked immunosorbent assay (ELISA) is an assay that measures the quantity of HIV-1 p24 capsid protein in a solution. First, an empty plate was coated with anti-p24 antibodies and then the plate was blocked with non-specific protein to prevent non-specific binding. Sample solution was added to the coated plate then unbound sample was washed off. P24 protein in the sample was captured by anti-p24 antibody. Next, enzyme-linked anti-p24 antibody was added to the captured p24 protein. Finally, after washing, enzyme substrate was added and the reaction induced a colour change that can be measured as optical density using a spectrometer. The following procedures were adapted from (97).

### 2.7.1 Inactivation of samples

Supernatants from the cell culture were transferred to a replicate 96-well plate and stored at -20°C. When ready, samples were heat inactivated with Empigen detergent (Sigma) for a final concentration of 0.5% Empigen at 56ºC for 1 hour.

### 2.7.2 Coating ELISA plates

High binding 96 well ELISA plates (Greiner) were coated overnight at rt with 100 µL of anti-p24 antibodies (D7320, Aalto) at 10 µg/mL in coating buffer containing 100 mM $NaHCO_3$ in deionized water at pH 8.5. D7320 is a purified, freeze-dried sheep polyclonal IgG raised against peptides from HIV-1 sequences that are essentially conserved between various HIV-1 stains, reconstituted in deionized water to 1 mg/mL stock.

### 2.7.3 Capturing of antigen

Next day, the plate was washed 3 times with wash buffer containing Tris-buffered saline (TBS) made of 1.44 M NaCl, 250 mM Trizma-HCL in deionized water at pH 7.5 supplemented with 0.05% Tween-20 using a 96 well plate washer (Dynex Technology). Wells were blocked with 2% Bovine Serum Albumin (BSA) (Sigma) in TBS for 1 hour at rt to prevent non-specific binding then washed 3 times as before.

Recombinant p24 protein (AG6054, Aalto) was used as a standard, typically in duplicate wells, by performing 2-fold serial dilution titration starting from 200 ng/mL in 10% FBS, TBS, 0.5% Empigen. The last wells in the titration series contained buffer alone and functioned as background wells. Samples and standards were transferred to p24 antibody coated ELISA plate at 100 µL per well and incubated at 37ºC for 2 hours with gentle agitation at 75 rpm. The

plates were washed 6 times with wash buffer using a Dynex plate washer, with one plate rotation after the third wash to ensure uniform washes.

### 2.7.4 Labelling of antigen

Biotinylated anti-p24 antibody (BC1071-BIOT, Aalto) was added to the plate at 1 µg/mL in 2% BSA, 20% FBS at 100 µL per well and incubated for 2 hours at rt. The plate was washed 6 times as before. Streptavidin-Horseradish peroxidase (HRP) (AbD Serotec) was added to the plate at 100 ng/mL in TBS, 2% BSA, 20% FBS at 100 µL per well and incubated for 1 hour at rt. The plates were washed 6 times as before.

TMB Turbo One-Step Substrate (Pierce) was added to the plate at 100 µL per well for 10 minutes until the colour of the standard wells turned bright yellow with gradual gradation from yellow to clear starting from the most concentrated to negative control wells. The reaction was stopped with 100 µL of 0.5 M $H_2SO_4$ which turned the colour into bright blue.

### 2.7.5 Analyzing data: SpectroMax

The plates were analysed using a SpectroMax M5 (Molecular Devices) plate reader using Absorbance setting at 450 nm and 570 nm with 1 times plate automix. Raw 450 nm values were subtracted from 570 nm values to control for pipetting errors. Background values from buffer wells were averaged and subtracted from the previous values to yield sample values. Standard values were used to create a graph that relates absorbance values to p24 concentration in ng/mL. A standard curve fit with a sigmoidal dose-response curve with variable slope was calculated to find an equation that best fitted the standard values. Sample absorbance values were entered into the equation and interpolated to yield p24 concentration in ng/mL using Prism 6 (GraphPad).

## 2.8 Multicolour flow cytometry

### 2.8.1 Antibodies

Cells were prepared for flow cytometry by staining them with fluorescence conjugated antibodies and matching isotype controls at the same concentration using surface marker or internal marker techniques. The following table lists the antibodies used in experiments.

| Target | Isotype | Description | Dilution | Source |
|---|---|---|---|---|
| CD3-v450 | Mouse IgG1, k | T cell surface marker | 1:50 | BD 560366 Isotype 560373 |
| CD14-PE | Mouse IgG2a,k | Macrophage surface marker | 1:50 | BD 555398 Isotype 555574 |
| CD14-APC | Mouse IgG1k | Macrophage surface marker | 1:10 | Biolegend 325608 Isotype 400121 |
| GFAP-Alexa Fluor 647 | Goat polyclonal IgG – stock 200 µg/mL | Astrocyte internal marker | 1:50 | Santa Cruz 6171 AF647 Isotype 45066 |

### 2.8.2 Staining cell surface markers

Cells were pelleted in a 96 well round bottom plate or 1.5 mL Eppendorf tube at 1500 rpm for 5 minutes and incubated in 2% FBS in PBS, 10 µg/mL normal human IgG (from Torben Schiffner) and conjugated antibody for 1 hour at 4ºC. Cells were washed with PBS and fixed with 4% formaldehyde in PBS at rt for 15 minutes. Cells were washed 3 times with PBS and re-suspended in 50-200 µL PBS for flow cytometry analysis.

### 2.8.3 Staining cell internal markers

Cells were pelleted in a 96 well round bottom plate or 1.5 mL Eppendorf tube at 1500 rpm for 5 minutes and permeabilized and labelled with conjugated antibody in 0.1% Saponin, 3% FBS, 0.009% Sodium Azide in PBS for 1-3 hours at rt. Cells were washed 3 times with PBS and re-suspended in 50-200 µL PBS for flow cytometry analysis.

### 2.8.4 Analyzing data: FACS Calibur or Cyan

Cells were collected on FACS Calibur (BD) or Cyan (Beckman Coulter) flow cytometers at 5,000-20,000 events per sample. The voltage was set by first analysing isotype control samples and adjusting the voltage so that most of the cells were in the lower range of the histogram or dot plot. Next, positive cells were analyzed to ensure that most of the cells were visible inside the graph. Single colour controls were analysed for compensation in experiments where multiple colours were used. Compensation was corrected for emission spectral overlap to ensure that the fluorescence signal detected in a particular channel was solely derived from the fluorochrome of interest. Analysis was done using FlowJo V10 software. Live cells were gated using side scatter channel (SSC) and forward scatter channel (FSC) using log scales. Most live cells have signals above $10^2$ in both SSC and FSC channels and appear in tight clusters in dot plots of SSC vs. FSC. Positive cells were gated by selecting cells with fluorescence signals higher than those in matching isotype samples.

### 2.8.5 Analyzing data: ImageStream

Alternatively, cells were analysed using an ImageStream X Mark II (Amnis) instrument, which combines both the power of flow cytometry and fluorescence microscopy. In this technology, each cell that passes through the electronic detection apparatus is imaged, counted, and analysed by lasers for biomarker detection. The samples were imaged with a 20x or 40x objectives with extended depth of field (EDF). Laser intensities were set based on single colour controls so that the maximum value did not cause spectral overlap in other channels as visualized by the microscopic images. Single colour controls were analysed at 10,000 events per sample for compensation in multicolor experiments. Samples were collected at 100,000-200,000 events per sample. A

compensation matrix was generated with IDEAS analysis software (Amnis) and applied to all raw data. Gating and data analysis are described in the following result chapters. Image processing was performed in IDEAS software and statistical analysis was performed in Prism. A Mann-Whitney unpaired non-parametric *t*-test was used to compare control and test samples; *$p$<0.1.

## 2.9 Light and Fluorescence Microscopy

Cells were stained for fluorescence microscopy with antibodies and antibody-tagged fluorochromes listed below.

| **Target** | **Isotype/Description** | **Dilution** | **Source** |
|---|---|---|---|
| Myogenin | Myogenic transcription marker, anti-mouse IgG1 | 1:500 | Santa Cruz |
| Myf5 | Myogenic transcription marker, anti-mouse IgG1 | 1:500 | Santa Cruz |
| MyoD | Myogenic transcription marker, anti-mouse IgG1 | 1:500 | Santa Cruz |
| H3K9me2 | Histone marker, anti-mouse IgG1 | 1:500 | Abcam |
| GFAP | Astrocyte marker, anti-rabbit | 1:500 | Abcam |
| p24 | HIV capsid marker Clone 37G12 | 1:600 | Polymun Scientific |
| **Fluorochrome** | **Isotype/Description** | **Dilution** | **Source** |
| Alexa Fluor 488 | Mouse IgG1 | 1:1000 | Life Technologies |
| Alexa Fluor 546 | Mouse IgG1 Rabbit Polyclonal | 1:1000 | Life Technologies |
| Alexa Fluor 633 | Mouse IgG1 Rabbit Polyclonal | 1:1000 | Life Technologies |
| DAPI | Nuclear marker | 1:5000 | Life Technologies |
| Hoechst | Nuclear marker | 2 µg/mL | Life Technologies |
| Vybrant Dye DiI | Membrane marker | 1:200 | Life Technologies |
| Abberior Star 635P | Rabbit Polyclonal | 1:100 | Abberior, Jackson ImmunoResearch, coupled in-house |
| Atto 490LS | Mouse IgG1 Clone 37G12 | 1:100 | Atto-Tec, Jackson ImmunoResearch Coupled in-house |

### 2.9.1 Staining for cellular markers

In general, cells were cultured in sterilized pre-packaged cell culture surfaces or on glass coverslips that had been sterilized by immersing in 70% Ethanol in PBS followed by 3 quick immersions in PBS. Cells were washed with PBS and fixed with 4% Paraformaldehyde or Formaldehyde (Electron Microscopy Sciences) in PBS for 15 minutes with rocking.

After fixation, samples were washed 3 times with PBS and permeabilized with 0.2% Triton X-100 (Sigma Aldrich) in PBS for 15 minutes, then washed 3 times in PBS. Samples were blocked with Blocking Buffer containing 3% bovine serum albumin (BSA) in PBS for 1 hour at rt with rocking. Samples were incubated in primary antibody diluted in Blocking Buffer for 1 hour at rt. After incubation, cells were washed 3 times with PBS. The last two steps were repeated with secondary antibody. During the last 10 minutes of staining, DAPI or Hoechst was added. Finally, the samples were washed 3 times with PBS. Alternatively, cells were blocked and permeabilized with PermWash solution containing 0.1% Saponin, 0.5% BSA, 5% human serum, 5% goat serum in PBS for 30 minutes. Cells were stained with primary and secondary antibodies as above but all the steps were performed using PermWash solution instead of Blocking Buffer or PBS. In some experiments, cell membranes were also stained with Vybrant Dye DiI (Life Technologies) for 15 minutes and washed 3 times with PBS.

The stained coverslips were mounted on glass slides using 30-50 µL of Permount (Fischer) or VectaShield Mounting Medium with DAPI (Vector Labs) and sealed around the edges with nail polish. The samples were stored at 4°C protected from light. To conserve reagents, for all antibody steps, coverslips were placed upside on 30-50 µL droplets of antibodies on parafilm sheet. For

washing steps, coverslips were placed back inside 24 well plate and washed with 1 mL of PBS and the solution was removed by aspiration for infected samples or by inversion of the plate in a sink for all other samples. The coverslip remained adhered to the plate by surface tension.

### 2.9.2 Live, widefield, and confocal microscopy

Light microscopy was acquired using the EVOS XL Imaging system (Life Technology) at 4x, 10x, and 20x magnification. The advantage of this microscope is that the cells can be imaged directly from a culture dish without any preparation. I used this microscope to image live cells in petri dish culture or haematoxylin and eosin stained samples using Hema Gurr rapid staining kit (VWR international) according to the manufacturer's instructions.

Live cell fluorescence imaging was performed using a Zeiss AxioVision 200 with a MRm charged couple device CCD camera and Colibri illumination with 20x or 40x oil-immersion objective at every 5 or 10 minutes for 6-24 hours. The microscope is located in a Category III laboratory for infectious disease studies. The microscope has an enclosed imaging chamber that was operated at 37°C with 5% $CO_2$ to mimick physiological conditions. Image analysis was performed using AxioVision v 4.8.2 software (238).

Fluorescence imaging was acquired on the confocal microscope Olympus FV-1000 or widefield microscope Olympus IX51 equipped with CCD camera using 20x, or 40x, 63x, 100x oil immersion objectives at 1024 x 1024 pixel images with 1-2 minutes scan time. Z-stack images were taken at 2-5 µm steps. Images were processed using Olympus FluorView v2.0b software. 3D reconstructions of z-stack images were processed using Imaris software.

### 2.9.3 Structured illumination microscopy

SIM was performed on a SI microscope built by Dr. Jeffrey Spector (102, 377) based around an upright microscope (Olympus BX-51). The excitation light of 488nm or 561nm laser enters the microscope tube lens and is focused on the sample through a 100X N.A. = 1.3 oil immersion objective. The fluorescence emitted from the sample was filtered using band pass filters 525/30 and 605/15 (Semrock Inc.) and imaged on an electron multiplying CCD camera (Princeton instruments). All hardware was controlled using custom written software (Visual Basic) based on ThorLabs APT controller software. SI images were acquired using 6 phases and 6 angles with an exposure time between 100 and 250 milliseconds per image. SI reconstruction was performed in custom written MATLAB software by Dr. Jeffrey Spector. Images were analysed with ImageJ software (NIH).

### 2.9.4 Stimulated emission depletion microscope

The STED microscope was based on an Abberior Instrument RESOLFT QUAD-P super-resolution microscope (Abberior Instruments) equipped with two excitation lasers: 480 nm and 640 nm (PicoQuant). The STED beam was produced by a Titanium: Sapphire laser system (MaiTai, Spectra-Physics). A phase-modifying plate (VPP-1a, RPC Photonics) was used in the STED beam path to generate a donut shaped focal spot. STED and excitation laser beams were spatially super-imposed and the fluorescence light was filtered using appropriate dichroic filters (AHF Analysentechnik). Images were taken using an oil immersion 100x with 1.40 NA objective (Olympus) and detected by a single photon counting avalanche photo diode (SPCM-AQRH-13, Excelitas Technologies) with fluorescence filters. Data were acquired using Inspector

software. STED imaging and reconstruction was performed by Dr. Jakub Chojnacki (23).

## 2.10 SEM

### 2.10.1 Sample fixing and staining

Cells were grown on sterilized glass coverslips. The samples were fixed with 4% formaldehyde in PBS for 15 minutes and washed 3 times in PBS. The samples were prepared and imaged in fluorescence microscopy. The samples were fixed with 2.5% gluteraldehyde in 0.1M PBS at pH 7.2-7.4 at rt for 1 hour. The samples were rinsed with 0.1M PBS or 0.1M Sodium Cacodylate Buffer (SCB) 3 times, 5 minutes each. The samples were stained with 1% $OsO_4$ in 0.1M SCB at rt for 1 hour and rinsed with Milli-Q water for 3 times, 5 minutes each.

### 2.10.2 Sample dehydrating

The samples were dehydrated with 30%, 50%, 70%, 95% ethanol in Milli-Q water for 5 minutes, 2 times each, and 100% ethanol in Milli-Q water 3 times, 10 minutes each. Finally, the ethanol was removed and the samples were dried using hexamethyldisilazane (HMDS) (Polysciences) for 3 minutes. The HMDS was immediately removed and placed overnight in a chemical hood with the lid open to allow complete desiccation. Alternatively, the sample was dried using AutoSamdri 815 Critical Point Dryer (Touismis) to remove ethanol using pressurized liquid $CO_2$ to avoid surface tension artifacts. For SEM, samples were mounted on SEM stubs and sputter coated using Q150R ES Dual Carbon/Sputter Coater (Quorum Technologies) with 15 nm gold and palladium.

### 2.10.3 Sample imaging

The JSM-6390 Scanning Electron Microscope (JEOL) was used for data collection. This microscope allows detailed imaging of the surface topography of whole cells. Imaging was done at acceleration voltage of 5 kV. Regions of interest were located at magnification of 100 – 500x and images were taken at 100-10,000x. Images were analyzed using the ImageJ software.

## 2.11 Transmission electron microscope

### 2.11.1 Sample staining

Cells were cultured on sterilized glass coverslips, gridded glass (MatTek), or plastic petri dishes (iBidi). The samples were fixed with 4% Formaldehyde in PBS for 15 minutes, washed 3 times in PBS. The samples were prepared and imaged by fluorescence microscopy. The samples were fixed with 2.5% gluteraldehyde in 0.1 M Sodium Cacodylate Buffer at pH 7.2 or 0.1M PBS for 1 hour at rt then rinsed in sodium Cacodylate buffer 3 times, 15 minutes each. The samples were stained in 1% osmium tetroxide in sodium Cacodylate buffer at rt for 1 hour, rinsed with fresh Milli-Q water 3 times, 5 minutes each. Samples were stained with 2% uranyl acetate in Milli-Q water for 2 hours at 4°C protected from light.

### 2.11.2 Sample dehydration

The samples were rinsed with water for 10 minutes then dehydrated in 30%, 50%, 70%, 80%, 90%, 95% ethanol in water for 10 minutes each at rt, then 100% ethanol 3 times, 30 minutes each. Resin was prepared by mixing 10 mL Agar 100 (Agar Scientific) with 300 µL of Benzyl dimethylamine catalyst (Electron Microscopy Sciences) on a rotator for 30 minutes until the mixture was a homogenous golden color. After dehydration, the ethanol was removed and

the samples were incubated with 2:1 100% dry ethanol: Agar100 resin for 1 hour, then 1:1 100% dry ethanol: Agar100 resin for 2-3 hours, and 1:2 100% dry ethanol: Agar100 resin for 1 hour in the chemical hood. The samples were incubated in 100% Agar100 overnight at rt. The next day, the resin was changed in the morning and again in the afternoon. The samples were incubated for 24-48 hours at in the 60°C oven, then heated in a 56°C oven and then immediately plunged into liquid nitrogen. The rapid temperature changes induced differential expansion rates between the culture dish and the resin block, causing the culture dish to lift off. The resin block was trimmed using a razor blade to create a trapezoidal pyramid with the cells at the top.

### 2.11.3 Sample polishing

When needed, the surfaces of the samples were trimmed by semi-thin sectioning (150-500 nm) using a glass knife. The glass knife was made using a KMR3 knife maker machine (Leica) by cutting glass knife strips (Electron Microscopy Sciences) into squares then into right angled triangles with durable and sharp edges. The glass knife was inserted into an ultramicrotome EM UCT or UC7 machine (Leica) to section the samples. Once the samples were trimmed, a diamond knife replaced the glass knife in the ultramicrotome machine and was used to cut the samples into thin sections (100 nm). The sections were transferred to a 200 nm mesh Copper grid with a round metal loop.

### 2.11.4 Sample post-staining

At this stage, the samples were post-stained with lead citrate to increase contrast. Milli-Q water was warmed on a hotplate. Lead citrate was filtered with a 0.22 um syringe filter and centrifuged for 1 minute at 14,000 rpm to ensure that there were no precipitates in the staining solution. A sheet of parafilm was

placed on the bench. A droplet of 20 µL lead citrate for each copper grid was pipetted on the parafilm. Sodium hydroxide pellets were added around the droplets to scavenge excess carbon dioxide and care was taken to prevent exhalation near the samples. Each grid was transferred to separate droplets of stain, section side down, and incubated covered for 5 minutes at rt. Meanwhile, a line of three 200 µL droplets was pipetted next to each droplet of lead stain. When the lead staining was completed, the samples were dried by gently touching to edge to a Whatman filter paper and placed on a droplet of water, section side down. This process was repeated 3 times, 1 minute for the last wash. The grids were placed, section side up, on a Whatman filter paper to dry. The samples were then ready for imaging.

### 2.11.5 Sample imaging

The FEI Tecnai 12 TEM with a 4 Megapixel Gatan Ultrascan™ 1000 CCD camera was used for data collection. Regions of interest were located at a nominal magnification of 100x. Images were taken at 100-100,000x magnification using Gatan Digital Micrograph software at 120 kV high tension using a lanthanum hexaboride (LaB6) electron source. Images were analysed using the ImageJ software.

## 2.12 Focused ion beam scanning electron microscopy

### 2.12.1 Sample preparation – chemical fixation

The cells of interest were cultured in gridded glass (MatTek) or plastic petri dishes (iBidi). The samples were fixed with 4% Formaldehyde in PBS for 15 minutes then imaged using fluorescence microscopy, recording the alpha-numeric code, which indicated the location of the region (102, 346, 378). The culture medium was replaced with 3 PBS exchanges then the cells were fixed in

2% gluteraldehyde in 0.1 M sodium Cacodylate buffer pH 7.0 for 1 hour at rt. The sample was washed with sodium Cacodylate buffer 3 times, 10 minutes each. The cells were post-fixed with 1% osmium tetroxide in sodium Cacodylate for 1 hour at rt and washed with sodium Cacodylate twice and 0.1 M sodium acetate pH 4.2 buffer once for 10 minutes each. The cells were stained with 0.5% uranyl acetate in sodium acetate buffer for 1 hour in RT followed by three washes in sodium acetate for 10 minutes each.

The sample was dehydrated with ethanol in de-ionized water 35%, 50%, 70%, 95%, twice for 10 minutes each, 100% ethanol three times for 10 minutes, and embedded in PolyBed 812 Luft formulations Embedding Kit/BDMA (PolySciences). Resin components were made at the following proportion: 4.7g EPON, 2.5 g DDSA, 2.8 g NMA, and 150 µL BMDA, which yielded about 15 mL. The sample was left in the chemical hood on a rotator overnight. The next day, the resin was replaced with freshly made resin and placed in 56ºC oven for 48 hours to induce polymerization. Hydrofluoric acid 48 wt % was used to remove the glass bottom without disrupting the resin block. This acid was neutralized with sodium hydroxide. Alternatively, the sample was heated in a 56°C oven and then immediately plunged into liquid nitrogen. The rapid temperature changes induced differential expansion rates between the culture dish and the resin block, causing the culture dish to lift off. The sample was mounted as described below.

### 2.12.2 Sample preparation – high pressure freezing

Alternatively, the cell sample was prepared using high pressure freezing quick substitution (HPF-QS) as described by Kent McDonald (379, 380). Cells were cultured on sapphire discs (Leica) that had been sterilized in 70% ethanol and air dried in the tissue culture hood. Immediately before high pressure

freezing, the sample medium was exchanged with 20% BSA in culture medium as a cryo-protectant for the cells. Three mock runs were performed with the EMPACT2 high pressure freezer (Leica) to ensure that the target parameters were 2000 Pa and a cooling rate of 10,000-20,000 °C per second with smooth freezing curves. The cells were kept submerged in a liquid nitrogen bath.

Fixative solution of 1% $OsO_4$ (Electron Microscopy Sciences), 0.5% Uranyl Acetate (Sigma Aldrich) and 5% deionized water in 100% acetone (Sigma Aldrich) was added to cryovials with O-ring seals, one for each sample. A heater block (Cole Parmer) and the cryovials containing fixative solution were cooled in liquid nitrogen inside a small foam box for 15 minutes to allow the temperature to equilibrate. In a control cryovial, a thermocouple probe (Omega Engineering) was submerged in 100% acetone to monitor temperature changes over time.

Frozen sapphire disc samples were transferred to the cooled cryovials containing fixative in liquid nitrogen vapour phase to avoid rapid temperature changes. The liquid nitrogen was poured out of the foam box and the heater block was placed horizontally in the empty foam box on a shaker at 100 rpm until the temperature reaches rt, which took 3 hours. This short staining and dehydration technique was termed HPF-QS.

The samples were rinsed 3 times with pure acetone. The sapphire discs were transferred to a flat bottom-embedding capsule with the cells facing up. The samples were slowly infiltrated with Epon 812 resin (Electron Microscopy Sciences) made as above using 50% resin: acetone for 1 hour, 100% resin for 1 hour, and 100% resin overnight at rt. The next day, fresh resin replaced the old resin and the samples were polymerized in 56°C oven for 48 hours. The resin blocks were removed from the embedding capsules. A razor blade was used to

trim resin around the sapphire disc. The samples were immersed in liquid nitrogen then in 56°C oven alternatively until the sapphire disc lifts off due to differential expansion rate. The sample was mounted as described below.

### 2.12.3 Sample mounting

The resin block was trimmed using a handheld rotary tool (Dremel) then a razor blade to create a trapezoidal pyramid with the cells at the top. The resin debris were removed in deionized water using a sonicator for 6 minutes. Finally, the embedded resin block was mounted on a specimen stub using colloidal silver paint (Electron Microscopy Sciences) and sputter coated with gold for 30 seconds to increase conductivity. The samples were handled with gloved hand to avoid imparting moisture.

### 2.12.4 Sample imaging

A Zeiss NVision 40 Crossbeam Microscope (Carl Zeiss NTS) equipped with Atlas3D software (Fibics Inc., Ottawa) was used for data collection. The resin block was imaged with an electron beam at 15 kV to locate the cells based on the surface topographical features. The sample stub was tilted to 54º and a 1 um layer of carbon and a 0.5 µM layer of platinum was deposited on the region of interest using a gas injection system with a FIB of 30 kV and 300 pA–1.5 nA. A trapezoidal trench was created using a 13-27 nA ion beam and the cliff face was polished with a 300-700 pA ion beam in front of the region of interest. A 300-700 pA focused ion beam iteratively removed 16-48 nm slices from the cross-section while an electron beam scanned the newly revealed surface at 4-16 nm per pixel resolution. The images were recorded using energy selective back scattered electron (ESB) detector at 1.5 kV with an aperture size of 60 µm. The result is a stack of 2D scanning electron microscopy images.

### 2.12.5 Image analysis

The individual 2D images were merged into a single stack, then cropped and aligned using customized scripts written by Dr. Bradley Lowekamp based on the image processing program IMOD (UC Boulder). Features of interest were automatically selected with Avizo Fire (Visualization Sciences Group) or 3DSlicer (www.slicer.com) using a threshold tool that highlighted features within a specified range of pixel intensity. The automatic segmentation was polished manually using Avizo Fire or 3D Slicer. The 2D segmentations were converted into polygons to produce 3D visualizations using Avizo Fire or Autodesk 3D Studio Max software. Statistical measurements of features were automatically calculated using customized script in combination with 3D Slicer.

# 3 3D Imaging of Skeletal Muscle Cell Differentiation

## 3.1 Introduction

The growth and differentiation mechanisms of cells are carefully controlled by the cell cycle system. Disruptions of these mechanisms can lead to a host of diseases, most notably cancer (381), and in many cases premature death. Powerful new technologies for chemical and structural imaging of cells are now becoming available and they provide a unique opportunity to study the mechanisms associated with cell growth and differentiation. In this way, the consequences of genetic mutation or perturbation can be detected and effective diagnosis and treatments can be identified. To 1) establish the utility of these imaging approaches and 2) characterize the differentiation mechanism of cells in a healthy, well established system, I analyzed the differentiation pathway of C2C12, an immortalized murine cell line (349), from skeletal myoblasts into myotubes. This model system recapitulates the finely tuned cellular development mechanisms of many lineage-specific cells, from progenitor cells into post-mitotic terminally differentiated cells. Thus, information discovered here may also be applied to other cells in the body.

The process of skeletal muscle differentiation is governed by a dynamic and parallel relationship between both genetic expression and structural organization. In early embryonic development, mesodermal stem cells give rise to myogenic progenitor cells, termed myoblasts, which proliferate rapidly and differentiate to form myotubes. When the multinucleated myotubes reach a post-mitotic state, they fuse together to form muscle fibers and produce proteins to induce muscle contraction (382). When the muscle fibers have matured, the cellular growth rate reaches a steady peak and then declines. During this process, some progenitor cells remain quiescent as adult stem cells, termed

satellite cells. Under specific signaling stimulus, the satellite cells can be activated to repopulate the myogenic progenitor pool and replace the terminally differentiated cells to repair and maintain tissue homeostasis (383–386).

Myogenesis and skeletal muscle function depends on the spatiotemporal regulation of the gene expression. It has been shown that subcellular structures such as nuclear lamins (387), nuclear membrane (388–390) and NPC (390–393) can regulate the gene expressions, structural organizations, and cellular functions during muscle differentiation. Additionally, the chromatin arrangements and their spatial relationships to other nuclear structures have been shown to play in important role in the induction or repression of gene expression (394, 395).

To explore the parallel genetic and structural changes that occur in the skeletal muscle cells during differentiation, I applied correlative FIB-SEM. Genetic changes associated with differentiation are first followed by widefield and super-resolution SIM, and these are correlated with changes in the ultrastructures and subcellular structures observed by 3D FIB-SEM at nanometer resolution. The delicate subcellular features were preserved for EM using HPF-QS, which enhances the contrast of the features and reduces the introduction of artifacts commonly observed in conventional chemical fixation.

The combination of these advanced sample preparation and imaging technologies provide visualization of whole cells and their subcellular structures, including the nuclei, euchromatin, heterochromatin, NPC, and mitochondria. Using Slicer 3D software, I applied automated segmentation to reconstruct the images into 3D models. Reconstructed cellular components can be analyzed quantitatively to objectively characterize and compare the structural features of these cells. I show that these techniques can be useful tools for analyzing the

genetic phenotypes and structural organization of cells in 3D at high resolution. Methods described here could be useful for cellular characterization and diagnostic applications. Taken together, quantitative and qualitative analyses reveal that, despite various morphological changes that occur during differentiation, many architectural characteristics are conserved, implying their central roles in cellular functions. This chapter discusses both the technical advances in high resolution imaging technology and the basic biological insights into muscle cell development.

## 3.2 Myogenic expressions reveal the differentiation state of cell

Skeletal myogenesis, a process that commits myogenic precursor cells to terminal differentiation, is regulated by myogenic regulatory factors (MRF). MRFs are proteins that bind to DNA sequences to regulate the transcription of genes from DNA to messenger RNA. MRFs are expressed transiently in a hierarchical order during the skeletal muscle differentiation process from Pax 3, Pax 7, Myf5, MyoD, Myf4 to Myogenin (396–406). The expression of MRFs induces mononuclear myoblasts to align in parallel with each other and fuse together to generate elongated multinucleated myotubes, eventually forming into long muscle fibers (405, 406).

To monitor this process, I plated C2C12 skeletal cells at low density as mononuclear myoblasts with polygonal morphology. When the cells reached 90% density, differentiation medium was added. Within a few hours, the cells began to align themselves parallel to each other as myocytes and in a few days, the myoblasts fused into elongated multinucleated myotubes (Figure 3.1 A-B). As the cells differentiated and changed their ultra-structural morphology, Myogenin expression, a later stage MRF, was observed to progressively increase in the nuclei of the cells. After 5-7 days in differentiation medium,

almost all of the cells had fused together and the majority of the nuclei strongly expressed Myogenin (Figure 3.1 C-F). In this way, the differentiation state of the cells can be characterized by the intensity of the MRF expression and the morphology of the cells.

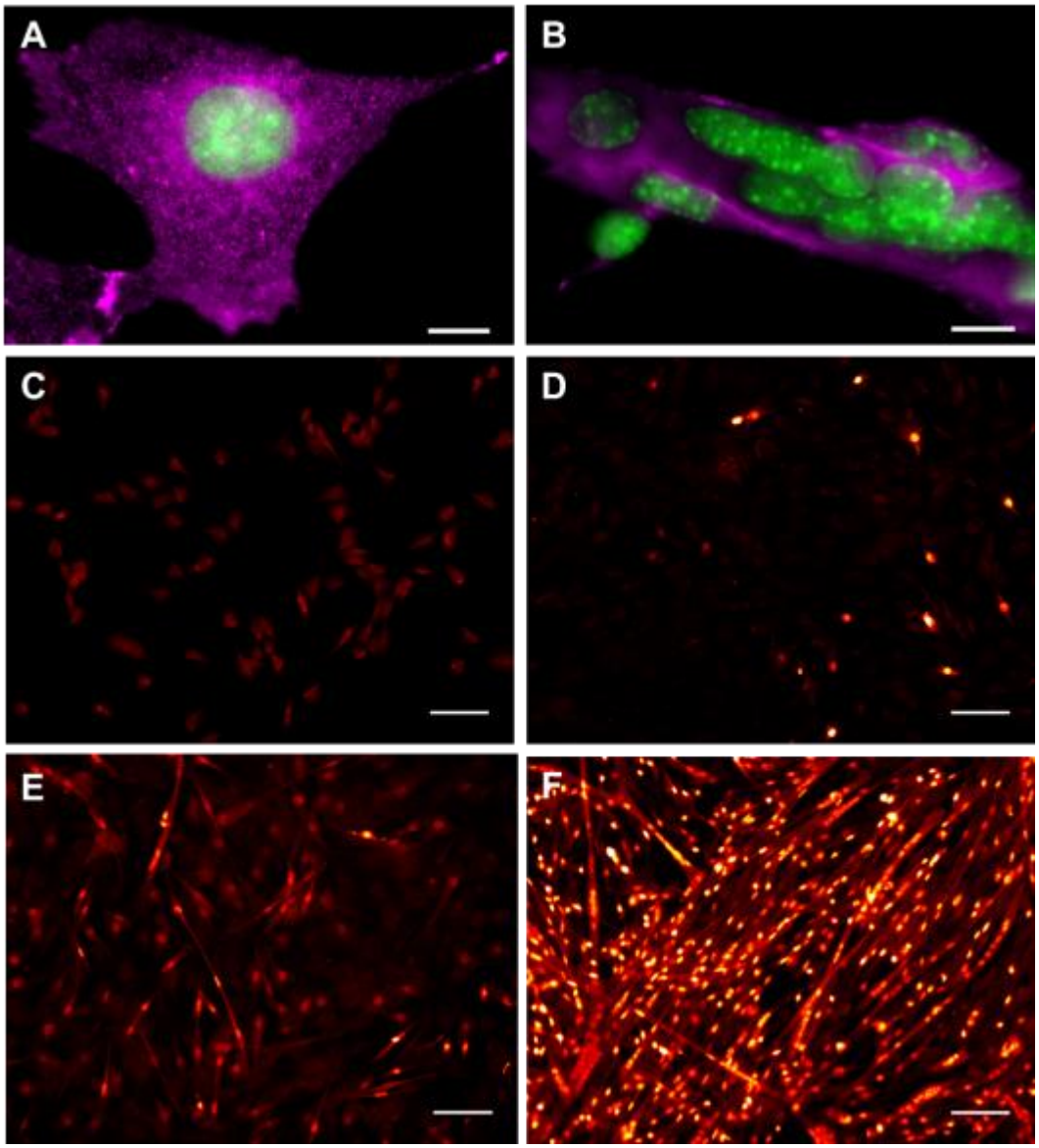


**Figure 3.1** C2C12 mouse skeletal muscle cells were stained with DAPI (green) and DiI (magenta) to label the cell nucleus and membrane, respectively. Myoblast (A) contains a single nucleus with polygonal morphology. When myoblasts fuse together into myotubes (B), the cell contains multiple nuclei that string together in a linear formation inside the cylindrical tube. Myogenin (red) expression is monitored over the course of 7 days as the cells differentiate from myoblast to myotube (C-F). Myogenin expression increased in the nuclei over time with the highest signal originating from nuclei inside fused myotubes. Panels A-B scale bars: 10 µm, C-F: 100 µm.

## 3.3 Myogenic expression is absent in the “zones of exclusion”

The expression of transcription regulatory factors determines the terminal fate of the cell. For example, down-regulation of Myogenin can reverse the cell differentiation state (407) and the absence of Myogenin can lead to severe dysfunction in muscle growth (408). To further analyze the pattern of MRF expression in the nuclei of the cells, I applied super-resolution SIM microscopy. At day 1, myoblasts showed low or no expression of MRFs (Figure 3.2 A-C). However at day 7, low levels of Myf5, and high levels of Myogenin and MyoD were observed in the nuclei of the cells (Figure 3.2 D-I).

In particular, the expression pattern of Myf5, Myogenin and MyoD reveals similar distinct “zones of exclusion,” which are areas inside the nucleus where the MRF expression is absent (Figure 3.2 E-F, H-I). These areas do not correlate with DNA or heterochromatic histones as observed by DAPI and anti-H3K9me2 antibodies, respectively (Figure 3.2 J-L). The fluorescence images suggest the existence of physical structures inside the “zones of exclusion” that preclude expression of the myogenic factors.

To investigate the sub-nuclear structure that excluded MRF expression inside the nucleus, I turned to correlative fluorescence 3D FIB-SEM. I first stained C2C12 cells with DAPI and anti-Myogenin antibody and imaged the cells in a widefield fluorescence microscope (Figure 3.2 M-N). Next, I prepared the samples for EM and imaged the same cells observed in fluorescence microscopy but this time in 3D FIB-SEM. EM images revealed the “zones of exclusion” observed in fluorescence microscopy correlate with the electron dense features in the nucleus, known as nucleoli (Figure 3.2 O) (409–411). Although the nucleoli are not bound by membrane, it is evident from these images that these structures are compartmentalized in distinct physical space

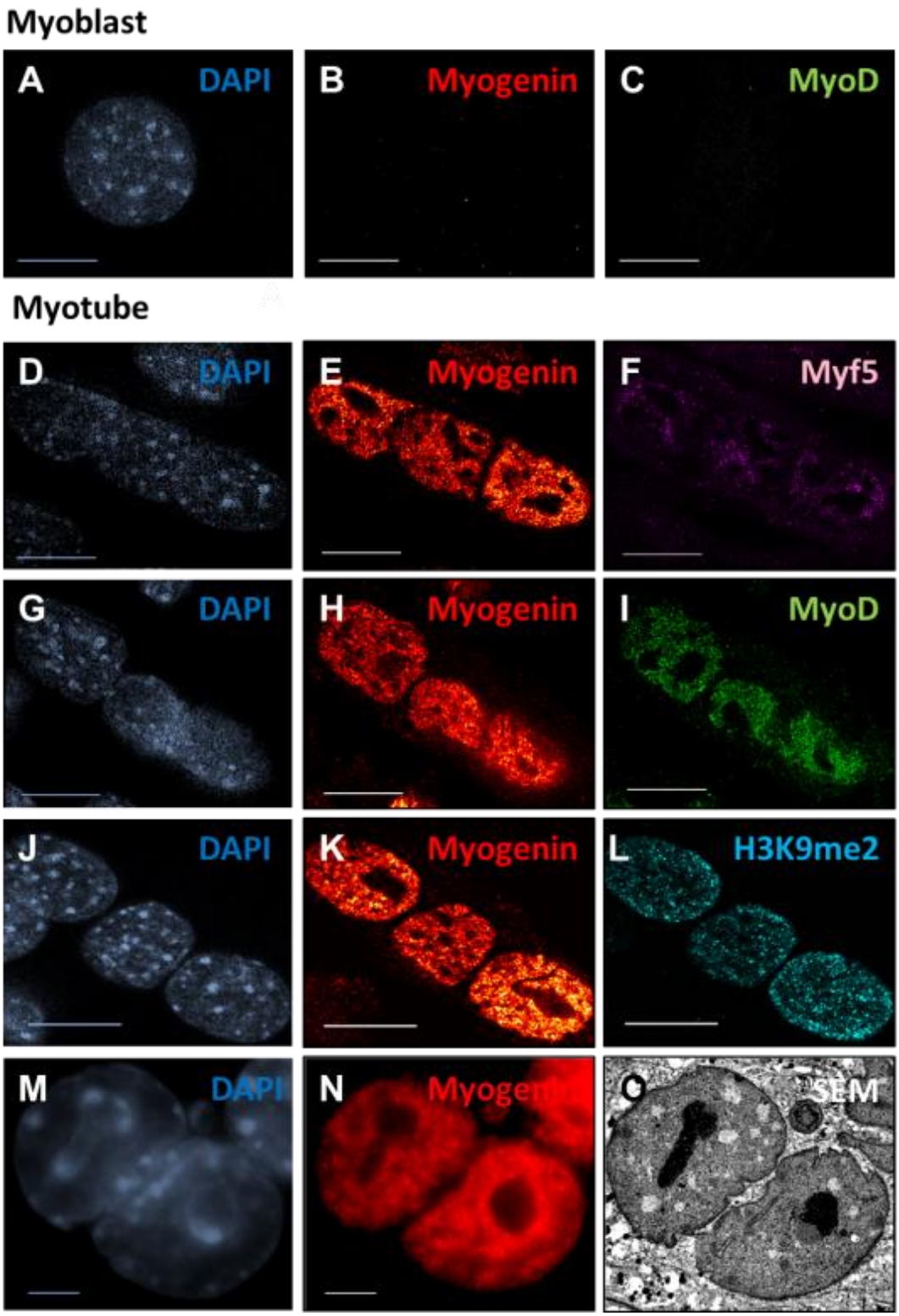


**Figure 3.2** Correlative fluorescence FIB-SEM imaging of myogenic regulatory factors show “zones of exclusion.” Super resolution structured illumination microscopy images (A-L), widefield fluorescence microscopy images (M-N), and FIB-SEM images (O) of C2C12 mouse muscle cells. Nuclei of myoblasts were stained with DAPI (A), Myogenin (B), and MyoD (C). Nuclei of myotubes were stained with DAPI (D, G, J, M), Myogenin (E, H, K, N), Myf5 (F), MyoD (I), H2K9me2 (L). Panels A-O scale bars: 10 µm.

with DNA localizing in spherical densities around the perimeter while MRFs are entirely excluded from these regions.

## 3.4 HPF-QS preserves structural features of cells in 3D FIB-SEM

To explore the extent to which the changes in gene expression profile are paralleled by specific, interpretable changes in cellular structures, I applied 3D FIB-SEM. Preparation of the delicately thin cells for EM required a technique that could preserve the fragile organelles and minimize the introduction of fixation artifacts. Phase contrast (Figure 3.3 A) and differential interference contrast (DIC) (Figure 3.3 B) show the skeletal muscle cells are adherent with a single nucleus residing in the center of the cell membrane in a myoblast or a satellite cell (Figure 3.3 B) or a string of nuclei in a fused myotube (Figure 3.3 A). The nucleus appears to be a relatively smooth and a raised and prominent feature of the cell (Figure 3.3 B).

I experimented with a few methods to prepare these cells for EM. In the first method, I detached cells from the culture dish and stained them using pelleted conventional chemical fixation techniques. EM images of pelleted, chemically fixed cells (Figure 3.3 C-D) reveal high contrast subcellular structures, including nuclei, mitochondria, lysosomes, Golgi apparatus, and endoplasmic reticulum. However, these structures were distorted by the detachment and pelleting steps, causing the features to appear wrapped around a central focal point. To overcome this distortion, I applied an *in situ* chemical fixation technique, which preserved the linear formation of the string of nuclei inside the myotube (Figure 3.3 E), similar to those observed in light microscopy (Figure 3.3 A). Euchromatin and heterochromatin appeared as low and high density regions inside the nucleus, respectively. Nucleoli were observed as dark spherical densities inside the nuclei. Cell membrane and nuclear membrane

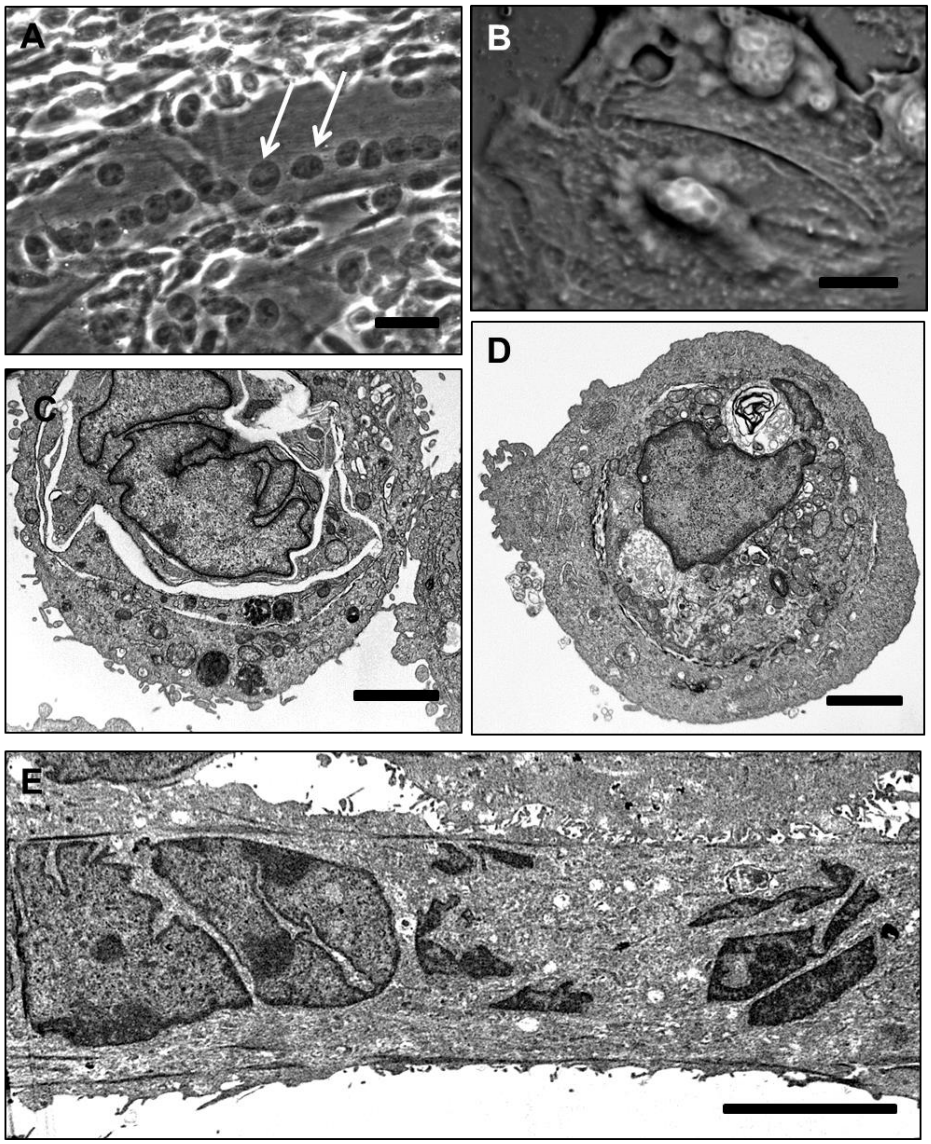


**Figure 3.3** Widefield microscopy (A) of C2C12 myotubes shows long skeletal muscle fibers with multiple nuclei (arrows) inside the tubular membrane structures. A DIC image (B) of C2C12 cells shows adherent cells contain prominent protruded nuclei. SEM images of C2C12 cells prepared by chemical fixation of pelleted cells (C-D) and by chemical fixation of *in situ* cells (E). Panel A scale bar: 20 µm, B and E: 10 µm, C-D: 2 µm.

were well defined but the nuclei appeared to be divided into small sections in individual 2D images, suggesting that the structures contained membrane folds. I hypothesized that the nuclear ruffles could be artifacts introduced by the chemical fixation technique, which uses formaldehyde and gluteraldehyde. Aldehydes are known to cause cellular structures, especially nuclei, to oscillate between swelling and shrinking within minutes during fixation (412, 413).

To avoid aldehyde artifacts, I prepared the samples using HPF-QS as introduced by Kent McDonald (379, 380, 414). As described above, conventional chemical fixation techniques revealed nuclei with many folds delineated by high contrast nuclear membrane (Figure 3.4 A). However, HPF-QS revealed smooth nuclei with enhanced contrast in the sub-nuclear features, particularly chromatin and the nucleolus (Figure 3.4 B). 3D reconstruction of the nuclear structure using stacks of FIB-SEM images showed that the chemically fixed nuclei (Figure 3.4 C-E) had significantly more folds than the HPF-QS prepared nuclei (Figure 3.4 F-H).

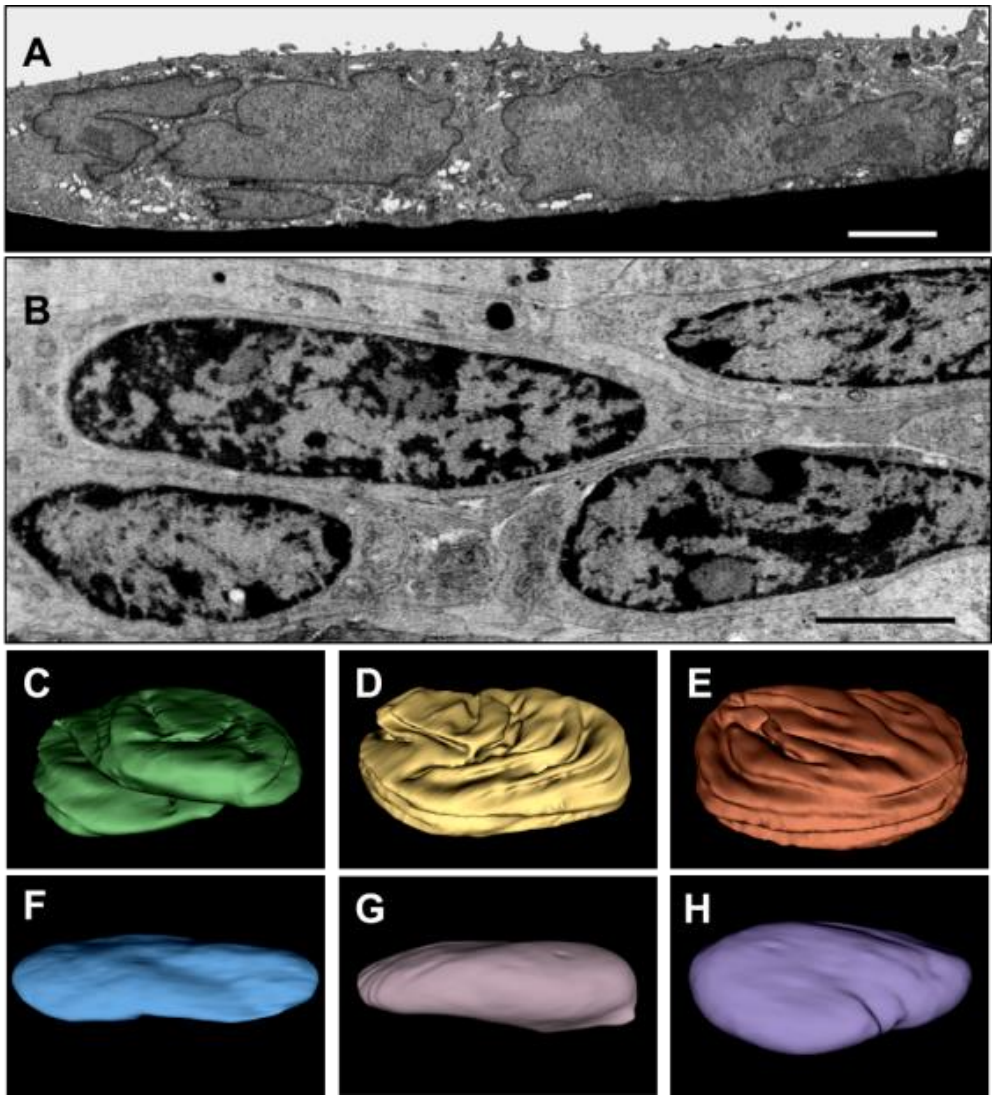


**Figure 3.4** SEM images of C2C12 myotubes prepared by chemical fixation of in situ cells (A) and by HPF-QS of in situ cells (B). Reconstructed 3D FIB-SEM images of nuclei inside C2C12 myotubes prepared by chemical fixation (C-E) and HPF-QS (F-H) of *in situ* cells. Panels A-B scale bars: 2 µm.

To analyze the extent of the nuclear folds, I created an algorithm to automatically fill in the concavity created by the membrane indentation (Figure 3.5 A-D), and quantified the volume of the concavity. Visually, the nuclei prepared by chemical fixation appeared to have more concavity than the nuclei prepared by HPF-QS (Figure 3.5 A vs C). This observation was confirmed by the auto-filled colored regions that highlight the concave regions (Figure 3.5 B vs D). Although the volumes of the nuclei were similar (Figure 3.5 E), the volume of nuclear concavities in HPF-QS nuclei were significantly lower than those of the chemically fixed samples (Figure 3.5 F), suggesting that HPF-QS introduced fewer structural artifacts than conventional *in situ* EM sample preparation technique. The 3D reconstructions of the nuclei also recapitulate the smooth nuclear features previously observed in light and DIC microscopy image (Figure 3.3 A-B). Based on quantitative and qualitative analysis, I concluded that for the analysis of subcellular structure in 3D FIB-SEM, HPF-QS is a reliable technique to preserve the integrity of the native cell structure.

Of note, these structural artifacts described might be exaggerated due to the fragility and thinness of the skeletal muscle cells analyzed here. In other cases, chemical fixation techniques might not introduce such dramatic effects and can be applied to detect membrane-bound structures with high contrast fidelity. The choice of either technique should be based on the final application, weighing both the requirements for structural preservation with imaging contrast.

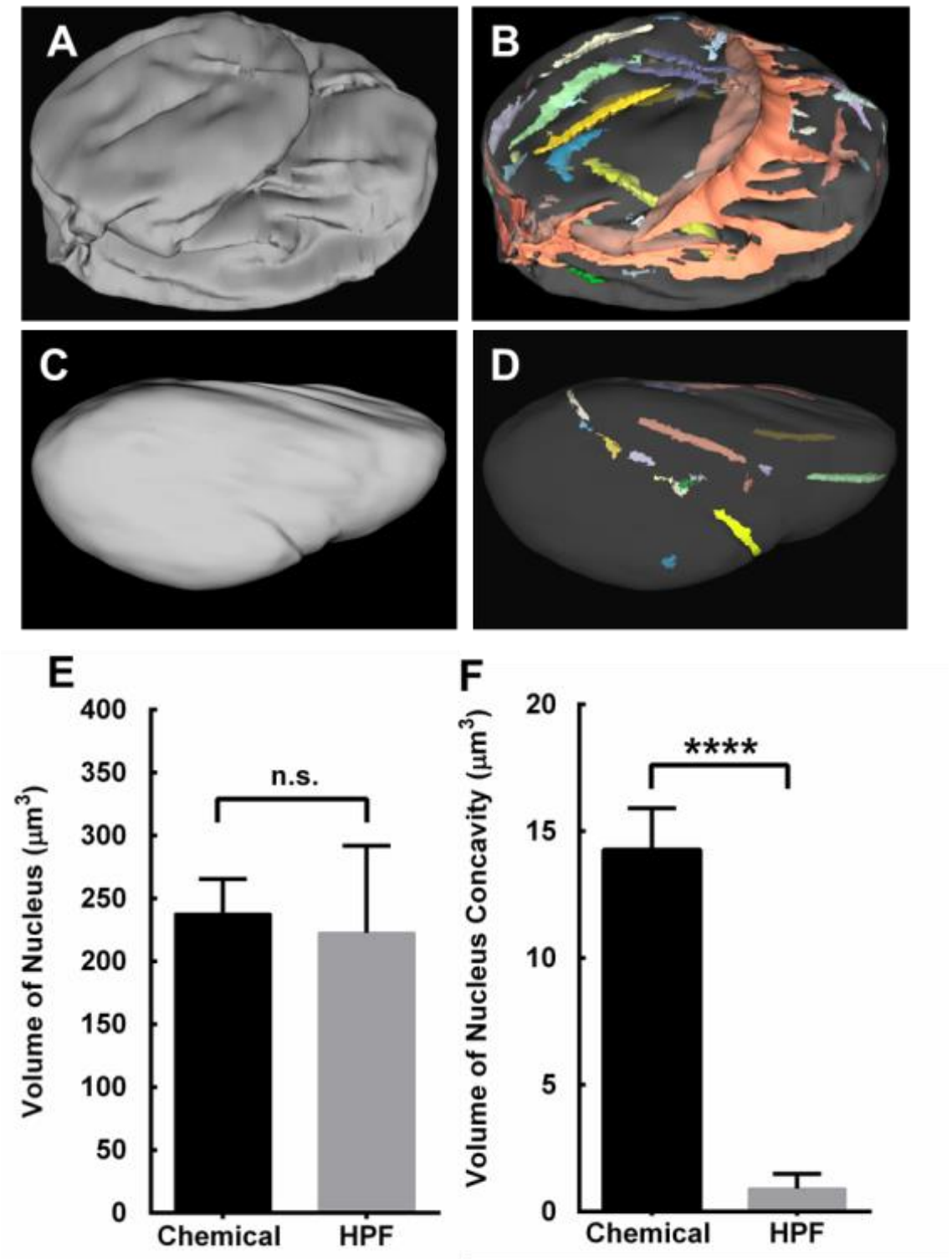


**Figure 3.5** Reconstructed 3D FIB-SEM images of nuclei inside C2C12 myotubes prepared by chemical fixation (A-B) and HPF-QS (C-D) of in situ cells. Volumes of nuclei concavity are colorized to show the extent of membrane folding (B, D). Graphs compare the volumes of nucleus (E) and the volumes of nucleus concavity (F) of nuclei inside C2C12 myotubes as prepared by chemical fixation and HPF-QS. Data from 7-9 chemically fixed nuclei and 6 HPF-QS nuclei with SD error bars. Mann Whitney unpaired non-parametric t-test, *$p < 0.1$.

## 3.5 Structural changes occur during muscle cell differentiation

After having established a reliable sample preparation technique, I explored the nuclear architecture of myoblasts and myotubes using HPF-QS sample preparation and 3D FIB-SEM. EM images revealed distinct, high contrast features in the nuclei of the cell, including heterochromatin, euchromatin, and nucleoli (Figure 3.6 A). Heterochromatin was observed as electron dense amorphous clusters found in the periphery of the nucleus and the nucleolus and dotted throughout the nucleus, whereas euchromatin was distributed throughout the nuclear space. Nucleoli were observed as spherical or ellipsoid, semi-electron dense structures with heterogeneous sizes inside the nucleus.

Magnified images of the nucleolus (Figure 3.6 C) reveal nucleolar components associated with rRNA and ribosome biogenesis, including fibrillar centers (f), dense fibrillar component (d), and granular component (g), as identified by (409, 415, 416). Chromatin and nucleolar components were automatically selected using a threshold algorithm in Slicer 3Dsoftware (Figure 3.6 B, D). Reconstructions of 3D FIB-SEM images of the nuclei reveal multiple nucleoli with regions of compact heterochromatin and distributed euchromatin (Figure 3.6 E). Quantitative analysis of the volumes occupied by the heterochromatin, euchromatin, and nucleoli inside the nuclei reveal that compared to myoblast nuclei, myotube nuclei have smaller sub-nuclear chromatin volumes (Figure 3.7 A). However, as a percentage of the total nuclear volume, myotube nuclei have similar percentages of euchromatin and heterochromatin and a third of the percentage of nucleoli compared to myoblast nuclei (Figure 3.7 B).

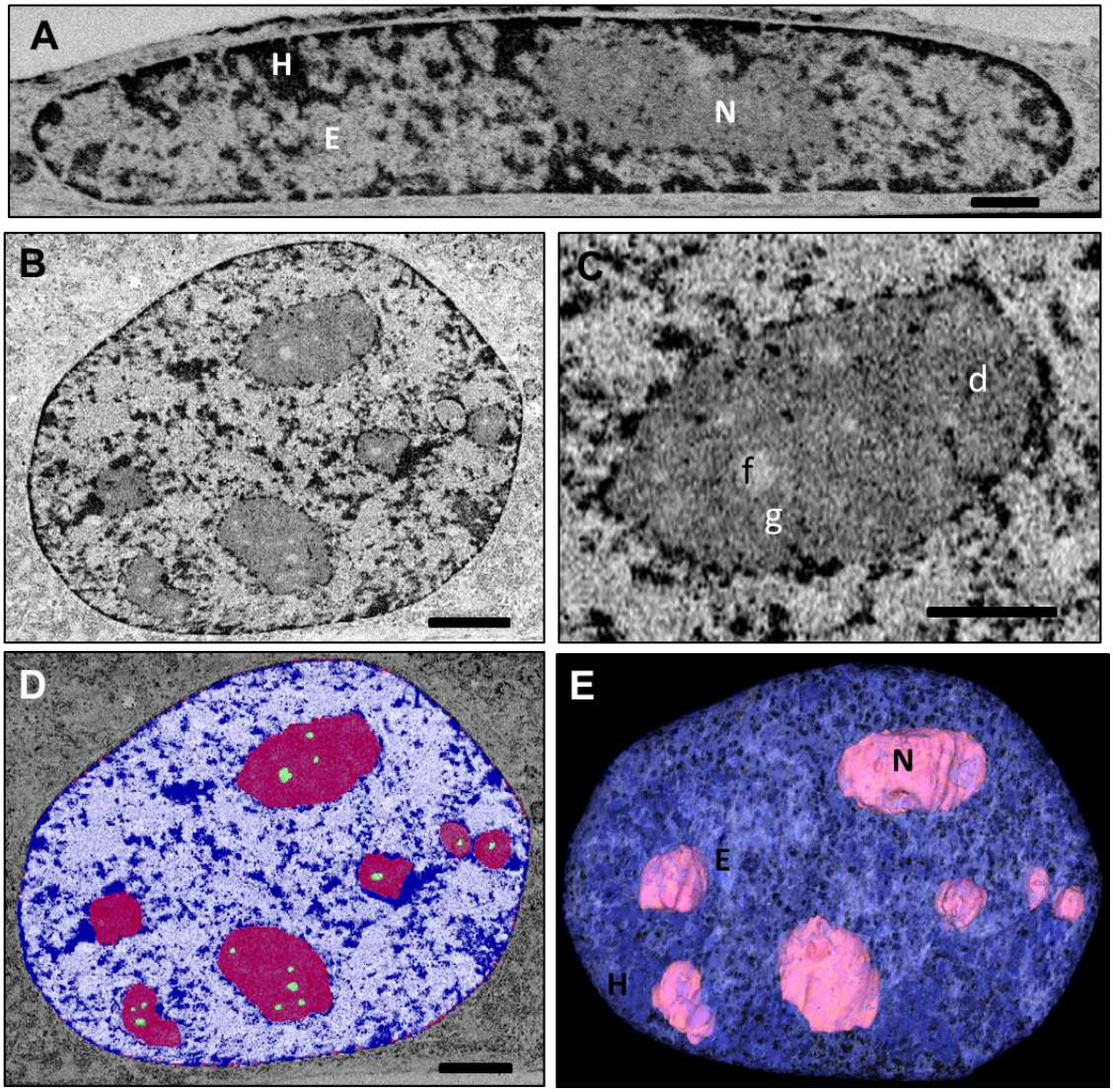


**Figure 3.6** A FIB-SEM image side view (A) and top view (B) of a HPF-QS prepared specimen showing a nucleus inside a C2C12 myoblast reveals the nucleolus (N), euchromatin (E), and heterochromatin (H). A magnified FIB-SEM image (C) reveals the components inside the nucleolus, including fibrillar centers (f), dense fibrillar component (d), and granular component (g). The artificially colored image (D) resulting from automatic segmentations of the nuclear components from (A-B) reveals nucleoli (pink), heterochromatin (navy blue), euchromatin (sky blue), and fibrillar centers (green). A reconstructed 3D FIB-SEM image (D) of a nucleus inside a C2C12 cell shows the organization of the nuclear components including nucleoli (pink), heterochromatin (navy blue), and euchromatin (sky blue). Panels A and C scale bars: 1 µm, B and D: 2 µm.

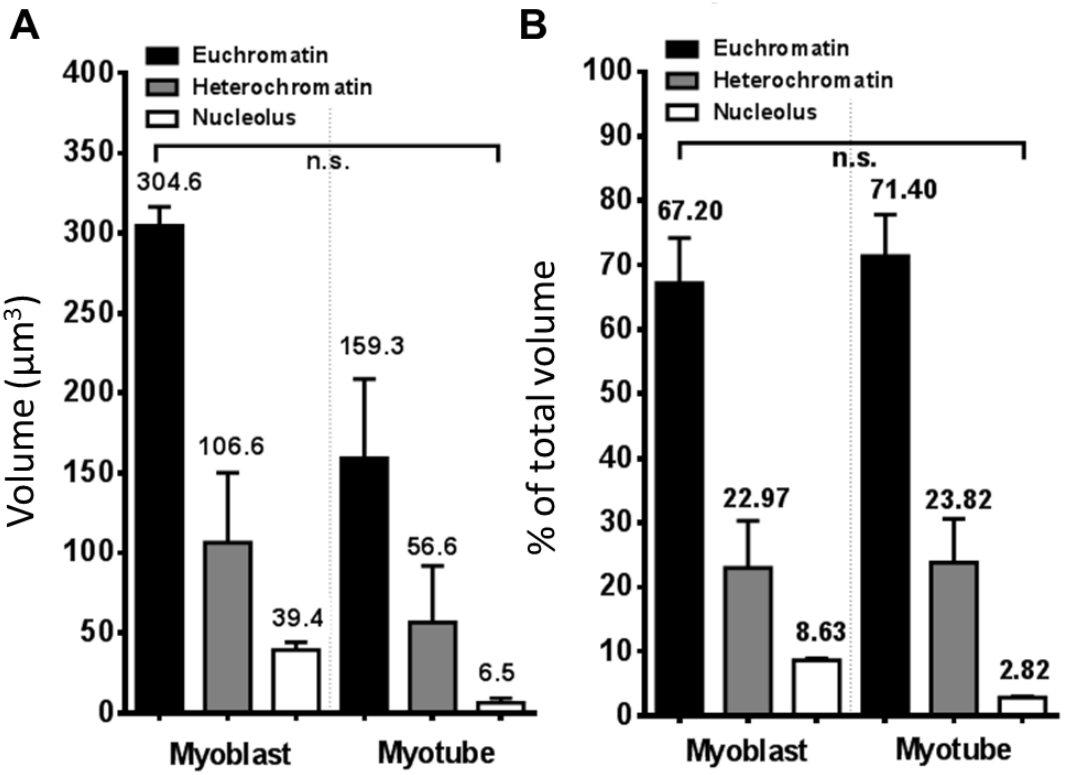


**Figure 3.7** Graphs compare the volume (E) and percent (F) of nuclear components inside the nuclei of C2C12 myoblasts and myotubes. Data from 3 nuclei from myoblasts and 3 nuclei from myotubes with 1 SD error bars. Mann Whitney unpaired non-parametric t-test, *p < 0.1.

As the myoblasts differentiated, the cells fused together into elongated myotubes with multiple nuclei. 3D reconstructions of FIB-SEM images showed that the nuclei of myotubes (Figure 3.8 C-D) are longer than the nuclei of myoblasts (Figure 3.8 A-B). Using reconstructed 3D FIB-SEM models, I generated a quantitative analysis that showed that the myotube nuclei are slightly elongated in the x direction, significantly flattened in the y direction, and remained relatively unchanged in the z direction (Figure 3.8 E) compared to myoblast nuclei. Thus, along with the ultra-structural changes in the whole cell architecture, the nuclei also elongate and flatten most likely to conform to the cylindrical structures of the muscle fibers.

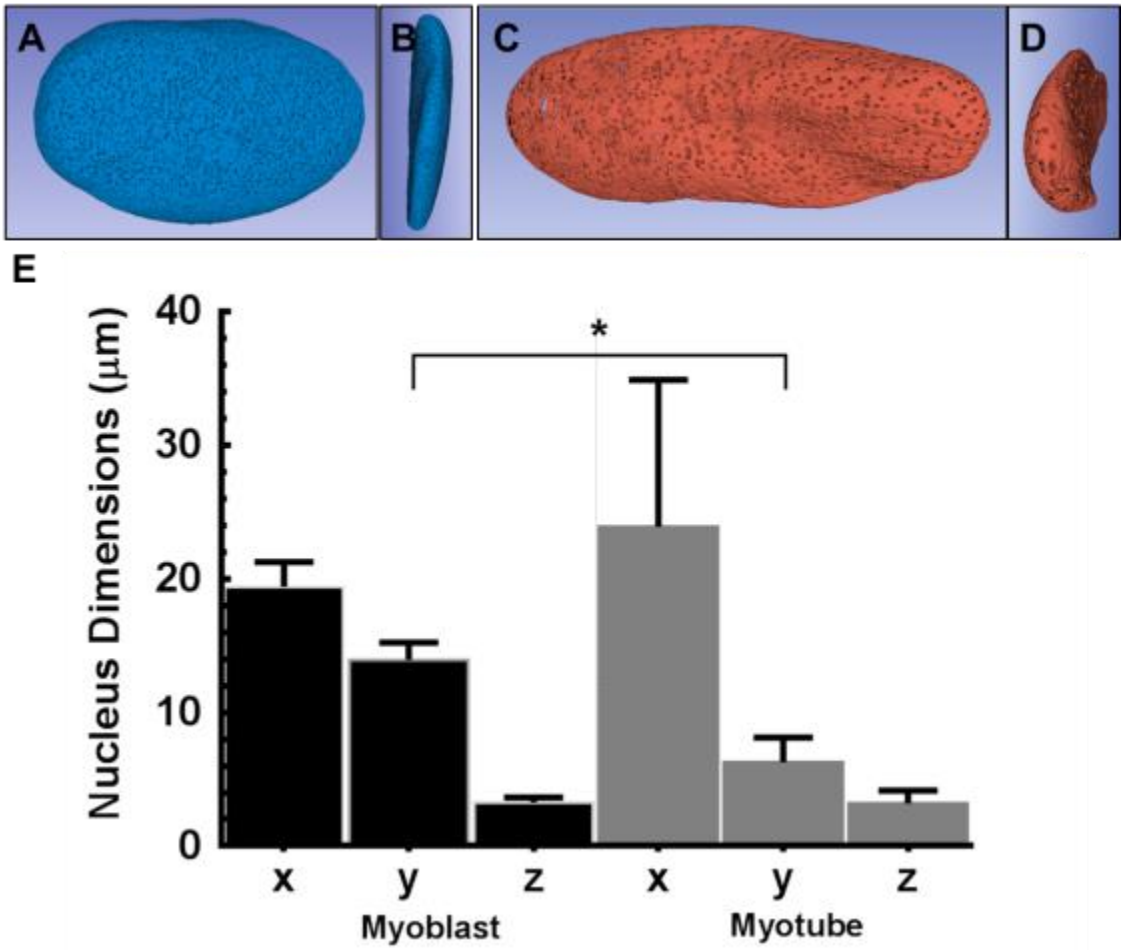


**Figure 3.8** Reconstructed 3D FIB-SEM image of a HPF-QS prepared specimen showing a nucleus inside a C2C12 myoblast (A-B) and myotube (C-D); top view (A, C), side view (B, D). The punctate dots on the nuclear membranes represent NPC. The graphs compare the dimensional changes in x, y, z coordinates between myoblasts and myotubes (E). Data from 3 nuclei from myoblasts and 6 nuclei from myotubes with 1 SD error bars. Mann Whitney unpaired non-parametric t-test, *p < 0.1.

Outside the nucleus, 3D FIB-SEM can clearly resolve the structures of cytoplasmic organelles. One organelle that plays a central role in supporting cellular processes is the mitochondrion, which can be clearly identified in EM based on the morphology, electron density, and presence of cristae. Mitochondria of myoblasts (Figure 3.9 A-B) had round morphology while mitochondria of myotubes had elongated morphology (Figure 3.9 C).

Reconstructions of 3D FIB-SEM images reveal spherical mitochondria in myoblasts (Figure 3.9 D) and tubular mitochondria in myotubes (Figure 3.9 E).

Even though the mitochondria of both myoblasts and myotubes have similar volumes (Figure 3.9 F), the myotube mitochondria are longer in the x direction and similar size in the y and z dimensions compared to the myoblast mitochondria. This evidence suggests that along with cell membrane fusion, the individual mitochondria may fuse together into long tubular structures to provide energy for the longer and more complex cells.

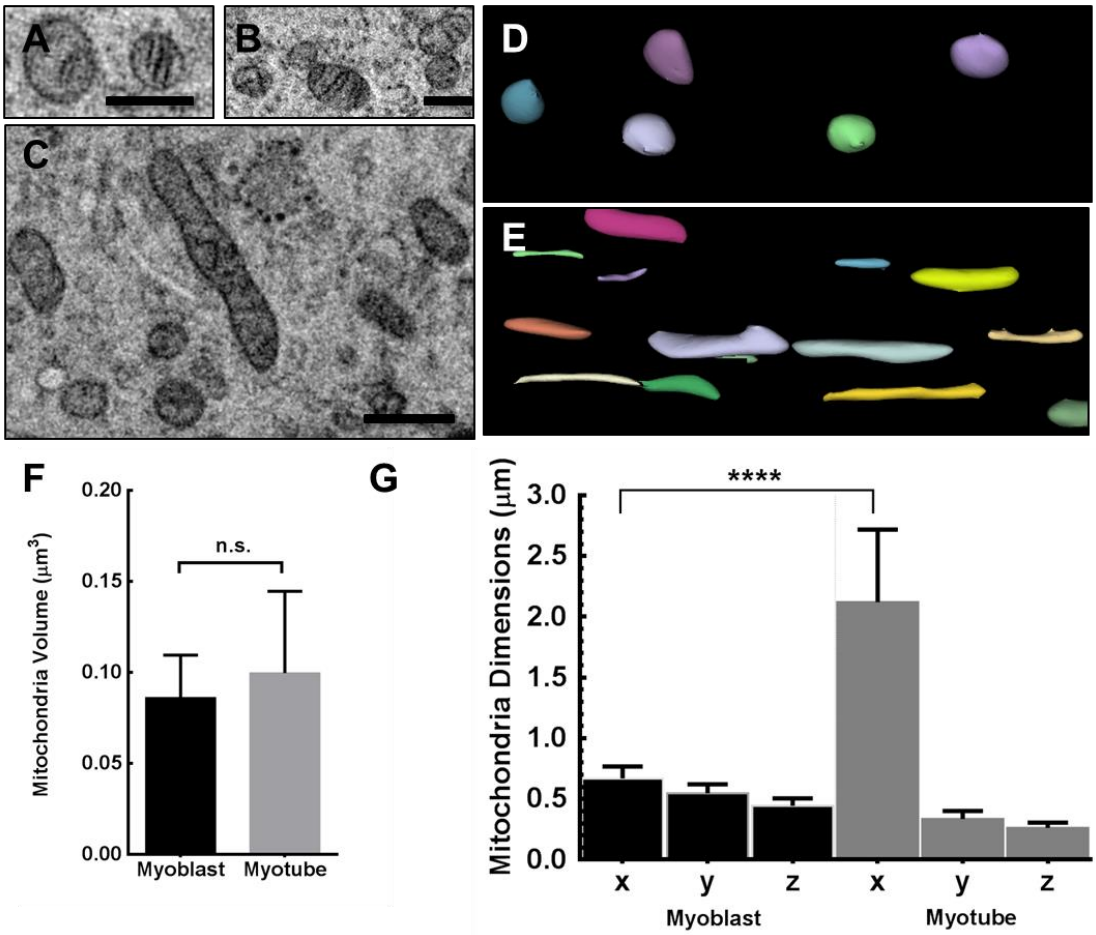


**Figure 3.9** FIB-SEM images of a HPF-QS prepared specimen showing mitochondria of C2C12 cells (A-C). Re-constructed 3D FIB-SEM images of mitochondria inside a C2C12 myoblast (D) and a myotube (E). Graphs compare the volumes of mitochondria (F) and mitochondrial dimensions x, y, z, (G) inside a C2C12 myoblast and a myotube. Data from 17 mitochondria from a myoblast and 16 mitochondria from a myotube with 1 SD error bars. Mann Whitney unpaired non-parametric t-test, *p < 0.1.Scale bars: 500 nm

Magnified FIB-SEM images of the cell nuclei show the electron dense heterochromatin along the nuclear periphery contains many spherical low density voids with diameters of ~130-155 nm, indicative of NPC, (Figure 3.10 A)

as supported by (329). Automatic segmentation and reconstruction of the NPC provides a map of the distribution of the NPC, which shows that NPC were organized in clusters distributed randomly throughout the nuclear membrane.

Quantitative analysis showed that although the surface area (Figure 3.10 A), volume (Figure 3.10 B), and NPC number (Figure 3.10 C) of the myotube nuclei are approximately half of myoblast nuclei, the number of NPC per surface area unit remained similar (Figure 3.10 F). The conserved NPC density suggests that the distances and arrangements between NPC play a critical role in their structure and function. Despite dramatic changes in the nuclear membrane morphology, the NPC density remains similar.

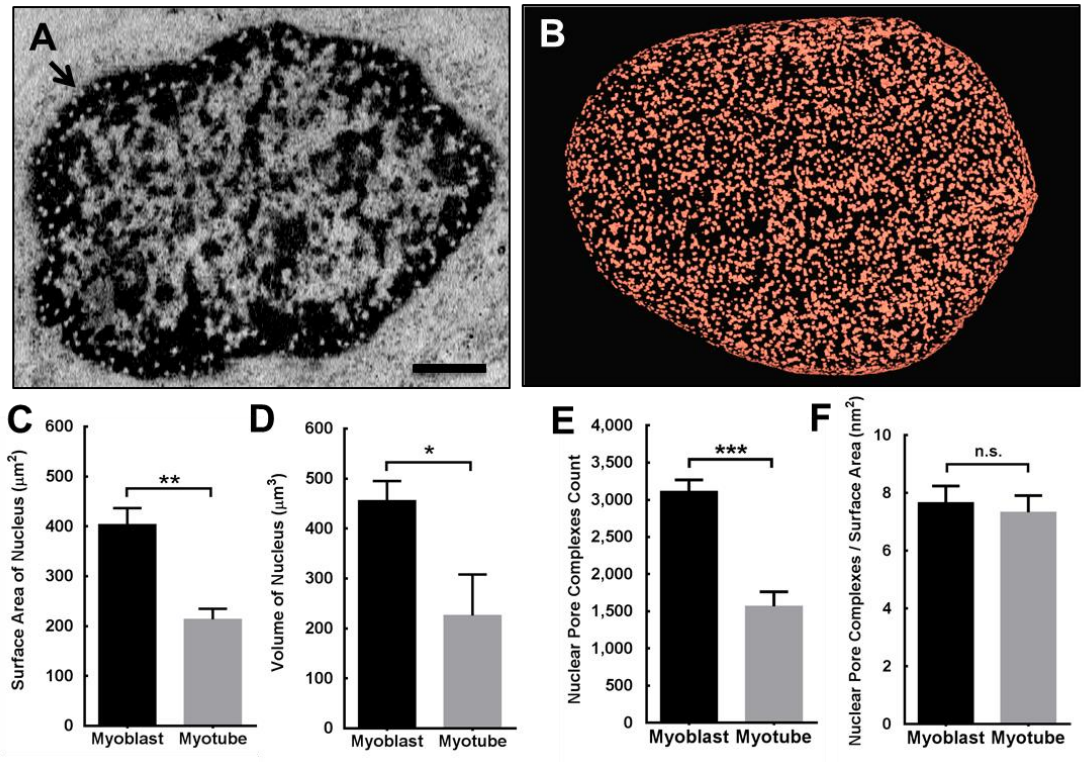


**Figure 3.10** FIB-SEM image (A) of a HPF-QS prepared specimen showing a nucleus inside a C2C12 cell. NPC (white dots, arrow) were evenly distributed along the heterochromatin (black) that border the perimeter of the nucleus. Reconstructed 3D FIB-SEM image (B) of panel (A) shows the NPC inside a C2C12 nucleus. Graphs compare the surface area of the nucleus (A), volume of the nucleus (B), NPC count (C), and number of NPC per surface area ($\mu m^2$) (D) inside C2C12 myoblasts and myotubes. Data from 3 nuclei in myoblasts and 3 nuclei in myotubes with 1 SD error bar. Mann Whitney unpaired non-parametric t-test, *$p < 0.1$. Panel A scale bar: 2 μm.

## 3.6 Discussion

Correlative super-resolution immunofluorescence microscopy using SIM and 3D FIB-SEM are powerful imaging tools that provide detailed information about cellular phenotype and structural morphology (102, 346, 378, 417). Here, I applied these techniques to explore the characteristics associated with the differentiation of the skeletal muscle cell pathway. Knowledge of both the genetic and structural changes that occur in a model system provides a basis for understanding cellular development and establishes a baseline for future comparisons of these mechanisms in healthy cells with those of diseased cells.

In this study, correlative 3D FIB-SEM shows that progenitor skeletal muscle cells, myoblasts, elongated the nuclei during the differentiation process. The changes in nuclear morphology support the parallel alignment and subsequent fusion of cells to form long striated myotubes. Although the nuclear length increased, the nuclear volume, nuclear surface area, and nucleolar volume decreased at the later stage of the differentiation process. The reduction in size of the nuclei and nucleoli suggest a down-regulation in the cell proliferative activity, typical of cells undergoing terminal differentiation and settling into cell growth arrest (418). Additionally, the reduction in nucleolar volume reduced the “zones of exclusion,” providing more physical space for the expression of myogenic regulatory factors inside the nuclei. Increased levels of MRF expression induces terminal differentiation and myogenesis (396–406).

In contrast, the sizes of nuclei and nucleoli significantly enlarge in dividing cells (419) and cancer cells (420–422), which correlates with increased rates of cellular proliferation and the up-regulation of rRNA synthesis and ribosome biogenesis (420–424). Enlarged nuclear components and increased ribosome production have been directly linked to the expression of mutated

tumor suppressor genes pRb and p53, which promote uncontrollable growth of cancerous cells (422). Thus, characterizing the sizes and shapes of the cell nuclei and nucleoli can provide insight in the cellular proliferation status. These variables could be used as diagnostic markers to identify potentially cancerous cells.

The nuclear membrane of normal skeletal muscle cell remains smooth throughout the differentiation process whereas cancer cells can be detected based on their irregular nuclear contours (424). The concavity volume measurement, used in Figure 3.5, could therefore be applied as a metric to differentiate between the smooth ultrastructure of normal cells versus the uneven contour of cancer cells.

Although the size and shape of the nucleus changed during the differentiation process, NPC remained in tight clusters that were distributed across the nuclear membrane, as observed previously in yeast cells (425), which suggests that the locations of NPC are important to cellular functions. The density of NPC over the nuclear surface unit area also remained constant across multiple nuclei from both myoblasts and myotubes. This evidence suggests that the muscle cells maintain similar rates of nuclear transport despite dramatic cellular morphology changes. The number and density of NPC have been linked to cellular activity during the cell cycle, with the highest density occurring during interphase (425). In fact, it has been shown that proliferating cells have a higher rate of nuclear transport than quiescent cells (426) and that NPC play an important role in gene regulation and cellular proliferation (391, 392, 425, 427, 428). It is likely that the density of NPC fluctuates during the cell cycle process to support cell division but settles down

after terminal differentiation and cell growth arrest. Monitoring the number and densities of NPC can provide insights into the activity of the cells.

Like the cell nuclei, the mitochondria also elongate in the late stage of differentiation, which provides energy and supports the overall tubular structure of the muscle fibers. Mitochondrial elongation most likely occurs through the fusion of multiple mitochondria suggested by the similar y and z dimensions of the mitochondria found in both myoblasts and myotubes but significantly longer x dimension in myotube mitochondria. Indeed, it has been reported that mitochondrial fusion is required for maintaining mitochondrial DNA stability in skeletal muscle cells because it helps reduce stress and prevents excess DNA mutation (429, 430).

Despite the increase in length, the mitochondrial volume remains similar. In contrast, the mitochondria of cells undergoing necrosis (431) or containing mitochondrial DNA mutations (429) are enlarged in the form of “giant mitochondria”. Similarly, mitochondria in cancer cells are significantly bigger, which protects the cancerous cells from apoptosis signals and promotes tumor growth (432). Characterizing the size and morphology of mitochondria in cells can lead to knowledge about the cell health status and function.

Taken together, I present multilevel metrics that could be automatically computed to quantitatively characterize the structural morphology of whole cells and their subcellular features. These metrics can be applied as variables in cancer diagnostics and characterization of cell development in stem cell studies.

Along with biological these insights, I present technical advances in the field of microscopy. Super-resolution SIM revealed the expression of cell regulatory factors which control the fate of the cell, in great detail. HPF-QS

techniques preserve the structure of the cell boundary and interior features with high fidelity while 3D FIB-SEM reveals cellular morphology at a resolution an order of magnitude higher than that available in light microscopy.

In particular, this combination of imaging technology enables quick and autonomous quantification of the number, size, morphological characteristics, and density of cellular organelles, such as nucleolus, NPC and mitochondria. In addition, these features are placed in context with other sub-cellular components and the entire cell as a whole. High resolution imaging can also map the patterns of heterochromatin and euchromatin and other DNA structures inside the nucleus that are responsible for regulating the fate of the cell. Further advances in correlative 3D FIB-SEM that significantly increase data throughput and reduce cost will enable this technology to become a regular diagnostic and characterization tool used to study various biological fields from stem cells, cancer and aging, to infectious diseases.

# 4 HIV-1 transfer from macrophages to astrocytes

## 4.1 Introduction

Within the first few days of infection, HIV-1 virions can rapidly migrate into the brain parenchyma (433), leading to HIV-1-associated neurological complications, including HIV-1-associated dementia, and in some cases death. Microglia and perivascular MDM are the main cell types that become productively infected (80, 246, 271). Resident microglia and perivascular MDM produce viral proteins, chemotactic signals, and inflammatory cytokines that recruit circulating MDM and T cells into the brain during neuroinflammation (434, 435). Some of these infiltrating MDM and T cells are productively infected with HIV-1; thus, their transmigration into the brain parenchyma contributes to an increase in the CNS viral load (80, 434). Once these immune cells cross the BBB, the first cell type that they encounter are astrocytes, which wrap their endfeet around the blood vessels to modulate the BBB permeability and maintain tissue homeostasis (436, 437). The frequent interactions between astrocytes and infected or virus-bearing cells make the astrocytes highly vulnerable to HIV-1 exposure. Since astrocytes are the most abundant cells in the brain (438), HIV-1 infection in astrocytes *in vivo* (173) poses a major challenge in eliminating virus from the CNS.

Unlike microglia and MDM, astrocytes have been described as harboring a restricted or latent infection because they do not actively produce virions, but HIV-1 has been detected in astrocytes both *in vivo* and *in vitro* (271, 311, 439) (Section 1.7). *In vitro* data show that stimulation of HIV-1 transfected astrocytes with cytokines induced transitory releases of virions, and contact with uninfected T cells enabled virion transfer (287, 296, 299). However, these cells were

transfected with an infectious viral genome to bypass entry barriers. It is therefore possible that viral production in astrocytes may not occur naturally.

I hypothesized that HIV-1 could be transmitted to uninfected astrocytes by cell to cell contact with infected MDM and T cells, a mechanism which is more efficient than cell free entry (94, 440). Characterizing the cell-cell interactions at the contact junction between immune cells and astrocytes is therefore of interest for understanding potential mechanisms of HIV-1 dissemination and its interruption. In the following chapters, I analyze the interactions between HIV-1 infected MDM (Chapter 4) and T cells (Chapter 5) and uninfected target astrocytes. I also explore the permissivity of primary HFA to HIV-1 infection, and the ability of astrocytes to transfer virions to uninfected permissive cells.

## 4.2 No evidence of productive infection of astrocytes by free HIV-1

HIV-1 primarily infects cells by binding the CD4 receptor and a chemokine co-receptor, mainly CXCR4 or CCR5 (441, 442). However, astrocytes have very low or no CD4 and CXCR4 or CCR5 expression. The absence of HIV-1 receptors on astrocytes raises questions about the infectivity of astrocytes, since it is unclear how HIV-1 would fuse with the target cell membrane to enter the cell in a productive manner. It has been suggested that HIV-1 entry may occur through receptor-independent mechanisms, detected by p24 ELISA, viral RNA and DNA by PCR, and microscopy (284, 287, 299, 443). As described above, transfection of astrocytes or inoculation with pseudo-typed viruses resulted in the production of p24 antigens, suggesting that there are no obvious blocks to viral replication once the virus genome has successfully entered the cell (296, 310).

To determine whether astrocytes can become infected with HIV-1 by the free mode (Figure 4.1), I incubated HFA and TZM-bl overnight with $10^{-3}$-$10^{0}$

MOI reporter viruses containing LucR, controlled by the HIV-1 promoter, and expressing various HIV-1 Envs: Bal-LucR (CCR5-tropic), YU2-LucR (CCR5-tropic) or NL4.3-LucR (CXCR4-tropic). Cells that transcribe these viral genomes also transcribe the luciferase gene and produce luciferase enzyme. At the appropriate time points, the cells were lysed and Renilla luciferin substrate added. The luciferase enzymes produced by the cell catalyze the oxidation of luciferin, which releases excess energy by emitting light. The luminescent signal is proportional to the steady state mRNA level; thus, the cell transcriptional activity of the HIV-1 genome can be accurately measured by the released light (360).

One day post infection, I washed the cells and added 10 μM of AZT (444), an NRTI used for the treatment of HIV/AIDS. On days 2, 4, 7, 9, 11 post-infection, I removed the supernatant to measure p24 antigen by capture ELISA assay and lysed the cells to measure R-RLU. As a positive control, I performed the same experiment in parallel with TZM-bl (353, 361).

HFA expressed no statistically significant R-RLU signal above background level at any time point tested, implying a lack of productive infection. Additionally, the levels of p24 antigen released into the supernatant from the HFA were similarly low in both untreated and AZT-treated cells, and decreased rapidly after T = 0, suggesting that they were unlikely to represent productive HFA infection but rather release of adsorbed and/or internalized virions. In contrast, the p24 levels in TZM-bl cultures remained relatively constant with the p24 level in NL4.3-LucR samples decreasing after day 7 post-infection. The addition of AZT reduced the R-RLU and p24 level in TZM-bl cultures compared to untreated-AZT cultures, indicating that AZT inhibited productive HIV-1

infection in TZM-bl but not HFA. Together these results support the hypothesis that astrocytes do not become productively infected with either X4 or R5 HIV-1 through free mechanisms.

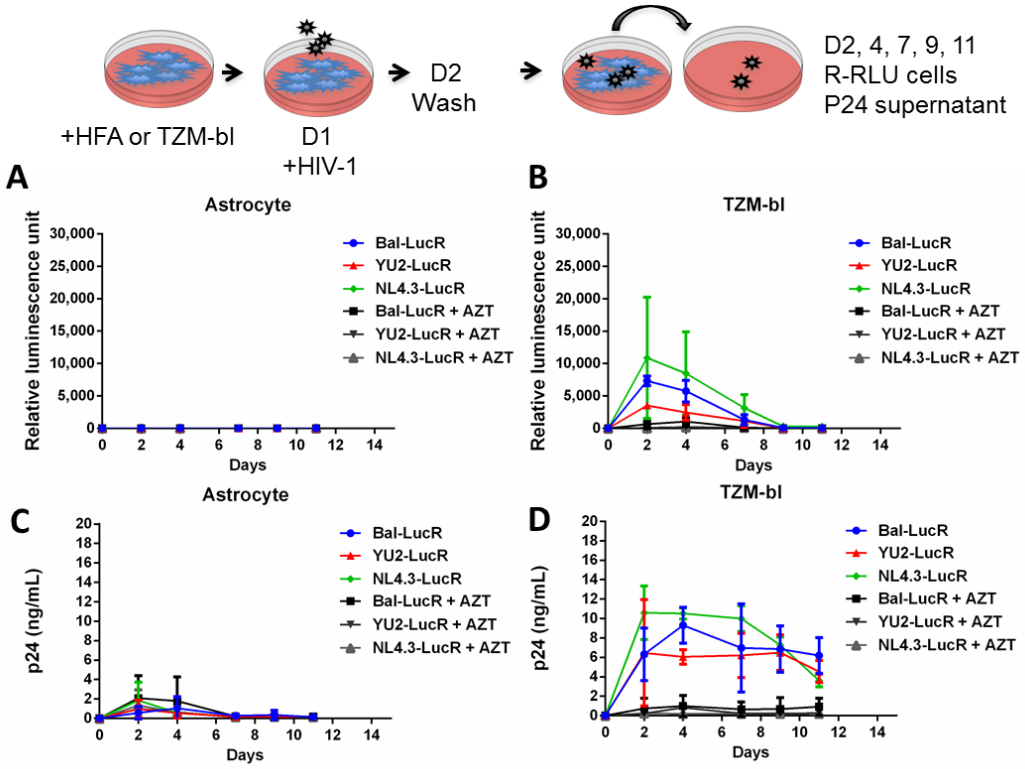


**Figure 4.1** Cell free HIV-1 infection of HFA and TZM-bl cells. HFA (A, C) and TZM-bl (B, D) were incubated with Bal-LucR, YU2-LucR, and NL4.3-LucR viruses overnight. Next day, all wells were washed and AZT was added at 10 μM to +AZT wells. On day 2, 4, 7, 9, 11 post infection, R-RLU signal was measured from lysed cells (A, B) and viral p24 proteins was measured from the supernatant (C, D). Data from 4 experiments performed in triplicate with mean ± 1 standard deviation (SD).

## 4.3 Astrocytes can transfer virus to neighboring cells

Although the viral genome was not obviously transcribed in HFA exposed to free HIV-1, virions bound to the astrocyte surface and/or internalized into a recycling internal compartment could still be transferred to neighboring cells, as suggested previously in DC-T cells (296, 299, 374, 445, 446). To test this hypothesis, I incubated HFA overnight with Bal-LucR, YU2-LucR, and NL4.3-LucR at $10^{-3}$-$10^{0}$ MOI. Next day, I washed the cells carefully and on days 2, 4, 7, 9, 11 post infection, I added primary human T cells. I co-cultured the HFA

and T cells for 3 additional days and then transferred the non-adherent T cells to another plate, lysed, and measured R-RLU. As a positive control for viral infection I performed the experiment in parallel with primary human MDM from two donors, and to control for virus adsorbing directly to the tissue culture wells, I used empty wells treated the same way as those containing HFA or MDM (Figure 4.2 C-E). Flow cytometry confirmed that the T cells removed by washing were ~94-99% $CD3^+$, indicating a high level of T cell purity with negligible contamination by the adherent cell types (Figure 4.2 A-B). The background values detected in the empty wells incubated with virus and then washed were consistently below $10^1$ RLU, and this was then used as the cutoff for background signal.

T cells cultured with MDM maintained a high level of R-RLU expression over the entire experimental period, while T cells cultured with HFA expressed similarly high level of R-RLU expression over the first 2 days but then decreased, with the different viruses showing different kinetics of decay. YU2-LucR samples rapidly declined to background levels ($<10^1$) at day 4, whereas Bal-LucR samples persisted until day 11 and NL4.3-LucR beyond day 11. NL4.3-LucR virus was most efficiently transferred by both MDM and HFA cultures to T cells, a finding which agrees with previous reports of CXCR4 T cell tropism (441). MDM are generally not productively infected with NL4.3 viruses, therefore, the transfer of viruses in NL4.3-LucR MDM-T cell co-culture, and possibly in other co-cultures, might be due to *trans*-infection of T cells by virus captured and archived by MDM (42, 47, 90, 445).

I repeated the experiment, but this time instead of adding T cells on days 2, 4, 7, 9, 11, I added TZM-bl. Because TZM-bl is stably transfected with the Firefly luciferase reporter gene (351, 352), for these experiments, I maintained

the indicator cells in the co-culture after 3 days of incubation, washed the wells carefully, lysed the cells, and measured the F-RLU. Measurement of F-RLU detected viral genome transcription only inside infected TZM-bl and not associated with HFA or MDM. F-RLU levels of TZM-bl remained consistently high in MDM cultures and started high but decreased rapidly to insignificant levels at day 4 in astrocyte cultures (Figure 4.2 F-G). Interestingly, the YU2-LucR virus that gave the weakest signal in the T cell transfer assay (Figure 4.2 C-D) resulted in the highest signal in the TZM-bl transfer assay (Figure 4.2 F-G); this difference is most likely due to cell type-specific viral tropism.

I repeated this experiment with 4 other HIV-1 isolates that were green fluorescence protein (GFP) or mCherry-tagged, both to assess the transfer infectivity of some other viral strains (eg. JRFL and CHO77) and to evaluate the infectivity of fluorescence protein- tagged viruses that I would use in later imaging experiments, I used JRFL Gag-iGFP from Phillipe Benaroch (P.B.), JRFL Gag-iGFP from Ben Chen (B.C.), JRFL, and CHO77 mCherry (Figure 4.2 H-I). JRFL virus was isolated from the front lobe (F.L.) of an HIV-1-infected patient (named J.R.) (447). HIV-1 JRFL Gag -iGFP is an NL4.3 based HIV-1 IMC with the GFP inserted into gag gene between MA and CA and contains the JRFL sequence. The V3-loop V92th014.12 was inserted instead of the NL4.3 to make the IMC CCR5-tropic (448). Two variations exist, one from B.C. (449, 450) and the other from P.B (448) that has been passaged in MDM culture to increase macrophage tropism; these clones are expected to have slightly different infectivity. CH077 is a CCR5-tropic transmitted/founder virus strain (51).

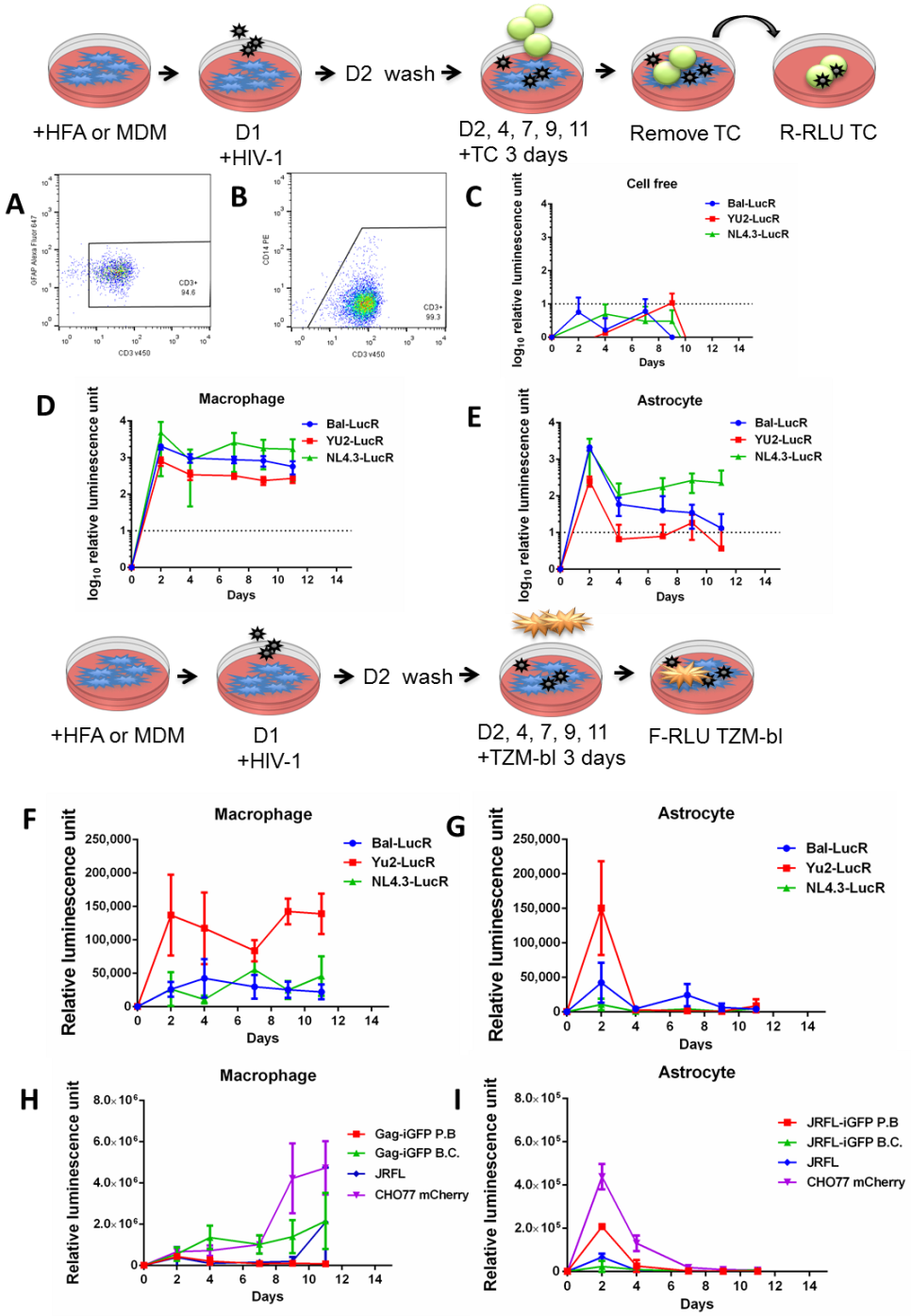


**Figure 4.2** Transfer of HIV-1 from HFA and MDM to T cells and TZM-bl. MDM from 2 donors (D), HFA (E) and empty wells (C) were incubated with Bal-LucR, YU2-LucR, and NL4.3-LucR viruses overnight. The next day, cells were washed. T cells were added at day 2, 4, 7, 9, 11 post-infection and allowed to remain in the co-culture for 3 days. T cells were removed from co-culture, lysed, and R-RLU was measured. Data from 4 experiments performed in triplicate with mean ± 1 SD. Flow cytometry shows that T cells harvested from HFA (A) and MDM (B) co-cultures contain >94-99% $CD4^+$ T cells. The experiment was repeated by overlaying MDM or HFA exposed to Bal-LucR, YU2-LucR, NL4.3-LucR (F-G), Gag JRFL-iGFP from P. B., Gag JRFL-iGFP from B. C., JRFL, CHO77 mCherry with TZM-bl (H-I). TZM-bl were lysed within the co-culture F-RLU were measured. Data from 2 experiments performed in triplicate with mean ± 1 SD.

TZM-bl in both MDM and HFA cultures exposed to transmitted/founder virus CHO77had the highest F-RLU signal. F-RLU signals in MDM cultures were higher than those in HFA cultures by a factor of ~10. TZM-bl in the MDM cultures had high levels (0.5-1.0 x $10^6$) of F-RLU and showed increasing levels over time, while the TZM-bl in the astrocyte cultures had high levels (1.0-5.0x$10^5$) of F-RLU initially that decreased rapidly over time. Although in the long term astrocytes were not as effective as MDM at transferring virions to neighboring cells, in the first few days after exposure to HIV-1, astrocytes effectively transferred virions to reporter cells. These data are consistent with MDM becoming productively infected with R5 HIV-1 and transferring virus over extended periods to permissive cells, and capturing and archiving X4 virus for transmission *in trans*, whereas astrocytes appear resistant to productive infection by all viruses but archive virus for short term transfer *in trans* to permissive cells.

The fact that astrocytes transferred virions to another cells without apparently being productively infected suggests that the virions were bound to the surface of the cell and/or actively taken up into a compartment that might be surface-connected as has been described for DC and MDM (42, 47, 90, 366, 445). The addition of proteases has previously been shown to reduce or eliminate the infectivity of surface-bound but not internalized HIV-1 (46, 364, 366, 451), and similarly Nabs inhibit surface HIV-1 infectivity but not the infectivity of viruses within intracellular compartments (197, 198, 452, 453).

To test this hypothesis, I incubated HFA overnight with Bal-LucR, YU2-LucR, and NL4.3-LucR at $10^{-3}$-$10^0$ MOI. The next day, the cells were incubated with 0.25% (2.5 mg/mL) trypsin-EDTA for 5 minutes (46, 364, 451), or 200 µg/mL pronase for 30 minutes at 4ºC (364, 366), or a cocktail of bNabs (10E8,

PGT121, VRC01) at 10 µg/mL per antibody for 1 hour at 37ºC (Figure 4.3). I chose the trypsin concentration based on the highest trypsin concentration used in previous studies (46, 364, 451). I chose the pronase concentration that could prevent virion transfer of >90% of DC reported in (366). I chose these 3 bNabs because they target multiple epitopes on the Env trimer: 10E8 targets MPER on gp41, PGT121 targets a glycopeptide epitope associated with the V3 loop, VCR01 targets CD4 binding site (Figure 1.11) and all have been shown to neutralize ~70-98% of viral strains with *in vivo* sterilizing immunity observed at serum concentrations <10 µg/mL (197, 198, 452, 453). HFA were carefully washed and on days 2, 4, 7, 9, 11 post-infection, TZM-bl were added. The TZM-bl were co-cultured for 3 additional days, then lysed and analyzed for F-RLU signal. As a positive control, I performed the same experiment in parallel with MDM.

My data show that TZM-bl incubated with HFA exposed to virus without inhibitors expressed high F-RLU levels after 2 days post infection which decreased rapidly by day 4. Adding trypsin, pronase or bNabs into the HFA culture followed by washing and addition of TZM-bl resulted in insignificant levels of F-RLU expression. By contrast, in MDM cultures, the addition of trypsin, pronase, or bNabs only partially reduced the F-RLU expression in a virus-dependent manner, showing that MDM continued to transfer viruses to TZM-bl. These viruses may originate from *de novo* production and/or from inaccessible intracellular compartments. Because MDM do not typically become productively infected with non-macrophage tropic X4 NL4.3-LucR virus, the F-RLU signal in TZM-bl cultured with NL4.3-LucR-exposed MDM is likely to be primarily due to virions trapped within enzyme and bNAb-inaccessible compartments and later released to the target cells. These results support the

model that HFA do not become infected after exposure to virus and do not take up virions into inaccessible intracellular compartments.

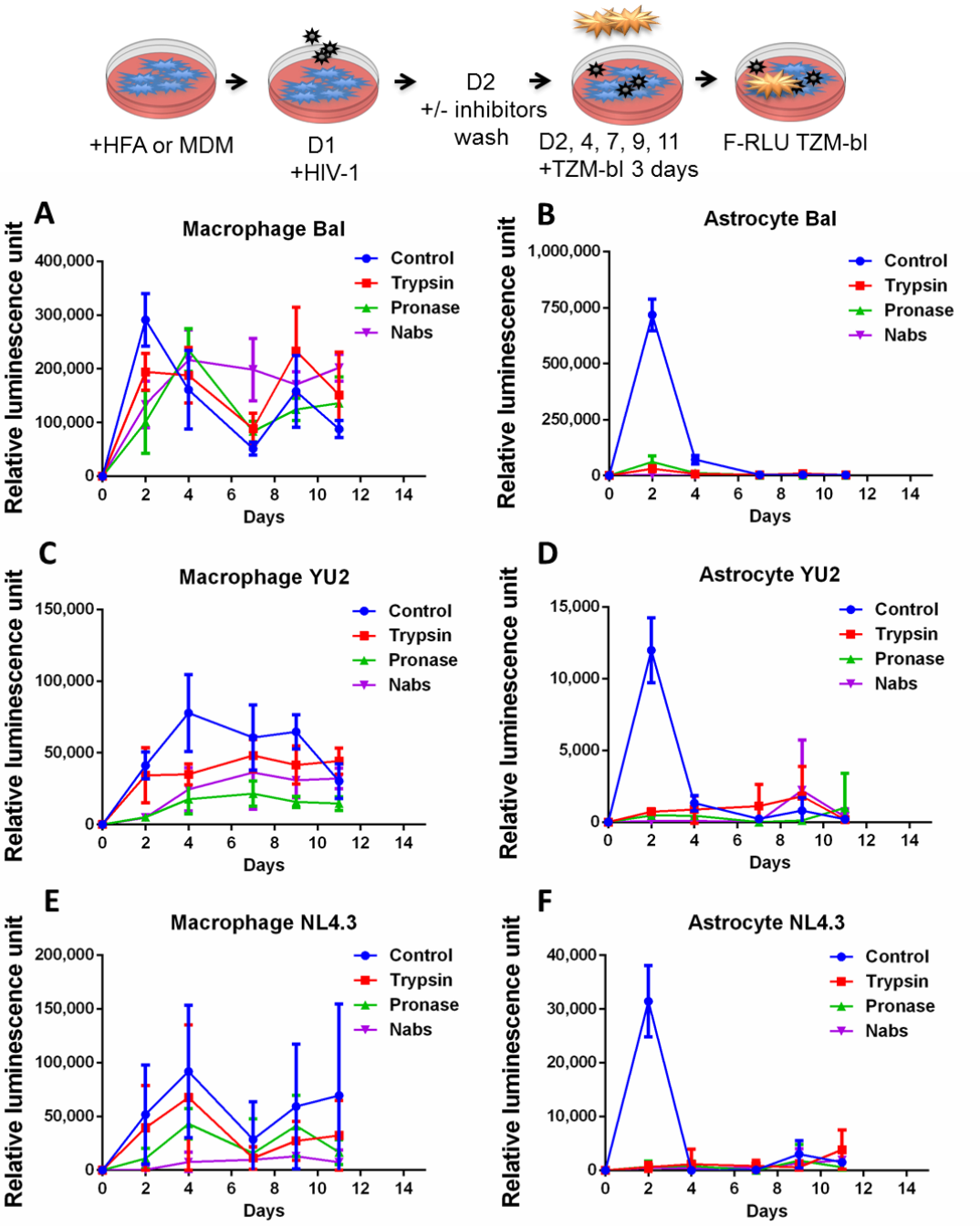


**Figure 4.3** Viruses adhere to the surface of HFA. MDM from 2 donors (A, C, E) and HFA (B, D, F) were incubated with Bal-LucR, YU2-LucR, and NL4.3-LucR viruses overnight. Next day, cells were washed and incubated with 0.25% Trysin for 5 minutes, or 10 µg/mL neutralizing antibody cocktail (10E8, PGT121, VRC01) for 1 hour at 37ºC, or 200 µg/mL pronase for 30 minutes at 4ºC. Cells were washed and TZM-bl were added on days 2, 4, 7, 9, 11 and co-cultured for 3 days, then F-RLU was measured. Data from 2 experiments performed in triplicate with mean ± 1 SD.

## 4.4 Transfer of virus from astrocytes can be blocked

If HFA capture virus and transfer it to neighboring cells, then blocking HIV-1 attachment to the astrocyte plasma membrane may prevent HIV-1 onward transmission. To test this, I pre-incubated HFA with a selection of inhibitors designed to interfere with virus binding to cell surface receptors (10 µM PRO 2000 (454–459) or 10 mM mannan (371) or 10 µg/mL anti-ICAM-1 antibody (36, 48, 460) or 5 mM EDTA (373)), or to prevent cell surface receptor clustering by preventing cytoskeletal remodeling (5 µM jasplakinolide (96, 103)), or to enzymatically remove cell surface receptors prior to virus binding (200 µg/mL pronase at 4ºC for 90 minutes or 0.25%, or trypsin at 37ºC for 5 minutes).

PRO 2000 is a negatively charged polyanion used as the principal active ingredient in a microbicide to prevent HIV-1 infection (367, 368). The polymer may interact electrostatically with positively charged regions on HIV-1 NL4.3 virions (53, 461–464) and analogous regions on the R5 viruses, preventing viral attachment to negatively charged structures on the astrocyte membrane. The PRO 2000 concentration selected was based on (465), which shows that the usage of PRO 2000 at >10 µM reduced cell viability; here I used the highest concentration (10 µM) that still preserved >90% cell viability.

The mannan concentration selected was based on (371), which shows that the addition of mannan blocked HIV-1 binding to MDM and subsequent transfer to T cells. Mannan binds to the same carbohydrate recognition domains as gp120 on the mannose receptor and competitively interfere with virion attachment to receptor-expressing cells such as MDM (371).

The EDTA concentration was based on (373), which show that EDTA prevented virion binding to erythrocytes. EDTA was also shown to inhibit HIV-1

binding to MDM mediated by mannose receptor, as it is a calcium chelator and will prevent Env interaction with all calcium-requiring c-type lectins (371).

Anti-ICAM1 blocks the interaction between LFA-1 and ICAM-1 that stabilizes VS interactions, such as that between DC, CD4+ T cells, and MDM (36, 48, 460). The anti-ICAM-1 concentration selected was based on (460), which shows that ICAM-1 impaired HIV-1 transmission from DC to T cells.

Jasplakinolide stabilizes actin, which has been shown to play a role in mediating cytoskeletal restructuring of VS that enhances HIV-1 transfer between T cells (96, 103). I used a slightly higher concentration 5 µM instead of 1 µM used in (96, 103) to ensure complete stabilization of the cytoskeleton of MDM and HFA. Visual inspection revealed cells with smaller and rounder morphology, indicating slight detachment from the tissue culture.

HFA were incubated with Bal-LucR, YU2-LucR, and NL4.3-LucR viruses at $10^{-3}$-$10^{0}$ MOI for 4 hours. Cells were washed carefully and TZM bl cells were added. Three days after co-culture F-RLU was measured (Figure 4.4 A-C). None of the inhibitors significantly affected the uptake and transfer of infectivity of the two R5 viruses from HFA to TZM-bl. By contrast, PRO 2000 had the most substantial inhibitory effect on TZM-bl cultured with HFA exposed to NL4.3-LucR, and EDTA, jasplakinolide and pronase all had lower but still significant inhibitory activity. To investigate this further I carried out a titration of PRO 2000 from 0-100 µM; at higher concentrations, PRO 2000 abrogated the infection of TZM-bl in all three HIV-1 isolates (Figure 4.4 D). PRO 2000 had no effect on YU2-LucR and Bal-LucR but resulted in >50% inhibition on NL4.3-LucR at <10 µM most likely because X4 viruses have higher positive charge than R5 viruses (462, 463), therefore, it would take less amount of PRO 2000 to competitively bind to HIV-1 and prevent subsequent viral attachment to the astrocytes.

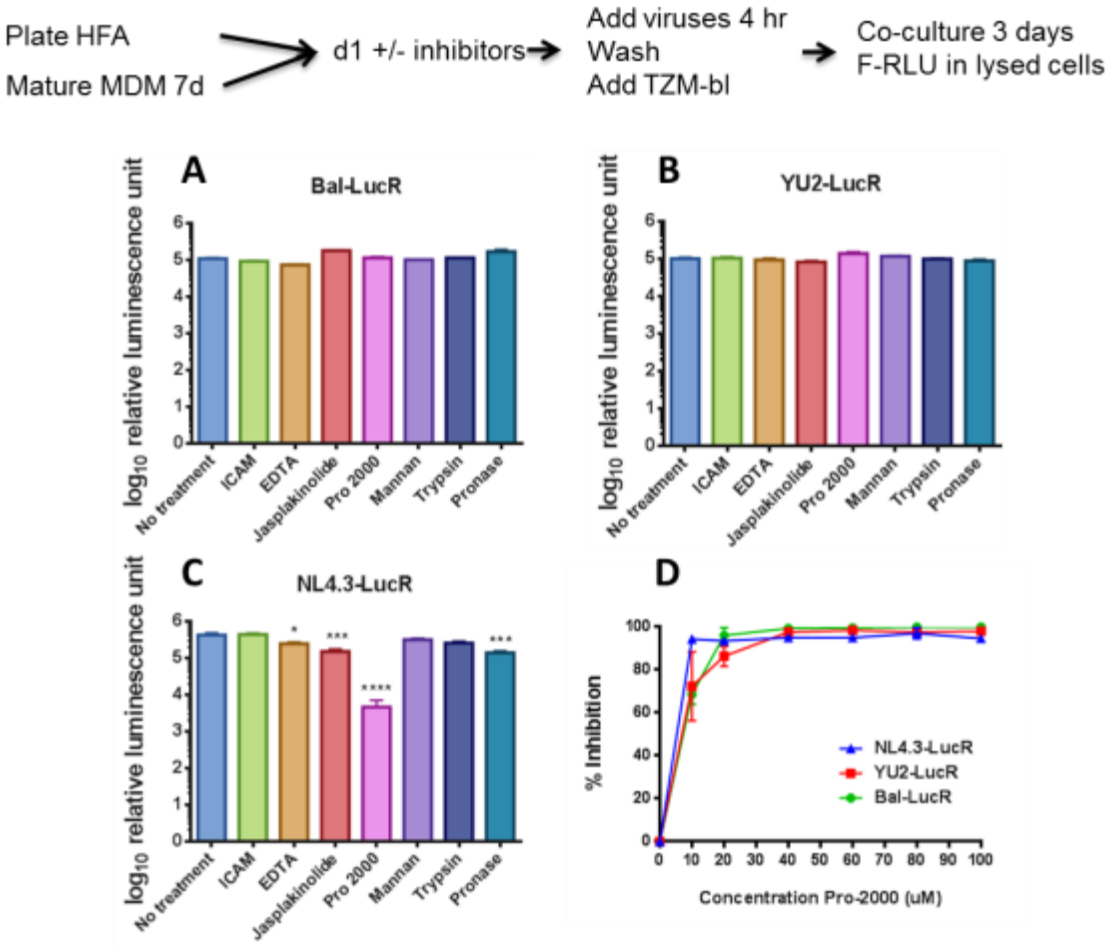


**Figure 4.4** Transfer of viruses from HFA can be blocked. HFA were incubated with 10 µM PRO 2000 or 10 mM Mannan or 10 µg/mL anti-ICAM-1 antibody or 5 mM EDTA or 5 µM Jasplakilonide at 37ºC or 200 µg/mL pronase at 4ºC for 90 minutes or 0.25% trypsin at 37ºC for 5 minutes. HFA were incubated with Bal-LucR (A), YU2-LucR (B), and NL4.3-LucR (C) viruses for 4 hours. Cells were washed and TZM bl cells were added. Three days after co-culture F-RLU was measured. Data from 3 experiments performed in triplicate with mean ±1 SD. Astrocytes were incubated with a titration of PRO 2000 (D) for 90 minutes then Bal-LucR, YU2-LucR, and NL4.3-LucR viruses for 4 hours. Cells were washed and TZM bl were added. Three days after co-culture F-RLU was measured. Experiment was performed in triplicate with mean ± 1 SD. Mann Whitney unpaired non-parametric t-test, *p < 0.1.

## 4.5 Macrophages actively interact with astrocytes

My results strongly suggest that HFA do not become productively infected with HIV-1 but harbor virions on the cell surface membrane or in a surface-accessible compartment. These virions can be transferred to uninfected cells, leading to their productive infection. Although the precise mechanism of viral

attachment to the HFA membrane is still unclear, electrostatic interactions between positively charged regions of Env on virions and negatively charged molecules on the cell membrane appear to play an important role, particularly for the CXCR4-tropic virus tested. The apparently non-specific nature of viral attachment to the astrocyte plasma membrane makes astrocytes a potential short-term viral reservoir. However, although free virions appear unable to productively infect astrocytes, it is possible that the higher efficiency of viral infection mediated by direct cell-to-cell spread may overcome entry blocks to the virus, allowing infection.

To investigate this idea, I first explored the interactions between infected or uninfected MDM and HFA. As with all systems used to investigate cell-to-cell viral transfer, it is only possible to analyze the movement of virus between individual infected-target cell conjugates using imaging techniques, since other approaches are unable to dissociate the infectivity signal in the infected from that within the target cell. I added uninfected HFA to adherent MDM that were uninfected or infected with HIV-1 JRFL-iGFP from B.C. at $10^{-3}$-$10^{0}$ MOI (449). I chose this IMC because it is GFP-tagged R5, which enabled me to visually inspect the infection level of MDM, and it is neurotropic so virus cultured from this IMC may be transferred to HFA efficiently. Additionally, MDM exposed to virus cultured from B.C. IMC transferred virions to TZM-bl better than those exposed to virus cultured from P.B. IMC (Figure 4.2 H).

After an overnight incubation, I fixed, stained and imaged the cells using SEM. The images revealed the distinct ultra-structural differences between the two cell types: astrocytes are flat and smooth with thin, branched processes and MDM are bulbous with extensive membrane sheets.

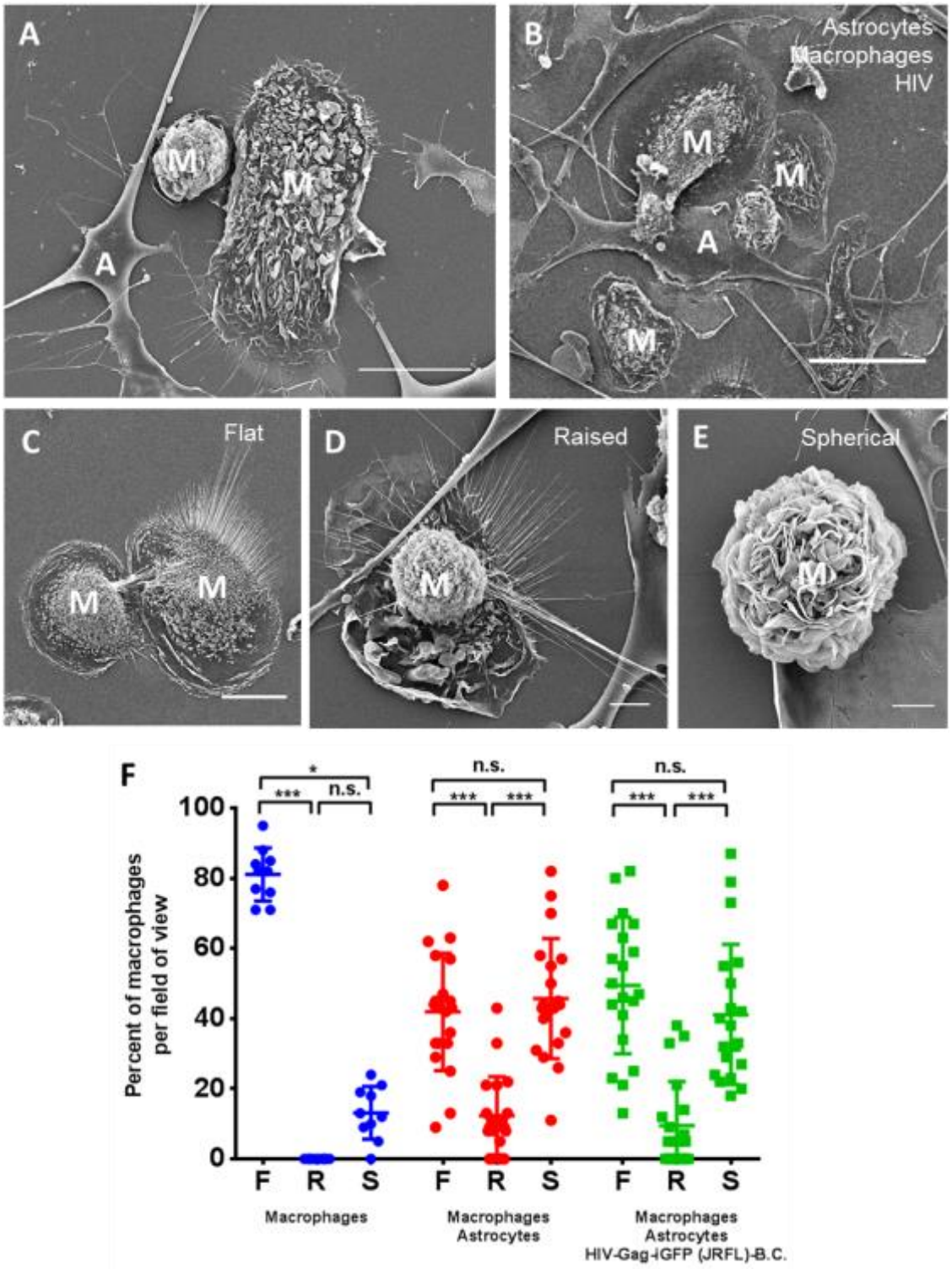


**Figure 4.5** MDM “M” actively interact with HFA “A”. SEM images of uninfected MDM cultured alone or uninfected or HIV-1 Gag-iGFP JRFL (B. C.) infected MDM co-cultured with HFA overnight. MDM changed shape from flat “F” (C) to raised “R” (D) to spherical “S” (E). Quantification of MDM morphological changes was calculated by counting the number of MDM in each category in >10 randomly selected SEM images from each type of sample. Experiment was performed in duplicates with mean ± 1 SD. Panel A, C-E scale bars: 25 µm, B: 50 µm.

I classified MDM into three distinct morphological types: flat (F), raised (D) and spherical (E) (Figure 4.5). Based upon the literature (466) and my data below (Figure 4.5) it seems that the flat cells are highly motile, the raised cells are lifting from the solid support, and the spherical cells are activated within the culture (466, 467). Spherical cells could be undergoing polarization toward M1 pro-inflammatory state (348). Quantification of each morphological type revealed that most (~80%) uninfected MDM cultured alone (without added cytokines) have a flat, fried egg-type morphology, while MDM cultured with HFA were approximately 45% flat, ~10% raised, and ~45% spherical (Figure 4.5 F).

The proportions of each phenotype were similar whether the MDM were uninfected or infected (~30-40% MDM were infected by visual inspection in fluorescence microscopy) (Figure 4.5 F). These data suggest that contact with HFA may activate MDM. Although HFA were added on top of adherent MDM, in many instances, MDM were observed extending membrane sheets toward the HFA, potentially tethering the two cells together (Figure 4.5 B). This suggests that MDM actively interact with HFA by detaching themselves from the substrate and becoming highly mobile, crawling around and onto HFA. The presence of HIV-1 infected MDM did not appear to affect the cellular behavior; instead it was the presence of the HFA that induced MDM morphological changes.

## 4.6 Macrophages extend filopodia toward astrocytes

Although SEM provides a high resolution and finely detailed glimpse into the interactions between MDM and HFA, this technology is limited to a single time point using fixed cells, and does not readily reveal the presence of virus. To overcome this limitation, I imaged cells using live fluorescence microscopy. I infected MDM with fluorescence HIV-1 JRFL Gag-iGFP virus from P.B at $10^{-3}$-

$10^0$ MOI. I chose to use the isolate from P.B. instead of B.C consistent with the SEM studies, because I wanted to capture HFA uptake of virions, and I had previously observed that HFA exposed to virus cultured from P.B. IMC transferred virions to TZM-bl more efficiently than those exposed to virus cultured from B.C. IMC (Figure 4.2 H).

I cultured infected MDM and HFA in 2 separate compartments, divided by a removable silicon insert on the same Ibidi imaging dish. This experimental setup enabled relatively synchronized imaging of the cellular interactions within the monolayer. After the culture insert was removed, ~80-90% MDM became motile and gradually moved towards the HFA. By 24 hours, MDM had crossed the 500 µm gap where the insert previously was located and interacted with the HFA. Live cell video of MDM- HFA conjugates show that MDM extended filopodia toward the HFA. When the HFA moved away from the HIV-1 infected MDM, the infected MDM enlarged its cell membrane and extended filopodial protrusion toward the HFA (Figure 4.6). Virions were observed associated with the filopodial extension. It is apparent from this video that infected MDM migrated and extended filopodia containing virions toward uninfected HFA.

## 4.7 Macrophages transfer virions to astrocytes

Live cell imaging offered information on the motility and morphology of the cells but introduced photo-toxicity at high magnification, which may have altered the cellular morphology of the fragile HFA and induced cell death. I therefore returned to fixed cell imaging and applied confocal imaging to visualize the interactions between HIV-1 Gag JRFL-iGFP from P.B. infected MDM at $10^{-3}$-$10^0$ MOI and HFA after an overnight incubation (Figure 4.7 A-D).

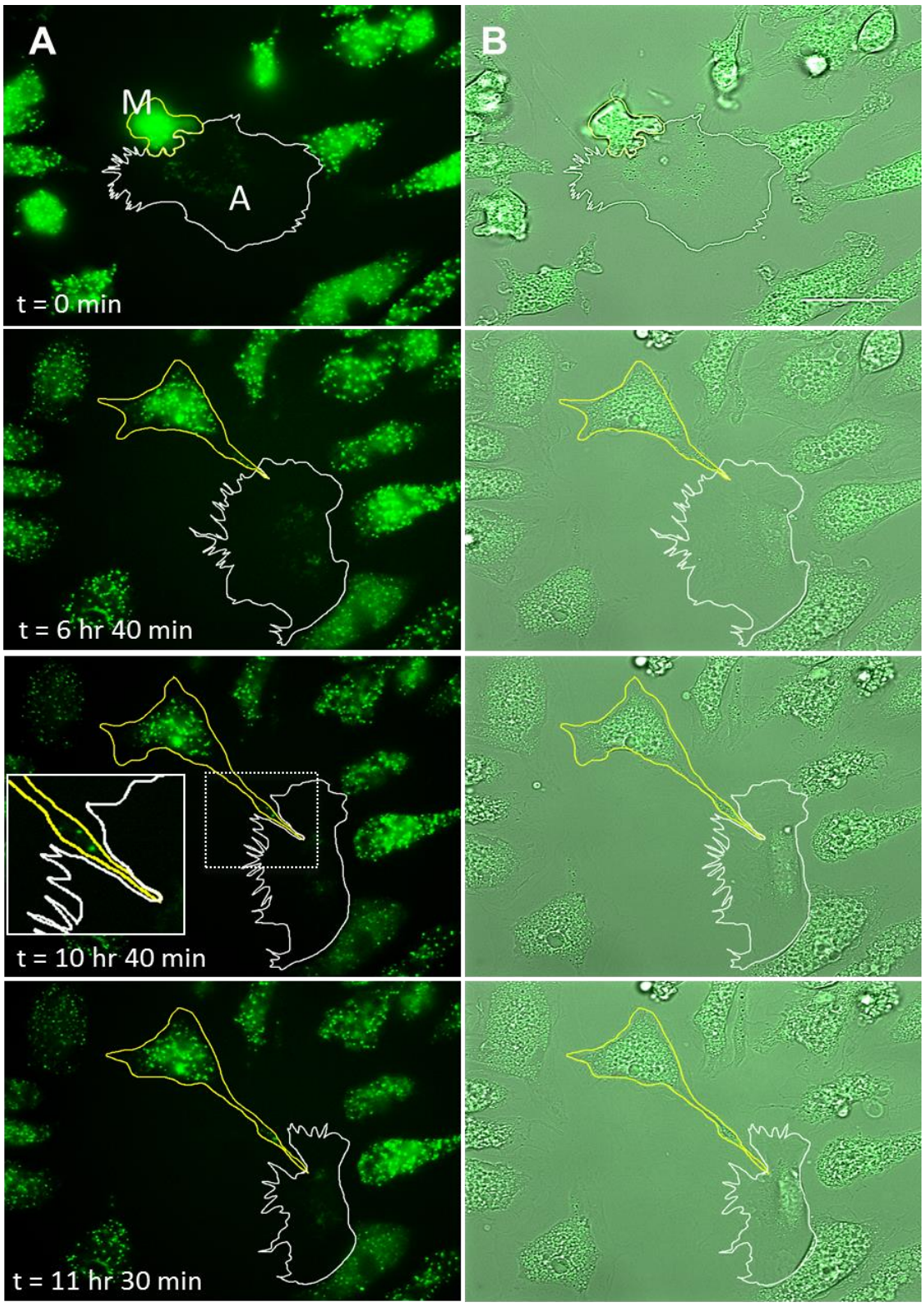


**Figure 4.6** Live cell imaging of HIV-1 infected MDM and HFA. MDM ("M" yellow) were infected with HIV-1 Gag-iGFP JRFL (P. B.) and co-cultured with HFA ("A" white). Outlines were traced based on cell morphology observed in phase contrast images. (A) Fluorescence images of HIV-1 GFP and (B) overlays of GFP channel and phase contrast show an infected MDM inserting a membrane protrusion decorated with virions toward a migrating HFA. Scale bars 50 µm. Inset (center) shows HIV-1 decorated membrane protrusion at higher magnification.

So as to unequivocally confirm the morphological distinction of astrocytes, I labeled the HFA with anti-GFAP antibody tagged with Alexa Fluor 647. The infected MDM were visualized using the fluorescence signal from the GFP tagged reporter virus. Figures 4.7 A-D show widefield microscopy images of HFA co-cultured with infected MDM on gridded coverslips. In several cases MDM have fused together to form giant multi-nucleated cells (Figure 4.7 D arrows). The astrocytes remained long and flat with no sign of apoptosis (blebbing) and no formation of syncytia, a structure typically observed in infected, receptor-expressing cells (292–294). In no case did HFA express GFP fluorescence signal, an indication of either productive infection or of uptake of infected material by astrocytes. At this resolution, there was no evidence of HFA infection via contact with infected MDM.

At the ~180 nm resolution offered by confocal imaging, it was difficult to determine whether virus might be transferred from infected MDM to HFA. I therefore collaborated with Dr. Jakub Chojnacki to image the cell-cell contact region by super-resolution STED microscopy. STED microscopy requires photo-switchable fluorochrome to detect molecules of interest, thus, instead of using the fluorescence reporter viruses HIV-1 Gag-iGFP JRFL as before, I use un-tagged virus. I infected MDM with HIV-1 Bal at $10^{-3}$-$10^{0}$ MOI and co-cultured them with HFA for 3 hours or 24 hours. The next day, the HFA were fixed and labeled with anti-GFAP antibody tagged with Alexa Fluor 647 and virus was labeled with anti-p24 antibody tagged with Atto 490LS. STED microscopy shows the virions surrounding the plasma membrane of the astrocytes (Figure 4.7 E-F).

Cell conjugates were imaged as a *z*-stack in 3D STED (12 images per sample). The distance from the virion to HFA membrane was calculated. Virions

were chosen +/-3 µm from the closest astrocyte plasma membrane. Areas full of free virus were avoided. Analysis was concentrated on areas with contacting MDM-HFA conjugates. Each image in the z-stack was analyzed separately under assumption that each virus particle is located at the point of its brightest fluorescence signal. Images with a significant number of particles localized directly above or below the astrocyte membrane were omitted. Quantification of the distances between HIV-1 particles and the HFA plasma membrane in the *x-y* plane is shown in Figure 4.8. After 3 hours of co-culture, the virions were almost entirely localized on the plasma membrane of the astrocytes, whereas after 24 hours of co-culture, >50% of individual virions were beneath the astrocyte membrane, as defined by the boundary of the GFAP expression. This evidence suggests that the virions may be taken up by HFA.

To visualize the cell-cell contact region at even higher resolution, I imaged the cells using TEM. I infected MDM with HIV-1 NLENG-Bal GFP virus at $10^{-3}$-$10^{0}$ MOI for >7 days and co-cultured them with HFA overnight. The next day, I fixed the cells and stained HFA with anti-GFAP antibody tagged with Alexa Fluor 647. I imaged the cell-cell contact region using widefield fluorescence microscopy to confirm the high MDM infection rate by visualizing the GFP fluorescence signal and identifying the contact areas between MDM and labelled HFA. Then I fixed the cells, stained and embedded the sample for EM. I imaged the samples using high resolution TEM (Figure 4.9). The distinct differences in cellular morphology enabled easy identification of the cells: HFA are flat with thin straight filopodia, whereas MDM have many vesicles with extensive curly membrane sheets. TEM shows the MDM harbored virions inside vesicular compartments and made direct contact with HFA. MDM membrane sheets were aligned in parallel to the HFA membrane over extended distances.

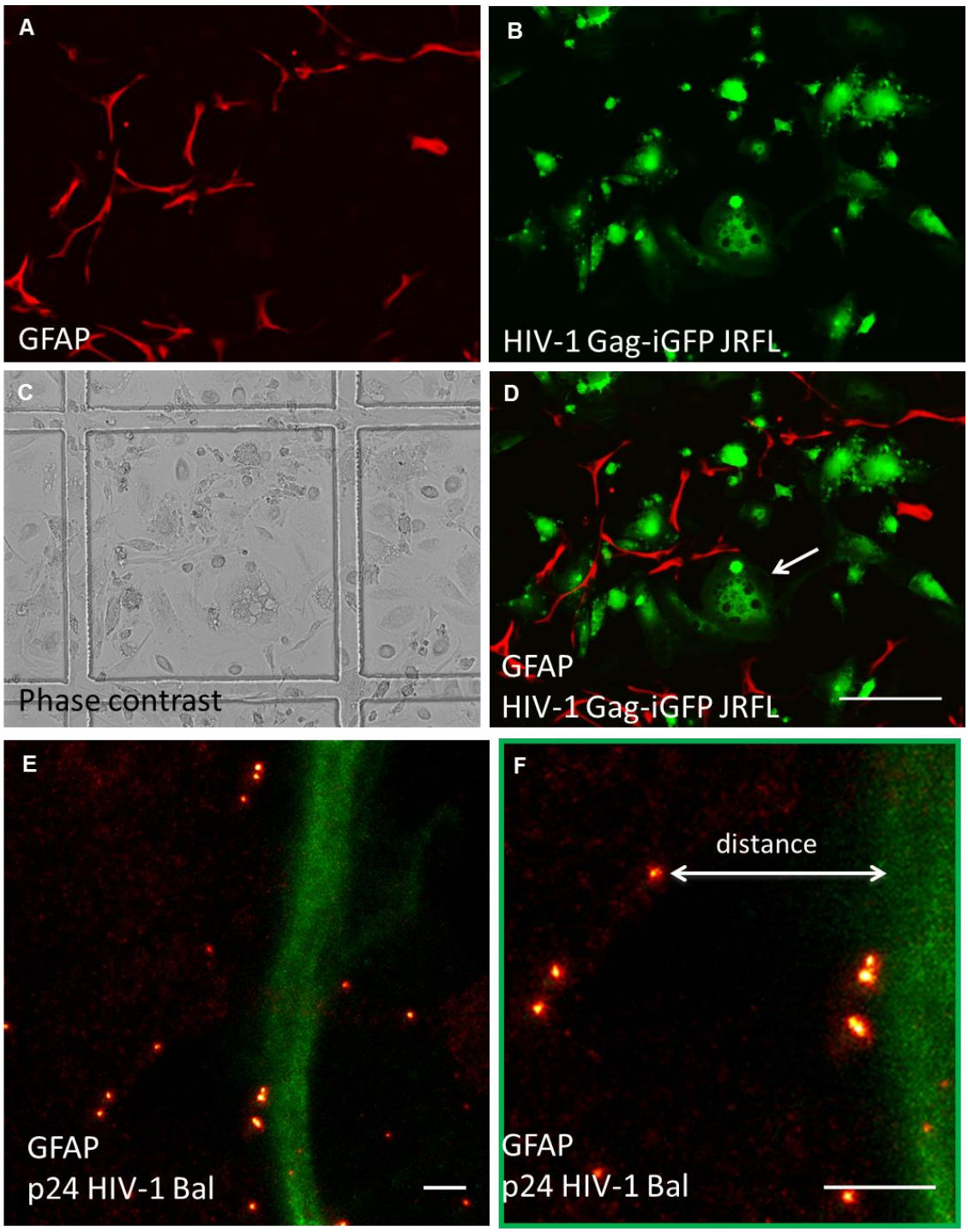


**Figure 4.7** Widefield fluorescence microscopy of HFA stained with anti-GFAP antibody Alexa Fluor 647 (A, red channel) co-cultured with MDM infected with HIV-1 Gag JRFL-iGFP (P. B.) (B, green channel) overnight (A-D). Overlay of red and green channels shows a high level of infection in MDM but no GFP signal in astrocyte, indicating no or low level of HIV-1 entry (D). Phase contrast shows healthy HFA with many multinucleated MDM. STED microscopy image from a 3D STED stack of HFA stained with anti-GFAP Alexa Fluor 647 (green) and co-cultured with HIV-1 Bal infected MDM labelled with anti-p24 antibody 37G12 Atto 490LS (red) for 3 hours. STED images were taken in collaboration with Dr. Jakub Chojnacki at Weatherall Institute of Molecular Medicine. Panels A-D scale bars: 50 µm, E: 1 µm , F: 0.5 µm.

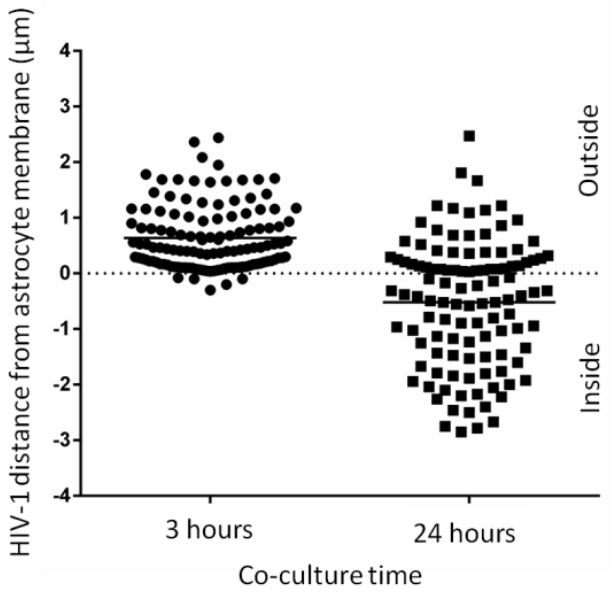


**Figure 4.8** Quantification of HIV-1 distance from HFA membrane from STED images as in Figure 4.7 E-F. The distance between the virions to the astrocyte membrane were measured in the xy plane and analyzed graphically. Data from 2 independent experiments, 12 images per sample.

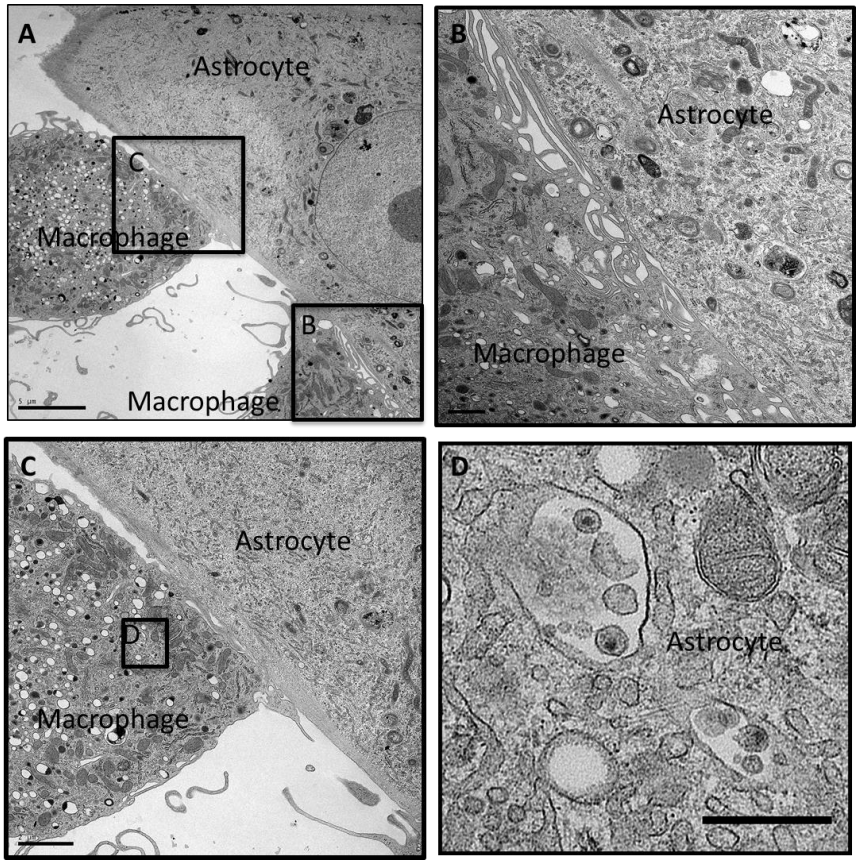


**Figure 4.9** TEM of HIV-1 infected MDM interacting with HFA. MDM were infected with HIV-1 NLENG-Bal GFP, co-cultured overnight with HFA, and then processed for TEM; panels (B-D) are magnified regions from panel (A). Magnified image of panel (C) reveals a compartment inside a MDM containing HIV-1 virions (D). Panel A scale bar: 5 µm, B: 1 µm, C: 2 µm; D: 0.5 µm.

## 4.8 Astrocytes adsorb HIV-1 through contact with infected cells

To quantify the uptake of virus or virus-containing cellular material by uninfected HFA interacting with HIV-1 infected MDM, I used flow cytometry. I co-cultured ~250,000 MDM (each from 5 different donors (M2-M6)) or iPS-MDM (from 1 donor (iM1)) infected with HIV-1 NLENG-Bal GFP (468) at $10^{-3}$-$10^{0}$ MOI with 15,000 uninfected HFA for 8-10 days. Because HFA were highly proliferative, after 8-10 days, assuming that the population growth approximately doubled every ~3 days (based on prior experience), each culture should contain ~200,000-400,000 HFA. In total, there should be about 1:1 MDM to HFA. I chose HIV-1 NLENG-Bal GFP because it is a reporter virus; integration of viral genome induces production of GFP proteins that diffuse into the cells. Cells containing diffusible virus emit a higher fluorescence signal compared to those containing non-diffusible virus; this confers an advantage for flow cytometry analysis. I generated iPS-MDM to compare their infectivity and viral transfer efficiency with those of primary MDM. These cells were first derived from human fibroblasts, then de-differentiated into iPS cells, then re-differentiated into monocytes and MDM.

I labeled MDM with anti-CD14 antibody and HFA with anti-GFAP antibody and matching isotypes as controls. I collected at least 20,000 live cells in flow cytometry. During data collection, I gated the live cells, which typically had forward scatter and side scatter signals above $10^{2}$ and could be easily identified by the most dense cell cluster (Figure 4.10 A). After data collection, I analyzed MDM and HFA unstained and stained with matching isotypes and used those results to gate negative and positive cells (Figure 4.10 B-C). (Figure 4.10 A-C) illustrate the gating strategy from one donor experiment. I expected that CD14+ cells should comprise ~50% of all cells in culture: across all the

cultures, I found <1-53% of cells were CD14+ (28.8+14.2=43% for (Figure 4.10 C)). From the CD14+ population, <1-99% were also HIV-1 GFP+ (14.2/43=33% for (Figure 4.10 C)). The wide ranges of MDM percentage and infectivity might be due to donor variability and cell viability, and/or the rapid proliferative rate of HFA might result in rapid depletion of nutrients available for the non-proliferative MDM. MDM associated with virions might also succumb to cytopathic effects induced by HIV-1. The combined effect of viral toxicity in MDM and the highly replicative HFA might account for the wide ranges of MDM population and MDM infectivity observed in these cultures.

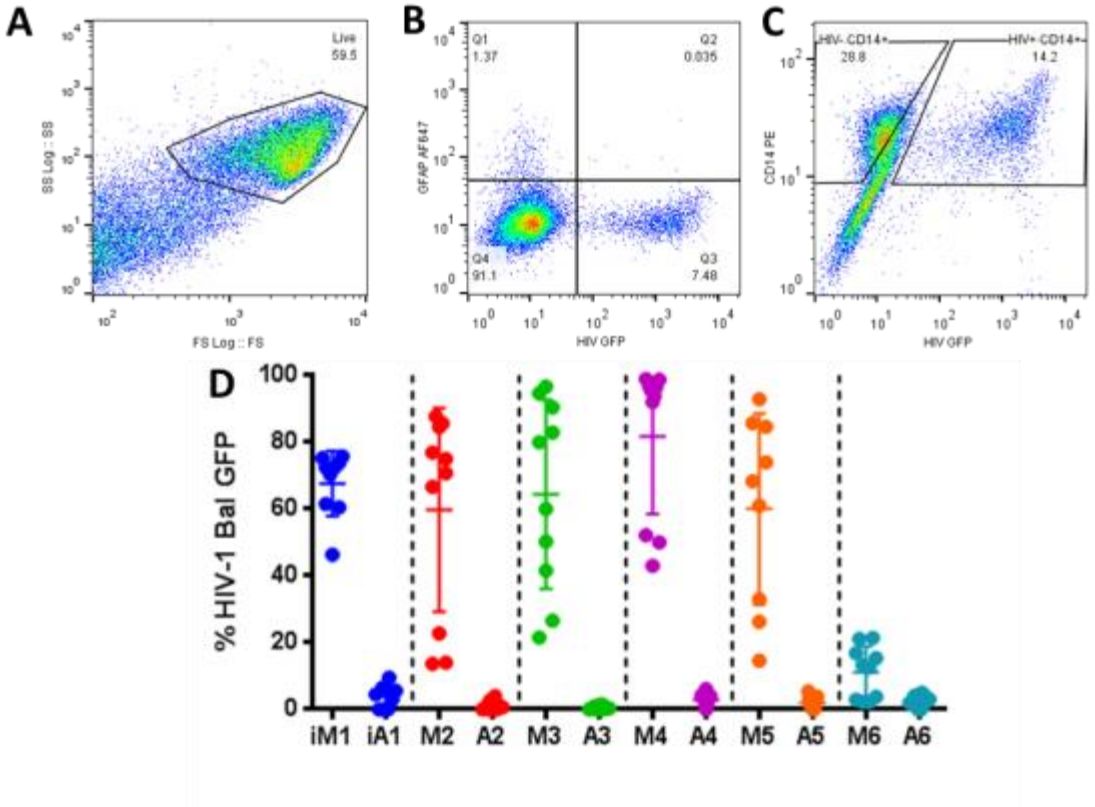


**Figure 4.10** HFA "A" adsorb HIV-1 viruses through contact with infected MDM "M". MDM from 5 donors (M2-M6), or 1 iPS-DM donor (iM1) were matured for 7 days and incubated with HIV-1 NLENG-Bal GFP for 7 days. HFA were added on top of the MDM for 8-10 days. Data was analyzed by flow cytometry. Gating was based on live cell (A) and isotype samples (B-C). Data from 3 experiments performed in triplicate with mean and ± 1 SD.

In all cultures, <1-3% of all cells were GFAP+ (1.37+0.035=1.41% for (Figure 4.10 B)); although by visual inspection using microscopy, >50% of the

cells in the co-culture were HFA based on morphology. Within the GFAP+ population, <1-9.5% were also HIV-1 GFP+ (0.035/1.41=0.02% for (Figure 4.10 B)). The percentages of GFAP+ cells were small because only activated HFA express GFAP. In addition, HFA are derived from fetal samples not mature tissues, thus, they express a high level of GFAP initially but significantly decrease GFAP expression over multiple divisions. Nevertheless, flow cytometry data show that although there was a high rate of infection or viral association in MDM detected by the positive expression of GFP signal in $CD14^+$ cells, there was a very low percentage of $GFAP^+$ astrocyte that expressed GFP (Figure 4.10 A-D). iPS-MDM yielded similar results to primary MDM. One MDM donor, M6, did not have very high percentage of HIV-1 GFP signal compared to the other donors reflecting expected donor variability in infectivity.

Because there were very few GFAP+ HIV-1 GFP+ cells, I wanted to visualize each of these cells and determine the location of the GFP signal. I repeated the experiment and applied ImageStream technology, which combines the power of fluorescence microscopy with flow cytometry, to visualize the HFA that contained HIV-1 GFP signal. More than 100,000 live cells were collected and gated based on the focus of the cell images measured by gradient RMS and then based on the aspect ratio versus area (Figure 4.11 A left 2 panels). Matching isotypes were used to determine positive and negative gates (Figure 4.11 A right 2 panels).

On average, approximately 19-20% of CD14+ cells and <3-6% of GFAP+ cells had HIV-1 GFP signal. ImageStream images of GFAP+ HIV-1 GFP+ cells show that HFA either formed conjugates with the infected MDM and the GFP signal mainly originated from the MDM itself (Figure 4.11 B middle panel) or HFA took up HIV-1 GFP debris (Figure 4.11 B-C bottom panels.) In the case of

HIV-1 infected iPS-MDM – HFA conjugates, the GFP signal appeared to transfer from the iPS – MDM to the astrocyte at the cell-cell contact zone (Figure 4.11 C middle panel). There was no evidence that HFA were infected with HIV-1, which would be indicated by the presence of GFP signal throughout the cells as in infected MDM (Figure 4.11 B-C top panels).

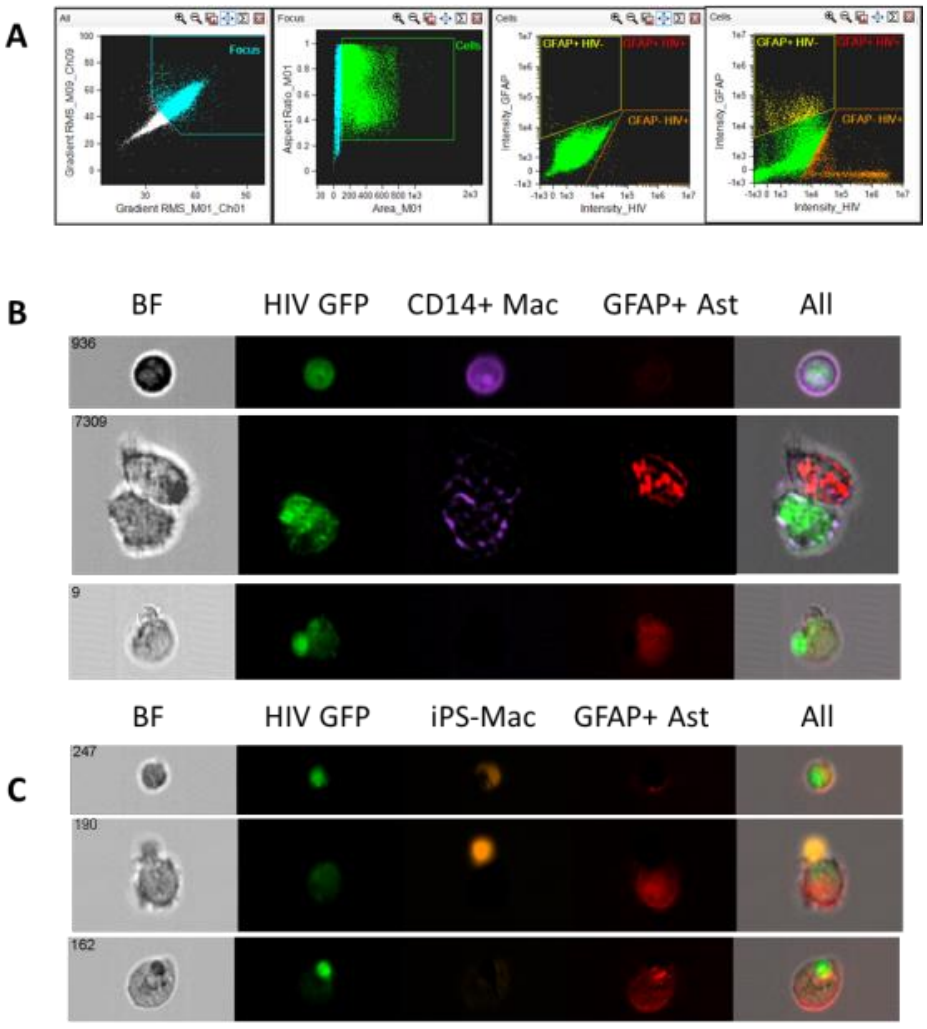


**Figure 4.11** HFA adsorb HIV-1 viruses through contact with infected MDM. MDM or iPS-MDM were matured for 7 days and incubated with HIV-1 NLENG-Bal GFP for 7 days. HFA were added on top of the MDM and co-cultured for 6 days. Data was collected by ImageStream. Gating was performed based on focus, aspect ratio vs. area, and isotype samples (A). Data from 2 experiments performed with 3-6 replicates. Representative images from MDM-HFA (B) and iPS-MDM-HFA cultures (C).

## 4.9 Future direction: microvesicles role in viral transfer?

In addition to transferring virions to astrocytes, HIV-1 infected MDM also released circular membrane vesicles into the extracellular milieu, termed

microvesicles (469). Fluorescence microscopy revealed many examples of HIV-1 NLENG-Bal GFP infected MDM that have fused together to form multi-nucleated cells. These giant multi-nucleated cells released microvesicles radially around the cell body (Figure 4.12 A-D). In some circumstances, the multi-nucleated cell polarized its cell body toward the HFA (Figure 4.12 E-F) after an overnight incubation. TEM images also captured high-resolution images of HIV-1 infected MDM releasing pockets of membrane vesicles toward a HFA and the same HFA harboring an endosomal compartment containing microvesicles near the surface of the cell (Figure 4.13).

Microvesicles can play an important role in mediating cell-cell communication (469–471). HIV-1 Nef proteins stimulate the secretion of microvesicles containing signaling proteins and Nef through the cell endosomal trafficking machinery; these microvesicles can be transferred from infected cells to uninfected cells (472, 473). Exosomes containing Nef have been reported to fuse with target cells, triggering activation–induced cell death through the apoptosis pathway in CD4+ T cells, and with virions, which can restore viral infectivity in Nef-deficient virions even after maturation (474, 475). Infected PBMC, platelets and megakaryocytes have been observed to transfer microvesicles containing co-receptors CCR5 and CXCR4 to co-receptor negative cells; target cells apparently “acquire” the required HIV-1 receptors and become susceptible to infection (84, 476). Exosomes can also contain apolipoprotein B mRNA editing enzyme, catalytic polypeptide-like 3G

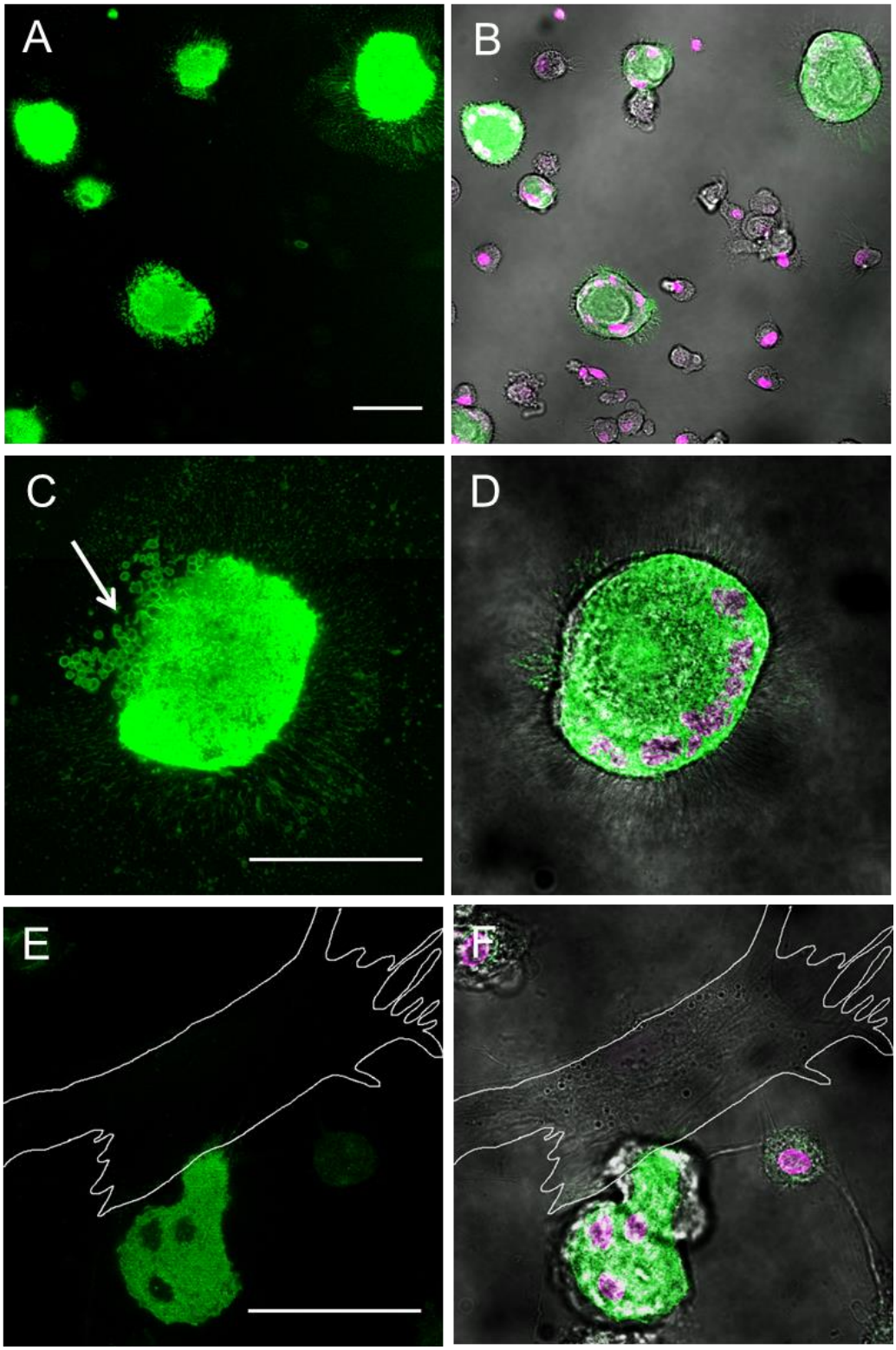


**Figure 4.12** MDM and multi-nucleated cells infected with HIV-1 produce microvesicles. Fluorescence images of HIV-1 GFP channel (green) (A, C, E) and overlays of HIV-1 GFP (green), DAPI (magenta), and phase contrast channels (B, D, F) reveal HIV-1 NLENG-Bal GFP infected MDM and multi-nucleated cells releasing micro-vesicles (arrow) into the supernatant. A cluster of HIV-1 infected MDM polarized toward an MDM (white outline) after an overnight incubation. Scale bars: 50 µm.

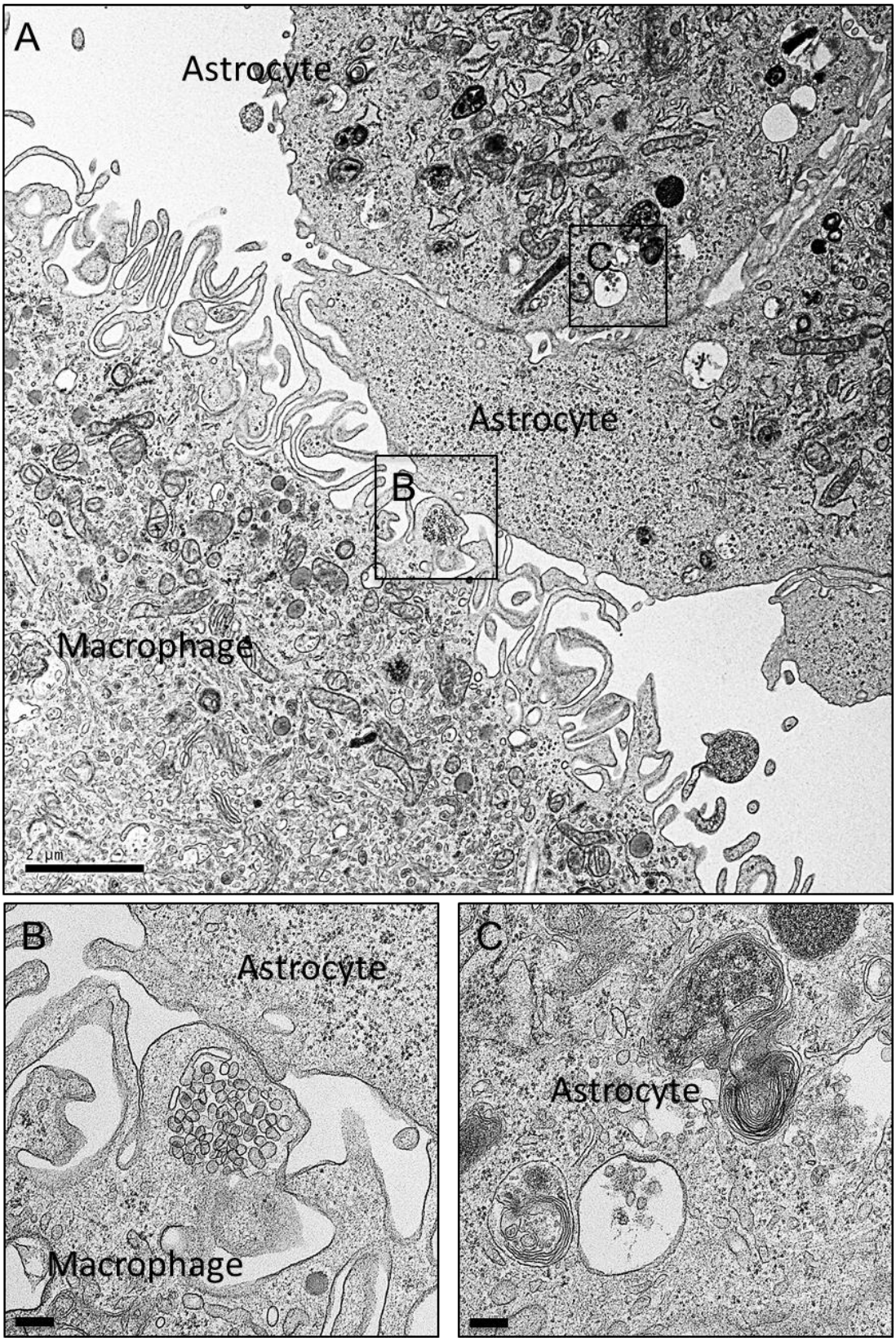


**Figure 4.13** TEM of HIV-1 infected MDM releasing microvesicles toward an HFA. MDM (A-B bottom left) were infected with HIV-1 NLENG-Bal GFP and co-cultured with HFA (A-B top right, C) overnight. Magnified images of panel (A) reveal a cluster of microvesicles budding from a MDM to an HFA(B) and a cluster of microvesicles inside an HFA endosome/lysosome (C). Panel A scale bar: 2 µm, B-C: 0.2 µm.

(APOBEC3G), that can reduce the accumulation of HIV-1 RT products and Gag and Vif proteins, which support innate anti-viral immunity (477). Taken together, these microvesicles may mediate the transfer of functional proteins, RNAs, microRNA, and mRNAs and intercellular communication signals (reviewed in (469, 471)) between MDM and HFA, which may help explain the association of these viral proteins with uninfected HFA, and could potentially enhance or suppress HIV-1 transfer from MDM to HFA and viral spread in the brain.

## 4.10 Discussion

### 4.10.1 Cell free HIV-1 interactions with HFA

Because astrocytes lack major HIV-1 receptors, current literature presents conflicting views on the mechanism of HIV-1 entry in astrocytes (284, 287, 326, 443). The data presented here show that HFA did not become productively infected with HIV-1 through a free mode. Despite the intimate physical connections between HIV-1 infected MDM and HFA, which exposed HFA to high local concentrations of virus, HFA did not appear to be productively infected through cell-cell contact. The absence of viral replication in astrocytes might be attributed to the inefficient translation of HIV-1 structural proteins (309, 478). HFA exposed to infectious virus or HIV-1 infected MDM showed no morphological changes commonly seen in other infected cells, such as syncytium formation (292–294, 479) or apoptosis (148, 191, 480–482), but may still respond to foreign antigens and intercellular signaling by undergoing reactive gliosis (267, 483–485).

The presence of viral products in astrocytes may be attributed to viral particles or virus-containing debris taken up through the endocytosis or phagocytosis pathways. Previous reports show that astrocytes phagocytose dead or dying cells and debris to protect neurons (323–325, 486, 487).

However, compared to MDM, astrocytes are highly inefficient at degrading the ingested materials (325). Through this mechanism, astrocytes could take up virions or fragments of virus infected cells and harbor them for a prolonged period of time, acting as viral reservoirs. Within this context, it is possible that virions and viral genomes can be detected within the astrocytes (246, 269, 271, 277, 439, 488) without the cells actually becoming infected themselves.

In addition, electrostatic interactions appear to play a major role in enabling viruses to adhere to the astrocyte cell membrane, particularly for the X4-tropic NL4.3 virus. The addition of competing negatively charged polymers or enzymes to remove cell surface membrane molecules prevented viral transfer. Previous reports have shown that this strategy is effective in preventing the transmission of human T-cell lymphotropic virus type 1 (HTLV-1) and herpes simplex virus in mammalian cells (489–491). The non-specific binding mechanism of HIV-1 to astrocytes, the most abundant cell types in the CNS, which are highly vulnerable to infiltrating virions and virus-bearing cells due to their proximity to the perivascular regions, may play an important role in promoting rapid pathogenesis.

### 4.10.2 Viral transfer from astrocytes to neighboring cells

My data suggest that virions associated with astrocytes are surface accessible; mature virions may reside on the surface, or inside surface-connected compartments (107, 110), or trapped in partially hidden spaces within the complex membrane network of astrocytes. The addition of proteases or bNabs subsequent to incubation of HFA with free HIV-1 interfered with the transfer of surface-bound virions to neighboring uninfected cells. The mechanism described here is reminiscent of *trans*-infection mechanism observed in the HIV-1 transmission from infected DC to uninfected CD4+ T

cells. In DC-mediated *trans*-infection, mature virions are captured at the mucosa on the surface membrane of DC and efficiently transferred to uninfected CD4+ T cells across IS (366, 374, 445, 446). Although prevalent model of HIV-1 *trans*-infection suggest that DC internalize intact virions and transfer them to target T cells, Greene et. al. (366) show that virion internalizations do occur but the virions involved in *trans*-infection are surface bound. Similarly, astrocytes may passively transfer surface bound virions to neighboring cells; this concept has been previously proposed in (305), which suggests that astrocytes harbor virions in CD81+ vesicles. This paper also stated that the surface-bound virions were resistant to trypsin treatment, a finding that is incongruent with my data. The difference could be because the cells are at a different activation state, the trypsin treatment used, TrypLE, was milder than 0.25% Trypsin, and data measurements was performed using FACS and microscopy, which can be less sensitive than the luciferase system.

### 4.10.3 Interactions between HIV-1 infected MDM and HFA

Uninfected astrocytes can adsorb viruses from the extracellular milieu or directly from another cell. Here, I observed MDM interacting actively with HFA, in many cases crawling on top of the target cells. Some HIV-1 infected MDM extended thin filopodia decorated with HIV-1 virions toward HFA. The virions appear to move back and forth along the filopodia in live cell imaging (Figure 4.6), similar to a mechanism described previously as viral “surfing” (98, 100–102, 492–494). Unlike other VS that features interdigitated membrane extensions from both host and target cells (99, 102, 495), the synapses between MDM-astrocyte features an open and smooth structure with the two cell membranes simply apposing each other.

In addition to transferring virions, HIV-1 infected MDM or giant multi-nucleated cells also dispersed microvesicles toward the HFA. The target HFA appears to harbor cytoplasmic compartments such as endosome that contain similar microvesicles. This suggests a mechanism by which MDM may transfer viral products or other molecules toward astrocytes, which can promote pathogenesis. This model may explain the presence of viral proteins and gene products inside astrocytes without leading to productive infection. Additionally, microvesicles can be used to facilitate intercellular communication, which can stimulate and sustain cellular activation and neuroinflammation (469–471). As HIV-1 host cells, MDM may not be able to productively infect astrocytes, however, their high motility, proclivity for cell-cell interactions, and efficient viral production enable them to transfer virions to astrocytes effectively.

### 4.10.4 Implications for CNS pathogenesis

Although exposures to HIV-1 virions or infected MDM do not lead to productive infection in astrocytes, this cell type is still an effective conduit to transmit HIV-1 through the CNS because 1) astrocytes exist in large numbers and proliferate quickly in respond to neurological insult, 2) astrocytic exposures to HIV-1 proteins and HIV-1 infected cells can disrupt cellular functions, leading to homeostatic imbalance in the CNS, and 3) astrocytes can take up mature virions on the surface membrane and harbor them in hidden reservoirs then subsequently transfer them to another cell without succumbing to cytopathic effects (303, 316, 496).

# 5. HIV-1 transmission from T cells to astrocytes

## 5.1. Introduction

As discussed in the previous chapter, HIV-1 spread in the brain parenchyma may occur through HIV-1 infected perivascular macrophages and microglia. Because the astrocyte endfeet surround blood vessels, these cells are also exposed to HIV-1 carrying T cells crossing the BBB. While the notion of “Trojan macrophages” as a possible mechanism for transport of HIV-1 to the CNS has been discussed extensively (171), infected T cells could also play this role, especially if the BBB is compromised by inflammation, particularly in the process of immune reconstitution (80, 497, 498). Since HIV-1-infected T cells can form VS with other cell types (120, 499), I hypothesize that infected T cells might form adhesive junctions with astrocytes, resulting in transfer of virus to the astrocytes. Investigating whether infected T cells form VS with astrocytes and characterizing the spatial organization of VS formed at T cell–astrocyte adhesive junctions is therefore of interest for understanding potential mechanisms of HIV-1 transfer in the brain.

To study the interactions of HIV-1-infected T cells with uninfected astrocytes, I applied FIB-SEM, which can capture the structure of the cell-cell contact zone in its entirety at nanometer resolution in 3D (99, 107, 378, 495, 500, 501). Here, I present a structural study of VS formed at the junction between HIV-infected CD4+ T cell lines, Jurkat and H9 cells, and primary HFA. I compare the similarities and differences between VS presented here and those formed by different cell types, as previously published. These insights extend the generality of my hypothesis (99, 102)that, in VS, membrane processes from both uninfected cells and infected cells or virus-bearing cells contribute actively

to facilitate virion transfer at cell-cell contact zones. The cell culture parts of this project was performed in collaboration with Dr. Guanhan Li at the NIH.

## 5.2. Astrocyte take up HIV-1 through contact with infected cells

To determine whether astrocytes can take up HIV-1 through contact with infected T cells, I co-cultured HFA with Jurkat-Tat-R5 acutely infected HIV-1 NLENG-Bal GFP. Jurkat-tat-R5 is human T cell line that has endogenous CXCR4 and CD4 expression, and is stably transfected with human CCR5; these cells can be infected with both X4 and R5-tropic viruses. Cells were stained with anti-CD3 antibody for T cells and anti-GFAP antibody for HFA and analyzed on day 2, 5, 7, 10, 13 post co-cultures (Figure 5.1 D). Gating was performed based on live cell and matching isotype samples (Figure 5.1 A-C). Data analysis shows that over time, the percentage of CD3+ T cells and GFAP+ HFA associated with HIV-1 GFP increased at a similar rate from 0 to ~12-20% (Figure 5.1 D). The similar kinetic suggests that infected Jurkat-tat-R5 may mediate HIV-1 transfer to HFA.

I repeated the same experiment by co-culturing HFA with Jurkat-tat-R5 acutely infected with HIV-1 NLENG-Bal GFP and HIV-1 NL4.3-GFP for 11 days to compare the viral tropism. I also applied ImageStream technology, which combines the power of fluorescence microscopy with flow cytometry, to visualize the HFA that contained HIV-1 GFP signal (as in Figure 4.11). When I compared the ratio of infected Jurkat-tat-R5 to HFA associated with HIV-1 GFP, I noticed that the ratio of Bal-GFP co-culture was significantly higher than that of NL4.3-GFP co-culture (Figure 5.1 E), which suggests that HFA can take up virions or virion-containing debris from Jurkats infected with X4-tropic viruses more efficiently than Jurkats infected with R5-tropic viruses. For this reason, I used

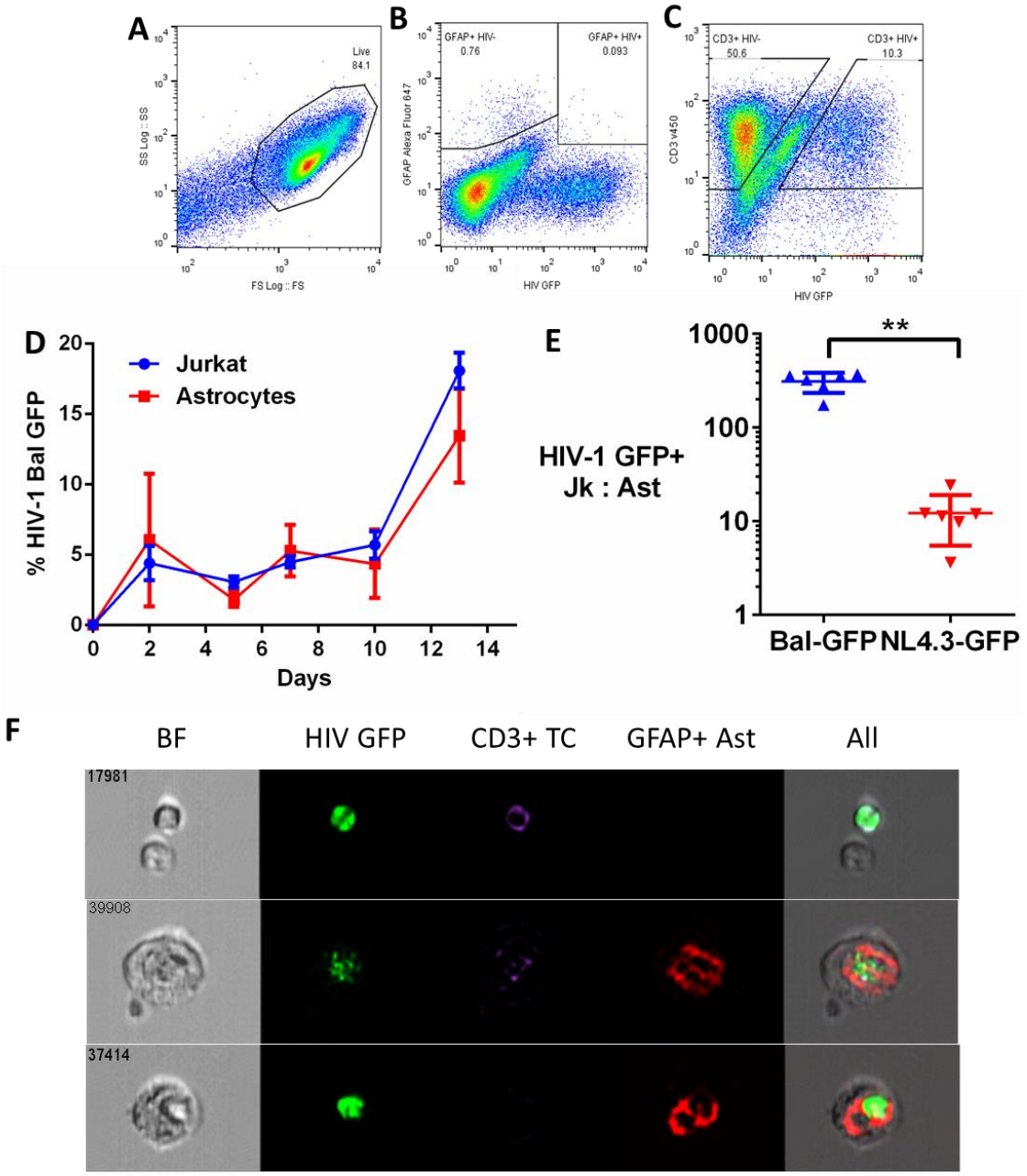


**Figure 5.1** Flow cytometry analysis of HFA co-cultured with Jurkat-tat-R5 acutely infected with HIV-1 NLENG-Bal GFP. The samples were stained with anti-CD3 v450 antibody and anti-GFAP Alexa Fluor 647 and analyzed on day 2, 5, 7, 10, 13 post co-culture (D). Gating was based on live cell (A) and isotype samples (B-C). Data from 2 experiments performed in 6 replicates with mean ± 1 SD. HFA were co-cultured with Jurkat-tat-R5 acutely infected with HIV-1 NLENG-Bal GFP or NL4.3-GFP for 11 days and analyzed by ImageStream (E). Data from 2 experiments performed in 3 replicates with mean ± 1 SD. Gating was performed the same way as (Figure 4.11 A). Representative images from HIV-1 NLENG-Bal GFP (bottom) or NL4.3-GFP (top two images) infected Jurkat-tat-R5-HFA.

CXCR4-tropic viruses for the rest of my experiments. ImageStream reveals HFA associated with HIV-1 GFP signal typically contain 1) both punctate CD3 and HIV-1 GFP signals, suggesting HFA took up infected Jurkat debris, or 2) clusters of bright GFP signal, suggesting HFA took up viral particles but not necessarily became infected themselves. These types of interactions are analogous to those that I observed in macrophages from (Figure 4.11). I conclude that HFA exposed to infected T cells take up virions or virion-containing debris.

## 5.3. T cells interact actively with astrocytes

To analyze the interactions between T cells and astrocytes, I cultured primary HFA with another T cell line, H9 cells, uninfected or chronically infected with X4-tropic HIV-1 IIIB. I chose H9 cells instead of Jurkat-tat-R5 as before because I could obtain them from the NIH AIDS Reagent Program as uninfected or chronically infected cells; the infection rate of chronically infected cells may be higher than acutely infected cells and can confer an advantage for imaging rare events like viral transfer. HFA were cultured overnight on an imaging dish. The next day, HFA and uninfected or infected H9 cells were separately labeled with membrane dye: carboxyfluorescein succinimidyl ester (CFSE) (green) for astrocytes and Vybrant DiI (red/magenta) for H9 cells. H9 cells were added to the HFA and live cell imaging began immediately.

Within the first few minutes, H9 cells moved freely around the culture. Many H9 cells subsequently settled onto HFA after 10 minutes and remained associated with the HFA for more than 3 hours after initial contact, suggesting a potential mechanism that tethered the two cells together (Figure 5.2 A-B). Some H9 cells moved above and below the astrocyte membrane surface in the first 20 minutes, causing extrusion of HFA membrane around the H9 cells and the

appearance of depressions in the HFA surface (Figure 5.2 C-F). Subsequently, infected H9 cells remained above the HFA membrane for more than 3 hours. H9 cells that adhered to the HFA extended large membrane sheets along the astrocyte surface and rotated them radially for more than 3 hours, appearing to sample the surface of the HFA membrane (Figure 5.2 G-H). Some H9 cells moved side to side along the length of the astrocyte.

Unlike uninfected H9 cells, infected H9 cells often formed syncytia. When these syncytia burst, debris was released into the surrounding environment, much of which became associated with astrocyte membranes through passive fluid diffusion (Figure 5.2 I-J). Over 3 hours, the HFA membrane was observed to express both the original membrane dye (green) and the H9 cell membrane dye (magenta).

Together, these observations suggest that uninfected and infected H9 cells actively interact with HFA, appearing to probe the surface of the cell. The complex astrocytic membrane protrusions may play a role in tethering the H9 cells to the HFA membrane. If an infected H9 cell undergoes apoptosis or necrosis, the cell may release cellular fragments and viral products in the extracellular milieu. Neighboring HFA could trap these now free virions or virion-containing cell debris onto the membrane surface, potentially leading to viral transfer.

## 5.4. Astrocyte change shape after contact with HIV-1 infected T cells

As a response to brain injury, astrocytes often undergo astrogliosis, a process that induces rapid cellular proliferation, hypertrophy, and increased expression of GFAP (268, 502). GFAP supports the structure and movement of

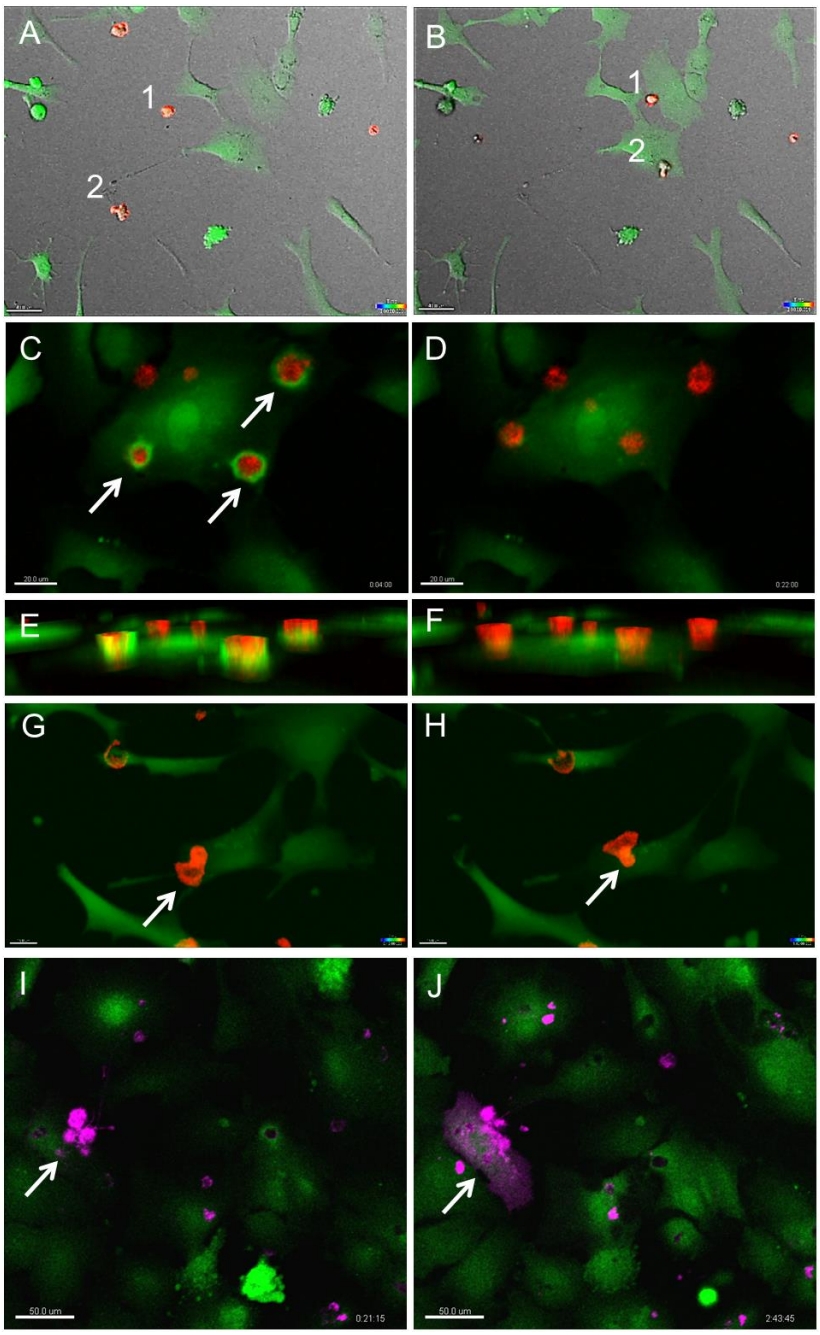


**Figure 5.2** H9 cells interact with HFA. (A-J) Selected images from 24 movies. (A-B) Overlay of phase contrast and fluorescence images reveal H9 cells, labeled with DiI (red, white arrows) that have migrated toward HFA, labeled with CSFE (green) in 10 minutes and remained attached for >3 hours. Fluorescence images reveal (C-F) H9 cells (red, white arrows) moved below (C-E) and above (D-F) the HFA (green) for 20 minutes and remained above the membrane surface for >3 hours; (C, D) top view, (E, F) side view. (G-H) An H9 cell (red, white arrows) attached to an HFA (green) actively spreads membrane sheets radially for >3 hours. (I-J) H9 cells chronically infected with HIV-1 IIIb (magenta, white arrows) released cell debris on the surface of the astrocyte membrane (green), causing astrocytic uptake of the H9 cell magenta membrane dye. Panel A-B, I-J scale bars: 50 µm, C-H: 20 µm.

astrocytic processes. Here, I assessed the morphological changes that occurred in cultured primary HFA upon contact with H9 cells chronically infected with HIV-1 IIIb or acutely infected with the HIV-1 NL4-3-based reporter virus NLENG1 (Figure 5.3). Cultured HFA displayed compact polygonal shapes when cultured on their own (Figure 5.3 A), with uninfected H9 cells (Figure 5.3 D), or with cell free virus (Figure 5.3 B-C). However, when exposed to infected H9 cells (Figure 5.3 E-F), HFA showed dramatic changes in cellular morphology, with a clear increase in the prevalence of membrane extensions. While the presence of HIV-1 has been shown to stimulate the expression of GFAP, a well-known astrocytic response to pathogens, including HIV-1 (265, 266, 268), it is the presence of infected H9 cells that is required for morphological changes (Figure 5.3 E-F versus B-C) and the presence of membrane extensions.

The membrane extensions formed in the co-culture of astrocytes and HIV-1 IIIb-infected H9 cells can measure more than 478 microns in length, which is longer than 14 times its cell body (Figure 5.3 I). These membrane extensions were branched, radiating outward from the cell body (Figure 5.3 J-K). SIM microscopy demonstrated that within each membrane extension, intermediate filaments twisted into a bundle (Figure 5.3 L) that could provide structural support to filopodial extensions (266).

To obtain a quantitative estimate of the extent of these morphological alterations, I quantified the area of GFAP expression per HFA (Figure 5.3 G-H) using automated tools for 2D image segmentation (outlined in Figure 5.4). Co-culture with uninfected H9 cells did not alter the overall area covered by GFAP in HFA, as compared to GFAP protein distribution in HFA cultured alone.

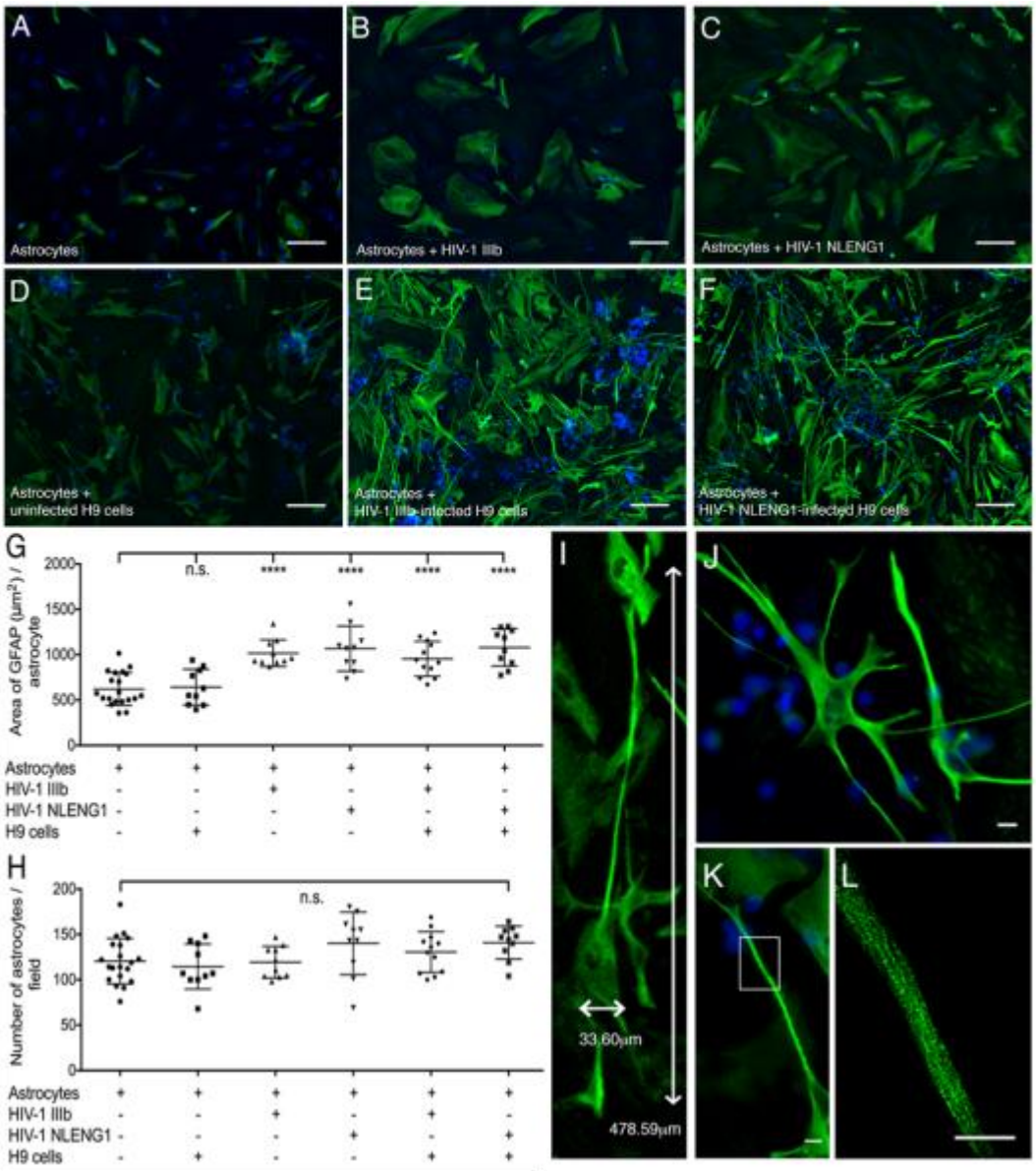


**Figure 5.3** HFA extend membrane protrusions in the presence of HIV-1 infected T cell lines. (A-F) Fluorescence microscopy images of (A) primary human fetal astrocytes cultured (A) alone or with (B) HIV-1 IIIb, (C) NLENG1, (D) uninfected H9 cells, (E) HIV-1 IIIb chronically infected H9 cells, and (F) NLENG1 acutely infected H9 cells for 24 hours. Intermediate filaments were labeled with GFAP (green); nuclei were labeled with DAPI (blue). (G-H) Quantitative analysis of cells in >10 images cultured under each (A-F) conditions. (G) The average area of GFAP expression per HFA and (H) the average number of HFA per field of view. (I-K) HFA cultured as in (E) have long, branched membrane protrusion with thin cell bodies. Structured illumination microscopy image (L) of white box in (K) revealed twisting intermediate filament bundles in HFA membrane extension. Panels A-F scale bars: 50 µm, J-L: 10 µm.

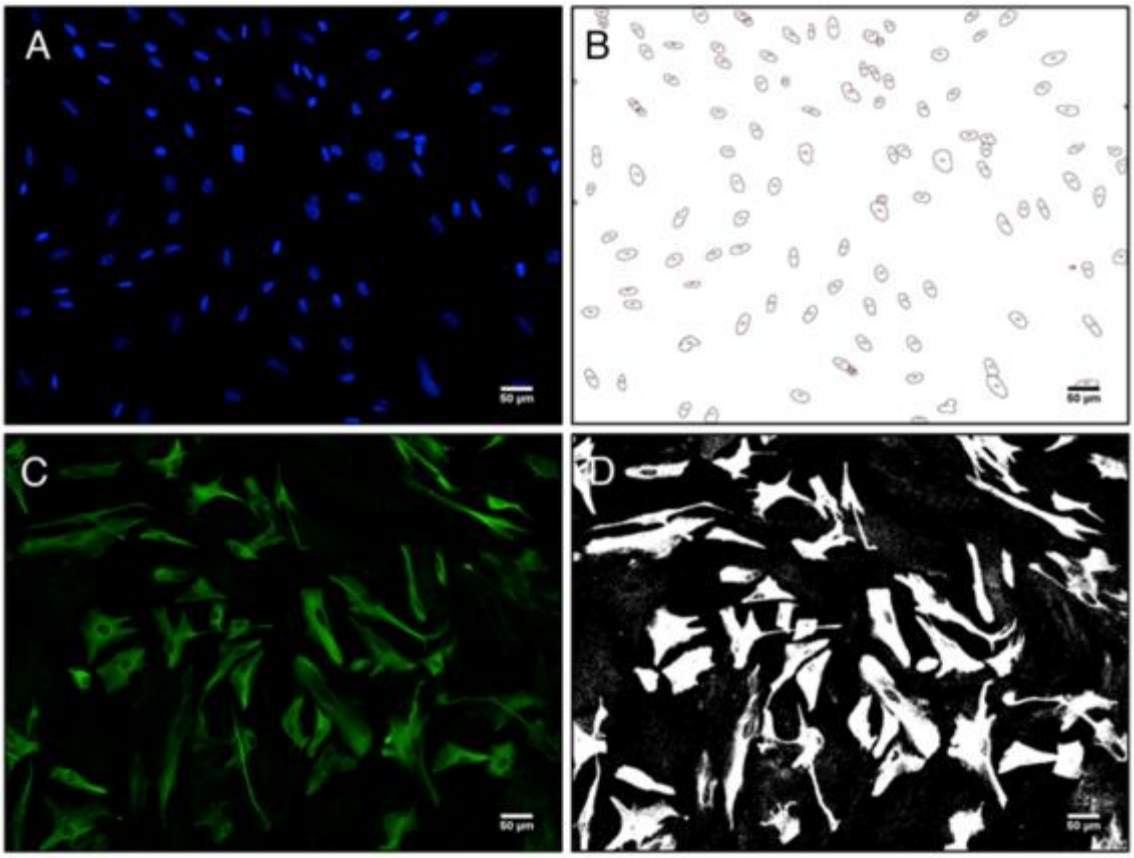


**Figure 5.4** Automated image analyses reveal the number of cells and area of GFAP expression per human fetal astrocyte, as applied in Figure 5.3 (G-H). (A) Fluorescence image of HFA nuclei labeled with DAPI (blue); (B) application of a binary mask based on the pixel intensity profile identified discrete cells from image (A). (C) Fluorescence image of astrocyte labeled with GFAP antibody (green); (D) application of a binary mask based on the pixel intensity profile defined the area of GFAP expression from image (C)

However, co-culture with HIV-1-infected H9 cells or free HIV-1 resulted in a measurable increase in the area of GFAP distribution, suggesting that the presence of HIV-1 mediated an increase in GFAP expression. These results show that the presence of HIV-1-infected T cells induced significant increases in both membrane extensions and GFAP expression on primary HFA, which are two physiological hallmarks of reactive astrogliosis (266, 485, 502).

## 5.5. Architecture of the T cell-astrocyte synapse

To explore the potential connection between the formation of membrane extensions and HIV-1 transmission, I investigated the structures using correlative FIB-SEM of contact zones between HIV-1 IIIb-infected H9 cells and

HFA co-cultured overnight (102, 378). Since HFA can be very large, it was important to use methods that could ensure that the FIB-SEM imaging was directed specifically to regions of cell-cell contact. I used light microscopy (Figure 5.5 A) and low-dose topographical SEM (Figure 5.5 B) to identify cell-cell contact zones, taking advantage of the striking morphological differences between the elongated HFA and the spherical HIV-1 IIIb infected H9 cells. Once the cells and the contact regions were identified, I carried out targeted FIB-SEM imaging to obtain 3D reconstructions of the HFA–H9 cell synapse.

Individual block face SEM images through the contact zone show cell boundaries, organelle distribution, and the presence of budding and mature HIV-1 particles in the region between the two cells (Figure 5.6 A-C). Reconstruction (Figure 5.6 D) and visualization of the 2D image stack as a 3D volume (Figure 5.7) shows that the contact zone between infected H9 cells and HFA is different both from the membrane interdigitation observed in DC T cells VS (99, 495) and from the membrane spreading observed in T cells VS (102). Instead, the central feature of the astrocyte–H9 cell contact zone is a set of filopodial extensions emanating from the HFA (Figure 5.7 A). These protrusions extended directly towards the HIV-infected H9 cell and were surrounded with HIV-1 particles. The presence of the filopodial extensions covered with HIV-1 virions suggests the mechanism of virus “surfing” described previously (100, 492–494), in which extension of these long filopodia contributes to infection by enabling the virions to cross the void between neighboring cells. Transparent visualization of synapse structure reveals the localization of virions at the cell-cell contact zone (Figure 5.7 B). The architecture of the VS between the HIV-infected H9 cells and HFA supports the hypothesis that, in this system, morphological changes in uninfected HFA influence the distribution of viruses at

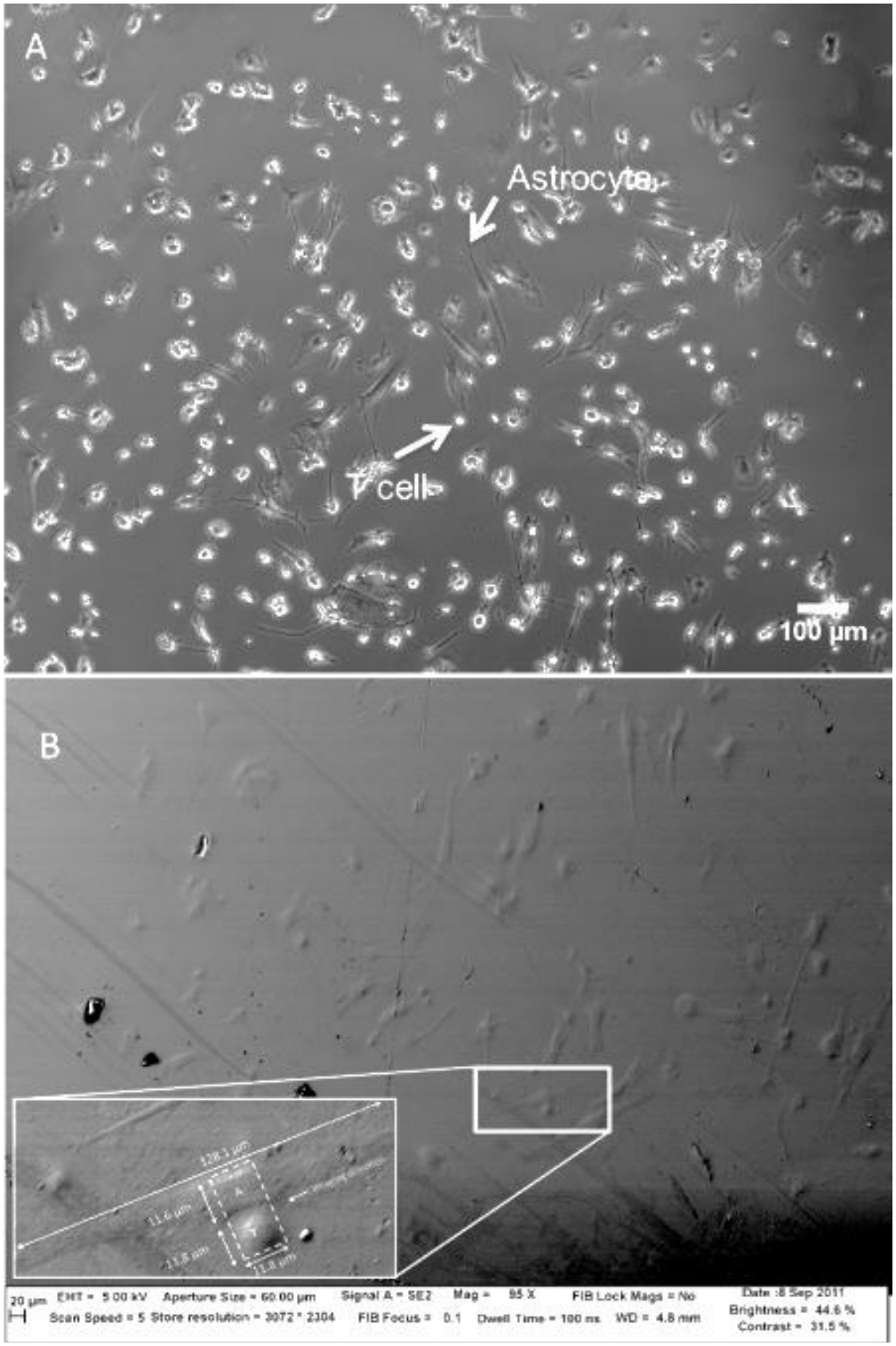


**Figure 5.5** HFA and H9 cells can be readily distinguished based on morphological differences. (A) Phase contrast image of HFA (elongated) co-cultured with HIV-1 IIIb-infected H9 cells (spherical) for 24 hours. Scale bar: 100 µm. (B) Topographical SEM image of a resin-embedded block of HFA co-cultured with HIV-1 IIIb-infected H9 cells. An HFA-H9 cell conjugate is highlighted in white box. (Inset) Higher magnification shows the nuclei of two adjacent cells. One cell is ~ 10X longer than the other (128.1 µm versus 11.8 µm), suggesting an HFA “A” and H9 cell “T” conjugate. FIB-SEM imaging was performed on the area denoted by the dotted white box in the direction of the white arrow. Scale bar: 20 µm.

the contact zones, and may facilitate infection by allowing virions to localize at the cell-cell junction.

To further explore the variety of VS that can occur between HFA and HIV-1 infected H9 cells, I imaged several additional variants of the filopodial-rich VS shown in Figure 5.7. In some instances, the filopodia appear to be very thick, essentially forming a large branch emanating from the central body of the HFA (Figure 5.8 A-D). In others, thin HFA membrane extensions form VS containing concentrated HIV-1 clusters at the contact zone between the HFA and infected H9 cell were observed (Figure 5.8 E-F). Visualization of the entire contact zone in 3D illustrates that what may appear as a pair of non-interacting cells in a 2D image (Figure 5.8 C) is instead a slice through an extensive cell-cell contact region (Figure 5.8 D). Further, in instances where single slices show cells that are far apart, collections of filopodial extensions emanating from different regions of the astrocyte are observed, all appearing to direct towards virions emerging from the infected T cell membrane (Figure 5.8 E-F).

To extend these findings, I also explored the structures of the VS between HFA and another T cell line, Jurkat cells acutely infected with HIV-1 NLENG1-GFP. I co-cultured the cells overnight in a gridded imaging dish and imaged them in fluorescence microscopy (Figure 5.9 A) to locate infected Jurkat-HFA conjugates. I applied correlative FIB-SEM imaging to locate the same cell pairs. In 3D FIB-SEM, I observed the HFA extending a filopodium inside a Jurkat cell which contained multiple vesicles with budding and mature virions (Figure 5.9 B). In another conjugate, with 2D FIB-SEM images, I observed polarization of the HFA nucleus and cellular membrane toward the Jurkat cell where the two cells were contacting (Figure 5.9 D, I). However, within the same pair of cells, in areas where the two cells were not in contact,

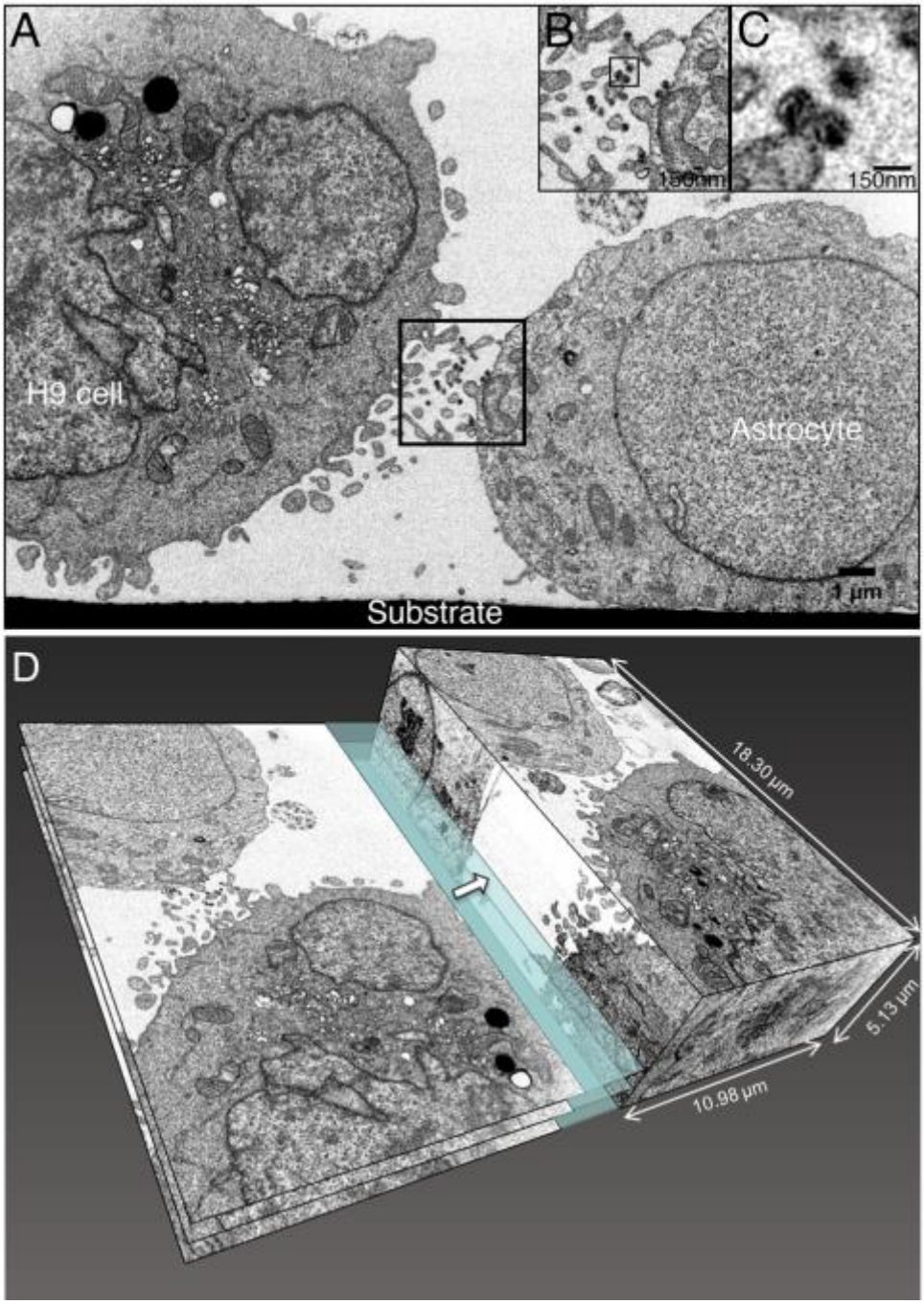


**Figure 5.6** H9 cells transfer virions to HFA via interdigitated membrane protrusions originated from both cells. (A) 2D FIBSEM image of a HIV-1 IIIb chronically infected H9 cell (left) and an uninfected HFA (right), co-cultured overnight. The HFA adhered to the substrate while the H9 cell remains suspended in the culture medium. Scale bar: 1 µm. (B) In the synaptic region (A, black box), H9 cell and HFA extended thin filopodia across the synapse with virions trapped at the junction. (C) Three virions (B, black box) have dark, conical-shaped densities in the center, indicative of mature viral capsids. Inset scale bars: 150 nm. (D) The stack of 2D FIB-SEM images were reconstructed into a 3D volume with dimension of 18 x 5 x 10 $\mu m^3$.

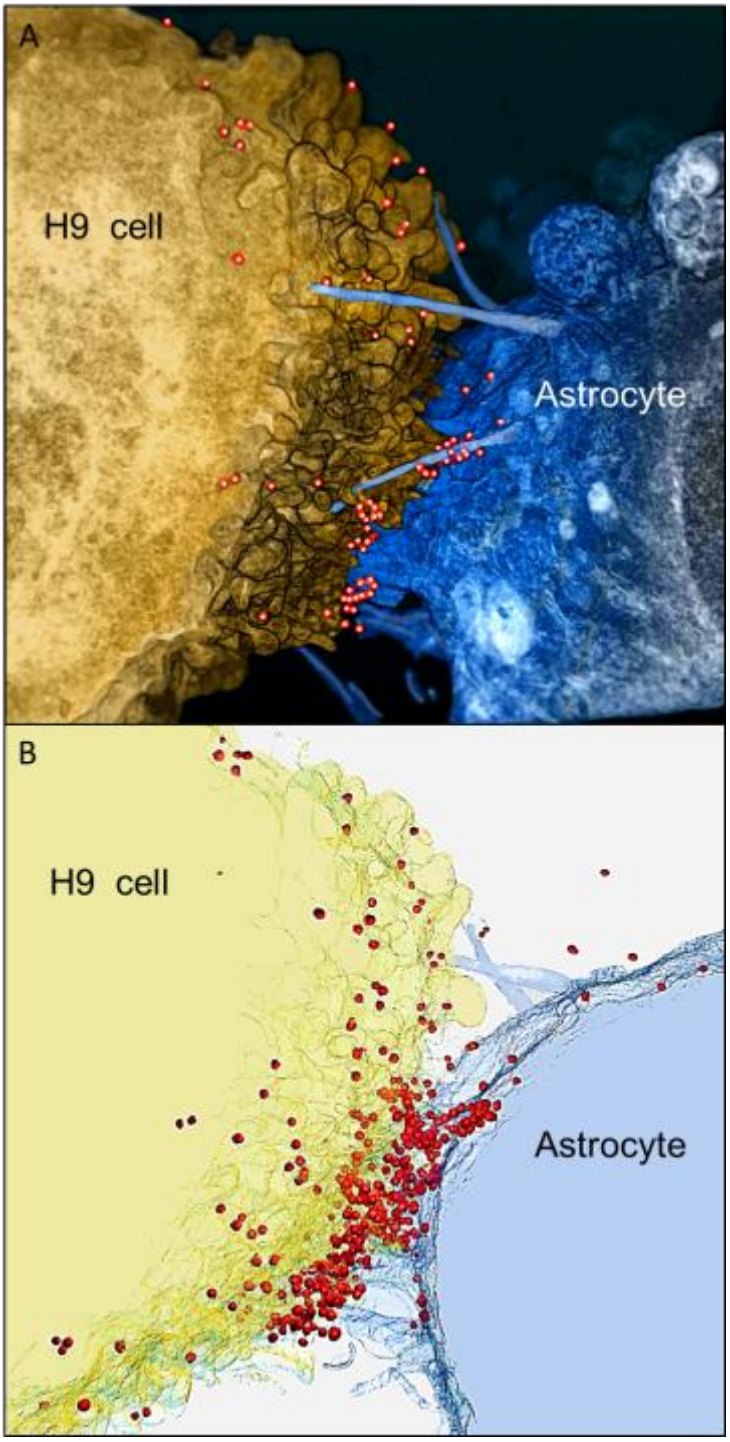


**Figure 5.7** HIV virions localize along membrane extensions within the H9 cell-astrocyte VS. (A) 3D rendering of the FIBSEM image stack containing the contact zone between the HIV-1 IIIb (red) infected H9 cell (gold) and HFA (blue). The target cell has extended long filopodial bridges (center) toward the infected cell across the intercellular gap. HIV-1 virions were observed adjacent to the filopodial bridges. (B) Semi-transparent visualization of the H9 cell and HFA revealed the dense accumulation of HIV-1 at the cell-cell contact zone.

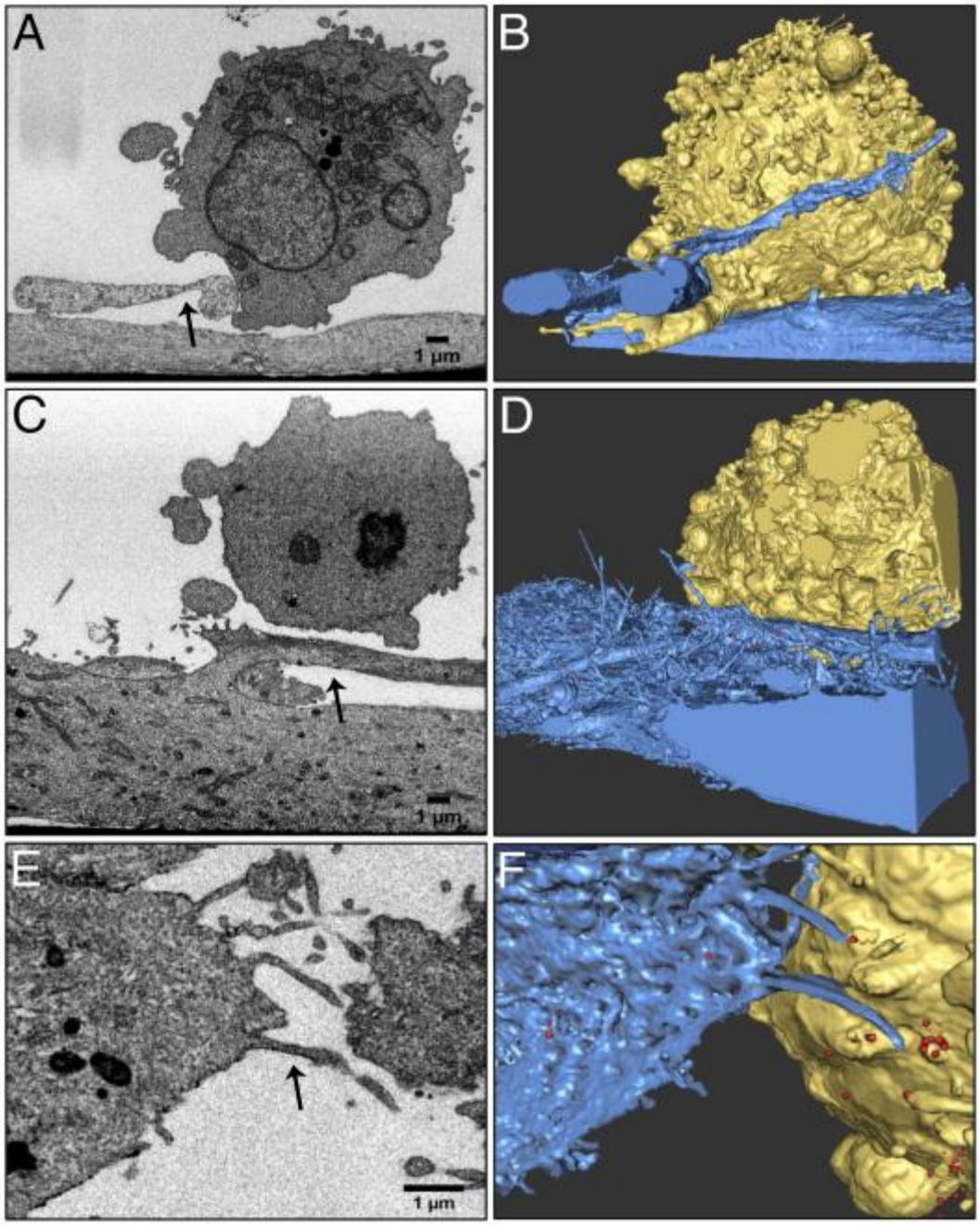


**Figure 5.8** Structural variations in membrane contact at the HFA–H9 cell VS. (A, C, E) 2D FIB-SEM images and (B, D, F) 3D semi-automatic, segmented reconstructions of HIV-1 IIIb (red) infected H9 cells (gold) and HFA (blue) co-cultured overnight. Scale bars: 1 µm. (A, B) An HFA has extended a thick membrane protrusion (arrow) toward the HIV-infected H9 cell, forming an extensive contact zone with a H9 cell filopodium. (C, D) A thick HFA membrane protrusion (arrow) has closed the intracellular gap between the HFA and the HIV-1 infected H9 cell. HIV-1 virions were found concentrated in the elbow and along the length of the thick astrocytic protrusion. (E, F) A cluster of HFA filopodia (arrow) extended towards a group of HIV-1 virions located on the H9 cell membrane.

the nucleus remained flat (Figure 5.9 C). Magnified regions of the cell-cell contact revealed vesicles inside Jurkat cells with budding and mature virions (Figure 5.9 E). In an area with a mature virion between the Jurkat-HFA contact zone, I observed multiple open and closed vesicles on the surface of the HFA (Figure 5.9 F). Filopodia with a budding virus at the tip were observed extended from the Jurkat cell towards the HFA (Figure 5.9 G). In some instances, the Jurkat cell inserted a filopodia inside the HFA (Figure 5.9 H, I inset). These observations suggest that astrocytes play a role in facilitating their own infection by extending processes toward HIV-1 infected T cells.

## 5.6. Astrocytes internalize virions in vesicles

Since HIV-1 bind to HFA (Figure 5.1, 5.6-5.8), I investigated whether these attached virions might be internalized into the cells via a membrane fusion or endocytic mechanism. In principle, the viruses could enter by fusion at the plasma membrane. Alternatively, they could be internalized first then remain inactive or fuse into an internal membrane. Analysis of the architecture of various cell-cell contact zones provides evidence for the latter mechanism, with the FIB-SEM data providing 3D snapshots of viruses before (Figure 5.10 A-B), in the process of (Figure 5.10 C-D) and following internalization in an astrocyte membrane cluster (Figure 5.10 E-F). Since FIB-SEM imaging generated 3D structures of the virion-containing compartments in their entirety, it is clear that the compartments are vesicles that are completely bounded by an intracellular membrane, and are not merely surface connected invaginations of the plasma membrane that trap HIV-1 virions, as seen in macrophages (106, 110). FIB-

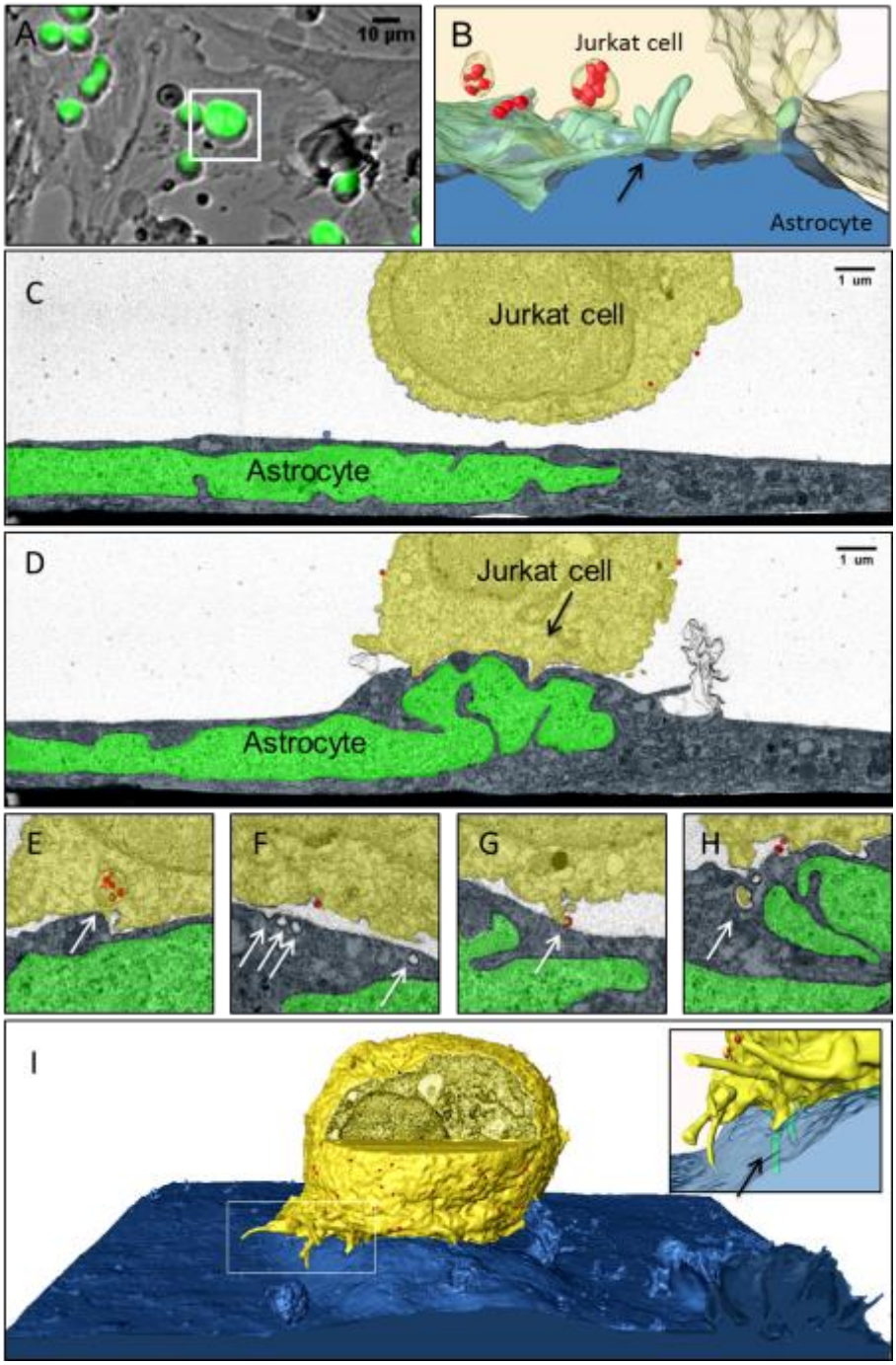


**Figure 5.9** HFA polarized to NLENG1-GFP-infected Jurkat cells in an overnight co-culture. (A) Overlay of brightfield and fluorescence microscopy image of infected Jurkat (green) and HFA. (B) A 3D FIB-SEM image reveals an HFA (blue) that inserted a filopodia (arrow) inside a virion (red) containing Jurkat cell (gold). (C-D) 2D FIB-SEM images of HFA membrane (blue) and nucleus (green) interacting with infected Jurkat cells taken at different z-planes. (E-H) Magnified images of the contact region revealed (E) virions-containing vesicle inside Jurkat cell, (F) vesicles at the HFA membrane surface near a virion, (G) a budding virion on a Jurkat filopodial tip, and (H) Jurkat filopodia inserting inside the HFA membrane. (I) 3D visualization confirmed astrocytic membrane polarization and Jurkat cell filopodia insertion into astrocyte membrane (inset). Scale bars: 1 µm.

SEM also captured an example of a dying HFA containing HIV-1 associated vesicle with extensive membrane blebs; death might be induced by cytopathic effects associated with viral contact (Figure 5.10 G-H).

## 5.7. Discussion

Determining the 3D architecture of VS and virus distribution at this specialized zone of cell-cell contact is central to understanding the mechanisms of cell-to-cell spread of HIV-1. VS, as originally defined by Sattentau (95), and as structurally defined by a number of 3D structural analyses including my present work, are cytoskeleton-dependent, stable adhesive junctions across which virus is transmitted by directed transfer (93, 94, 96–99, 101, 120, 495, 503, 504). The concentration of viruses at the synapse enables more effective infection of permissive target cell. The complex VS structure shields the virions, at least partially, from the immune system (237, 238). In earlier studies of VS formed at the junction between HIV-1-pulsed DCs and uninfected CD4+ T cells, membrane extensions from both cell types are involved at the zone of cell-cell contact (99, 495).

Biochemical experiments have shown that, at least in the case of immature DCs, these membrane extensions are induced following engagement of DC-SIGN by Env proteins in a cascade involving Src kinases, Cdc42, Pak1 and Wasp (495). In synapses formed by mature DCs, large sheet-like membrane extensions encase the T cell near the sites of cell-cell contact, enabling close access of the shorter filopodial extensions from the T cell to virion-rich channels near the surface of the DC (Figure 5.11 A). Interestingly, despite the general similarities in the nature of the membrane extensions observed on immature and mature DCs, the envelopment of the T cell seen with mature DCs is not observed with immature DCs (Figure 5.11 B). Nevertheless,

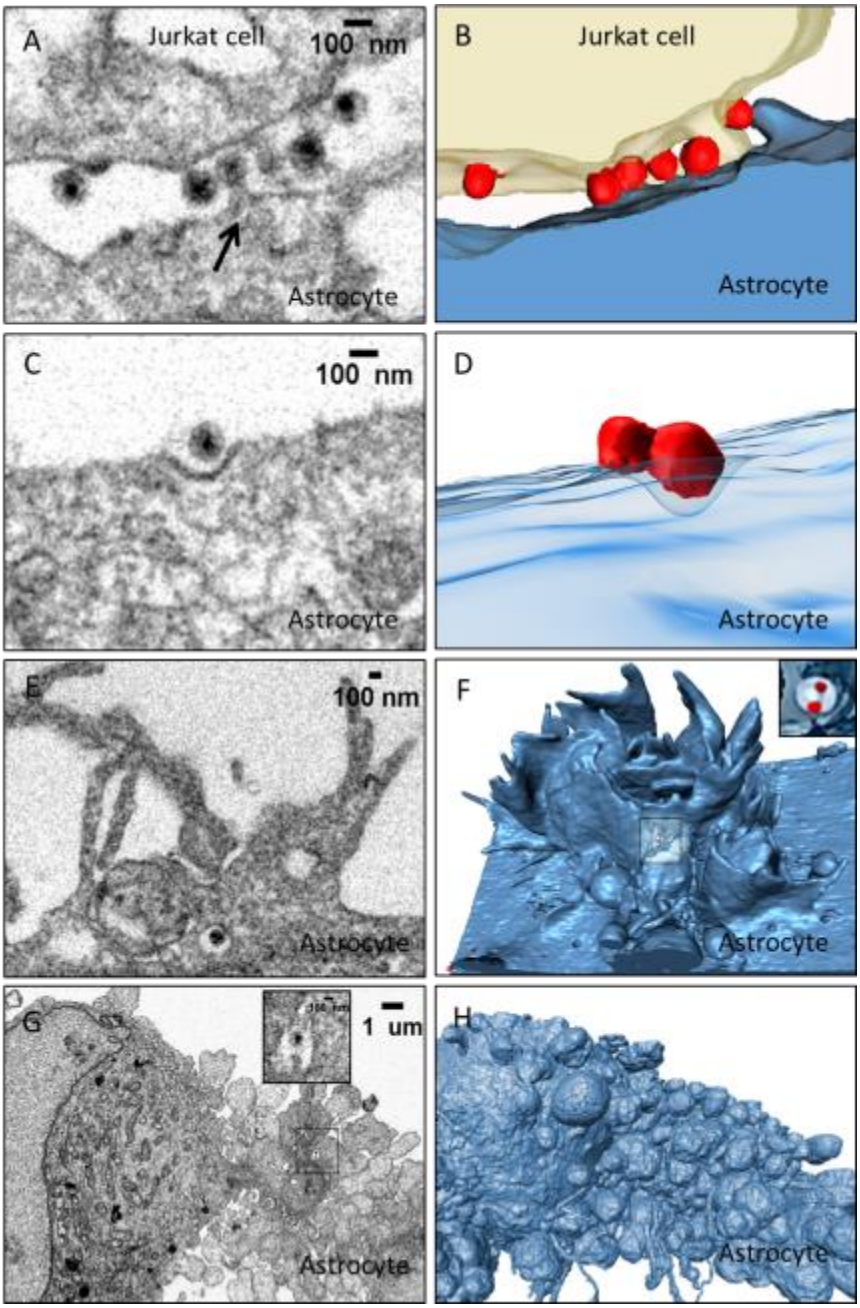


**Figure 5.10** Internalization of HIV-1 by HFA. HFA (blue) were co-cultured with Jurkat cells (gold) infected with NLENG1-GFP viruses (red) overnight. (A, C, E, G) 2D FIB-SEM images and (B, D, F, H) 3D colored visualizations of cell-cell contact zones. (A-B) Budding and mature HIV-1 virions are localized at the synaptic region between Jurkat cells and HFA. Dark densities indicative of HIV-1 virion cores are observed. One virion (arrow) appears to be attached to an astrocytic membrane protrusion. Both Jurkat cells and astrocytes have extended small filopodia toward each other. (C-D) Two HIV-1 virions resided directly above an invaginated region outlined by a dark density along the HFA cell membrane, indicative of an open clathrin coated vesicle. (E-F) Two HIV-1 virions were encapsulated at the center of a network of astrocytic membrane sheets that project upward, creating an intricate cabbage-like structure that effectively harbored HIV-1 virions in the crevices. (G-H) One HIV-1 virion was observed at the center of an HFA that was undergoing apoptosis.

in VS formed by both immature and mature DCs, virus delivery appears to also involve membrane extensions from the uninfected cell. These different formations are likely a reflection of the normal cellular contacts formed by these types of cells, but still represent important features for HIV-1 cell-to-cell transmission at these synapses.

Unlike in contacts formed with DCs, infected and uninfected primary CD4+ T cells extensively wrapped membrane around neighboring cells, with HIV-1 virions found clustered at the periphery of the contact zone (505). In other cases, T cell-T cell VS involves actin-dependent recruitment of HIV-1 receptor and adhesion molecules and polarization of virions at the synaptic cleft (96). These structures are semi-permeable and, thus, sensitive to entry inhibitors (120). Occasionally, long membrane extensions, some more than 30 µm in length, were also observed connecting T cells together (101, 102). Live imaging of HIV-1 VS in T cells has indicated that virions can transfer either along filopodia ("virus surfing") (98, 101) or directly across a synapse (505, 506). Given the snapshot nature of this study, however, it is not clear whether the membrane extensions revealed are formed by the same mechanism as those noted previously. Nevertheless, as reported for other VS (98, 101), the long-distance membrane contacts observed may likewise enable the transfer of HIV-1 to uninfected cells by virus surfing.

At the synapses formed between astrocytes and infected Tcells, extensions from both cells form a filopodial network at the cell-cell contact zone (Figure 5.11 D). The extended membrane projections from the astrocytes were extended directly at the infected H9 cell, providing a conduit for HIV-1 to "surf" along the projections towards the uninfected cell. This network is reminiscent of the filopodial bridges observed in the rat XC sarcoma cell line model system,

which are stabilized by the presence of target cell receptor molecules at the tip of the membrane extension and Env proteins on the infected cell surface (98, 492), and which facilitate viral transfer via an actin-dependent process. Nevertheless, the structure of the astrocyte membrane extensions, with high levels of GFAP, a protein restricted primarily to astrocytes, is likely specific to this cell type; suggesting that while the general presence of membrane extensions is shared among many cell types, there are unique characteristics of these interactions that are cell-type specific.

These observations suggest that the type of interaction between infected and uninfected cells is particular to the cell types involved in the synapse; thus, spatial architecture of zones of cell-to-cell transmission may vary significantly between different types of VS. The membrane extensions from APCs, T cells, and astrocytes could be formed from close but “not-yet-touching” cells to close the gap (98), or could be “sticky” trailing pseudopodia left from previously touching cells that are beginning to move apart (101, 499). Nevertheless, the similarities between the various VS shown here and elsewhere (99, 102, 495) suggest that the common element of membrane projections may provide a useful route for exploring therapeutics aimed at blocking cell-to-cell transfer by disrupting the extension and/or stabilization of membrane protrusions. A schematic summary of the four different types of VS architectures observed by EM is presented in (Figure 5.11); this is not an exhaustive list of VS reported but simply represents a variety of VS to illustrate the diversity in physical structures.

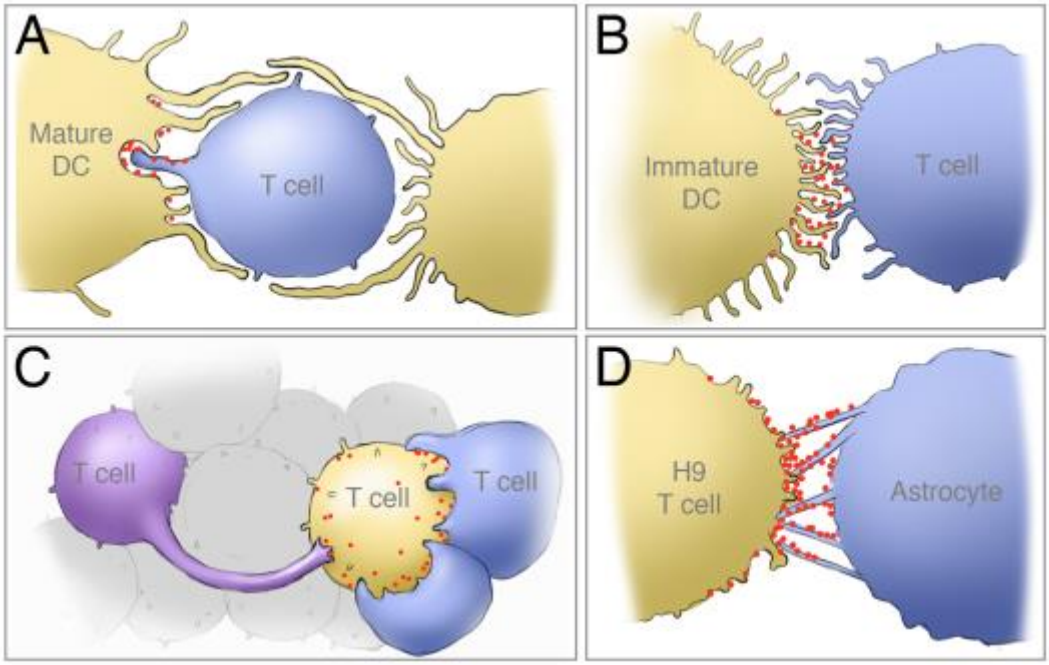


**Figure 5.11** Schematic illustration of the membrane architectures of four distinct types of cell-cell contact at HIV-1 VS determined by 3D electron microscopy. This is not an exhaustive list of VS, but a representative sample to show the diversity of VS structures. (A) Encasement of the target cell by mature dendritic cells (DC) and interaction of filopodia from the target T cell with viral reservoirs in DCs (99). (B) Network of filopodial extensions at the cell-cell contact zone that enable virus transfer from the surface of immature DCs to uninfected CD4+ T cells (495). (C) Rearrangement and shape change of an uninfected CD4+ T cell enabling extensive membrane contact with HIV-1 infected T cell (102). (D). Membrane bridges extend from HFA at regions of contact with HIV-1 infected T cells, providing a mechanism for viruses to “surf” from the infected cell to the astrocyte (102).

While light and EM studies have begun to provide insights into some of the structural themes associated with HIV-1 transfer at VS (96, 99, 102, 495, 503, 504, 507), the molecular mechanisms leading to their formation are poorly understood. The observation of membrane extensions from the uninfected cells suggests that there may be a signal that is sensed by the uninfected cell, such as a chemical messenger or perhaps even monomeric gp120 that diffuses and initiates signaling by binding to co-receptors on target cells, as has previously been suggested (482). Indeed, it has been shown that human papillomavirus type 31 virus can stimulate viral uptake and cytoskeleton-dependent retrograde

transport along filopodia (493), although this has not been directly observed in the HIV-1 VS.

There is little doubt that cytoskeletal remodeling must be an essential component of the changes in cellular morphology at the synapse. Thus, actin polymerization inhibitors, such as cytochalasin D that disrupts HIV-1 localization at synapses formed by mature DCs (99), dramatically reduces the number of membrane protrusions, and decreases HIV-1 transfer at IS formed with immature DCs (495). Similarly, in T cell synapses, inhibitors of active remodeling, such as Cytochalasin D, latrunculin-A and jasplakinolide, interfered with receptor recruitment or conjugate formation that facilitated viral transfer across VS (96).

HIV-1-induced membrane extensions in astrocytes appear to involve increases in expression of intermediate filaments. It seems plausible that the structural features unique to the different types of VS are merely variations on the cellular repertoire of physiologically relevant membrane rearrangements necessary for cell-cell communication, but subverted by HIV-1 to achieve infection of target cells. A better understanding of the chemical mechanisms involved in VS formation may thus provide valuable insights not only into strategies for preventing the spread of HIV/AIDS but also into some of the general principles involved in cell-cell communication.

# 6 Discussion

## 6.1 Correlative FIB-SEM

Powerful new imaging technologies are available, enabling us to answer fundamental biological questions in the context of health and disease. In this thesis, I describe the optimization of a developing, new technology known as correlative FIB-SEM, which combines the power of live cell and immunofluorescence imaging with the high resolution imaging offered by EM. I applied this technology to study muscle cell differentiation mechanism using qualitative characterization and semi-automatic image processing to generate unbiased quantitative descriptions.

The strength of this technology lies in the ability to derive both genetic and structural information on whole cell and sub-cellular features. Many studies focus on genetic analysis; in some cases, microscopy is applied but at low resolution that provides ambiguous or limited information. Incorporating super-resolution microscopy, such as STED or SIM, and correlative FIB-SEM technology into the current biological toolset will enable researchers to interpret mechanistic functions from both chemical and structural perspectives. This technology can be used to characterize cellular states: differentiated vs. undifferentiated in stem cell studies or normal vs. abnormal state in cancer, infectious diseases, and aging studies. The multi-level quantitative metrics provide rapid and unbiased interpretations of the data.

### 6.1.1 Challenges and future opportunities

The main challenges of this new technology are the time it takes to acquire a 3D structure (a single whole cell imaged takes 3 days in FIB-SEM vs. 3 minutes in optical microscopy) and the instability of the FIB-SEM software and hardware systems. To image the samples, the specimens have to be fixed and

stained with heavy metals, which may introduce artifacts, such as enlargement or reduction of physical features and metal precipitate depositions that can be misinterpreted for cellular features. Fixation and staining protocols usually need to be optimized for each sample type. These challenges can be overcome by a new technique termed cryo-FIB-SEM, which enables fast 3D imaging of large native frozen samples (508). New electron detector, such as FEI direct electron detector that enables high resolution images of biological materials, may provide an opportunity to image cellular processes at higher resolution while preserving biological structures by limiting the electron dose necessary to generate high contrast images (509).

The complex interplay between the electron beam, ion beam, platinum and carbon gas deposition system, vacuum system, etc. requires every component to be well aligned and work in sync at all time. I expect that soon the software will be fully developed and as a result, the hardware system will also stabilize. Imaging time will significantly speed up to a cell a day. Image processing tools will be refined, enabling automatic quantitative structure analysis. This technology can be applied to characterize tissues and whole cells as well as their subcellular structures in the laboratories for research and in the hospital for diagnosis. Because many diseases can be characterized by both genetic and structural abnormalities, correlative FIB-SEM can allow the user to visualize cellular structures in minute details.

## 6.2 HIV-1 transfer from macrophages and T cells to astrocytes

I applied correlative FIB-SEM and a wide variety of virological and imaging techniques to answer questions about HIV-1 transmission in the brain. *In vivo,* macrophages and CD4+ T cells are the principal cells that efficiently produce virus and contribute to disease progression in the brain (435). The

migratory nature of these cells enables them to transfer infectious particles to naïve bystander cells. Their transmigration across the BBB and presence in the brain parenchyma may lead to viral transfer to the most populous resident glia cell, astrocytes.

Although previous reports, when taken together, suggest that astrocytes become infected with HIV-1 but in a non-productive manner, my data suggest that astrocytes do not become infected. Virions bind to the surface of the cells partly through electrostatic interactions and can be neutralized with protease or bNabs. Some virions are found inside vesicles, but these are likely to be surface accessible based on my inhibitor studies. Astrocytes are phagocytic and endocytic and may engulf virions or viral-containing debris from dead/dying cells and the extracellular environment, although the mechanism of uptake is not well-defined at the moment. Because astrocytes are inefficient at degrading ingested materials (325), the viral products may reside inside or on the cell surface for extended periods. In astrocyte-CD4+ T cell contacts, virions appear to “surf” along the filopodial membrane formed by the target cell, migrating across the void from the infected CD4+ T cell to the astrocyte. Both cells form complex filopodial interdigitations that trap virions inside the crevices of the network. In contrast, in astrocyte-macrophage contact, both cell plasma membranes are closely apposed to each other. Virions associated with astrocytes can be transferred to another cell using a *trans*-infection mechanism, leading to productive infection. Together, my data agree with published observations of astrocytes containing viral products (viral DNA, RNA, viral proteins, virions, etc.), harboring virions and later transferring them to other cells. However, the evidence from my experiments suggests that astrocytes are unlikely to be directly infected.

The strengths of these studies lie in the high resolution optical and EM imaging techniques applied to visualize cell-cell interactions combined with functional assays to measure viral infectivity, which provide high throughput quantitative data for robust statistical analysis. Approaching biological questions with multiple techniques reveals the multi-faceted nature of interactions between astrocytes and infected cells and provide insight into HIV-1 spread in the brain.

### 6.2.1 Challenges and future opportunities

The main challenge with conducting research on primary brain cells is sample availability. I attempted to acquire astrocytes from the brain tissues of epileptic patients after a surgical procedure but these cells are fragile and can only survive *ex vivo* for 1 week. There are a variety of immortalized astrocytic cell lines available; however, for this thesis I used primary HFA to mimic as closely as possible the *in vivo* situation. Unlike mature astrocytes, HFA are primary cells derived from second trimester fetal tissues, thus they are highly proliferative and their GFAP expression decrease at later passages. The differences between fetal and terminally differentiated mature astrocytes might influence the behavior of the cells.

Because HFA sources are limited, I could not obtain autologous HFA and MDM and T cells for these experiments to avoid potential heterologous donor reactions. In other experiments tried to address the limitations of brain macrophage source by using iPS cells. Using published protocols from the Oxford Stem Cell lab, I derived MDM from iPS cells (347). Although genetically similar to primary MDM, iPS-MDM have different morphology; it is not clear how this difference might affect HIV-1 permissivity but caution must be taken when interpreting experimental data conducted on iPS-derived cells as a model for *in*

*vivo* processes. However, iPS cells may become a renewable cell source for research, especially for cells located in inaccessible tissues, such as the human brain. The Oxford Stem Cell lab is also developing a protocol to generate astrocytes from iPS cells. I expect that within a few years, it will be possible to obtain autologous MDM, T cells, and astrocytes from a single donor using iPS cells.

My data show that HIV-1 binds to astrocytes at least in part by via electrostatic interactions that can be blocked by adding negatively charged competing polyanion molecules, such as PRO 2000. Previous studies have shown that PRO 2000-containing microbicide gels are not effective in preventing HIV-1 sexual transmission (367, 368); however, this compound might be effective in blocking HIV-1 attachment to astrocytes. For future studies, I would test PRO 2000 and other negatively charged molecules, like dextran sulfate (489) to determine if they can block HIV-1 binding to astrocytes. The combination of antiretroviral drugs (444) and polyanions might effectively eliminate persistent viral presence in astrocytes, although in practical terms the use of polyanions in the brain may well have major safety issues. In future studies I would like to try to define the cell surface molecules implicated in HIV-1 attachment to the astrocyte surface.

Both astrocytes and macrophages are highly heterogeneous in structure and function. Tissue-specific differences may influence HIV-1 permissivity and transmission across cell-cell contacts. Future studies that include a wider variety of astrocytes and CNS-specific perivascular macrophages may provide more insight into the mechanism of viral transmission. Along with perivascular macrophages, microglia are major targets of HIV-1 in the brain (271, 273, 510). I attempted to study viral transfer from microglia to astrocytes but primary

microglia can only survive in culture for 1 week and they are morphologically and phenotypically similar to macrophages, making it difficult to definitively distinguish the two cell types (254, 255, 261). Microglial cell availability from brain tissue is limited but this problem may also be resolved with iPS stem cell technology.

Due to time constraints, I only attempted to inhibit macrophage-astrocyte interactions leading to infection. It would be instructive to also test the inhibitors on T cell-astrocyte interactions as well. In particular, because the T cell-astrocyte synapse appears to mediate viral transfer across the filopodial bridge, I would test agents that interfere with cytoskeleton structure, such as jasplakinolide, cytochalasin, to block synaptic formation and viral migration (96, 440, 494).

Most experiments presented here were conducted in 2D cell monolayer but actual cell-cell interactions occur in 3D environments. Future experiments can be conducted in 3D cell culture system, *ex vivo* tissues, or *in vivo* animal models to more closely mimic cellular interactions in the human body. I tried to address this problem by obtaining discarded brain tissues after surgical operations but these tissues are fragile and degrade quickly within a few days. With optimized growth conditions, it will be possible to conduct experiments and image cellular behavior in high resolution optical and EM microscopy. Imaging brain tissues in correlative FIB-SEM will provide a wealth of information on the architecture of the cell-cell contact region. The complexity of the system will be multiplied many fold changing from 2D to 3D analysis, especially due to the extensive astrocytic contact with neighboring cells (one astrocyte can contact tens of thousands of synapses) (263). New technologies will need to be developed to address these future challenges.

## 6.3 Conclusion

My work here provides novel insight into HIV-1 spread in the brain. Although I challenge the prevailing model that astrocytes become infected with HIV-1, I also provide an alternative model that is consistent with the published findings: astrocytes take up virions and transfer them through *trans*-infection mechanisms. I also present a variety of imaging and biological techniques to address fundamental questions about HIV-1 spread in the brain. Many more experiments are needed to understand how to reduce or eradicate viral reservoirs in the human body. My hope is that future research will enhance the quality of life for HIV-1 infected patients and prevent HIV-1 associated neurodegeneration.

# References


1. **Fauci AS**. 2011. AIDS: let science inform policy. Science **333**:13.

2. **Kalish ML, Wolfe ND, Ndongmo CB, McNicholl J, Robbins KE, Aidoo M, Fonjungo PN, Alemnji G, Zeh C, Djoko CF, Mpoudi-Ngole E, Burke DS, Folks TM**. 2005. Central African hunters exposed to simian immunodeficiency virus. Emerg. Infect. Dis. **11**:1928–1930.

3. **Marx PA, Alcabes PG, Drucker E**. 2001. Serial human passage of simian immunodeficiency virus by unsterile injections and the emergence of epidemic human immunodeficiency virus in Africa. Philos. Trans. R. Soc. Lond. B. Biol. Sci. **356**:911–920.

4. **Marlink R, Kanki P, Thior I, Travers K, Eisen G, Siby T, Traore I, Hsieh CC, Dia MC, Gueye EH**. 1994. Reduced rate of disease development after HIV-2 infection as compared to HIV-1. Science **265**:1587–1590.

5. **Donnelly C, Leisenring W, Kanki P, Awerbuch T, Sandberg S**. 1993. Comparison of transmission rates of HIV-1 and HIV-2 in a cohort of prostitutes in Senegal. Bull. Math. Biol. **55**:731–743.

6. **Kanki PJ, Travers KU, Mboup S, Hsieh CC, Marlink RG, Gueye-Ndiaye A, Siby T, Thior I, Hernandez-Avila M, Sankalé JL, Ndoye I, Essex ME**. 1994. Slower heterosexual spread of HIV-2 than HIV-1. Lancet **343**:943–946.

7. **Clavel F, Mansinho K, Chamaret S, Guetard D, Favier V, Nina J, Santos-Ferreira MO, Champalimaud JL, Montagnier L**. 1987. Human immunodeficiency virus type 2 infection associated with AIDS in West Africa. N. Engl. J. Med. **316**:1180–1185.

8. **Campbell-Yesufu OT, Gandhi RT**. 2011. Update on human immunodeficiency virus (HIV)-2 infection. Clin. Infect. Dis. **52**:780–787.

9. **Aichelburg A, Pett S, Cooper D**. 2002. AIDS: Understanding HIV Transmission. eLS.

10. **Zhu T, Korber BT, Nahmias AJ, Hooper E, Sharp PM, Ho DD**. 1998. An African HIV-1 sequence from 1959 and implications for the origin of the epidemic. Nature **391**:594–597.

11. **Masur H, Michelis MA, Greene JB, Onorato I, Stouwe RA, Holzman RS, Wormser G, Brettman L, Lange M, Murray HW, Cunningham-Rundles S**. 1981. An outbreak of community-acquired Pneumocystis carinii pneumonia: initial manifestation of cellular immune dysfunction. N. Engl. J. Med. **305**:1431–1438.

12. **Fauci AS**. 2008. 25 years of HIV. Nature **453**:289–90.

13. **Barre-Sinoussi F, Chermann JC, Rey F, Nugeyre MT, Chamaret S, Gruest J, Dauguet C, Axler-Blin C, Vezinet-Brun F, Rouzioux C, Rozenbaum W, Montagnier L**. 1983. Isolation of a T-lymphotropic retrovirus from a patient at risk for acquired immune deficiency syndrome (AIDS). Science (80-. ). **220**:868–871.

14. **Gallo RC, Sarin PS, Gelmann EP, Robert-Guroff M, Richardson E, Kalyanaraman VS, Mann D, Sidhu GD, Stahl RE, Zolla-Pazner S, Leibowitch J, Popovic M**. 1983. Isolation of human T-cell leukemia virus in acquired immune deficiency syndrome (AIDS). Science **220**:865–867.

15. **Briggs JAG, Wilk T, Welker R, Kräusslich H-GG, Fuller SD**. 2003. Structural organization of authentic, mature HIV-1 virions and cores. EMBO J. **22**:1707–15.

16. **Kwong PD, Wyatt R, Robinson J, Sweet RW, Sodroski J, Hendrickson WA**. 1998. Structure of an HIV gp120 envelope glycoprotein in complex with the CD4 receptor and a neutralizing human antibody. Nature **393**:648–59.

17. **Arhel N**. 2010. Revisiting HIV-1 uncoating. Retrovirology **7**:96.

18. **Engelman A, Cherepanov P**. 2012. The structural biology of HIV-1: mechanistic and therapeutic insights. Nat. Rev. Microbiol. **10**:279–90.

19. **Freed EO**. 2001. HIV-1 replication. Somat. Cell Mol. Genet. **26**:13–33.

20. **Sierra S, Kupfer B, Kaiser R**. 2005. Basics of the virology of HIV-1 and its replication. J. Clin. Virol.

21. **Wilen CB, Tilton JC, Doms RW**. 2012. HIV: Cell binding and entry. Cold Spring Harb. Perspect. Med. **2**.

22. **Sougrat R, Bartesaghi A, Lifson JD, Bennett AE, Bess JW, Zabransky DJ, Subramaniam S**. 2007. Electron tomography of the contact between T cells and SIV/HIV-1: Implications for viral entry. PLoS Pathog. **3**:0571–0581.

23. **Chojnacki J, Staudt T, Glass B, Bingen P, Engelhardt J, Anders M, Schneider J, Muller B, Hell SW, Krausslich H-G**. 2012. Maturation-Dependent HIV-1 Surface Protein Redistribution Revealed by Fluorescence Nanoscopy. Science (80-. ).

24. **Zhu P, Chertova E, Bess J, Lifson JD, Arthur LO, Liu J, Taylor KA, Roux KH**. 2003. Electron tomography analysis of envelope glycoprotein trimers on HIV and simian immunodeficiency virus virions. Proc. Natl. Acad. Sci. U. S. A. **100**:15812–15817.

25. **Freed EO, Martin MA**. 1996. Domains of the human immunodeficiency virus type 1 matrix and gp41 cytoplasmic tail required for envelope incorporation into virions. J. Virol. **70**:341–351.

26. **Cosson P**. 1996. Direct interaction between the envelope and matrix proteins of HIV-1. EMBO J. **15**:5783–5788.

27. **Murakami T, Freed EO**. 2000. The long cytoplasmic tail of gp41 is required in a cell type-dependent manner for HIV-1 envelope glycoprotein incorporation into virions. Proc. Natl. Acad. Sci. **97**:343–348.

28. **Dalgleish AG, Beverley PC, Clapham PR, Crawford DH, Greaves MF, Weiss RA**. The CD4 (T4) antigen is an essential component of the receptor for the AIDS retrovirus. Nature **312**:763–7.

29. **Clapham PR, Weber JN, Whitby D, McIntosh K, Dalgleish AG, Maddon PJ, Deen KC, Sweet RW, Weiss RA**. 1989. Soluble CD4 blocks the infectivity of diverse strains of HIV and SIV for T cells and monocytes but not for brain and muscle cells. Nature **337**:368–70.

30. **Feng Y, Broder CC, Kennedy PE, Berger EA**. 1996. HIV-1 entry cofactor: functional cDNA cloning of a seven-transmembrane, G protein-coupled receptor. Science **272**:872–7.

31. **Dragic T, Litwin V, Allaway GP, Martin SR, Huang Y, Nagashima KA, Cayanan C, Maddon PJ, Koup RA, Moore JP, Paxton WA**. 1996. HIV-1 entry into CD4+ cells is mediated by the chemokine receptor CC-CKR-5. Nature **381**:667–673.

32. **Deng H, Liu R, Ellmeier W, Choe S, Unutmaz D, Burkhart M, Di Marzio P, Marmon S, Sutton RE, Hill CM, Davis CB, Peiper SC, Schall TJ, Littman DR, Landau NR**. 1996. Identification of a major co-receptor for primary isolates of HIV-1. Nature **381**:661–666.

33. **Ugolini S, Mondor I, Sattentau QJ**. 1999. HIV-1 attachment: Another look. Trends Microbiol.

34. **Saphire AC, Bobardt MD, Zhang Z, David G, Gallay PA**. 2001. Syndecans serve as attachment receptors for human immunodeficiency virus type 1 on macrophages. J. Virol. **75**:9187–9200.

35. **Mondor I, Ugolini S, Sattentau QJ**. 1998. Human immunodeficiency virus type 1 attachment to HeLa CD4 cells is CD4 independent and gp120 dependent and requires cell surface heparans. J. Virol. **72**:3623–3634.

36. **Jolly C, Mitar I, Sattentau QJ**. 2007. Adhesion molecule interactions facilitate human immunodeficiency virus type 1-induced virological synapse formation between T cells. J. Virol. **81**:13916–13921.

37. **Carreno M-P, Chomont N, Kazatchkine MD, Irinopoulou T, Krief C, Mohamed A-S, Andreoletti L, Matta M, Belec L**. 2002. Binding of LFA-1 (CD11a) to intercellular adhesion molecule 3 (ICAM-3; CD50) and ICAM-2 (CD102) triggers transmigration of human immunodeficiency virus type 1-infected monocytes through mucosal epithelial cells. J. Virol. **76**:32–40.

38. **Ballana E, Pauls E, Senserrich J, Clotet B, Perron-Sierra F, Tucker GC, Esté JA**. 2009. Cell adhesion through alpha-V-containing integrins is required for efficient HIV-1 infection in macrophages. Blood **113**:1278–1286.

39. **Arthos J, Cicala C, Martinelli E, MacLeod K, van Ryk D, Wei D, Xiao Z, Veenstr TD, Conrad TP, Lempicki RA, McLaughlin S, Pascuccio M, Gopaul R, McNally J, Cruz CC, Censoplano N, Chung E, Reitano KN, Kottilil S, Goode DJ, Fauci AS**. 2008. HIV-1 envelope protein binds to and signals through integrin alpha4 beta7, the gut mucosal homing receptor for peripheral T cells. Nat. Immunol. **9**:301–309.

40. **Sommerfelt MA, Asjo B**. 1995. Intercellular adhesion molecule 3, a candidate human immunodeficiency virus type 1 co-receptor on lymphoid and monocytoid cells. J. Gen. Virol. **76**:1345–1352.

41. **Cook DG, Fantini J, Spitalnik SL, Gonzalez-Scarano F**. 1994. Binding of human immunodeficiency virus type I (HIV-1) gp120 to galactosylceramide (GalCer): relationship to the V3 loop. Virology **201**:206–214.

42. **Geijtenbeek TB, Kwon DS, Torensma R, van Vliet SJ, van Duijnhoven GC, Middel J, Cornelissen IL, Nottet HS, KewalRamani VN, Littman DR, Figdor CG, van Kooyk Y**. 2000. DC-SIGN, a dendritic cell-specific HIV-1-binding protein that enhances trans-infection of T cells. Cell **100**:587–597.

43. **Cardona-Maya W, López-Herrera A, Velilla-Hernández P, Rugeles MT, Cadavid ÁP**. 2006. The role of mannose receptor on HIV-1 entry into human spermatozoa. Am. J. Reprod. Immunol. **55**:241–245.

44. **Lai J, Bernhard OK, Turville SG, Harman AN, Wilkinson J, Cunningham AL**. 2009. Oligomerization of the macrophage mannose receptor enhances gp120-mediated binding of HIV-1. J. Biol. Chem. **284**:11027–11038.

45. **Fanibunda SE, Modi DN, Gokral JS, Bandivdekar AH**. 2011. HIV gp120 binds to mannose receptor on vaginal epithelial cells and induces production of matrix metalloproteinases. PLoS One **6**.

46. **Kwon DS, Gregorio G, Bitton N, Hendrickson WA, Littman DR**. 2002. DC-SIGN-mediated internalization of HIV is required for trans-enhancement of T cell infection. Immunity **16**:135–144.

47. **Boggiano C, Manel N, Littman DR**. 2007. Dendritic cell-mediated trans-enhancement of human immunodeficiency virus type 1 infectivity is independent of DC-SIGN. J. Virol. **81**:2519–2523.

48. **Schiffner T, Sattentau QJ, Duncan CJA**. 2013. Cell-to-cell spread of HIV-1 and evasion of neutralizing antibodies. Vaccine.

49. **Clapham PR, McKnight Á**. 2001. HIV-1 receptors and cell tropism. Br. Med. Bull. **58**:43–59.

50. **Parrish NF, Wilen CB, Banks LB, Iyer SS, Pfaff JM, Salazar-Gonzalez JF, Salazar MG, Decker JM, Parrish EH, Berg A, Hopper J, Hora B, Kumar A, Mahlokozera T, Yuan S, Coleman C, Vermeulen M, Ding H, Ochsenbauer C, Tilton JC, Permar SR, Kappes JC, Betts MR, Busch MP, Gao F, Montefiori D, Haynes BF, Shaw GM, Hahn BH, Doms RW**. 2012. Transmitted/founder and chronic subtype C HIV-1 use CD4 and CCR5 receptors with equal efficiency and are not inhibited by blocking the integrin α4β7. PLoS Pathog. **8**.

51. **Keele BF, Giorgi EE, Salazar-Gonzalez JF, Decker JM, Pham KT, Salazar MG, Sun C, Grayson T, Wang S, Li H, Wei X, Jiang C, Kirchherr JL, Gao F, Anderson JA, Ping L-H, Swanstrom R, Tomaras GD, Blattner WA, Goepfert PA, Kilby JM, Saag MS, Delwart EL, Busch MP, Cohen MS, Montefiori DC, Haynes BF, Gaschen B, Athreya GS, Lee HY, Wood N, Seoighe C, Perelson AS, Bhattacharya T, Korber BT, Hahn BH, Shaw GM**. 2008. Identification and characterization of transmitted and early founder virus envelopes in primary HIV-1 infection. Proc. Natl. Acad. Sci. U. S. A. **105**:7552–7557.

52. **McGowan J, Shah S**. 2010. Understanding HIV Tropism. Physicians' Res. Netw. Noteb. **15**.

53. **Gonzalez-Perez MP, O'Connell OJ, Lin R, Sullivan WM, Bell J, Simmonds P, Clapham PR**. 2012. Independent evolution of

macrophage-tropism and increased charge between HIV-1 R5 envelopes present in brain and immune tissue. Retrovirology.

54. **Edo-Matas D, Rachinger A, Setiawan LC, Boeser-Nunnink BD, van 't Wout AB, Lemey P, Schuitemaker H**. 2012. The evolution of human immunodeficiency virus type-1 (HIV-1) envelope molecular properties and coreceptor use at all stages of infection in an HIV-1 donor-recipient pair. Virology **422**:70–80.

55. **Coetzer M, Nedellec R, Salkowitz J, McLaughlin S, Liu Y, Heath L, Mullins JI, Mosier DE**. 2008. Evolution of CCR5 use before and during coreceptor switching. J. Virol. **82**:11758–11766.

56. **Connor RI, Sheridan KE, Ceradini D, Choe S, Landau NR**. 1997. Change in coreceptor use correlates with disease progression in HIV-1--infected individuals. J. Exp. Med. **185**:621–628.

57. **Verhofstede C, Nijhuis M, Vandekerckhove L**. 2012. Correlation of coreceptor usage and disease progression. Curr. Opin. HIV AIDS.

58. **Brumme ZL, Goodrich J, Mayer HB, Brumme CJ, Henrick BM, Wynhoven B, Asselin JJ, Cheung PK, Hogg RS, Montaner JSG, Harrigan PR**. 2005. Molecular and clinical epidemiology of CXCR4-using HIV-1 in a large population of antiretroviral-naive individuals. J. Infect. Dis. **192**:466–474.

59. **Goodenow MM, Collman RG**. 2006. HIV-1 coreceptor preference is distinct from target cell tropism: a dual-parameter nomenclature to define viral phenotypes. J. Leukoc. Biol. **80**:965–972.

60. **Yi Y, Shaheen F, Collman RG**. 2005. Preferential use of CXCR4 by R5X4 human immunodeficiency virus type 1 isolates for infection of primary lymphocytes. J. Virol. **79**:1480–6.

61. **Duncan CJA, Sattentau QJ**. 2011. Viral determinants of HIV-1 macrophage tropism. Viruses **3**:2255–2279.

62. **Simmons G, Wilkinson D, Reeves JD, Dittmar MT, Beddows S, Weber J, Carnegie G, Desselberger U, Gray PW, Weiss RA, Clapham PR**. 1996. Primary, syncytium-inducing human immunodeficiency virus type 1 isolates are dual-tropic and most can use either Lestr or CCR5 as coreceptors for virus entry. J. Virol. **70**:8355–8360.

63. **Bleul CC, Wu L, Hoxie JA, Springer TA, Mackay CR**. 1997. The HIV coreceptors CXCR4 and CCR5 are differentially expressed and regulated on human T lymphocytes. Proc. Natl. Acad. Sci. U. S. A. **94**:1925–1930.

64. **Dai J, Agosto LM, Baytop C, Yu JJ, Pace MJ, Liszewski MK, O'Doherty U**. 2009. Human immunodeficiency virus integrates directly into naive resting CD4+ T cells but enters naive cells less efficiently than memory cells. J. Virol. **83**:4528–4537.

65. **Baldauf H-M, Pan X, Erikson E, Schmidt S, Daddacha W, Burggraf M, Schenkova K, Ambiel I, Wabnitz G, Gramberg T, Panitz S, Flory E, Landau NR, Sertel S, Rutsch F, Lasitschka F, Kim B, König R, Fackler OT, Keppler OT**. 2012. SAMHD1 restricts HIV-1 infection in resting CD4+ T cells. Nat. Med.

66. **Wynn T a, Chawla A, Pollard JW**. 2013. Macrophage biology in development, homeostasis and disease. Nature **496**:445–55.

67. **Sarantis H, Grinstein S**. 2012. Subversion of phagocytosis for pathogen survival. Cell Host Microbe.

68. **Murray PJ, Wynn TA**. 2011. Protective and pathogenic functions of macrophage subsets. Nat. Rev. Immunol.

69. **Liu Y-C, Zou X-B, Chai Y-F, Yao Y-M**. 2014. Macrophage polarization in inflammatory diseases. Int. J. Biol. Sci. **10**:520–9.

70. **Collman R, Godfrey B, Cutilli J, Rhodes A, Hassan NF, Sweet R, Douglas SD, Friedman H, Nathanson N, Gonzalez-Scarano F**. 1990. Macrophage-tropic strains of human immunodeficiency virus type 1 utilize the CD4 receptor. J. Virol. **64**:4468–4476.

71. **Raposo RAS, Trudgian DC, Thomas B, van Wilgenburg B, Cowley SA, James W**. 2011. Protein kinase C and NF-κB-dependent CD4 downregulation in macrophages induced by T cell-derived soluble factors: consequences for HIV-1 infection. J. Immunol. **187**:748–759.

72. **Shen R, Richter HE, Clements RH, Novak L, Huff K, Bimczok D, Sankaran-Walters S, Dandekar S, Clapham PR, Smythies LE, Smith PD**. 2009. Macrophages in vaginal but not intestinal mucosa are monocyte-like and permissive to human immunodeficiency virus type 1 infection. J. Virol. **83**:3258–3267.

73. **Shen R, Meng G, Ochsenbauer C, Clapham PR, Grams J, Novak L, Kappes JC, Smythies LE, Smith PD**. 2011. Stromal down-regulation of macrophage CD4/CCR5 expression and NF-kB activation mediates HIV-1 non-permissiveness in intestinal macrophages. PLoS Pathog. **7**.

74. **Gorry PR, Bristol G, Zack JA, Ritola K, Swanstrom R, Birch CJ, Bell JE, Bannert N, Crawford K, Wang H, Schols D, De Clercq E, Kunstman K, Wolinsky SM, Gabuzda D**. 2001. Macrophage tropism of human immunodeficiency virus type 1 isolates from brain and lymphoid tissues predicts neurotropism independent of coreceptor specificity. J. Virol. **75**:10073–10089.

75. **Salimi H, Roche M, Webb N, Gray LR, Chikere K, Sterjovski J, Ellett A, Wesselingh SL, Ramsland PA, Lee B, Churchill MJ, Gorry PR**. 2012. Macrophage-tropic HIV-1 variants from brain demonstrate alterations in the way gp120 engages both CD4 and CCR5. J. Leukoc. Biol.

76. **Gorry PR, Taylor J, Holm GH, Mehle A, Morgan T, Cayabyab M, Farzan M, Wang H, Bell JE, Kunstman K, Moore JP, Wolinsky SM, Gabuzda D**. 2002. Increased CCR5 affinity and reduced CCR5/CD4 dependence of a neurovirulent primary human immunodeficiency virus type 1 isolate. J. Virol. **76**:6277–92.

77. **Martín J, LaBranche CC, González-Scarano F**. 2001. Differential CD4/CCR5 utilization, gp120 conformation, and neutralization sensitivity between envelopes from a microglia-adapted human immunodeficiency virus type 1 and its parental isolate. J. Virol. **75**:3568–3580.

78. **Schnell G, Joseph S, Spudich S, Price RW, Swanstrom R**. 2011. HIV-1 replication in the central nervous system occurs in two distinct cell types. PLoS Pathog. **7**.

79. **Speck RF, Esser U, Penn ML, Eckstein DA, Pulliam L, Chan SY, Goldsmith MA**. 1999. A trans-receptor mechanism for infection of CD4-negative cells by human immunodeficiency virus type 1. Curr. Biol. **9**:547–550.

80. **González-Scarano F, Martín-García J**. 2005. The neuropathogenesis of AIDS. Nat. Rev. Immunol. **5**:69–81.

81. **Olinger GG, Saifuddin M, Spear GT**. 2000. CD4-Negative Cells Bind Human Immunodeficiency Virus Type 1 and Efficiently Transfer Virus to T Cells. J. Virol. **74**:8550–8557.

82. **Tateno M, Gonzalez-Scarano F, Levy JA**. 1989. Human immunodeficiency virus can infect CD4-negative human fibroblastoid cells. Proc. Natl. Acad. Sci. U. S. A. **86**:4287–4290.

83. **Muratori C, Sistigu A, Ruggiero E, Falchi M, Bacigalupo I, Palladino C, Toschi E, Federico M**. 2007. Macrophages transmit human immunodeficiency virus type 1 products to CD4-negative cells: involvement of matrix metalloproteinase 9. J. Virol. **81**:9078–87.

84. **Rozmyslowicz T, Majka M, Kijowski J, Murphy SL, Conover DO, Poncz M, Ratajczak J, Gaulton GN, Ratajczak MZ**. 2003. Platelet- and megakaryocyte-derived microparticles transfer CXCR4 receptor to CXCR4-null cells and make them susceptible to infection by X4-HIV. AIDS **17**:33–42.

85. **Kolodkin-Gal D, Hulot SL, Korioth-Schmitz B, Gombos RB, Zheng Y, Owuor J, Lifton MA, Ayeni C, Najarian RM, Yeh WW, Asmal M, Zamir G, Letvin NL**. 2013. Efficiency of cell-free and cell-associated virus in mucosal transmission of human immunodeficiency virus type 1 and simian immunodeficiency virus. J. Virol. **87**:13589–97.

86. **Sallé B, Brochard P, Bourry O, Mannioui A, Andrieu T, Prevot S, Dejucq-Rainsford N, Dereuddre-Bosquet N, Le Grand R**. 2010. Infection of macaques after vaginal exposure to cell-associated simian immunodeficiency virus. J. Infect. Dis. **202**:337–344.

87. **Piguet V, Sattentau Q**. 2004. Dangerous liaisons at the virological synapse. J. Clin. Invest. **114**:605–10.

88. **Permanyer M, Ballana E, Esté JA**. 2010. Endocytosis of HIV: Anything goes. Trends Microbiol.

89. **Kawamura T, Gulden FO, Sugaya M, McNamara DT, Borris DL, Lederman MM, Orenstein JM, Zimmerman PA, Blauvelt A**. 2003. R5 HIV productively infects Langerhans cells, and infection levels are regulated by compound CCR5 polymorphisms. Proc. Natl. Acad. Sci. U. S. A. **100**:8401–8406.

90. **Rinaldo CR**. 2013. HIV-1 Trans Infection of CD4(+) T Cells by Professional Antigen Presenting Cells. Scientifica (Cairo). **2013**:164203.

91. **Burleigh L, Lozach P-Y, Schiffer C, Staropoli I, Pezo V, Porrot F, Canque B, Virelizier J-L, Arenzana-Seisdedos F, Amara A**. 2006. Infection of dendritic cells (DCs), not DC-SIGN-mediated internalization of human immunodeficiency virus, is required for long-term transfer of virus to T cells. J. Virol. **80**:2949–57.

92. **Nobile C, Petit C, Moris A, Skrabal K, Abastado J-P, Mammano F, Schwartz O**. 2005. Covert human immunodeficiency virus replication in dendritic cells and in DC-SIGN-expressing cells promotes long-term transmission to lymphocytes. J. Virol. **79**:5386–5399.

93. **McDonald D, Wu L, Bohks SM, KewalRamani VN, Unutmaz D, Hope TJ**. 2003. Recruitment of HIV and its receptors to dendritic cell-T cell junctions. Science **300**:1295–1297.

94. **Sattentau Q**. 2008. Avoiding the void: cell-to-cell spread of human viruses. Nat. Rev. Microbiol. **6**:815–826.

95. **Jolly C, Sattentau QJ**. 2004. Retroviral spread by induction of virological synapses. Traffic **5**:643–650.

96. **Jolly C, Kashefi K, Hollinshead M, Sattentau QJ**. 2004. HIV-1 cell to cell transfer across an Env-induced, actin-dependent synapse. J. Exp. Med. **199**:283–93.

97. **Jolly C, Welsch S, Michor S, Sattentau QJ**. 2011. The regulated secretory pathway in CD4(+) T cells contributes to human immunodeficiency virus type-1 cell-to-cell spread at the virological synapse. PLoS Pathog. **7**:e1002226.

98. **Sherer NM, Lehmann MJ, Jimenez-Soto LF, Horensavitz C, Pypaert M, Mothes W**. 2007. Retroviruses can establish filopodial bridges for efficient cell-to-cell transmission. Nat. Cell Biol. **9**:310–315.

99. **Felts RL, Narayan K, Estes JD, Shi D, Trubey CM, Fu J, Hartnell LM, Ruthel GT, Schneider DK, Nagashima K, Bess JW, Bavari S, Lowekamp BC, Bliss D, Lifson JD, Subramaniam S**. 2010. 3D

visualization of HIV transfer at the virological synapse between dendritic cells and T cells. Proc. Natl. Acad. Sci. U. S. A. **107**:13336–13341.

100. **Aggarwal A, Iemma TL, Shih I, Newsome TP, McAllery S, Cunningham AL, Turville SG**. 2012. Mobilization of HIV spread by diaphanous 2 dependent filopodia in infected dendritic cells. PLoS Pathog. **8**.

101. **Sowinski S, Jolly C, Berninghausen O, Purbhoo MA, Chauveau A, Köhler K, Oddos S, Eissmann P, Brodsky FM, Hopkins C, Onfelt B, Sattentau Q, Davis DM**. 2008. Membrane nanotubes physically connect T cells over long distances presenting a novel route for HIV-1 transmission. Nat. Cell Biol. **10**:211–219.

102. **Do T, Murphy G, Earl LA, Del Prete GQ, Grandinetti G, Li G, Estes JD, Rao P, Trubey CM, Thomas J, Spector J, Bliss D, Nath A, Lifson JD, Subramaniam S**. 2014. 3D imaging of HIV-1 virological synapses reveals membrane architectures involved in virus transmission. J. Virol.

103. **Jolly C, Mitar I, Sattentau QJ**. 2007. Requirement for an intact T-cell actin and tubulin cytoskeleton for efficient assembly and spread of human immunodeficiency virus type 1. J. Virol. **81**:5547–5560.

104. **Groot F, Welsch S, Sattentau QJ**. 2008. Efficient HIV-1 transmission from macrophages to T cells across transient virological synapses. Blood **111**:4660–4663.

105. **Welsch S, Keppler OT, Habermann A, Allespach I, Krijnse-Locker J, Kräusslich HG**. 2007. HIV-1 buds predominantly at the plasma membrane of primary human macrophages. PLoS Pathog. **3**.

106. **Deneka M, Pelchen-Matthews A, Byland R, Ruiz-Mateos E, Marsh M**. 2007. In macrophages, HIV-1 assembles into an intracellular plasma membrane domain containing the tetraspanins CD81, CD9, and CD53. J. Cell Biol. **177**:329–41.

107. **Bennett AE, Narayan K, Shi D, Hartnell LM, Gousset K, He H, Lowekamp BC, Yoo TS, Bliss D, Freed EO, Subramaniam S**. 2009. Ion-abrasion scanning electron microscopy reveals surface-connected tubular conduits in HIV-infected macrophages. PLoS Pathog. **5**.

108. **Duncan CJ a, Russell R a, Sattentau QJ**. 2013. High multiplicity HIV-1 cell-to-cell transmission from macrophages to CD4+ T cells limits antiretroviral efficacy. AIDS **27**:2201–6.

109. **Welsch S, Groot F, Kräusslich H-G, Keppler OT, Sattentau QJ**. 2011. Architecture and regulation of the HIV-1 assembly and holding compartment in macrophages. J. Virol. **85**:7922–7927.

110. **Tan J, Sattentau QJ**. 2013. The HIV-1-containing macrophage compartment: A perfect cellular niche? Trends Microbiol.

111. **Harris AK, Bartesaghi A, Milne JLS, Subramaniam S**. 2013. HIV-1 envelope glycoprotein trimers display open quaternary conformation when bound to the gp41 membrane-proximal external-region-directed broadly neutralizing antibody Z13e1. J. Virol. **87**:7191–6.

112. **Liu J, Bartesaghi A, Borgnia MJ, Sapiro G, Subramaniam S**. 2008. Molecular architecture of native HIV-1 gp120 trimers. Nature **455**:109–113.

113. **Curlin ME, Zioni R, Hawes SE, Liu Y, Deng W, Gottlieb GS, Zhu T, Mullins JI**. 2010. HIV-1 envelope subregion length variation during disease progression. PLoS Pathog. **6**:e1001228.

114. **Verrier F, Borman AM, Brand D, Girard M**. 1999. Role of the HIV type 1 glycoprotein 120 V3 loop in determining coreceptor usage. AIDS Res. Hum. Retroviruses **15**:731–43.

115. **Wu L, Gerard NP, Wyatt R, Choe H, Parolin C, Ruffing N, Borsetti A, Cardoso AA, Desjardin E, Newman W, Gerard C, Sodroski J**. 1996. CD4-induced interaction of primary HIV-1 gp120 glycoproteins with the chemokine receptor CCR-5. Nature **384**:179–183.

116. **Trkola A, Dragic T, Arthos J, Binley JM, Olson WC, Allaway GP, Cheng-Mayer C, Robinson J, Maddon PJ, Moore JP**. 1996. CD4-dependent, antibody-sensitive interactions between HIV-1 and its co-receptor CCR-5. Nature **384**:184–187.

117. **Mercer J, Helenius A**. 2009. Virus entry by macropinocytosis. Nat. Cell Biol. **11**:510–520.

118. **Miyauchi K, Kim Y, Latinovic O, Morozov V, Melikyan GB**. 2009. HIV Enters Cells via Endocytosis and Dynamin-Dependent Fusion with Endosomes. Cell **137**:433–444.

119. **Dale BM, McNerney GP, Thompson DL, Hubner W, De Los Reyes K, Chuang FYS, Huser T, Chen BK**. 2011. Cell-to-cell transfer of HIV-1 via virological synapses leads to endosomal virion maturation that activates viral membrane fusion. Cell Host Microbe **10**:551–562.

120. **Martin N, Welsch S, Jolly C, Briggs JAG, Vaux D, Sattentau QJ**. 2010. Virological synapse-mediated spread of human immunodeficiency virus type 1 between T cells is sensitive to entry inhibition. J. Virol. **84**:3516–3527.

121. **Bukrinsky M**. A hard way to the nucleus. Mol. Med. **10**:1–5.

122. **Ambrose Z, Aiken C**. 2014. HIV-1 uncoating: Connection to nuclear entry and regulation by host proteins. Virology.

123. **Warren K, Warrilow D, Meredith L, Harrich D**. 2009. Reverse transcriptase and cellular factors: Regulators of HIV-1 reverse transcription. Viruses.

124. **Hu W-S, Hughes SH**. 2012. HIV-1 reverse transcription. Cold Spring Harb. Perspect. Med. **2**:.a006882.

125. **Zennou V, Petit C, Guetard D, Nerhbass U, Montagnier L, Charneau P**. 2000. HIV-1 genome nuclear import is mediated by a central DNA flap. Cell **101**:173–85.

126. **Sloan RD, Wainberg MA**. 2011. The role of unintegrated DNA in HIV infection. Retrovirology **8**:52.

127. **Meyerhans A, Breinig T**. 2003. Forms and function of intracellular HIV DNA. HIV Seq. … 14–21.

128. **Craigie R, Bushman FD**. 2012. HIV DNA integration. Cold Spring Harb. Perspect. Med. **2**.

129. **Rittner K, Churcher MJ, Gait MJ, Karn J**. 1995. The human immunodeficiency virus long terminal repeat includes a specialised initiator element which is required for Tat-responsive transcription. J. Mol. Biol. **248**:562–80.

130. **Liu J, Perkins ND, Schmid RM, Nabel GJ**. 1992. Specific NF-kappa B subunits act in concert with Tat to stimulate human immunodeficiency virus type 1 transcription. J. Virol. **66**:3883–3887.

131. **Kinoshita S, Chen BK, Kaneshima H, Nolan GP**. 1998. Host control of HIV-1 parasitism in T cells by the nuclear factor of activated T cells. Cell **95**:595–604.

132. **Frankel AD**. 1992. Activation of HIV transcription by Tat. Curr. Opin. Genet. Dev. **2**:293–298.

133. **Burnett JC, Miller-Jensen K, Shah PS, Arkin AP, Schaffer D V**. 2009. Control of stochastic gene expression by host factors at the HIV promoter. PLoS Pathog. **5**:e1000260.

134. **Weinberger LS, Burnett JC, Toettcher JE, Arkin AP, Schaffer D V**. 2005. Stochastic gene expression in a lentiviral positive-feedback loop: HIV-1 Tat fluctuations drive phenotypic diversity. Cell **122**:169–82.

135. **Flores O, Lee G, Kessler J, Miller M, Schlief W, Tomassini J, Hazuda D**. 1999. Host-cell positive transcription elongation factor b kinase activity is essential and limiting for HIV type 1 replication. Proc Natl Acad Sci U S A **96**:7208–7213.

136. **Peterlin BM, Price DH**. 2006. Controlling the Elongation Phase of Transcription with P-TEFb. Mol. Cell.

137. **Karn J, Stoltzfus CM**. 2012. Transcriptional and posttranscriptional regulation of HIV-1 gene expression. Cold Spring Harb. Perspect. Med. **2**:a006916.

138. **Jacks T, Power MD, Masiarz FR, Luciw PA, Barr PJ, Varmus HE**. 1988. Characterization of ribosomal frameshifting in HIV-1 gag-pol expression. Nature **331**:280–283.

139. **Martinez NW, Xue X, Berro RG, Kreitzer G, Resh MD**. 2008. Kinesin KIF4 regulates intracellular trafficking and stability of the human immunodeficiency virus type 1 Gag polyprotein. J. Virol. **82**:9937–9950.

140. **Murakami T**. 2012. Retroviral env glycoprotein trafficking and incorporation into virions. Mol. Biol. Int. **2012**:682850.

141. **Morita E, Sandrin V, McCullough J, Katsuyama A, Baci Hamilton I, Sundquist WI**. 2011. ESCRT-III protein requirements for HIV-1 budding. Cell Host Microbe **9**:235–242.

142. **Neil SJD, Zang T, Bieniasz PD**. 2008. Tetherin inhibits retrovirus release and is antagonized by HIV-1 Vpu. Nature **451**:425–430.

143. **Cooper A, García M, Petrovas C, Yamamoto T, Koup R a, Nabel GJ**. 2013. HIV-1 causes CD4 cell death through DNA-dependent protein kinase during viral integration. Nature **498**:376–9.

144. **Costin JM**. 2007. Cytopathic mechanisms of HIV-1. Virol. J. **4**:100.

145. **Doitsh G, Cavrois M, Lassen KG, Zepeda O, Yang Z, Santiago ML, Hebbeler AM, Greene WC**. 2010. Abortive HIV infection mediates CD4 T cell depletion and inflammation in human lymphoid tissue. Cell **143**:789–801.

146. **Espert L, Denizot M, Grimaldi M, Robert-Hebmann V, Gay B, Varbanov M, Codogno P, Biard-Piechaczyk M**. 2006. Autophagy is involved in T cell death after binding of HIV-1 envelope proteins to CXCR4. J. Clin. Invest. **116**:2161–2172.

147. **Doitsh G, Galloway NLK, Geng X, Yang Z, Monroe KM, Zepeda O, Hunt PW, Hatano H, Sowinski S, Muñoz-Arias I, Greene WC**. 2014. Cell death by pyroptosis drives CD4 T-cell depletion in HIV-1 infection. Nature **505**:509–14.

148. **Perfettini J-L, Castedo M, Roumier T, Andreau K, Nardacci R, Piacentini M, Kroemer G**. 2005. Mechanisms of apoptosis induction by the HIV-1 envelope. Cell Death Differ. **12 Suppl 1**:916–923.

149. **Terai C, Kornbluth RS, Pauza CD, Richman DD, Carson DA**. 1991. Apoptosis as a mechanism of cell death in cultured T lymphoblasts acutely infected with HIV-1. J. Clin. Invest. **87**:1710–1715.

150. **Smalls-Mantey A, Connors M, Sattentau QJ**. 2013. Comparative Efficiency of HIV-1-Infected T Cell Killing by NK Cells, Monocytes and Neutrophils. PLoS One **8**.

151. **Bomsel M, Alfsen A**. 2003. Entry of viruses through the epithelial barrier: pathogenic trickery. Nat. Rev. Mol. Cell Biol. **4**:57–68.

152. **Bomsel M**. 1997. Transcytosis of infectious human immunodeficiency virus across a tight human epithelial cell line barrier. Nat. Med. **3**:42–47.

153. **Dinh MH, Fahrbach KM, Hope TJ**. 2011. The Role of the Foreskin in Male Circumcision: An Evidence-Based Review. Am. J. Reprod. Immunol.

154. **Nilsson J, Kinloch-de-Loes S, Granath A, Sönnerborg A, Goh L-E, Andersson J**. 2007. Early immune activation in gut-associated and peripheral lymphoid tissue during acute HIV infection. AIDS **21**:565–574.

155. **Sandler NG, Bosinger SE, Estes JD, Zhu RTR, Tharp GK, Boritz E, Levin D, Wijeyesinghe S, Makamdop KN, del Prete GQ, Hill BJ, Timmer JK, Reiss E, Yarden G, Darko S, Contijoch E, Todd JP, Silvestri G, Nason M, Norgren RB, Keele BF, Rao S, Langer JA, Lifson JD, Schreiber G, Douek DC**. 2014. Type I interferon responses in rhesus macaques prevent SIV infection and slow disease progression. Nature **511**:601–605.

156. **McMichael AJ, Borrow P, Tomaras GD, Goonetilleke N, Haynes BF**. 2010. The immune response during acute HIV-1 infection: clues for vaccine development. Nat. Rev. Immunol. **10**:11–23.

157. **Perreau M, Levy Y, Pantaleo G**. 2013. Immune response to HIV. Curr. Opin. HIV AIDS **8**:333–40.

158. **Barouch DH, Whitney JB, Moldt B, Klein F, Oliveira TY, Liu J, Stephenson KE, Chang H-W, Shekhar K, Gupta S, Nkolola JP, Seaman MS, Smith KM, Borducchi EN, Cabral C, Smith JY, Blackmore S, Sanisetty S, Perry JR, Beck M, Lewis MG, Rinaldi W, Chakraborty AK, Poignard P, Nussenzweig MC, Burton DR**. 2013. Therapeutic efficacy of potent neutralizing HIV-1-specific monoclonal antibodies in SHIV-infected rhesus monkeys. Nature **503**:224–8.

159. **Lore K, Larsson M**. 2003. The role of dendritic cells in the pathogenesis of HIV-1 infection. APMIS **111**:776–88.

160. **Wu L, KewalRamani VN**. 2006. Dendritic-cell interactions with HIV: infection and viral dissemination. Nat. Rev. Immunol. **6**:859–68.

161. **Smith BA, Gartner S, Liu Y, Perelson AS, Stilianakis NI, Keele BF, Kerkering TM, Ferreira-Gonzalez A, Szakal AK, Tew JG, Burton GF**. 2001. Persistence of infectious HIV on follicular dendritic cells. J. Immunol. **166**:690–696.

162. **Burton GF, Keele BF, Estes JD, Thacker TC, Gartner S**. 2002. Follicular dendritic cell contributions to HIV pathogenesis. Semin. Immunol. **14**:275–284.

163. **Grouard G, Clark EA**. 1997. Role of dendritic and follicular dendritic cells in HIV infection and pathogenesis. Curr. Opin. Immunol. **9**:563–567.

164. **Tacchetti C, Favre A, Moresco L, Meszaros P, Luzzi P, Truini M, Rizzo F, Grossi CE, Ciccone E**. 1997. HIV is trapped and masked in the cytoplasm of lymph node follicular dendritic cells. Am. J. Pathol. **150**:533–42.

165. **Vinuesa CG, Linterman MA, Goodnow CC, Randall KL**. 2010. T cells and follicular dendritic cells in germinal center B-cell formation and selection. Immunol. Rev.

166. **Spiegel H, Herbst H, Niedobitek G, Foss HD, Stein H**. 1992. Follicular dendritic cells are a major reservoir for human immunodeficiency virus type 1 in lymphoid tissues facilitating infection of CD4+ T-helper cells. Am. J. Pathol. **140**:15–22.

167. **Ohba K, Ryo A, Dewan MZ, Nishi M, Naito T, Qi X, Inagaki Y, Nagashima Y, Tanaka Y, Okamoto T, Terashima K, Yamamoto N**. 2009. Follicular dendritic cells activate HIV-1 replication in monocytes/macrophages through a juxtacrine mechanism mediated by P-selectin glycoprotein ligand 1. J. Immunol. **183**:524–532.

168. **Fauci AS**. 2003. HIV and AIDS: 20 years of science. Nat. Med. **9**:839–843.

169. **Chun T-W, Nickle DC, Justement JS, Meyers JH, Roby G, Hallahan CW, Kottilil S, Moir S, Mican JM, Mullins JI, Ward DJ, Kovacs JA, Mannon PJ, Fauci AS**. 2008. Persistence of HIV in gut-associated lymphoid tissue despite long-term antiretroviral therapy. J. Infect. Dis. **197**:714–720.

170. **Zhang J, Perelson AS**. 2013. Contribution of follicular dendritic cells to persistent HIV viremia.Journal of virology.

171. **Kim W-K, Corey S, Alvarez X, Williams K**. 2003. Monocyte/macrophage traffic in HIV and SIV encephalitis. J. Leukoc. Biol. **74**:650–656.

172. **Fischer-Smith T, Bell C, Croul S, Lewis M, Rappaport J**. 2008. Monocyte/macrophage trafficking in acquired immunodeficiency syndrome encephalitis: lessons from human and nonhuman primate studies. J. Neurovirol. **14**:318–326.

173. **Churchill M, Nath A**. 2013. Where does HIV hide? A focus on the central nervous system. Curr. Opin. HIV AIDS **8**:165–9.

174. **Lamers SL, Gray RR, Salemi M, Huysentruyt LC, McGrath MS**. 2011. HIV-1 phylogenetic analysis shows HIV-1 transits through the meninges to brain and peripheral tissues. Infect. Genet. Evol. **11**:31–37.

175. **Johnston MI, Fauci AS**. 2007. An HIV vaccine--evolving concepts. N. Engl. J. Med. **356**:2073–2081.

176. **Chomont N, El-Far M, Ancuta P, Trautmann L, Procopio FA, Yassine-Diab B, Boucher G, Boulassel M-R, Ghattas G, Brenchley JM, Schacker TW, Hill BJ, Douek DC, Routy J-P, Haddad EK, Sékaly R-P**. 2009. HIV reservoir size and persistence are driven by T cell survival and homeostatic proliferation.Nature medicine.

177. **Chomont N, DaFonseca S, Vandergeeten C, Ancuta P, Sékaly R-P**. 2011. Maintenance of CD4+ T-cell memory and HIV persistence: keeping memory, keeping HIV. Curr. Opin. HIV AIDS **6**:30–36.

178. **Lafeuillade A**. 2012. Eliminating the HIV reservoir. Curr. HIV/AIDS Rep. **9**:121–131.

179. **Killian MS, Fujimura SH, Hecht FM, Levy JA**. 2006. Similar changes in plasmacytoid dendritic cell and CD4 T-cell counts during primary HIV-1 infection and treatment. AIDS **20**:1247–1252.

180. **Redel L, Le Douce V, Cherrier T, Marban C, Janossy A, Aunis D, Van Lint C, Rohr O, Schwartz C**. 2010. HIV-1 regulation of latency in the monocyte-macrophage lineage and in CD4+ T lymphocytes. J. Leukoc. Biol. **87**:575–588.

181. **Carter CC, Onafuwa-Nuga A, McNamara LA, Riddell J, Bixby D, Savona MR, Collins KL**. 2010. HIV-1 infects multipotent progenitor cells causing cell death and establishing latent cellular reservoirs. Nat. Med. **16**:446–451.

182. **Alter G, Teigen N, Ahern R, Streeck H, Meier A, Rosenberg ES, Altfeld M**. 2007. Evolution of innate and adaptive effector cell functions during acute HIV-1 infection. J. Infect. Dis. **195**:1452–1460.

183. **Chang JJ, Altfeld M**. 2010. Innate immune activation in primary HIV-1 infection. J. Infect. Dis. **202 Suppl** :S297–S301.

184. **Borrow P, Lewicki H, Hahn BH, Shaw GM, Oldstone MB**. 1994. Virus-specific CD8+ cytotoxic T-lymphocyte activity associated with control of viremia in primary human immunodeficiency virus type 1 infection. J. Virol. **68**:6103–6110.

185. **Koup RA, Safrit JT, Cao Y, Andrews CA, McLeod G, Borkowsky W, Farthing C, Ho DD**. 1994. Temporal association of cellular immune responses with the initial control of viremia in primary human immunodeficiency virus type 1 syndrome. J. Virol. **68**:4650–4655.

186. **Goonetilleke N, Liu MKP, Salazar-Gonzalez JF, Ferrari G, Giorgi E, Ganusov V V, Keele BF, Learn GH, Turnbull EL, Salazar MG, Weinhold KJ, Moore S, Letvin N, Haynes BF, Cohen MS, Hraber P, Bhattacharya T, Borrow P, Perelson AS, Hahn BH, Shaw GM, Korber BT, McMichael AJ**. 2009. The first T cell response to transmitted/founder virus contributes to the control of acute viremia in HIV-1 infection. J. Exp. Med. **206**:1253–1272.

187. **Bernardin F, Kong D, Peddada L, Baxter-Lowe LA, Delwart E**. 2005. Human immunodeficiency virus mutations during the first month of infection are preferentially found in known cytotoxic T-lymphocyte epitopes. J. Virol. **79**:11523–11528.

188. **Salazar-Gonzalez JF, Salazar MG, Keele BF, Learn GH, Giorgi EE, Li H, Decker JM, Wang S, Baalwa J, Kraus MH, Parrish NF, Shaw KS, Guffey MB, Bar KJ, Davis KL, Ochsenbauer-Jambor C, Kappes JC, Saag MS, Cohen MS, Mulenga J, Derdeyn CA, Allen S, Hunter E, Markowitz M, Hraber P, Perelson AS, Bhattacharya T, Haynes BF, Korber BT, Hahn BH, Shaw GM**. 2009. Genetic identity, biological phenotype, and evolutionary pathways of transmitted/founder viruses in acute and early HIV-1 infection. J. Exp. Med. **206**:1273–1289.

189. **Douek DC, Brenchley JM, Betts MR, Ambrozak DR, Hill BJ, Okamoto Y, Casazza JP, Kuruppu J, Kunstman K, Wolinsky S, Grossman Z, Dybul M, Oxenius A, Price DA, Connors M, Koup RA**. 2002. HIV preferentially infects HIV-specific CD4+ T cells. Nature **417**:95–98.

190. **Gougeon ML, Lecoeur H, Dulioust A, Enouf MG, Crouvoiser M, Goujard C, Debord T, Montagnier L**. 1996. Programmed cell death in peripheral lymphocytes from HIV-infected persons: increased susceptibility to apoptosis of CD4 and CD8 T cells correlates with lymphocyte activation and with disease progression. J Immunol **156**:3509–20.

191. **Cummins NW, Badley AD**. 2010. Mechanisms of HIV-associated lymphocyte apoptosis: 2010. Cell Death Dis. **1**:e99.

192. **Muro-cacho CA, Pantaleo G, Fauci S**. 1995. Analysis of Apoptosis in Lymph Nodes of HIV-Infected Person. J. Immunol. **154**:5555–5566.

193. **Lamkanfi M, Dixit VM**. 2010. Manipulation of host cell death pathways during microbial infections. Cell Host Microbe **8**:44–54.

194. **Mattapallil JJ, Douek DC, Hill B, Nishimura Y, Martin M, Roederer M**. 2005. Massive infection and loss of memory CD4+ T cells in multiple tissues during acute SIV infection. Nature **434**:1093–7.

195. **Kwong PD, Mascola JR, Nabel GJ**. 2013. Broadly neutralizing antibodies and the search for an HIV-1 vaccine: the end of the beginning. Nat. Rev. Immunol. **13**:693–701.

196. **Malbec M, Porrot F, Rua R, Horwitz J, Klein F, Halper-Stromberg A, Scheid JF, Eden C, Mouquet H, Nussenzweig MC, Schwartz O**. 2013. Broadly neutralizing antibodies that inhibit HIV-1 cell to cell transmission. J. Exp. Med. **210**:2813–21.

197. **Wu X, Yang Z-Y, Li Y, Hogerkorp C-M, Schief WR, Seaman MS, Zhou T, Schmidt SD, Wu L, Xu L, Longo NS, McKee K, O'Dell S, Louder MK, Wycuff DL, Feng Y, Nason M, Doria-Rose N, Connors M, Kwong PD, Roederer M, Wyatt RT, Nabel GJ, Mascola JR**. 2010. Rational

design of envelope identifies broadly neutralizing human monoclonal antibodies to HIV-1. Science **329**:856–861.

198. **Huang J, Ofek G, Laub L, Louder MK, Doria-Rose NA, Longo NS, Imamichi H, Bailer RT, Chakrabarti B, Sharma SK, Alam SM, Wang T, Yang Y, Zhang B, Migueles SA, Wyatt R, Haynes BF, Kwong PD, Mascola JR, Connors M**. 2012. Broad and potent neutralization of HIV-1 by a gp41-specific human antibody. Nature.

199. **Zhang ZQ, Casimiro DR, Schleif WA, Chen M, Citron M, Davies ME, Burns J, Liang X, Fu TM, Handt L, Emini EA, Shiver JW**. 2007. Early depletion of proliferating B cells of germinal center in rapidly progressive simian immunodeficiency virus infection. Virology **361**:455–464.

200. **Titanji K, Velu V, Chennareddi L, Vijay-Kumar M, Gewirtz AT, Freeman GJ, Amara RR**. 2010. Acute depletion of activated memory B cells involves the PD-1 pathway in rapidly progressing SIV-infected macaques. J. Clin. Invest. **120**:3878–3890.

201. **Clark SJ, Saag MS, Decker WD, Campbell-Hill S, Roberson JL, Veldkamp PJ, Kappes JC, Hahn BH, Shaw GM**. 1991. High titers of cytopathic virus in plasma of patients with symptomatic primary HIV-1 infection.The New England journal of medicine.

202. **Pantaleo G, Fauci AS**. 1996. Immunopathogenesis of HIV infection. Annu. Rev. Microbiol. **50**:825–54.

203. **U.S. Department of Health & Human Services**. CD4 Count.

204. **Center for Disease Control and Prevention (CDC)**. What is HIV/AIDS? - HIV Basics - HIV/AIDS.

205. **Daar ES, Moudgil T, Meyer RD, Ho DD**. 1991. Transient high levels of viremia in patients with primary human immunodeficiency virus type 1 infection. N Engl J Med **324**:961–4.

206. **Pantaleo G, Graziosi C, Fauci AS**. 1993. New concepts in the immunopathogenesis of human immunodeficiency virus infection. N. Engl. J. Med. **328**:327–35.

207. **Saag M, Deeks SG**. 2010. How do HIV elite controllers do what they do? Clin. Infect. Dis. **51**:239–41.

208. **Pantaleo G, Menzo S, Vaccarezza M, Graziosi C, Cohen OJ, Demarest JF, Montefiori D, Orenstein JM, Fox C, Schrager LK**. 1995. Studies in subjects with long-term nonprogressive human immunodeficiency virus infection. N. Engl. J. Med. **332**:209–216.

209. **Wei X, Ghosh SK, Taylor ME, Johnson VA, Emini EA, Deutsch P, Lifson JD, Bonhoeffer S, Nowak MA, Hahn BH**. 1995. Viral dynamics in human immunodeficiency virus type 1 infection. Nature **373**:117–122.

210. **Tan Q, Zhu Y, Li J, Chen Z, Han GW, Kufareva I, Li T, Ma L, Fenalti G, Li J, Zhang W, Xie X, Yang H, Jiang H, Cherezov V, Liu H, Stevens RC, Zhao Q, Wu B**. 2013. Structure of the CCR5 chemokine receptor-HIV entry inhibitor maraviroc complex. Science **341**:1387–90.

211. **Esté JA, Telenti A**. 2007. HIV entry inhibitors. Lancet.

212. **Cihlar T, Ray AS**. 2010. Nucleoside and nucleotide HIV reverse transcriptase inhibitors: 25 years after zidovudine. Antiviral Res.

213. **De Béthune M-P**. 2010. Non-nucleoside reverse transcriptase inhibitors (NNRTIs), their discovery, development, and use in the treatment of HIV-1 infection: a review of the last 20 years (1989-2009). Antiviral Res. **85**:75–90.

214. **De Clercq E**. 2004. Non-nucleoside reverse transcriptase inhibitors (NNRTIs): past, present, and future. Chem. Biodivers. **1**:44–64.

215. **Summa V, Petrocchi A, Bonelli F, Crescenzi B, Donghi M, Ferrara M, Fiore F, Gardelli C, Paz OG, Hazuda DJ, Jones P, Kinzel O, Laufer R, Monteagudo E, Muraglia E, Nizi E, Orvieto F, Pace P, Pescatore G, Scarpelli R, Stillmock K, Witmer M V., Rowley M**. 2008. Discovery of raltegravir, a potent, selective orally bioavailable HIV-integrase inhibitor for the treatment of HIV-AIDS infection. J. Med. Chem. **51**:5843–5855.

216. **Ghosh AK, Dawson ZL, Mitsuya H**. 2007. Darunavir, a conceptually new HIV-1 protease inhibitor for the treatment of drug-resistant HIV. Bioorganic Med. Chem. **15**:7576–7580.

217. **Brik A, Wong C-H**. 2003. HIV-1 protease: mechanism and drug discovery. Org. Biomol. Chem. **1**:5–14.

218. **Barouch DH**. 2008. Challenges in the development of an HIV-1 vaccine. Nature **455**:613–619.

219. **Gamble LJ, Matthews QL**. 2010. Current progress in the development of a prophylactic vaccine for HIV-1. Drug Des. Devel. Ther. **5**:9–26.

220. **Johnson M, Fauci A**. 2008. An HIV Vaccine — Challenges and Prospects. New Engliand J. Med.

221. **McMichael AJ, Koff WC**. 2014. Vaccines that stimulate T cell immunity to HIV-1: the next step. Nat. Immunol. **15**:319–22.

222. **Schiffner T, Sattentau QJ, Dorrell L**. 2013. Development of prophylactic vaccines against HIV-1. Retrovirology **10**:72.

223. **Pitisuttithum P, Gilbert P, Gurwith M, Heyward W, Martin M, van Griensven F, Hu D, Tappero JW, Choopanya K**. 2006. Randomized, double-blind, placebo-controlled efficacy trial of a bivalent recombinant glycoprotein 120 HIV-1 vaccine among injection drug users in Bangkok, Thailand. J. Infect. Dis. **194**:1661–71.

224. **Buchbinder SP, Mehrotra D V., Duerr A, Fitzgerald DW, Mogg R, Li D, Gilbert PB, Lama JR, Marmor M, del Rio C, McElrath MJ, Casimiro DR, Gottesdiener KM, Chodakewitz JA, Corey L, Robertson MN**. 2008. Efficacy assessment of a cell-mediated immunity HIV-1 vaccine (the Step Study): a double-blind, randomised, placebo-controlled, test-of-concept trial. Lancet **372**:1881–1893.

225. **McElrath MJ, De Rosa SC, Moodie Z, Dubey S, Kierstead L, Janes H, Defawe OD, Carter DK, Hural J, Akondy R, Buchbinder SP, Robertson MN, Mehrotra D V., Self SG, Corey L, Shiver JW, Casimiro DR**. 2008. HIV-1 vaccine-induced immunity in the test-of-concept Step Study: a case-cohort analysis. Lancet **372**:1894–1905.

226. **Karasavvas N, Billings E, Rao M, Williams C, Zolla-Pazner S, Bailer RT, Koup RA, Madnote S, Arworn D, Shen X, Tomaras GD, Currier JR, Jiang M, Magaret C, Andrews C, Gottardo R, Gilbert P, Cardozo TJ, Rerks-Ngarm S, Nitayaphan S, Pitisuttithum P, Kaewkungwal J, Paris R, Greene K, Gao H, Gurunathan S, Tartaglia J, Sinangil F, Korber BT, Montefiori DC, Mascola JR, Robb ML, Haynes BF, Ngauy V, Michael NL, Kim JH, de Souza, for the MOPH TAVEG Collab MS**. 2012. The Thai Phase III HIV Type 1 Vaccine Trial (RV144) Regimen Induces Antibodies That Target Conserved Regions Within the V2 Loop of gp120. AIDS Res. Hum. Retroviruses.

227. **De Souza MS, Ratto-Kim S, Chuenarom W, Schuetz A, Chantakulkij S, Nuntapinit B, Valencia-Micolta A, Thelian D, Nitayaphan S, Pitisuttithum P, Paris RM, Kaewkungwal J, Michael NL, Rerks-Ngarm S, Mathieson B, Marovich M, Currier JR, Kim JH**. 2012. The Thai phase III trial (RV144) vaccine regimen induces T cell responses that preferentially target epitopes within the V2 region of HIV-1 envelope. J. Immunol. **188**:5166–76.

228. **Montefiori DC, Karnasuta C, Huang Y, Ahmed H, Gilbert P, De Souza MS, McLinden R, Tovanabutra S, Laurence-Chenine A, Sanders-Buell E, Moody MA, Bonsignori M, Ochsenbauer C, Kappes J, Tang H, Greene K, Gao H, Labranche CC, Andrews C, Polonis VR, Rerks-Ngarm S, Pitisuttithum P, Nitayaphan S, Kaewkungwal J, Self SG, Berman PW, Francis D, Sinangil F, Lee C, Tartaglia J, Robb ML, Haynes BF, Michael NL, Kim JH**. 2012. Magnitude and breadth of the neutralizing antibody response in the RV144 and Vax003 HIV-1 vaccine efficacy trials. J. Infect. Dis. **206**:431–441.

229. **O'Connell RJ, Kim JH, Corey L, Michael NL**. 2012. Human immunodeficiency virus vaccine trials. Cold Spring Harb. Perspect. Med. **2**:a007351.

230. **Corti D, Lanzavecchia A**. 2013. Broadly neutralizing antiviral antibodies.Annual review of immunology.

231. **Zhou T, Xu L, Dey B, Hessell AJ, Van Ryk D, Xiang S-H, Yang X, Zhang M-Y, Zwick MB, Arthos J, Burton DR, Dimitrov DS, Sodroski J,**

**Wyatt R, Nabel GJ, Kwong PD**. 2007. Structural definition of a conserved neutralization epitope on HIV-1 gp120. Nature **445**:732–737.

232. **Klein JS, Bjorkman PJ**. 2010. Few and far between: How HIV may be evading antibody avidity. PLoS Pathog. **6**:1–6.

233. **Mascola JR, Montefiori DC**. 2003. HIV-1: nature's master of disguise. Nat. Med. **9**:393–4.

234. **Wei X, Decker JM, Wang S, Hui H, Kappes JC, Wu X, Salazar-Gonzalez JF, Salazar MG, Kilby JM, Saag MS, Komarova NL, Nowak MA, Hahn BH, Kwong PD, Shaw GM**. 2003. Antibody neutralization and escape by HIV-1. Nature **422**:307–312.

235. **Kwong PD, Doyle ML, Casper DJ, Cicala C, Leavitt SA, Majeed S, Steenbeke TD, Venturi M, Chaiken I, Fung M, Katinger H, Parren PWIH, Robinson J, Van Ryk D, Wang L, Burton DR, Freire E, Wyatt R, Sodroski J, Hendrickson WA, Arthos J**. 2002. HIV-1 evades antibody-mediated neutralization through conformational masking of receptor-binding sites. Nature **420**:678–82.

236. **Labrijn AF, Poignard P, Raja A, Zwick MB, Delgado K, Franti M, Binley J, Vivona V, Grundner C, Huang C-C, Venturi M, Petropoulos CJ, Wrin T, Dimitrov DS, Robinson J, Kwong PD, Wyatt RT, Sodroski J, Burton DR**. 2003. Access of antibody molecules to the conserved coreceptor binding site on glycoprotein gp120 is sterically restricted on primary human immunodeficiency virus type 1. J. Virol. **77**:10557–10565.

237. **Abela IA, Berlinger L, Schanz M, Reynell L, Günthard HF, Rusert P, Trkola A**. 2012. Cell-cell transmission enables HIV-1 to evade inhibition by potent CD4bs directed antibodies. PLoS Pathog. **8**.

238. **Duncan CJ a, Williams JP, Schiffner T, Gärtner K, Ochsenbauer C, Kappes J, Russell R a, Frater J, Sattentau QJ**. 2014. High-multiplicity HIV-1 infection and neutralizing antibody evasion mediated by the macrophage-T cell virological synapse. J. Virol. **88**:2025–2034.

239. **Steckbeck JD, Orlov I, Chow A, Grieser H, Miller K, Bruno J, Robinson JE, Montelaro RC, Cole KS**. 2005. Kinetic rates of antibody binding correlate with neutralization sensitivity of variant simian immunodeficiency virus strains. J. Virol. **79**:12311–20.

240. **Adamson DC, Kopnisky KL, Dawson TM, Dawson VL**. 1999. Mechanisms and structural determinants of HIV-1 coat protein, gp41-induced neurotoxicity. J. Neurosci. **19**:64–71.

241. **Lindl KA, Marks DR, Kolson DL, Jordan-Sciutto KL**. 2010. HIV-associated neurocognitive disorder: Pathogenesis and therapeutic opportunities. J. Neuroimmune Pharmacol.

242. **McArthur JC**. 2004. HIV dementia: An evolving disease, p. 3–10. *In* Journal of Neuroimmunology.

243. **Atwood WJ, Berger JR, Kaderman R, Tornatore CS, Major EO**. 1993. Human immunodeficiency virus type 1 infection of the brain. Clin. Microbiol. Rev.

244. **Dickson DW, Mattiace LA, Kure K, Hutchins K, Lyman WD, Brosnan CF**. 1991. Microglia in human disease, with an emphasis on acquired immune deficiency syndrome. Lab Invest **64**:135–156.

245. **Cosenza MA, Zhao M-L, Si Q, Lee SC**. 2002. Human brain parenchymal microglia express CD14 and CD45 and are productively infected by HIV-1 in HIV-1 encephalitis. Brain Pathol. **12**:442–455.

246. **Bagasra O, Lavi E, Bobroski L, Khalili K, Pestaner JP, Tawadros R, Pomerantz RJ**. 1996. Cellular reservoirs of HIV-1 in the central nervous system of infected individuals: identification by the combination of in situ polymerase chain reaction and immunohistochemistry. AIDS **10**:573–585.

247. **Koenig S, Gendelman HE, Orenstein JM, Dal Canto MC, Pezeshkpour GH, Yungbluth M, Janotta F, Aksamit A, Martin MA, Fauci AS**. 1986. Detection of AIDS virus in macrophages in brain tissue from AIDS patients with encephalopathy. Science **233**:1089–1093.

248. **Wiley CA, Schrier RD, Nelson JA, Lampert PW, Oldstone MB**. 1986. Cellular localization of human immunodeficiency virus infection within the brains of acquired immune deficiency syndrome patients. Proc. Natl. Acad. Sci. U. S. A. **83**:7089–7093.

249. **Vazeux R, Brousse N, Jarry A, Henin D, Marche C, Vedrenne C, Mikol J, Wolff M, Michon C, Rozenbaum W**. 1987. AIDS subacute encephalitis. Identification of HIV-infected cells. Am. J. Pathol. **126**:403–410.

250. **T. P-S, B.A. N, C. C-C**. 1987. HIV antigen in the brains of patients with the AIDS dementia complex. Ann. Neurol. **21**:490–496.

251. **Wiley CA, Nelson JA**. 1988. Role of human immunodeficiency virus and cytomegalovirus in AIDS encephalitis. Am. J. Pathol. **133**:73–81.

252. **Kure K, Weidenheim KM, Lyman WD, Dickson DW**. 1990. Morphology and distribution of HIV-1 gp41-positive microglia in subacute AIDS encephalitis - Pattern of involvement resembling a multisystem degeneration. Acta Neuropathol. **80**:393–400.

253. **Kierdorf K, Erny D, Goldmann T, Sander V, Schulz C, Perdiguero EG, Wieghofer P, Heinrich A, Riemke P, Hölscher C, Müller DN, Luckow B, Brocker T, Debowski K, Fritz G, Opdenakker G, Diefenbach A, Biber K, Heikenwalder M, Geissmann F, Rosenbauer F, Prinz M**. 2013. Microglia emerge from erythromyeloid precursors via Pu.1- and Irf8-dependent pathways. Nat. Neurosci. **16**:273–80.

254. **Chan WY, Kohsaka S, Rezaie P**. 2007. The origin and cell lineage of microglia: new concepts. Brain Res. Rev. **53**:344–354.

255. **Neumann H, Wekerle H**. 2013. Brain microglia: watchdogs with pedigree. Nat. Neurosci. **16**:253–255.

256. **Schmidtmayerova H, Nottet HS, Nuovo G, Raabe T, Flanagan CR, Dubrovsky L, Gendelman HE, Cerami A, Bukrinsky M, Sherry B**. 1996. Human immunodeficiency virus type 1 infection alters chemokine beta peptide expression in human monocytes: implications for recruitment of leukocytes into brain and lymph nodes. Proc. Natl. Acad. Sci. U. S. A. **93**:700–704.

257. **Eugenin EA, Osiecki K, Lopez L, Goldstein H, Calderon TM, Berman JW**. 2006. CCL2/monocyte chemoattractant protein-1 mediates enhanced transmigration of human immunodeficiency virus (HIV)-infected leukocytes across the blood-brain barrier: a potential mechanism of HIV-CNS invasion and NeuroAIDS. J. Neurosci. **26**:1098–1106.

258. **Meyenhofer MF, Epstein LG, Cho ES, Sharer LR**. 1987. Ultrastructural morphology and intracellular production of human immunodeficiency virus (HIV) in brain. J. Neuropathol. Exp. Neurol. **46**:474–484.

259. **Brack-Werner R**. 1999. Astrocytes: HIV cellular reservoirs and important participants in neuropathogenesis. AIDS **13**:1–22.

260. **Rutka JT, Murakami M, Dirks PB, Hubbard SL, Becker LE, Fukuyama K, Jung S, Tsugu A, Matsuzawa K**. 1997. Role of glial filaments in cells and tumors of glial origin: a review. J. Neurosurg. **87**:420–30.

261. **Gehrmann J, Matsumoto Y, Kreutzberg GW**. 1995. Microglia: Intrinsic immuneffector cell of the brain. Brain Res. Rev.

262. **Savchenko VL, Nikonenko IR, Skibo GG, McKanna JA**. 1997. Distribution of microglia and astrocytes in different regions of the normal adult rat brain. Neurophysiology **29**:343–351.

263. **Haydon PG, Carmignoto G**. 2006. Astrocyte control of synaptic transmission and neurovascular coupling. Physiol. Rev. **86**:1009–1031.

264. **Malchiodi-Albedi F, Paradisi S, Di Nottia M, Simone D, Travaglione S, Falzano L, Guidotti M, Frank C, Cutarelli A, Fabbri A, Fiorentini C**. 2012. Cnf1 improves astrocytic ability to support neuronal growth and differentiation in vitro. PLoS One **7**.

265. **Eng LF, Ghirnikar RS, Lee YL**. 2000. Glial Fibrillary Acidic Protein: GFAP-Thirty-One Years (1969–2000). Neurochem. Res. **25**:1439–1451.

266. **Middeldorp J, Hol EM**. 2011. GFAP in health and disease. Prog. Neurobiol.

267. **Pekny M, Nilsson M**. 2005. Astrocyte activation and reactive gliosis. Glia.

268. **Eng LF, Ghirnikar RS**. 1994. GFAP and astrogliosis. Brain Pathol. **4**:229–237.

269. **Epstein LG, Sharer LR, Cho ES, Myenhofer M, Navia B, Price RW**. HTLV-III/LAV-like retrovirus particles in the brains of patients with AIDS encephalopathy - Northwestern Scholars - SciVal Experts 4.6. AIDS Res. **1**:447–54.

270. **Churchill MJ, Gorry PR, Cowley D, Lal L, Sonza S, Purcell DFJ, Thompson KA, Gabuzda D, McArthur JC, Pardo CA, Wesselingh SL**. 2006. Use of laser capture microdissection to detect integrated HIV-1 DNA in macrophages and astrocytes from autopsy brain tissues. J. Neurovirol. **12**:146–52.

271. **Trillo-Pazos G, Diamanturos A, Rislove L, Menza T, Chao W, Belem P, Sadiq S, Morgello S, Sharer L, Volsky DJ**. 2003. Detection of HIV-1 DNA in microglia/macrophages, astrocytes and neurons isolated from brain tissue with HIV-1 encephalitis by laser capture microdissection. Brain Pathol. **13**:144–154.

272. **Nuovo GJ, Gallery F, MacConnell P, Braun A**. 1994. In situ detection of polymerase chain reaction-amplified HIV-1 nucleic acids and tumor necrosis factor-alpha RNA in the central nervous system. Am. J. Pathol. **144**:659–666.

273. **Takahashi K, Wesselingh SL, Griffin DE, McArthur JC, Johnson RT, Glass JD**. 1996. Localization of HIV-1 in human brain using polymerase chain reaction/in situ hybridization and immunocytochemistry. Ann. Neurol. **39**:705–711.

274. **Saito Y, Sharer LR, Epstein LG, Michaels J, Mintz M, Louder M, Golding K, Cvetkovich TA, Blumberg BM**. 1994. Overexpression of nef as a marker for restricted HIV-1 infection of astrocytes in postmortem pediatric central nervous tissues. Neurology **44**:474–481.

275. **Tornatore C, Chandra R, Berger JR, Major EO**. 1994. HIV-1 infection of subcortical astrocytes in the pediatric central nervous system. Neurology **44**:481–487.

276. **Ranki A, Nyberg M, Ovod V, Haltia M, Elovaara I, Raininko R, Haapasalo H, Krohn K**. 1995. Abundant expression of HIV Nef and Rev proteins in brain astrocytes in vivo is associated with dementia. AIDS **9**:1001–8.

277. **Nuovo GJ, Alfieri ML**. 1996. AIDS dementia is associated with massive, activated HIV-1 infection and concomitant expression of several cytokines. Mol. Med. **2**:358–366.

278. **Nath A, Hartloper V, Furer M, Fowke KR**. 1995. Infection of human fetal astrocytes with HIV-1: viral tropism and the role of cell to cell contact in viral transmission. J. Neuropathol. Exp. Neurol. **54**:320–30.

279. **McCarthy M, He J, Wood C**. 1998. HIV-1 strain-associated variability in infection of primary neuroglia. J. Neurovirol. **4**:80–89.

280. **Brack-Werner R, Kleinschmidt A, Ludvigsen A, Mellert W, Neumann M, Herrmann R, Khim MC, Burny A, Müller-Lantzsch N, Stavrou D**. 1992. Infection of human brain cells by HIV-1: restricted virus production in chronically infected human glial cell lines. AIDS **6**:273–285.

281. **Harouse JM, Bhat S, Spitalnik SL, Laughlin M, Stefano K, Silberberg DH, Gonzalez-Scarano F**. 1991. Inhibition of entry of HIV-1 in neural cell lines by antibodies against galactosyl ceramide. Science **253**:320–323.

282. **Harouse JM, Laughlin MA, Pletcher C, Friedman HM, Gonzalez-Scarano F**. 1991. Entry of human immunodeficiency virus-1 into glial cells proceeds via an alternate, efficient pathway. J. Leukoc. Biol. **49**:605–9.

283. **Chiodi F, Fuerstenberg S, Gidlund M, Asjö B, Fenyö EM**. 1987. Infection of brain-derived cells with the human immunodeficiency virus. J. Virol. **61**:1244–7.

284. **Liu Y, Liu H, Kim BO, Gattone VH, Li J, Nath A, Blum J, He JJ**. 2004. CD4-independent infection of astrocytes by human immunodeficiency virus type 1: requirement for the human mannose receptor. J. Virol. **78**:4120–4133.

285. **Chesebro B, Buller R, Portis J, Wehrly K**. 1990. Failure of human immunodeficiency virus entry and infection in CD4-positive human brain and skin cells. J. Virol. **64**:215–221.

286. **Keys B, Albert J, Kövamees J, Chiodi F**. 1991. Brain-derived cells can be infected with HIV isolates derived from both blood and brain. Virology **183**:834–839.

287. **Cheng-Mayer C, Rutka JT, Rosenblum ML, McHugh T, Stites DP, Levy JA**. 1987. Human immunodeficiency virus can productively infect cultured human glial cells. Proc. Natl. Acad. Sci. U. S. A. **84**:3526–30.

288. **Volsky B, Sakai K, Reddy MM, Volsky DJ**. 1992. A system for the high efficiency replication of HIV-1 in neural cells and its application to anti-viral evaluation. Virology **186**:303–8.

289. **Ensoli F, Ensoli B, Thiele CJ**. 1994. HIV-1 gene expression and replication in neuronal and glial cell lines with immature phenotype: effects of nerve growth factor. Virology **200**:668–676.

290. **Christofinis G, Papadaki L, Sattentau Q, Ferns RB, Tedder R**. 1987. HIV replicates in cultured human brain cells. Aids **1**:229–234.

291. **Dewhurst S, Sakai K, Bresser J, Stevenson M, Evinger-Hodges MJ, Volsky DJ**. 1987. Persistent productive infection of human glial cells by human immunodeficiency virus (HIV) and by infectious molecular clones of HIV. J. Virol. **61**:3774–3782.

292. **López-Balderas N, Huerta L, Villarreal C, Rivera-Toledo E, Sandoval G, Larralde C, Lamoyi E**. 2007. In vitro cell fusion between CD4+ and

HIV-1 Env+ T cells generates a diversity of syncytia varying in total number, size and cellular content. Virus Res. **123**:138–146.

293. **Sylwester A, Wessels D, Anderson SA, Warren RQ, Shutt DC, Kennedy RC, Soll DR**. 1993. HIV-induced syncytia of a T cell line form single giant pseudopods and are motile. J. Cell Sci. **106 ( Pt 3**:941–953.

294. **Shutt DC, Stapleton JT, Kennedy RC, Soll DR**. 1995. HIV-induced syncytia in peripheral blood cell cultures crawl by extending giant pseudopods. Cell. Immunol. **166**:261–274.

295. **Anderson JM**. 2000. Multinucleated giant cells. Curr. Opin. Hematol. **7**:40–47.

296. **Tornatore C, Nath A, Amemiya K, Major EO**. 1991. Persistent human immunodeficiency virus type 1 infection in human fetal glial cells reactivated by T-cell factor(s) or by the cytokines tumor necrosis factor alpha and interleukin-1 beta. J. Virol. **65**:6094–100.

297. **Weber J, Clapham P, McKeating J, Stratton M, Robey E, Weiss R**. 1989. Infection of brain cells by diverse human immunodeficiency virus isolates: Role of CD4 as receptor. J. Gen. Virol. **70**:2653–2660.

298. **Ma M, Geiger JD, Nath A**. 1994. Characterization of a novel binding site for the human immunodeficiency virus type 1 envelope protein gp120 on human fetal astrocytes. J. Virol. **68**:6824–8.

299. **Sabri F, Tresoldi E, Di Stefano M, Polo S, Monaco MC, Verani A, Fiore JR, Lusso P, Major E, Chiodi F, Scarlatti G**. 1999. Nonproductive human immunodeficiency virus type 1 infection of human fetal astrocytes: independence from CD4 and major chemokine receptors. Virology **264**:370–384.

300. **Dorf ME, Berman MA, Tanabe S, Heesen M, Luo Y**. 2000. Astrocytes express functional chemokine receptors. J. Neuroimmunol. **111**:109–21.

301. **Sanders VJ, Pittman CA, White MG, Wang G, Wiley CA, Achim CL**. 1998. Chemokines and receptors in HIV encephalitis. AIDS **12**:1021–1026.

302. **Gabuzda D, Wang J**. 2000. Chemokine receptors and mechanisms of cell death in HIV neuropathogenesis. J. Neurovirol. **6 Suppl 1**:S24–S32.

303. **Eugenin EA, Clements JE, Zink MC, Berman JW**. 2011. Human immunodeficiency virus infection of human astrocytes disrupts blood-brain barrier integrity by a gap junction-dependent mechanism. J. Neurosci. **31**:9456–9465.

304. **Hao HN, Lyman WD**. 1999. HIV infection of fetal human astrocytes: the potential role of a receptor-mediated endocytic pathway. Brain Res. **823**:24–32.

305. **Gray LR, Turville SG, HItchen TL, Cheng WJ, Ellett AM, Salimi H, Roche MJ, Wesselingh SL, Gorry PR, Churchill MJ**. 2014. HIV-1 entry and trans-infection of astrocytes involves CD81 vesicles. PLoS One **9**.

306. **Neil SJ, Aasa-Chapman MM, Clapham PR, Nibbs RJ, McKnight A, Weiss RA**. 2005. The promiscuous CC chemokine receptor D6 is a functional coreceptor for primary isolates of human immunodeficiency virus type 1 (HIV-1) and HIV-2 on astrocytes. J Virol **79**:9618–9624.

307. **Deiva K, Khiati A, Hery C, Salim H, Leclerc P, Horellou P, Tardieu M**. 2006. CCR5-, DC-SIGN-dependent endocytosis and delayed reverse transcription after human immunodeficiency virus type 1 infection in human astrocytes. AIDS Res Hum Retroviruses **22**:1152–1161.

308. **Chauhan A, Mehla R, Vijayakumar TS, Handy I**. 2014. Endocytosis-mediated HIV-1 entry and its significance in the elusive behavior of the virus in astrocytes. Virology **456-457**:1–19.

309. **Gorry PR, Howard JL, Churchill MJ, Anderson JL, Cunningham A, Adrian D, McPhee DA, Purcell DF**. 1999. Diminished production of human immunodeficiency virus type 1 in astrocytes results from inefficient translation of gag, env, and nef mRNAs despite efficient expression of Tat and Rev. J. Virol. **73**:352–361.

310. **Canki M, Thai JNF, Chao W, Ghorpade A, Potash MJ, Volsky DJ**. 2001. Highly Productive Infection with Pseudotyped Human Immunodeficiency Virus Type 1 (HIV-1) Indicates No Intracellular Restrictions to HIV-1 Replication in Primary Human Astrocytes. J. Virol. **75**:7925–7933.

311. **Gorry PR, Ong C, Thorpe J, Bannwarth S, Thompson KA, Gatignol A, Vesselingh SL, Purcell DFJ**. 2003. Astrocyte infection by HIV-1: mechanisms of restricted virus replication, and role in the pathogenesis of HIV-1-associated dementia. Curr. HIV Res. **1**:463–473.

312. **Messam CA, Major EO**. 2000. Stages of restricted HIV-1 infection in astrocyte cultures derived from human fetal brain tissue. J. Neurovirol. **6 Suppl 1**:S90–S94.

313. **Eugenin EA, Berman JW**. 2007. Gap junctions mediate human immunodeficiency virus-bystander killing in astrocytes. J. Neurosci. **27**:12844–50.

314. **Merrill JE, Koyanagi Y, Zack J, Thomas L, Martin F, Chen IS**. 1992. Induction of interleukin-1 and tumor necrosis factor alpha in brain cultures by human immunodeficiency virus type 1. J. Virol. **66**:2217–25.

315. **Hu S, Ali H, Sheng WS, Ehrlich LC, Peterson PK, Chao CC**. 1999. Gp-41-mediated astrocyte inducible nitric oxide synthase mRNA expression: involvement of interleukin-1beta production by microglia. J. Neurosci. **19**:6468–74.

316. **Zhou BY, Liu Y, Oh Kim B, Xiao Y, He JJ**. 2004. Astrocyte activation and dysfunction and neuron death by HIV-1 Tat expression in astrocytes. Mol. Cell. Neurosci. **27**:296–305.

317. **Brahmachari S, Fung YK, Pahan K**. 2006. Induction of glial fibrillary acidic protein expression in astrocytes by nitric oxide. J. Neurosci. **26**:4930–4939.

318. **Oh JW, Drabik K, Kutsch O, Choi C, Tousson A, Benveniste EN**. 2001. CXC chemokine receptor 4 expression and function in human astroglioma cells. J. Immunol. **166**:2695–704.

319. **Muratori C, Mangino G, Affabris E, Federico M**. 2010. Astrocytes contacting HIV-1-infected macrophages increase the release of CCL2 in response to the HIV-1-dependent enhancement of membrane-associated TNFα in macrophages. Glia **58**:1893–904.

320. **Szymocha R, Akaoka H, Brisson C, Beurton-Marduel P, Chalon A, Bernard A, Didier-Bazes M, Belin MF, Giraudon P**. 2000. Astrocytic alterations induced by HTLV type 1-infected T lymphocytes: a role for Tax-1 and tumor necrosis factor alpha. AIDS Res. Hum. Retroviruses **16**:1723–9.

321. **Boutet A, Salim H, Taoufik Y, Lledo PM, Vincent JD, Delfraissy JF, Tardieu M**. 2001. Isolated human astrocytes are not susceptible to infection by M- and T-tropic HIV-1 strains despite functional expression of the chemokine receptors CCR5 and CXCR4. Glia **34**:165–177.

322. **Lv J, Ma S, Zhang X, Zheng L, Ma Y, Zhao X, Lai W, Shen H, Wang Q, Ji J**. 2014. Quantitative proteomics reveals that PEA15 regulates astroglial Aβ phagocytosis in an Alzheimer's disease mouse model. J. Proteomics.

323. **Sturrock RR**. 1988. The beta astrocyte: its possible role as a central nervous system phagocyte. Anat. Anz. **166**:331–340.

324. **Sokolowski JD, Mandell JW**. 2011. Phagocytic clearance in neurodegeneration. Am. J. Pathol.

325. **Lööv C, Hillered L, Ebendal T, Erlandsson A**. 2012. Engulfing astrocytes protect neurons from contact-induced apoptosis following injury. PLoS One **7**.

326. **Vijaykumar TS, Nath A, Chauhan A**. 2008. Chloroquine mediated molecular tuning of astrocytes for enhanced permissiveness to HIV infection. Virology **381**:1–5.

327. **Heintzmann R, Ficz G**. 2006. Breaking the resolution limit in light microscopy. Brief. Funct. Genomic. Proteomic. **5**:289–301.

328. **Galbraith CG, Galbraith JA**. 2011. Super-resolution microscopy at a glance. J. Cell Sci. **124**:1607–11.

329. **Schermelleh L, Carlton PM, Haase S, Shao L, Winoto L, Kner P, Burke B, Cardoso MC, Agard DA, Gustafsson MGL, Leonhardt H, Sedat JW**. 2008. Subdiffraction multicolor imaging of the nuclear periphery with 3D structured illumination microscopy. Science **320**:1332–1336.

330. **Gustafsson MG**. 2000. Surpassing the lateral resolution limit by a factor of two using structured illumination microscopy. J. Microsc. **198**:82–87.

331. **Wildanger D, Rittweger E, Kastrup L, Hell SW**. 2008. STED microscopy with a supercontinuum laser source. Opt. Express **16**:9614–9621.

332. **Moneron G, Hell SW**. 2009. Two-photon excitation STED microscopy. Opt. Express **17**:14567–14573.

333. **Wildanger D, Medda R, Kastrup L, Hell SW**. 2009. A compact STED microscope providing 3D nanoscale resolution. J. Microsc. **236**:35–43.

334. **Punge A, Rizzoli SO, Jahn R, Wildanger JD, Meyer L, Schönle A, Kastrup L, Hell SW**. 2008. 3D reconstruction of high-resolution STED microscope images. Microsc. Res. Tech. **71**:644–650.

335. **Hell SW, Wichmann J**. 1994. Breaking the diffraction resolution limit by stimulated emission: stimulated-emission-depletion fluorescence microscopy. Opt. Lett. **19**:780–782.

336. **Kohashi T, Koike K**. 2001. A spin-polarized scanning electron microscope with 5-nm resolution. Japanese J. Appl. Physics, Part 2 Lett.

337. **Ven Kouwen L, Botman A, Hagen CW**. 2009. Focused electron-Beam-induced deposition of 3 nm dots in a scanning electron microscope. Nano Lett. **9**:2149–2152.

338. **Joy DC, Pawley JB**. 1992. High-resolution scanning electron microscopy. Ultramicroscopy.

339. **Murphy GE, Jensen GJ**. 2007. Electron cryotomography. Biotechniques.

340. **Haider M, Rose H, Uhlemann S, Kabius B, Urban K**. 1998. Towards 0.1 nm resolution with the first spherically corrected transmission electron microscope. J. Electron Microsc. (Tokyo). **47**:395–405.

341. **Smyth MS, Martin JH**. 2000. x ray crystallography. Mol. Pathol. **53**:8–14.

342. **Ren Y, Kruhlak MJ, Bazett-Jones DP**. 2003. Same serial section correlative light and energy-filtered transmission electron microscopy. J. Histochem. Cytochem. **51**:605–612.

343. **Mishchenko Y**. 2009. Automation of 3D reconstruction of neural tissue from large volume of conventional serial section transmission electron micrographs. J. Neurosci. Methods **176**:276–289.

344. **Hughes L, Hawes C, Monteith S, Vaughan S**. 2014. Serial block face scanning electron microscopy-the future of cell ultrastructure imaging. Protoplasma.

345. **Denk W, Horstmann H**. 2004. Serial block-face scanning electron microscopy to reconstruct three-dimensional tissue nanostructure. PLoS Biol. **2**.

346. **Narayan K, Danielson CM, Lagarec K, Lowekamp BC, Coffman P, Laquerre A, Phaneuf MW, Hope TJ, Subramaniam S**. 2014. Multi-resolution correlative focused ion beam scanning electron microscopy: applications to cell biology. J. Struct. Biol. **185**:278–84.

347. **Van Wilgenburg B, Browne C, Vowles J, Cowley SA**. 2013. Efficient, Long Term Production of Monocyte-Derived Macrophages from Human Pluripotent Stem Cells under Partly-Defined and Fully-Defined Conditions. PLoS One **8**.

348. **Leavy O**. 2013. Macrophages: The shape of things to come. Nat. Rev. Immunol. **13**:775–775.

349. **Yaffe D, Saxel O**. 1977. Serial passaging and differentiation of myogenic cells isolated from dystrophic mouse muscle. Nature **270**:725–727.

350. **Fulco M, Cen Y, Zhao P, Hoffman EP, McBurney MW, Sauve AA, Sartorelli V**. 2008. Glucose Restriction Inhibits Skeletal Myoblast Differentiation by Activating SIRT1 through AMPK-Mediated Regulation of Nampt. Dev. Cell **14**:661–673.

351. **Wei X, Decker JM, Liu H, Zhang Z, Arani RB, Kilby JM, Saag MS, Wu X, Shaw GM, Kappes JC**. 2002. Emergence of resistant human immunodeficiency virus type 1 in patients receiving fusion inhibitor (T-20) monotherapy. Antimicrob. Agents Chemother. **46**:1896–1905.

352. **Derdeyn CA, Decker JM, Sfakianos JN, Wu X, O'Brien WA, Ratner L, Kappes JC, Shaw GM, Hunter E**. 2000. Sensitivity of human immunodeficiency virus type 1 to the fusion inhibitor T-20 is modulated by coreceptor specificity defined by the V3 loop of gp120. J. Virol. **74**:8358–67.

353. **Montefiori DC**. 2009. Measuring HIV neutralization in a luciferase reporter gene assay. Methods Mol. Biol. **485**:395–405.

354. **Ali SH, DeCaprio JA**. 2001. Cellular transformation by SV40 large T antigen: interaction with host proteins. Semin. Cancer Biol. **11**:15–23.

355. **Ahuja D, Sáenz-Robles MT, Pipas JM**. 2005. SV40 large T antigen targets multiple cellular pathways to elicit cellular transformation. Oncogene **24**:7729–7745.

356. **Yang S, Delgado R, King SR, Woffendin C, Barker CS, Yang ZY, Xu L, Nolan GP, Nabel GJ**. 1999. Generation of retroviral vector for clinical studies using transient transfection. Hum. Gene Ther. **10**:123–132.

357. **Ansorge S, Lanthier S, Transfiguracion J, Durocher Y, Henry O, Kamen A**. 2009. Development of a scalable process for high-yield lentiviral vector production by transient transfection of HEK293 suspension cultures. J. Gene Med. **11**:868–876.

358. **Montefiori DC**. 2005. Evaluating neutralizing antibodies against HIV, SIV, and SHIV in luciferase reporter gene assays. Curr. Protoc. Immunol. **Chapter 12**:Unit 12.11.

359. **Godbey WT, Wu KK, Mikos AG**. 1999. Poly(ethylenimine) and its role in gene delivery. J. Control. Release **60**:149–160.

360. **Smale ST**. 2010. Luciferase assay. Cold Spring Harb. Protoc. **2010**:pdb.prot5421.

361. **Kim JH, Song H, Austin JL, Cheng W**. 2013. Optimized Infectivity of the Cell-Free Single-Cycle Human Immunodeficiency Viruses Type 1 (HIV-1) and Its Restriction by Host Cells. PLoS One **8**.

362. **Edmonds TG, Ding H, Yuan X, Wei Q, Smith KS, Conway JA, Wieczorek L, Brown B, Polonis V, West JT, Montefiori DC, Kappes JC, Ochsenbauer C**. 2010. Replication competent molecular clones of HIV-1 expressing Renilla luciferase facilitate the analysis of antibody inhibition in PBMC. Virology **408**:1–13.

363. **Cavrois M, Neidleman J, Greene WC**. 2008. The Achilles Heel of the Trojan horse model of HIV-1 trans-infection. PLoS Pathog.

364. **Wang J-H, Janas AM, Olson WJ, Wu L**. 2007. Functionally distinct transmission of human immunodeficiency virus type 1 mediated by immature and mature dendritic cells. J. Virol. **81**:8933–8943.

365. **Sarzotti-Kelsoe M, Bailer RT, Turk E, Lin C li, Bilska M, Greene KM, Gao H, Todd CA, Ozaki DA, Seaman MS, Mascola JR, Montefiori DC**. 2013. Optimization and validation of the TZM-bl assay for standardized assessments of neutralizing antibodies against HIV-1. J. Immunol. Methods.

366. **Cavrois M, Neidleman J, Kreisberg JF, Greene WC**. 2007. In vitro derived dendritic cells trans-infect CD4 T cells primarily with surface-bound HIV-1 virions. PLoS Pathog. **3**:0038–0045.

367. **McCormack S, Ramjee G, Kamali A, Rees H, Crook AM, Gafos M, Jentsch U, Pool R, Chisembele M, Kapiga S, Mutemwa R, Vallely A, Palanee T, Sookrajh Y, Lacey CJ, Darbyshire J, Grosskurth H, Profy A, Nunn A, Hayes R, Weber J**. 2010. PRO2000 vaginal gel for prevention of HIV-1 infection (Microbicides Development Programme

301): A phase 3, randomised, double-blind, parallel-group trial. Lancet **376**:1329–1337.

368. **Abdool Karim SS, Richardson BA, Ramjee G, Hoffman IF, Chirenje ZM, Taha T, Kapina M, Maslankowski L, Coletti A, Profy A, Moench TR, Piwowar-Manning E, Mâsse B, Hillier SL, Soto-Torres L**. 2011. Safety and effectiveness of BufferGel and 0.5% PRO2000 gel for the prevention of HIV infection in women.AIDS (London, England).

369. **Ji X, Gewurz H, Spear GT**. 2005. Mannose binding lectin (MBL) and HIV. Mol. Immunol.

370. **Hart ML, Saifuddin M, Uemura K, Bremer EG, Hooker B, Kawasaki T, Spear GT**. 2002. High mannose glycans and sialic acid on gp120 regulate binding of mannose-binding lectin (MBL) to HIV type 1. AIDS Res. Hum. Retroviruses **18**:1311–1317.

371. **Nguyen DG, Hildreth JEK**. 2003. Involvement of macrophage mannose receptor in the binding and transmission of HIV by macrophages. Eur. J. Immunol. **33**:483–493.

372. **Eisen S, Dzwonek A, Klein NJ**. 2008. Mannose-binding lectin in HIV infection. Future Virol.

373. **Beck Z, Brown BK, Wieczorek L, Peachman KK, Matyas GR, Polonis VR, Rao M, Alving CR**. 2009. Human erythrocytes selectively bind and enrich infectious HIV-1 virions. PLoS One **4**.

374. **McDonald D**. 2010. Dendritic Cells and HIV-1 Trans-Infection. Viruses.

375. **Liu J, Thorp SC**. 2002. Cell surface heparan sulfate and its roles in assisting viral infections. Med. Res. Rev.

376. **Vivès RR, Imberty A, Sattentau QJ, Lortat-Jacob H**. 2005. Heparan sulfate targets the HIV-1 envelope glycoprotein gp120 coreceptor binding site. J. Biol. Chem. **280**:21353–21357.

377. **Schermelleh L, Carlton PM, Haase S, Shao L, Winoto L, Kner P, Burke B, Cardoso MC, Agard D a, Gustafsson MGL, Leonhardt H, Sedat JW**. 2008. Structured Illumination Microscopy. Science (80-. ). **1332**:4–5.

378. **Murphy GE, Narayan K, Lowekamp BC, Hartnell LM, Heymann JAW, Fu J, Subramaniam S**. 2011. Correlative 3D imaging of whole mammalian cells with light and electron microscopy. J. Struct. Biol. **176**:268–278.

379. **McDonald K, Schwarz H, Müller-Reichert T, Webb R, Buser C, Morphew M**. 2010. “Tips and tricks” for high-pressure freezing of model systemsMethods in Cell Biology.

380. **Mcdonald KL, Webb RI**. 2011. Freeze substitution in 3 hours or less. J. Microsc. **243**:227–233.

381. **Hanahan D, Weinberg RA**. 2011. Hallmarks of cancer: The next generation. Cell.

382. **Blau HM, Pavlath GK, Hardeman EC, Chiu CP, Silberstein L, Webster SG, Miller SC, Webster C**. 1985. Plasticity of the differentiated state. Science **230**:758–766.

383. **Bentzinger CF, Wang YX, Rudnicki MA**. 2012. Building Muscle: Molecular Regulation of Myogenesis. Cold Spring Harb. Perspect. Biol.

384. **Rudnicki MA, Le Grand F, McKinnell I, Kuang S**. 2008. The molecular regulation of muscle stem cell function. Cold Spring Harb. Symp. Quant. Biol. **73**:323–331.

385. **Biressi S, Bjornson CRR, Carlig PMM, Nishijo K, Keller C, Rando TA**. 2013. Myf5 expression during fetal myogenesis defines the developmental progenitors of adult satellite cells. Dev. Biol. **379**:195–207.

386. **Buckingham M**. 2006. Myogenic progenitor cells and skeletal myogenesis in vertebrates. Curr. Opin. Genet. Dev.

387. **Dechat T, Pfleghaar K, Sengupta K, Shimi T, Shumaker DK, Solimando L, Goldman RD**. 2008. Nuclear lamins: major factors in the structural organization and function of the nucleus and chromatin. Genes Dev. **22**:832–853.

388. **Datta K, Guan T, Gerace L**. 2009. NET37, a nuclear envelope transmembrane protein with glycosidase homology, is involved in myoblast differentiation. J. Biol. Chem. **284**:29666–29676.

389. **Liu G-H, Guan T, Datta K, Coppinger J, Yates J, Gerace L**. 2009. Regulation of myoblast differentiation by the nuclear envelope protein NET39. Mol. Cell. Biol. **29**:5800–5812.

390. **Hall MN, Corbett AH, Pavlath GK**. 2011. Regulation of nucleocytoplasmic transport in skeletal muscleCurrent Topics in Developmental Biology.

391. **D'Angelo MA, Gomez-Cavazos JS, Mei A, Lackner DH, Hetzer MW**. 2012. A Change in Nuclear Pore Complex Composition Regulates Cell Differentiation. Dev. Cell.

392. **Capelson M, Doucet C, Hetzer MW**. 2010. Nuclear pore complexes: guardians of the nuclear genome. Cold Spring Harb. Symp. Quant. Biol. **75**:585–597.

393. **Asally M, Yasuda Y, Oka M, Otsuka S, Yoshimura SH, Takeyasu K, Yoneda Y**. 2011. Nup358, a nucleoporin, functions as a key determinant

of the nuclear pore complex structure remodeling during skeletal myogenesis. FEBS J. **278**:610–621.

394. **Zhao R, Bodnar MS, Spector DL**. 2009. Nuclear neighborhoods and gene expression. Curr. Opin. Genet. Dev.

395. **Markaki Y, Gunkel M, Schermelleh L, Beichmanis S, Neumann J, Heidemann M, Leonhardt H, Eick D, Cremer C, Cremer T**. 2010. Functional nuclear organization of transcription and DNA replication: a topographical marriage between chromatin domains and the interchromatin compartment. Cold Spring Harb. Symp. Quant. Biol. **75**:475–492.

396. **Francetic T, Li Q**. 2011. Skeletal myogenesis and Myf5 activation. Transcription **2**:109–114.

397. **Ott MO, Bober E, Lyons G, Arnold H, Buckingham M**. 1991. Early expression of the myogenic regulatory gene, myf-5, in precursor cells of skeletal muscle in the mouse embryo.Development (Cambridge, England).

398. **Sassoon D, Lyons G, Wright WE, Lin V, Lassar A, Weintraub H, Buckingham M**. 1989. Expression of two myogenic regulatory factors myogenin and MyoD1 during mouse embryogenesis. Nature **341**:303–307.

399. **Pinney DF, Pearson-White SH, Konieczny SF, Latham KE, Emerson CP**. 1988. Myogenic lineage determination and differentiation: evidence for a regulatory gene pathway. Cell **53**:781–793.

400. **Wright WE, Sassoon DA, Lin VK**. 1989. Myogenin, a factor regulating myogenesis, has a domain homologous to MyoD. Cell **56**:607–617.

401. **Dedieu S, Mazères G, Cottin P, Brustis J-J**. 2002. Involvement of myogenic regulator factors during fusion in the cell line C2C12. Int. J. Dev. Biol. **46**:235–241.

402. **Londhe P, Davie JK**. 2011. Sequential association of myogenic regulatory factors and E proteins at muscle-specific genes. Skelet. Muscle **1**:14.

403. **Rudnicki MA, Jaenisch R**. 1995. The MyoD family of transcription factors and skeletal myogenesis. Bioessays **17**:203–209.

404. **Sabourin LA, Rudnicki MA**. 2000. The molecular regulation of myogenesis. Clin. Genet. **57**:16–25.

405. **Sartorelli V, Caretti G**. 2005. Mechanisms underlying the transcriptional regulation of skeletal myogenesis. Curr. Opin. Genet. Dev. **15**:528–535.

406. **Hettmer S, Wagers AJ**. 2010. Muscling in: Uncovering the origins of rhabdomyosarcoma. Nat. Med. **16**:171–3.

407. **1. Mastroyiannopoulos NP, Nicolaou P, Anayasa M, Uney JB, Phylactou LA. 2012. Down-regulation of myogenin can reverse terminal muscle cell differentiation. PLoS One 7.Mastroyiannopoulos NP, Nicolaou P, Anayasa M, Uney JB, Phylactou LA**. 2012. Down-regulation of myogenin can reverse terminal muscle cell differentiation. PLoS One **7**.

408. **Myer A, Olson EN, Klein WH**. 2001. MyoD cannot compensate for the absence of myogenin during skeletal muscle differentiation in murine embryonic stem cells. Dev. Biol. **229**:340–350.

409. **Hernandez-Verdun D**. 2006. Nucleolus: From structure to dynamics. Histochem. Cell Biol.

410. **Raška I, Shaw PJ, Cmarko D**. 2006. Structure and function of the nucleolus in the spotlight. Curr. Opin. Cell Biol.

411. **Boisvert F-M, van Koningsbruggen S, Navascués J, Lamond AI**. 2007. The multifunctional nucleolus. Nat. Rev. Mol. Cell Biol. **8**:574–585.

412. **Pawley JB**. 1996. Handbook of Biological Confocal Microscopy, Second Edition. Opt. Eng.

413. **HAYAT MA**. 1981. 9 – Effects of Fixation, p. 262–298. *In* Fixation for Electron Microscopy.

414. **Walther P, Ziegler A**. 2002. Freeze substitution of high-pressure frozen samples: The visibility of biological membranes is improved when the substitution medium contains water. J. Microsc. **208**:3–10.

415. **Delloye-Bourgeois C, Goldschneider D, Paradisi A, Therizols G, Belin S, Hacot S, Rosa-Calatrava M, Scoazec J-Y, Diaz J-J, Bernet A, Mehlen P**. 2012. Nucleolar Localization of a Netrin-1 Isoform Enhances Tumor Cell Proliferation. Sci. Signal.

416. **Scheer U, Rose KM**. 1984. Localization of RNA polymerase I in interphase cells and mitotic chromosomes by light and electron microscopic immunocytochemistry. Proc. Natl. Acad. Sci. U. S. A. **81**:1431–1435.

417. **Wang T, Choi E, Monaco MCG, Campanac E, Medynets M, Do T, Rao P, Johnson KR, Elkahloun AG, Von Geldern G, Johnson T, Subramaniam S, Hoffman D, Major E, Nath A**. 2013. Derivation of neural stem cells from human adult peripheral CD34+ cells for an autologous model of neuroinflammation. PLoS One **8**.

418. **Ciemerych MA, Archacka K, Grabowska I, Przewoźniak M**. 2011. Cell cycle regulation during proliferation and differentiation of mammalian muscle precursor cells. Results Probl. Cell Differ. **53**:473–527.

419. **Morgan DO, Crosby ME**. 2007. Cell Cycle: Principles of Control. Yale J. Biol. Med. Yale Journal of Biology and Medicine.

420. **Derenzini M, Trerè D, Pession A, Montanaro L, Sirri V, Ochs RL**. 1998. Nucleolar function and size in cancer cells. Am. J. Pathol. **152**:1291–1297.

421. **Derenzini M, Trerè D, Pession A, Govoni M, Sirri V, Chieco P**. 2000. Nucleolar size indicates the rapidity of cell proliferation in cancer tissues. J. Pathol. **191**:181–186.

422. **Treré D, Ceccarelli C, Montanaro L, Tosti E, Derenzini M**. 2004. Nucleolar size and activity are related to pRb and p53 status in human breast cancer. J. Histochem. Cytochem. **52**:1601–1607.

423. **Montanaro L, Treré D, Derenzini M**. 2008. Nucleolus, ribosomes, and cancer. Am. J. Pathol. **173**:301–310.

424. **Chow K-H, Factor RE, Ullman KS**. 2012. The nuclear envelope environment and its cancer connections. Nat. Rev. Cancer.

425. **Winey M, Yarar D, Giddings TH, Mastronarde DN**. 1997. Nuclear pore complex number and distribution throughout the Saccharomyces cerevisiae cell cycle by three-dimensional reconstruction from electron micrographs of nuclear envelopes. Mol. Biol. Cell **8**:2119–32.

426. **Feldherr CM, Akin D**. 1993. Regulation of nuclear transport in proliferating and quiescent cells. Exp. Cell Res. **205**:179–186.

427. **Strambio-De-Castillia C, Niepel M, Rout MP**. 2010. The nuclear pore complex: bridging nuclear transport and gene regulation. Nat. Rev. Mol. Cell Biol. **11**:490–501.

428. **Wente SR, Rout MP**. 2010. The nuclear pore complex and nuclear transport. Cold Spring Harb. Perspect. Biol. **2**:a000562.

429. **Chen H, Vermulst M, Wang YE, Chomyn A, Prolla TA, McCaffery JM, Chan DC**. 2010. Mitochondrial fusion is required for mtdna stability in skeletal muscle and tolerance of mtDNA mutations. Cell **141**:280–289.

430. **Youle RJ, van der Bliek AM**. 2012. Mitochondrial Fission, Fusion, and Stress. Science (80-. ).

431. **Gdynia G, Keith M, Kopitz J, Bergmann M, Fassl A, Weber ANR, George J, Kees T, Zentgraf H-W, Wiestler OD, Schirmacher P, Roth W**. 2010. Danger signaling protein HMGB1 induces a distinct form of cell death accompanied by formation of giant mitochondria. Cancer Res. **70**:8558–8568.

432. **Chiche J, Rouleau M, Gounon P, Brahimi-Horn MC, Pouysségur J, Mazure NM**. 2010. Hypoxic enlarged mitochondria protect cancer cells from apoptotic stimuli. J. Cell. Physiol. **222**:648–657.

433. **Davis LE, Hjelle BL, Miller VE, Palmer DL, Llewellyn AL, Merlin TL, Young SA, Mills RG, Wachsman W, Wiley CA**. 1992. Early viral brain invasion in iatrogenic human immunodeficiency virus infection.Neurology.

434. **Williams DW, Eugenin EA, Calderon TM, Berman JW**. 2012. Monocyte maturation, HIV susceptibility, and transmigration across the blood brain barrier are critical in HIV neuropathogenesis. J. Leukoc. Biol.

435. **Yadav A, Collman RG**. 2009. CNS inflammation and macrophage/microglial biology associated with HIV-1 infection. J. Neuroimmune Pharmacol.

436. **Abbott NJ**. 2002. Astrocyte-endothelial interactions and blood-brain barrier permeability. J. Anat.

437. **Allen NJ, Barres BA**. 2009. Neuroscience: Glia - more than just brain glue. Nature **457**:675–7.

438. **Freeman MR**. 2010. Specification and morphogenesis of astrocytes. Science **330**:774–778.

439. **Churchill MJ, Wesselingh SL, Cowley D, Pardo CA, McArthur JC, Brew BJ, Gorry PR**. 2009. Extensive astrocyte infection is prominent in human immunodeficiency virus - associated dementia. Ann. Neurol. **66**:253–258.

440. **Zhong P, Agosto LM, Ilinskaya A, Dorjbal B, Truong R, Derse D, Uchil PD, Heidecker G, Mothes W**. 2013. Cell-to-Cell Transmission Can Overcome Multiple Donor and Target Cell Barriers Imposed on Cell-Free HIV. PLoS One **8**.

441. **Berger EA, Murphy PM, Farber JM**. 1999. Chemokine receptors as HIV-1 coreceptors: roles in viral entry, tropism, and disease. Annu. Rev. Immunol. **17**:657–700.

442. **Gorry PR, Ancuta P**. 2011. Coreceptors and HIV-1 pathogenesis. Curr. HIV/AIDS Rep.

443. **Schweighardt B, Shieh JT, Atwood WJ**. 2001. CD4/CXCR4-independent infection of human astrocytes by a T-tropic strain of HIV-1. J. Neurovirol. **7**:155–162.

444. **Gray LR, Tachedjian G, Ellett AM, Roche MJ, Cheng WJ, Guillemin GJ, Brew BJ, Turville SG, Wesselingh SL, Gorry PR, Churchill MJ**. 2013. The NRTIs Lamivudine, Stavudine and Zidovudine Have Reduced HIV-1 Inhibitory Activity in Astrocytes. PLoS One **8**.

445. **Wiley RD, Gummuluru S**. 2006. Immature dendritic cell-derived exosomes can mediate HIV-1 trans infection. Proc. Natl. Acad. Sci. U. S. A. **103**:738–743.

446. **Fahrbach KM, Barry SM, Ayehunie S, Lamore S, Klausner M, Hope TJ**. 2007. Activated CD34-derived Langerhans cells mediate transinfection with human immunodeficiency virus. J. Virol. **81**:6858–6868.

447. **Koyanagi Y, Miles S, Mitsuyasu RT, Merrill JE, Vinters H V, Chen IS**. 1987. Dual infection of the central nervous system by AIDS viruses with distinct cellular tropisms. Science **236**:819–822.

448. **Gaudin R, Berre S, Alencar B, Decalf J, Schindler M, Gobert FX, Jovive M, Benaroch P**. 2013. Dynamcs of HIV-containing compartments in macrophages reveal sequestration of virions and transient surface connections. PLoS One **8**:e69450.

449. **Chen P, Hübner W, Spinelli MA, Chen BK**. 2007. Predominant mode of human immunodeficiency virus transfer between T cells is mediated by sustained Env-dependent neutralization-resistant virological synapses. J. Virol. **81**:12582–12595.

450. **Hübner W, Chen P, Del Portillo A, Liu Y, Gordon RE, Chen BK, Hubner W, Portillo A**. 2007. Sequence of HIV-1 Gag localization and oligomerization monitored with live confocal imaging of a replication-competent fluorescently tagged HIV-1. J. Virol. **81**:12596–12607.

451. **Tang SB, Levy JA**. 1991. Inactivation of HIV-1 by trypsin and its use in demonstrating specific virus infection of cells. J. Virol. Methods **33**:39–46.

452. **Julien JP, Sok D, Khayat R, Lee JH, Doores KJ, Walker LM, Ramos A, Diwanji DC, Pejchal R, Cupo A, Katpally U, Depetris RS, Stanfield RL, McBride R, Marozsan AJ, Paulson JC, Sanders RW, Moore JP, Burton DR, Poignard P, Ward AB, Wilson IA**. 2013. Broadly Neutralizing Antibody PGT121 Allosterically Modulates CD4 Binding via Recognition of the HIV-1 gp120 V3 Base and Multiple Surrounding Glycans. PLoS Pathog. **9**.

453. **Moldt B, Rakasz EG, Schultz N, Chan-Hui P-Y, Swiderek K, Weisgrau KL, Piaskowski SM, Bergman Z, Watkins DI, Poignard P, Burton DR**. 2012. Highly potent HIV-specific antibody neutralization in vitro translates into effective protection against mucosal SHIV challenge in vivo. Proc. Natl. Acad. Sci.

454. **Sachdev DD, Zerhouni-Layachi B, Ortigoza M, Profy AT, Tuen M, Hioe CE, Klotman ME**. 2009. The differential binding and activity of PRO 2000 against diverse HIV-1 envelopes. J. Acquir. Immune Defic. Syndr. **51**:125–129.

455. **Teleshova N, Chang T, Profy A, Klotman ME**. 2008. Inhibitory effect of PRO 2000, a candidate microbicide, on dendritic cell-mediated human immunodeficiency virus transfer. Antimicrob. Agents Chemother. **52**:1751–1758.

456. **Tabet SR, Callahan MM, Mauck CK, Gai F, Coletti AS, Profy AT, Moench TR, Soto-Torres LE, Poindexter III AN, Frezieres RG, Walsh TL, Kelly CW, Richardson BA, Van Damme L, Celum CL**. 2003. Safety and acceptability of penile application of 2 candidate topical microbicides: BufferGel and PRO 2000 Gel: 3 randomized trials in healthy low-risk men and HIV-positive men.Journal of acquired immune deficiency syndromes (1999).

457. **Mayer KH, Karim SA, Kelly C, Maslankowski L, Rees H, Profy AT, Day J, Welch J, Rosenberg Z**. 2003. Safety and tolerability of vaginal PRO 2000 gel in sexually active HIV-uninfected and abstinent HIV-infected women.AIDS (London, England).

458. **Keller MJ, Zerhouni-Layachi B, Cheshenko N, John M, Hogarty K, Kasowitz A, Goldberg CL, Wallenstein S, Profy AT, Klotman ME, Herold BC**. 2006. PRO 2000 gel inhibits HIV and herpes simplex virus infection following vaginal application: a double-blind placebo-controlled trial. J. Infect. Dis. **193**:27–35.

459. **Lacey CJN, Wright A, Weber JN, Profy AT**. 2006. Direct measurement of in-vivo vaginal microbicide levels of PRO 2000 achieved in a human safety study. AIDS **20**:1027–1030.

460. **Wang J-H, Kwas C, Wu L**. 2009. Intercellular adhesion molecule 1 (ICAM-1), but not ICAM-2 and -3, is important for dendritic cell-mediated human immunodeficiency virus type 1 transmission. J. Virol. **83**:4195–4204.

461. **Naganawa S, Yokoyama M, Shiino T, Suzuki T, Ishigatsubo Y, Ueda A, Shirai A, Takeno M, Hayakawa S, Sato S, Tochikubo O, Kiyoura S, Sawada K, Ikegami T, Kanda T, Kitamura K, Sato H**. 2008. Net positive charge of HIV-1 CRF01 V3 sequence regulates viral sensitivity to humoral immunity. PLoS One **3**.

462. **Balasubramanian C, Chillemi G, Abbate I, Capobianchi MR, Rozera G, Desideri A**. 2012. Importance of V3 Loop Flexibility and Net Charge in the Context of Co-Receptor Recognition. A Molecular Dynamics Study on HIV gp120. J. Biomol. Struct. Dyn.

463. **Chandramouli B, Chillemi G, Giombini E, Capobianchi MR, Rozera G, Desideri A**. 2012. Structural dynamics of V3 loop with different electrostatics: implications on co-receptor recognition: a molecular dynamics study of HIV gp120. J. Biomol. Struct. Dyn.

464. **Hoffman NG, Seillier-Moiseiwitsch F, Ahn J, Walker JM, Swanstrom R**. 2002. Variability in the human immunodeficiency virus type 1 gp120 Env protein linked to phenotype-associated changes in the V3 loop. J. Virol. **76**:3852–3864.

465. **Gali Y, Delezeus O, Brouwers J, Addad N, Augustijins P, Bourlet T, Cognasse H, Aren K, Pozzetto B, Vanhan G**. 2010. In vitro evaluation of viability, integrity, and inflammation in genital epithelia upon exposure

to pharmaceutical excipient and candidate microbicide. Antimicrob. agents Chemother. **54**:5105–5114.

466. **Vogel DY, Heijnen PD, Breur M, de Vries HE, Tool AT, Amor S, Dijkstra CD**. 2014. Macrophages migrate in an activation-dependent manner to chemokines involved in neuroinflammation. J. Neuroinflammation **11**:23.

467. **Grabher C, Cliffe A, Miura K, Hayflick J, Pepperkok R, Rørth P, Wittbrodt J**. 2007. Birth and life of tissue macrophages and their migration in embryogenesis and inflammation in medaka. J. Leukoc. Biol. **81**:263–271.

468. **Kutsch O, Benveniste E, Shaw G, Levy D**. 2002. Direct and quantitative single-cell analysis of HIV-1 reactivation from latency. J. Virol. **76**:8776–8786.

469. **Meckes DG, Raab-Traub N**. 2011. Microvesicles and Viral Infection. J. Virol.

470. **Ratajczak J, Wysoczynski M, Hayek F, Janowska-Wieczorek A, Ratajczak MZ**. 2006. Membrane-derived microvesicles: important and underappreciated mediators of cell-to-cell communication. Leuk. Off. J. Leuk. Soc. Am. Leuk. Res. Fund, U.K **20**:1487–1495.

471. **Inal JM, Ansa-Addo EA, Stratton D, Kholia S, Antwi-Baffour SS, Jorfi S, Lange S**. 2012. Microvesicles in health and disease. Arch. Immunol. Ther. Exp. (Warsz).

472. **Ali SA, Huang M-B, Campbell PE, Roth WW, Campbell T, Khan M, Newman G, Villinger F, Powell MD, Bond VC**. 2010. Genetic characterization of HIV type 1 Nef-induced vesicle secretion. AIDS Res. Hum. Retroviruses **26**:173–192.

473. **Muratori C, Cavallin LE, Krätzel K, Tinari A, De Milito A, Fais S, D'Aloja P, Federico M, Vullo V, Fomina A, Mesri EA, Superti F, Baur AS**. 2009. Massive Secretion by T Cells Is Caused by HIV Nef in Infected Cells and by Nef Transfer to Bystander Cells. Cell Host Microbe **6**:218–230.

474. **Campbell TD, Khan M, Huang MB, Bond VC, Powell MD**. 2008. HIV-1 nef protein is secreted into vesicles that can fuse with target cells and virions. Ethn. Dis. **18**.

475. **Lenassi M, Cagney G, Liao M, Vaupotič T, Bartholomeeusen K, Cheng Y, Krogan NJ, Plemenitaš A, Peterlin BM**. 2010. HIV Nef is secreted in exosomes and triggers apoptosis in bystander CD4+ T cells. Traffic **11**:110–122.

476. **Mack M, Kleinschmidt A, Brühl H, Klier C, Nelson PJ, Cihak J, Plachý J, Stangassinger M, Erfle V, Schlöndorff D**. 2000. Transfer of the chemokine receptor CCR5 between cells by membrane-derived

microparticles: a mechanism for cellular human immunodeficiency virus 1 infection. Nat. Med. **6**:769–775.

477. **Khatua AK, Taylor HE, Hildreth JEK, Popik W**. 2009. Exosomes packaging APOBEC3G confer human immunodeficiency virus resistance to recipient cells. J. Virol. **83**:512–521.

478. **Neumann M, Felber BK, Kleinschmidt A, Froese B, Erfle V, Pavlakis GN, Brack-Werner R**. 1995. Restriction of human immunodeficiency virus type 1 production in a human astrocytoma cell line is associated with a cellular block in Rev function. J. Virol. **69**:2159–2167.

479. **Steain MC, Wang B, Saksena NK**. 2008. The possible contribution of HIV-1-induced syncytia to the generation of intersubtype recombinants in vitro. AIDS **22**:1009–1017.

480. **Stary G, Klein I, Kohlhofer S, Koszik F, Scherzer T, Müllauer L, Quendler H, Kohrgruber N, Stingl G**. 2009. Plasmacytoid dendritic cells express TRAIL and induce CD4+ T-cell apoptosis in HIV-1 viremic patients. Blood **114**:3854–3863.

481. **Chen D, Wang M, Zhou S, Zhou Q**. 2002. HIV-1 Tat targets microtubules to induce apoptosis, a process promoted by the pro-apoptotic Bcl-2 relative Bim. EMBO J. **21**:6801–6810.

482. **Weissman D, Rabin RL, Arthos J, Rubbert A, Dybul M, Swofford R, Venkatesan S, Farber JM, Fauci AS**. 1997. Macrophage-tropic HIV and SIV envelope proteins induce a signal through the CCR5 chemokine receptor. Nature **389**:981–985.

483. **Okamoto M, Wang X, Baba M**. 2005. HIV-1-infected macrophages induce astrogliosis by SDF-1 and matrix metalloproteinases. Biochem. Biophys. Res. Commun. **336**:1214–1220.

484. **Sabri F, Titanji K, De Milito A, Chiodi F**. 2003. Astrocyte activation and apoptosis: their roles in the neuropathology of HIV infection. Brain Pathol. **13**:84–94.

485. **Sofroniew M V., Vinters H V.** 2010. Astrocytes: Biology and pathology. Acta Neuropathol.

486. **Iacono RF, Berría MI**. 1999. Cell differentiation increases astrocyte phagocytic activity. A quantitative analysis of both GFAP labeling and PAS-stained yeast cells. Medicina (B. Aires). **59**:171–175.

487. **Iacono RF, Berría MI**. 2000. A quantitative approach to correlate astrocyte differentiation and phagocytic activity. Biocell **24**:145–150.

488. **Blumberg BM, Gelbard HA, Epstein LG**. 1994. HIV-1 infection of the developing nervous system: central role of astrocytes in pathogenesis. Virus Res. **32**:253–267.

489. **Romer D, Brighty DW, Robson CL, Sattentau QJ**. 2009. Candidate polyanionic microbicides inhibit human T-cell lymphotropic virus type 1 receptor interactions, cell-free infection, and cell-cell spread. Antimicrob. Agents Chemother. **53**:678–687.

490. **Piñon JD, Klasse PJ, Jassal SR, Welson S, Weber J, Brighty DW, Sattentau QJ**. 2003. Human T-cell leukemia virus type 1 envelope glycoprotein gp46 interacts with cell surface heparan sulfate proteoglycans. J. Virol. **77**:9922–9930.

491. **WuDunn D, Spear PG**. 1989. Initial interaction of herpes simplex virus with cells is binding to heparan sulfate. J. Virol. **63**:52–58.

492. **Lehmann MJ, Sherer NM, Marks CB, Pypaert M, Mothes W**. 2005. Actin- and myosin-driven movement of viruses along filopodia precedes their entry into cells. J. Cell Biol. **170**:317–325.

493. **Smith JL, Lidke DS, Ozbun MA**. 2008. Virus activated filopodia promote human papillomavirus type 31 uptake from the extracellular matrix. Virology **381**:16–21.

494. **Schelhaas M, Ewers H, Rajam??ki ML, Day PM, Schiller JT, Helenius A**. 2008. Human papillomavirus type 16 entry: Retrograde cell surface transport along actin-rich protrusions. PLoS Pathog. **4**.

495. **Nikolic DS, Lehmann M, Felts R, Garcia E, Blanchet FP, Subramaniam S, Piguet V**. 2011. HIV-1 activates Cdc42 and induces membrane extensions in immature dendritic cells to facilitate cell-to-cell virus propagation. Blood **118**:4841–4852.

496. **Seifert G, Schilling K, Steinhäuser C**. 2006. Astrocyte dysfunction in neurological disorders: a molecular perspective. Nat. Rev. Neurosci. **7**:194–206.

497. **Johnson TP, Patel K, Johnson KR, Maric D, Calabresi P a, Hasbun R, Nath A**. 2013. Induction of IL-17 and nonclassical T-cell activation by HIV-Tat protein. Proc. Natl. Acad. Sci. U. S. A. **110**:13588–93.

498. **Williams KC, Hickey WF**. 1996. Traffic of lymphocytes into the CNS during inflammation and HIV infection. J. NeuroAIDS. **1**:31–55.

499. **Murooka TT, Deruaz M, Marangoni F, Vrbanac VD, Seung E, von Andrian UH, Tager AM, Luster AD, Mempel TR**. 2012. HIV-infected T cells are migratory vehicles for viral dissemination. Nature.

500. **Heymann JAW, Hayles M, Gestmann I, Giannuzzi LA, Lich B, Subramaniam S**. 2006. Site-specific 3D imaging of cells and tissues with a dual beam microscope. J. Struct. Biol. **155**:63–73.

501. **Heymann JAW, Shi D, Kim S, Bliss D, Milne JLS, Subramaniam S**. 2009. 3D Imaging of mammalian cells with ion-abrasion scanning electron microscopy. J. Struct. Biol. **166**:1–7.

502. **Pekny M, Wilhelmsson U, Bogest??l YR, Pekna M, Bogestål YR**. 2007. The role of astrocytes and complement system in neural plasticity. Int. Rev. Neurobiol. **82**:95–111.

503. **Martin N, Sattentau Q**. 2009. Cell-to-cell HIV-1 spread and its implications for immune evasion. Curr. Opin. HIV AIDS **4**:143–149.

504. **Sourisseau M, Sol-Foulon N, Porrot F, Blanchet F, Schwartz O**. 2007. Inefficient human immunodeficiency virus replication in mobile lymphocytes. J. Virol. **81**:1000–1012.

505. **Rudnicka D, Feldmann J, Porrot F, Wietgrefe S, Guadagnini S, Prévost M-C, Estaquier J, Haase AT, Sol-Foulon N, Schwartz O**. 2009. Simultaneous cell-to-cell transmission of human immunodeficiency virus to multiple targets through polysynapses. J. Virol. **83**:6234–6246.

506. **Hübner W, McNerney GP, Chen P, Dale BM, Gordon RE, Chuang FYS, Li X-D, Asmuth DM, Huser T, Chen BK**. 2009. Quantitative 3D video microscopy of HIV transfer across T cell virological synapses. Science **323**:1743–1747.

507. **Klasse PJ**. 2012. The molecular basis of HIV entry. Cell. Microbiol.

508. **Schertel A, Snaidero N, Han H-M, Ruhwedel T, Laue M, Grabenbauer M, Möbius W**. 2013. Cryo FIB-SEM: volume imaging of cellular ultrastructure in native frozen specimens. J. Struct. Biol. **184**:355–60.

509. **Bai X-C, Fernandez IS, McMullan G, Scheres SHW**. 2013. Ribosome structures to near-atomic resolution from thirty thousand cryo-EM particles. Elife **2**:e00461.

510. **Minagar A, Shapshak P, Fujimura R, Ownby R, Heyes M, Eisdorfer C**. 2002. The role of macrophage/microglia and astrocytes in the pathogenesis of three neurologic disorders: HIV-associated dementia, Alzheimer disease, and multiple sclerosis. J. Neurol. Sci. **202**:13–23.

511. **Koff WC**. 2012. HIV vaccine development: challenges and opportunities towards solving the HIV vaccine-neutralizing antibody problem. Vaccine **30**:4310–5.

512. **Yoo TS, Bliss D, Lowekamp BC, Chen DT, Murphy GE, Narayan K, Hartnell LM, Do T, Subramaniam S**. 2012. Visualizing cells and humans in 3D: biomedical image analysis at nanometer and meter scales. IEEE Comput. Graph. Appl. **32**:39–49.